![IPICYT logo]

INSTITUTO POTOSINO DE INVESTIGACIÓN CIENTÍFICA Y TECNOLÓGICA, A.C.

POSGRADO EN NANOCIENCIAS Y MATERIALES

Design of Plasmonic Gold Nanoantennas and their Evaluation for Photothermal Therapy

Tesis que presenta

I.M. Karla Alejandra López Varela

Para obtener el grado de

Doctora en Nanociencias y Materiales

Director de la Tesis:
Dr. José Luis Rodríguez López

Comité Tutoral
Dr. Francisco Javier González Contreras
Dr. Rubén Hipólito López Revilla
Dr. Miguel Ávalos Borja
Dra. Claudia Escudero Lourdes
Dra. Gladis Judith Labrada Delgado

San Luis Potosí, S.L.P., 26 de Abril del 2018

IPICYT

Constancia de aprobación de la tesis

La tesis *"Design of Plasmonic Gold Nanoantennas and their Evaluation for Photothermal Therapy"* presentada para obtener el Grado de Doctora en Ciencias Aplicadas en la opción de Nanociencias y Nanotecnología fue elaborada por **Karla Alejandra López Varela y** aprobada el **veintiséis de abril del dos mil diecisiete** por los suscritos, designados por el Colegio de Profesores de la División de Materiales Avanzados del Instituto Potosino de Investigación Científica y Tecnológica, A.C.

Dr. José Luis Rodríguez López
Director de la tesis

Dra. Gladis Judith Labrada Delgado
Miembro del Comité Tutoral

Dr. Rubén Hipólito López Revilla
Miembro del Comité Tutoral

Dr. Miguel Avalos Borja
Miembro del Comité Tutoral

Dr. Francisco Javier González Contreras
Miembro del Comité Tutoral

Dra. Claudia Escudero Lourdes
Miembro del Comité Tutoral

Institutional Credits

The present thesis was carried out in the Laboratory of Synthesis, Properties and Applications of Nanostructures of the Advanced Materials Division of the Institute for Scientific & Technological Research at San Luis Potosí, under the supervision of PhD. José Luis Rodríguez López.

While performing the work the author received a scholarship from the National Council for Science and Technology (Registry No. 250290) and from the Institute for Scientific & Technological Research at San Luis Potosí.

Esta tesis fue elaborada en el Laboratorio de Síntesis, Propiedades y Aplicaciones de Nanoestructuras de la División de Materiales Avanzados del Instituto Potosino de Investigación Científica y Tecnológica, A.C., bajo la dirección del Dr. José Luis Rodríguez López.

Durante la realización del trabajo el autor recibió una beca académica del Consejo Nacional de Ciencia y Tecnología (No. de registro 250290) y del Instituto Potosino de Investigación Científica y Tecnológica, A. C.
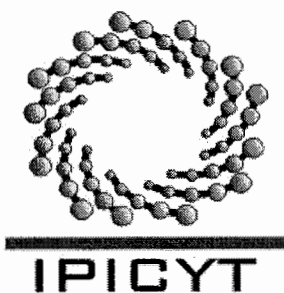
Instituto Potosino de Investigación Científica y Tecnológica, A.C.

Acta de Examen de Grado

El Secretario Académico del Instituto Potosino de Investigación Científica y Tecnológica, A.C., certifica que en el Acta 047 del Libro Primero de Actas de Exámenes de Grado del Programa de Doctorado en Ciencias Aplicadas en la opción de Nanociencias y Nanotecnología está asentado lo siguiente:

En la ciudad de San Luis Potosí a los 26 días del mes de abril del año 2018, se reunió a las 16:00 horas en las instalaciones del Instituto Potosino de Investigación Científica y Tecnológica, A.C., el Jurado integrado por:

Dr. Miguel Avalos Borja	**Presidente**	**IPICYT**
Dr. Francisco Javier González Contreras	**Secretario**	**UASLP**
Dra. Claudia Escudero Lourdes	**Sinodal externo**	**UASLP**
Dra. Gladis Judith Labrada Delgado	**Sinodal**	**IPICYT**
Dr. Rubén Hipólito López Revilla	**Sinodal**	**IPICYT**

a fin de efectuar el examen, que para obtener el Grado de:

DOCTORA EN CIENCIAS APLICADAS
EN LA OPCION DE NANOCIENCIAS Y NANOTECNOLOGÍA

sustentó la C.

Karla Alejandra López Varela

sobre la Tesis intitulada:

Design of Plasmonic Gold Nanoantennas and their Evaluation for Photothermal Therapy

que se desarrolló bajo la dirección de

Dr. José Luis Rodríguez López

El Jurado, después de deliberar, determinó

APROBARLA

Dándose por terminado el acto a las 18:10 horas, procediendo a la firma del Acta los integrantes del Jurado. Dando fe el Secretario Académico del Instituto.

A petición de la interesada y para los fines que a la misma convengan, se extiende el presente documento en la ciudad de San Luis Potosí, S.L.P., México, a los 26 días del mes de abril de 2018.

Dr. Horacio Flores Zúñiga
Secretario Académico

Mtra. Ivonne Lizette Cuevas Vélez
Jefa del Departamento del Posgrado

INSTITUTO POTOSINO
DE INVESTIGACIÓN
CIENTÍFICA Y TECNOLÓGICA, A.C.
IPICYT
SECRETARIA ACADEMICA

This work is dedicated to my advisor
PhD. José Luis Rodríguez López

Great things are done by a series
of small things brought together.
Vincent Van Gogh

Acknowledgments

Along this process I had been blessed with the support, knowledge and so many life lessons from my beloved family and my dearest friends. I will always be thankful to all of you.

Table of Contents

Resumen

Diseño de Nanoantenas Plasmónicas de Oro y su Evaluación para Terapia Fototérmica

Las nanopartículas de oro (AuNPs) anisotrópicas han destacado como materiales con propiedades prometedoras para ser aplicados en la terapia fototérmica localizada (PTT) de células malignas. Las AuNPs anisotrópicas tienen la facilidad de modular la respuesta de la resonancia del plasmón superficial (SPR), siendo esto una respuesta óptica clave para su aplicación como agentes teranósticos (nanoantenas). Para este propósito, las nanopartículas con ramificaciones son un modelo ideal, debido a la concentración de campo electromagnético en sus vértices. En este trabajo, estandarizamos el protocolo de síntesis de nanopartículas de oro multirramificadas (MB-AuNPs) mediante el método de dos pasos (semilla – crecimiento). La respuesta óptica de las MB-AuNPs fue evaluada por espectroscopia UV-Vis y su morfología por microscopía electrónica de barrido y transmisión (SEM y TEM) Una vez evaluado su respuesta óptica y la monodispersidad del coloide, las MB-AuNPs fueron evaluadas por termografía dinámica (DIRT) en un matriz modelo de las propiedades de la piel.[1] La densidad de partículas presentes en el coloide sintetizado, fue determinado mediante espectroscopia de plasma inducido (ICP). Cuando se pretende aplicar un sistema nanoestructurado en áreas biológicas, es necesario el diseño cuidadoso de la cobertura, ya que las moléculas en su superficie van a proporcionar las señales que determinen su tiempo de circulación por la sangre, su biocompatibilidad y la selectividad al sitio objetivo para administrar la terapia. Debido a esto, y con la intención de diseñar MB-AuNPs para aplicaciones médicas, se diseñó un conjugado con albúmina sérica bovina (MB-AuNPs@BSA). La evaluación mas básica de la formación del conjugado se realizó por espectroscopias UV-Vis y de fluorescencia. La interacción de la proteína con la superficie de la MB-AuNPs fue analizada por espectroscopia Raman, y así se determinó la permanencia de su estructura básica y por lo tanto de su función. La formación de una corona proteica fue determinada mediante la cuantificación de proteína por UV-Vis y micrografías HRTEM del conjugado. La eficiencia y estabilidad del conjugado fue analizada por medición del potencial Z y a través de la interacción del complejo con cibacron blue. Finalmente, se llevaron a cabo análisis toxicológicos de las MB-AuNPs y del conjugado en diferentes líneas celulares. Los modelos *in-vitro* elegidos forman parte de los principales sistemas con los pueden interactuar las nanopartículas de forma inintencionada después de ser administradas vía intravenosa. Se evaluó la viabilidad celular y la proliferación por conteo con hematímetro, así como la actividad mitocondrial y la integridad de la membrana plasmática por métodos colorimétricos.

PALABRAS CLAVE. Nanopartículas de oro, estructuras ramificadas, modelos simuladores de piel humana, termografía dinámica infrarroja, conjugación con proteínas, citotoxicidad.

(1)   López-Varela, K.A.; Cayetano-Castro, N.; Kolosovas-Machuca, E.S.; González, F.J.; Chiwo, F.S.; and Rodríguez-López, J.L., Dynamic Infrared Thermography of Nanoheaters Embedded in Skin-Equivalent Phantoms. *J. Nanomater.* **2018**, *2018*, 1–8. DOI: 10.1155/2018/3847348.

Abstract

Design of Plasmonic Gold Nanoantennas and their Evaluation for Photothermal Therapy

Anisotropic gold nanoparticles (AuNPs) are known as promising tools for localized photo-thermal therapy (PTT) of malignant cells. These anisotropic AuNPs present tunable surface plasmon resonances (SPR) with ideal NIR optical response to be applied as theranostic agents (nanoantennas systems). To this purpose, nanoparticles with branches are suitable because of the electromagnetic field concentrated at their vertices. In this work, we standardized a protocol to synthesize multibranched gold nanoparticles (MB-AuNPs) by the seed-growth method, and found size-seed dependence tunability on the hierarchy of branching. The optical response of MB-AuNPs was evaluated by UV-Vis spectroscopy, and their morphology by electronic microscopy (SEM and HRTEM). Once evaluated the optical response and monodispersity of AuNPs, we tested the MB-AuNPs immersed in skin-equivalent phantoms by dynamic infrared thermography (DIRT).[1] The particle density of the synthesized colloids, has being determined by inducted coupled plasma spectrometry (ICP).

Once a nano-synthesized system is being intended for biological purposes, it is necessary to carefully design the surface layer. In principle, the molecules at the surface of nanoparticles (NPs) will provide the signals to its long-term circulation, their biocompatibility and the selectivity to target cellular sites. Therefore, in this work and for intended medical applications of MB-AuNPs, a conjugated complex was prepared with bovine serum albumin (MB-AuNPs@BSA). The optical signals of the conjugate formation were evaluated by UV-Vis and fluorescence spectroscopy. The interaction of the protein with the surface of the MB-AuNPs was analyzed by Raman spectroscopy, to ensure the structure and function preservation of the protein. The full formation of a protein corona was determined by protein quantification in a microplates reader and later observed by HRTEM. The efficiency and stability of the conjugated was analyzed by Z-potential and through the interaction of the conjugated complex with cibacron blue.
Toxicological test of bare MB-AuNPs and MB-AuNPs@BSA were performed in different cell lines. The models in-vitro were chosen according to main systems of indirect interaction of intravenously administered NPs. Cell viability and proliferation, mitochondrial activity and membrane integrity were analyzed.

(1)   López-Varela, K.A.; Cayetano-Castro, N.; Kolosovas-Machuca, E.S.; González, F.J.; Chiwo, F.S.; and Rodríguez-López, J.L., Dynamic Infrared Thermography of Nanoheaters Embedded in Skin-Equivalent Phantoms. *J. Nanomater.* **2018**, *2018*, 1–8. DOI: 10.1155/2018/3847348.

1. General Introduction

Chapter Contents

1.1. Cancer as Fundamental Scientific Research and Social Problem

Cancer cells break the most basic rules of cell behavior by which multicellular organisms are built and maintained, and they exploit every kind of opportunity to do so. The effort to combat cancer has led to many fundamental discoveries in cell biology. Many proteins have been discovered because abnormalities in their function can lead to uncontrolled growth, increased division, decreased death, or other aberrant characteristics of cancer cells.[1]

1.1.1. Historical Facts

Human paleopathology, is the study of abnormalities and disease in ancient populations, by the examination of human remains. Teaches us that tumors have existed as long as humans and animals have been on this planet. The first forms of cancer were found in animal bones, specifically, in the tail of dinosaur found in Wyoming, United States. One of the tail vertebrae shows a growth, there is a discussion about if is a vascular tumor or an exostosis. A similar discussion developed in connection with an abnormality found on the shaft of a femur of Homo erectus, discovered on Java in the nineteenth century.[2] An exostosis, is a benign bony enlargement of the deeper portion of the external auditory meatus. This lesion accounts for nearly half of all benign bone tumors, most of them develops in humans before the age 30. The hereditary condition of multiple exostosis syndrome, involves multiple bones in which an occasional one may undergo malignant degeneration.[3] A Paleolithic skull with seven holes in it was discovered in the Joan d'Os cave in the Pyrenees, this condition has been ascribed to a multiple myeloma or to lytic metastases of a carcinoma. Osteosarcomas, a strongly proliferating cancer, were discovered in the upper arm of a human skeleton, and in the femur of a cave bear; both dating from the last ice age in Münsingen in Switzerland. Nasopharyngeal carcinomas and osteosarcomas have been identified in human mummies from ancient Egypt, and also human remains showing traces of cancer have been found in Peru.[2]

The oldest written descriptions of medical matters have been found on Egyptian papyrus. In the Edwin Smith papyri, written around 2650 B.C, the text deals mainly with wounds and their treatment, but also describes eight cases of disease, for which the writing says "there is no treatment". There were tumors or ulcers of the breast that were removed by cauterization with a tool called the fire drill. It is assumed that most of the information in the Edwin Smith papyrus, is derived from documents written in the time of Imhotep, the highest priest, physician, and architect of the first pyramid and vizier to King Djoser. The Ebers papyrus, with 110 pages is the longest of all the medical papyrus. It describes prescriptions and medicaments, and

mentions a number of different tumors classified in the time within the inflammations, and even if not distinction was yet made between tumors and inflammations, they were distinguished among them and the different types of treatments required. The Kahoun papyrus from 1950 BC, contains a description of a uterine carcinoma that mentions the peculiar smell of burnt flesh and the specific pains associated with this condition.[2,4]

The ancient Sanskrit epic *Ramayana*, is part of the Hindu scriptures. It describes events that are supposed to have taken place around 1200-1000 B.C. and was written down around 400-200 B.C. It contains descriptions of cancers and their treatment.[2]

In ancient China, India, Persia, Babylonia and Egypt they believed in the "will of the gods" and religious dogmas overruled rational thinking, and the natural disasters and the illnesses were beyond human understanding and could not be controlled by the common human beings. And they think that the only possible salvation laid in the hands of the priests, who offered human and animal sacrifices. Unlike the previous cultures, the Hellenistic thinking was "every free man is master of his own fate", and this led to the development of democracy and intellectual approach based more on the knowledge than on belief. One of the exponents of this new approach was the physician Hippocrates (460-377 BC), known as the "father of medicine". Probably his most important contribution was that he liberated medicine from the shackles of religion, superstition and magic and that he paved the way for a scientific approach based on systematic, accurate observation and logical thinking.[2]

Hippocrates introduced a theory or the cause of disease based on the ideas of the Greek natural philosopher Empedocles (490–430 BC), according to whom the universe was built up of four elements: *earth*, *air*, *fire* (energy) and *water*. Hippocrates thought that the body was built up of the four fluids, known as the humors, they were the *biological counterparts* of these elements. The blood, formed in the heart, was the counterpart of air; phlegm, originating in the brain, corresponded to water; black bile, originating in the spleen, to earth; and yellow bile

from the liver to fire. He regarded health as due to a proper balance in the admixture of these humors, and disease as due to an unbalanced mixture. Too much or too little blood, phlegm or bile was the reason for all diseases. This theory of the constitution of the body and the cause of disease later came to be known as the *humoral theory*. **Hippocrates postulated that the cancer was the result of too much black bile**.

The medical term **oncology** is a derived Greek word for tumor "*oncos*"; Hippocrates coined the terms "*carcinos*" and "*carcinoma*" to describe a non-ulcerating and ulcerating tumors. *Carcinos* means **crab** in Greek, while the corresponding Latin word is **cancer**. It is thought that Hippocrates may have used the term crab because untreated breast cancer is often surrounded by swollen veins resembling the many legs of a crab. Hippocrates also used the terms "*scirrhos*" which means hard, to describe tumors that feel hard on palpation. He was the first to divide tumors into "*benign*" and "*malignant*". He probably included swellings due to inflammation as well as less life-threating tumors under the heading benign.

After the fall of the Greek empire, Rome took over the task of supporting the development of the scientific knowledge of medicine. Aurelius Cornelius Celsus (30 BC – AD 38) was a member of an aristocratic Roman family, who was probably not a physician but an encyclopedist. He translated the Greek term *carcinos* into cancer, and drew up a classification of the various forms of cancer. He also described edema due to the pressure of a tumor on the surrounding tissue, and considered the reaction of the lymphatic system as a subsidiary symptom of cancer. He was the first to discover the phenomenon of metastasis.

The Greek physician Claudius Galenus (130-200 AD), elaborated the medical system originally developed by Hippocrates, he was defensor of the humoral theory, and believed that the deposition of black bile in certain parts of the body such as the lips, tongue or breast led to the development of tumors that he called cancer. He also introduced the term *sarcoma* (from the Greek *sarcos* = flesh) to describe a tumor that looked meaty when cut through.[2]

Sun Simiao (581-672), a Chinese physician during the Tang dynasty (618-907) described most diseases, including cancer. He divided tumors into six types: *bony, fatty, stony* and *suppurating*, and *tumors of the muscles* and the *blood vessels*. Xue Ji (1488-1558) a physician of the Ming dynasty, gives a different classification of cancers than that of Sun Simiao in his *Wake Shuyao* (Essentials of external medicine). Xue Ji distinguished tumors of the *circulatory system*, from those of *respiratory organs*, *the muscles, the nerves* and *the bones*.

During the Middle Ages, from 10th to 14th century, healing was only possible by prayers and divine intervention; astrology, alchemy, magic and exorcism replaced a rational approach to the diagnosis and treatment of diseases, including cancer. Because of that, no advances of any significance were achieved during this whole period. The first autopsy since the days of Ptolemy in Alexandria was performed in 1286 in Cremona, and it was performed to trace the cause of a mysterious epidemic. A forensic post-mortem was performed in Bologna in 1302, and after that, autopsies were carried out increasingly often, not only to track down diseases or to support court judgments but also for educational purposes. Modino de Liuzzi (1275-1326), adscribed to the University of Bologna as a physician and anatomist, performed autopsies to support his lectures.

At the Renaissance the rationalist style of argumentation on a metaphysical basis that had held sway from the time of Galen was now given a more empirical slant, with experiment as the basis. William Harvey (1578-1657) described the circulation of the blood in 1628. Gasparo Aselli (1581-1626) was the first author to publish an account of the lymphatic system. The Flemish physician and anatomist Andries van Wesel, better known under the name of Vesalius (1514-1564), was the author of the first complete textbook of anatomy, entitled De *humani corporis fabrica libri septem* (Seven books on the workings of the human body). Vesalius was unable to discover black bile in the course of his experiments, though there was plenty of blood and lymph. The discovery of lymph gradually caused this fluid to replace black bile in medical thinking, and then the French philosopher and mathematician René Descartes (1596-1650) put forward his "*Lymph Theory*" of the etiology of cancer. He

postulated that when lymph leakeage out of the lymph ducts, the fluid gave rise to a benign tumor. However, when the lymph was subjected to local fermentation or degeneration, a malignant tumor were produced. John Hunter (1728-1793), a Scottish surgeon claimed that tumor tissue, like normal tissue, receives its nourishment from the host and develops in accordance with the same fundamental biological laws. He further stated that "*coagulated lymph*", later identified as fibrin, was the omnipotent "*blastema*" from which both normal and pathologic organisms grew.[2] He also suggested that some cancers might be cured by surgery and described how the surgeon might decide which cancers to operate on. If the tumor had not invaded nearby tissue and was "*moveable*", he said, "*there is no impropriety in removing it*".[4] The Parisian surgeon Henri Francois le Dran (1685-1770), rejected the humoral doctrine in favor of the theory that cancer is a local complaint, at least in its early stages, and the passage of a single drop of cancerous lymph through one of the neighboring lymph nodes was enough to contaminate the entire system.[2]

The seventeenth-century medical literature contains a few sparse mentions of the finding of hard, enlarged glands in the ipsilateral armpit in cases of breast cancer. There were no explicit mentions of cancer as the cause of death, though there was a vague idea that death was due to a toxin secreted by the cancer. The Italian professor of anatomy Hieronymus Fabricius (1537-1619) drew a distinction between swellings due to inflammation and cancers, and warned against incomplete removal of the tumor. The Italian surgeon Marcus Aurelius Severinus (1580-1656) described the myxosarcoma (a sarcoma of the soft tissues). He distinguished between cancers and benign swellings of the breast. If he operated on the breast, he also removed the lymph nodes.

The first cancer hospital in the world was opened at 1740 in Rheims by Jean Godinot, with the aim of relieving the physical and mental suffering of cancer patients. Bernard Peyrilhe (1735-1804) was the first in the literature to suggest that a liquid living agent of infection, later identified as a virus, could be the cause of cancer. He demonstrated that cancer starts as a local process and spreads along the lymph ducts. Eighteenth-century publications on the nature of cancer were the first to demonstrate an incipient

understanding of the problem of metastasis. In 1735, De Gorter wrote about "cancerous substances" which, having gained access to the blood circulation, can give rise to a metastasis from one gland to another. Joseph Récamier (1774-1852) described the way in which cancer cells could penetrate blood vessels.

There were important advances in the field of pathological anatomy in the period from 1761 to 1845. Giovanni Battista Morgagni (1682-1771), a Padua anatomist, correlated the autopsy findings for seven hundred patients with their clinical data. He made a systematic descriptions of the diseases of the head, the thoracic cavity, the abdomen, etc. Morgagni, who is sometimes called the father of pathological anatomy, differentiated between malignant neoplasms and benign swellings due for example to aneurysms, strumas, gummas, exostoses, steatomas, and he also described cancers of the lungs, esophagus, stomach, rectum and uterus.[5] The pathologist Marie-Francois Xavier Bichat (1771-1802) distinguished between the *tumorous parenchyma* (essential element of the growth) and its *non-tumorous stroma* (framework), thus indicating that one and the same lesion could have two aspects, one malignant and the other benign. His investigations further corroborated previous suggestions that cancers were not built up of black bile or lymph.[2]

René Théophile Hyacinthe Laënnec (1781-1826) was pupil of Bichat, he invented the stethoscope, and stated that tumors could grow in all types of tissues, he regarded cancer as abnormal growth of normal tissue. After François Raspail (1794-1878) introduced the freeze-cut technique in 1827, made possible to cut thin sections of tissue so that they could be studied under a microscope. Sir Everard Home (1756-1832) was the first to publish a book on cancer containing data obtained with the aid of a microscope, including illustrations showing microscopic sections of cancerous tissue. The German pathologist Johannes Müller (1801-1858) stated that there was no essential difference between the structure of cancerous growths and that of normal tissue. He distinguished the different types of tumors on the basis of their microscopic structure and described *anaplasia* as a widely occurring phenomenon, definitively demonstrating that cancers are built up of cells and not of coagulated lymph. He believed, however, that the cancer cells were not derived from normal

tissue but grew out of a mass of undifferentiated cells known as blastema that was interspersed between normal tissues. Rudolf Virchow (1821-1902) student of Müller, suggested that the cell is the key element in the origin of cancer.

The *blastema theory* of the origin of cancer was further elaborated by Julius Vogel (1814-1880) in 1845 when the posited that each tissue had its own blastema. Vogel assumed that tumors developed from amorphous blastema, which was converted into cells under the influence of the histological and chemical environment. Friedrich Führer expanded the blastema theory. He distinguished three types of blastema, the albuminous (turbid, proteinoid), the chondromatous (cartilaginous) and the gelatinous, each type being responsible for a particular type of cancer. Adolph Hannover (1814-1894) from Copenhagen published in 1843 the book *Das Epithelioma*, in which he observed that cancer cells often resemble epithelial cells, this led him to coin the term *epithelioma* for cancer. Epithelium is derived from the Greek epi, meaning on or above, and thele meaning nipple. The meaning of this word has gradually expanded to include all tissue covering the skin and internal cavities of the bodies; the endothelium and mesothelium are specialized forms of epithelium. The term epithelioma has been gradually replaced by carcinoma.[2]

Virchow stated the *Omnis Cellula e Cellula Theory*, at his book *Cellular Pathology*, the cell was the fundamental unit in which disease processes operate and that all cells arose from other cells, but he did not assume that the initial cell in this line was derived from blastema.[6] One of the Virchow law's apply to oncology is that "each tumor originates from the cells of the organ in which it develops".[2] According to Virchow, the manner in which metastatic diffusion takes place is by means of certain fluids and these possess the power of producing an infection which disposes different parts to ta reproduction of a mass of the same nature as the one which originally existed. Robert Remak (1815-1865) studied skin cancers with the aid of serial microscopic sections, and he showed that epitheliomas were of epithelial origin and that metastases take place out of these cells. Heinrich Wilhelm von Waldeyer-Hastz (1836-1921) came to the same conclusion for gastroenterologic tumors, he also explained how metastases could be formed as the result of the growth of the

tumor through the wall of the blood vessels and lymph ducts, and described the formation of cancer-cell embolisms.

In 1886, the French internist Louis Bard (1857-1930) summarized the conclusions of most of his predecessors concerning the genesis of cancer, he postulated that a tissue can only produce a tumor with the same histologic structure as itself.[2]

## 1.1.2.	Basics of Cancer

## 1.1.2.1.	Normal Cells and Tissues

The tissues of the body can be divided into four main groups:

- The mesenchyme: general supporting tissues collectively.
- The epithelium: tissue specific cells.
- The hemato-lymphoid system: the defense cells.
- The nervous system.

The mesenchyme consists of connective tissue fibroblasts which make collagen fibers and associated proteins, bone, cartilage, muscle, blood vessels, and lymphatic. The epithelial cells are the specific, specialized cells of the different organs, for example, skin, intestine, liver, glands, etc. The hemato-lymphoid system consists of a wide group of cells, mostly derived from precursor cells in the bone marrow which give rise to all the red and white blood cells. In addition, some of these cells (lymphocytes and macrophages) are distributed throughout the body either as free cells or as fixed constituents of other organs, for example, in the liver, or as separate organs such as the spleen and lymph nodes. Lymph nodes are specialized nodules of lymphoid cells, which are distributed throughout the body and act as filters to remove cells, bacteria, and other foreign matter. The nervous system is made up of the central nervous system (the brain and spinal cord and their coverings) and the peripheral nervous system, which is comprised of nerves leading from these central structures.[7]

The specific cells are grouped in organs which have a standard pattern (Fig. 1.1). There is a layer of epithelium, the tissue-specific cells, separated from the supporting mesenchyme by a semipermeable basement membrane. The supporting tissues (or stroma) are made up of connective tissue (collagen fibers) and fibroblasts (which make collagen), which may be supported on a layer of muscle and/or bone depending on the organ. Blood vessels, lymphatic vessels, and nerves pass through

13

the connective tissue and provide nutrients and nervous control among other things for the specific tissue cells. In some instances, for example, the skin and intestinal tract, the epithelium which may be one or more cells thick depending on the tissue, covers surfaces. In others it may form a system of tubes (*e.g.* in the lung or kidney), or solid cords (*e.g.* liver), but the basic pattern remains the same. Different organs differ in structure only in the nature of the specific cells and the arrangement and distribution of the supporting mesenchyme.[7]
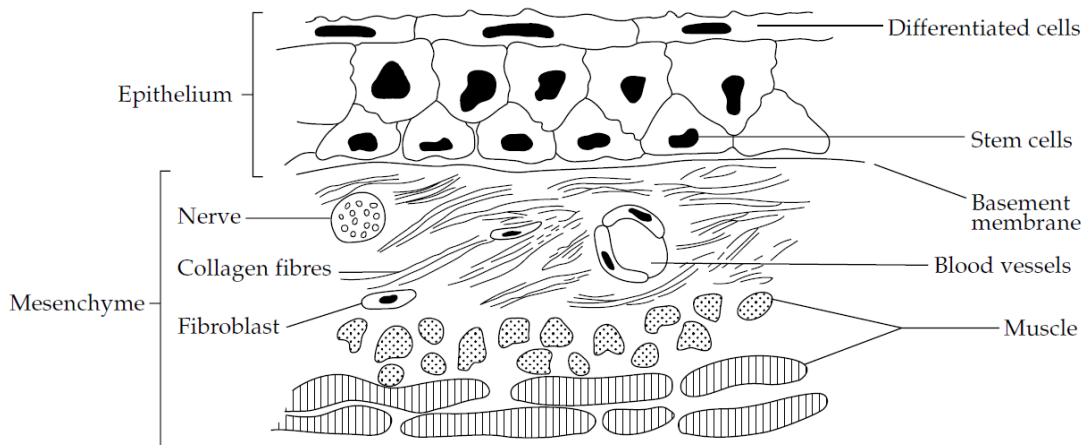
Figure 1.1.   A typical tissue showing epithelial and mesenchymal components.

1.1.2.2.   Control of Growth in Normal Tissues

It is important to make the distinction between the terms 'growth' and 'proliferation'. Growth is used here to refer to an increase in size of a cell, organ, tissue, or tumor and proliferation to an increase in the number of cells by division. 'Growth' is often used as a loose term for both of these processes but the distinction is particularly important now that factors controlling both of these processes are becoming clear. In normal development and growth there is a very precise mechanism that allows individual organs to reach a fixed size, which for all practical purposes, is never exceeded. If a tissue is injured, the surviving cells in most organs begin to divide to replace the damaged cells. When this has been completed, the process stops, that is, the normal control mechanisms persist throughout life. Although most cells in the embryo can proliferate, not all adult cells retain this ability. In most organs there are

14

special reserve or stem cells, which are capable of dividing in response to a stimulus such as an injury to replace organ-specific cells. The more highly differentiated a cell is, for example, muscle or nerve cells, the more likely it is to have lost its capacity to divide. In some organs, particularly the brain, the most highly differentiated cells, the nerve cells, can only proliferate in the embryo, although the special supporting cells in the brain continue to be able to proliferate. A consequence of this, as we shall see later, is that tumors of nerve cells are only found in the very young and tumors of the brain in adults are derived from the supporting cells.[7]

1.1.2.3. The Cell Cycle

To coordinate their behavior, the cells send, receive, and interpret an elaborate set of extracellular signals that serve as social controls, directing each of them how to act. As a result, each cell behaves in a socially responsible manner: resting, growing, dividing, differentiating, or dying, as needed for the good of the organism.[1] In human body with more than 10^{14} cells, billions of cells experience mutations every day, potentially disrupting the social controls. Most dangerously, a mutation may give one cell a selective advantage, allowing it to grow and divide more vigorously and survive more readily than its neighbors and to become a founder of a growing mutant clone. Over time, repeated rounds of mutation, competition, and natural selection operating within the population of somatic cells can cause matters to go from bad to worse. These are the basic ingredients of cancer: it is a disease in which an individual mutant clone of cells begins by prospering at the expense of its neighbors, but in the end the descendants of this clone can destroy the whole cellular society.[1]

1.1.2.4. Tumor Growth of Neoplasia

Tumor cells differ from normal cells in their lack of response to normal control mechanisms and cancer cells are defined by two heritable properties:

- They reproduce in defiance of the normal restraints on cell growth and division.

15

- They invade and colonize territories normally reserved for other cells.

An abnormal cell that grow (increases in mass) and proliferates (divides) out of control will give rise to a tumor, or neoplasm. Given these qualifications we can classify tumors into three main groups:

1. Benign tumors may arise in any tissue, grow locally, and cause damage by local pressure or obstruction. However, the neoplastic cells do not become invasive, and removing or destroying the mass locally achieves a complete cure.

2. *In-situ* tumors usually develop in epithelium and are usually but not invariably, small. The cells have the morphological appearance of cancer cells but remain in the epithelial layer. They do not invade the basement membrane and supporting mesenchyme. Various degrees of dysplasia, that is, epithelial irregularity but not identifiable as cancer *in-situ* are recognized in some tissues and these may sometimes precede cancer *in-situ*.

3. Cancers are malignant tumors, with a specific ability to invade and destroy surrounding tissue. The tumor cells need nutrients via the bloodstream and produce a range of proteins that stimulate the growth of blood vessels into the tumor, thus allowing continuous growth to occur. The new vessels are not well formed and are easily damaged so that the invading tumor cells may penetrate these and lymphatic vessels. Tumor fragments may be carried in these vessels to local lymph nodes or to distant organs where they may produce secondary tumors, called metastases. Cancers may arise in any tissue. Although there may be a progression from benign to malignant, this is far from invariable. Many benign tumors never become malignant.[1,7]

1.1.2.5.   Causes of Cancer and the Process of Carcinogenesis

Carcinogenesis (the process of cancer development) is a multistage process (see Fig. 1.2). In an animal, the application of a cancer-producing agent (carcinogen) does not lead to the immediate production of a tumor. Cancers arise after a long

latent period and multiple carcinogen treatments are more effective than a single application. At least three major stages are involved. The first was termed **initiation** and was found to involve mutagenic effects of the carcinogen on skin stem cells. The second stage, which can be induced by a variety of agents that are not directly carcinogenic in their own right, was termed **promotion**. Following chronic treatment of carcinogen-initiated mouse skin with promoting agents, papillomas (benign skin tumors) arise. The major effect of promoters seems to be their ability to promote clonal expansion of initiated cells. Finally in the third stage, **progression**, some of these benign tumors either spontaneously or following additional treatment with carcinogens, progress to invasive tumors.[7]
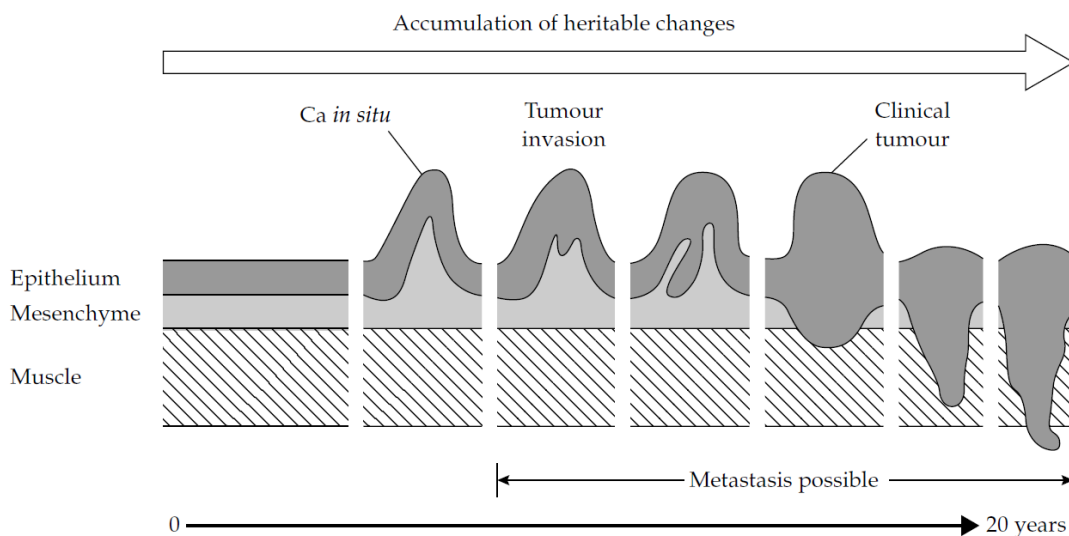
Figure 1.2. Tumor development showing progression from normal to invasive tumor via accumulation of heritable changes over a long period of time. The rate of acquisition of these changes will be influenced by environmental exposure and host response.[7]

1.1.2.5.1. Chemical Carcinogenesis

Our knowledge of chemical carcinogenesis goes back more than two centuries. The London physician John Hill (1716-1775) concluded in 1761 that excessive use of snuff leads to cancer of the nasal cavity, while thirty-four years later Samuel Thomas von Sömmerring (1755-1830) described the association between carcinoma of the lips and pipe smoking. The London surgeon Sir Percival Pott (1713-1788)

established a relationship between the chimney-sweeps and the cancer of the scrotum, and a prolonged contact of the skin with soot-impregnated clothing and the subsequent development of skin cancer. The description of cancer caused by soot was followed by accounts of skin cancers due to tar, coal, lignite and lubricating oil. From a histologic point of view, these cancers were all carcinomas, often multiple. They occurred mainly on the hands, arms and scrotum, often being preceded by dermatitis.[2]

In the early 1920s to the 1930s, Ernest Kennaway (1881-1958), William Mayneord (1902-1988), I. Hieger (1901-1988), J. W. Cook (1900-1975) and C. L. Hewett analyzed coal-tar and discovered that it contains the polycyclic hydrocarbons benzoanthracene and benzopyrene that have a highly carcinogenic effect. In 1895 Lugwing Rehn (1849-1930) pointed out the possible relationship between aromatic amines and cancer of the bladder. In 1932, metal derivative was found to have a carcinogenic effect, due to ten cases of nasal cancer found among workers in a nickel refinery. The mining of asbestos started in 1878, later was reported that people working with asbestos were developing pulmonary fibrosis that increase the risk of lung cancer, along with smoking cigarettes.

In 1950 Cook, Duffy and Schoental[8] reported that metabolic products of livings cells have carcinogenic properties, such as aflatoxin B1, which is produced by *Aspergillus flavus*, a fungus that grows for example on peanut plants, this toxin has been found to be able to cause liver cancer. In 1973 Bruce Ames (1928-) introduced the Ames test, to find substances that are mutagenic. The test makes use of *Salmonella typhimurium*, a bacterial strain that is very sensitive to mutation because its DNA repair capacity is low and the cell wall is readily permeable. Bacteria that have undergone mutation cannot produce histidine, and as a result, they can only grow if the culture medium contains histidine. The mutated bacteria is placed on a histidine-free culture medium with the substance to be tested. If this substance is mutagenic, it can change the DNA of the salmonella back to the form that allows the bacteria to make histidine.

1.1.2.5.2. Radiation-induced Carcinogenesis

Many articles published throughout the entire twentieth century contained clinical and experimental data demonstrating that radiation energy can cause cancer in both man and animals. Ultraviolet (UV) solar radiation can lead to a form of skin cancer, depending on the intensity of the radiation and the sensitivity of the skin and the ability of epidermal cells to repair the damage to DNA caused by the sunlight. The German Franz Albert Frieben (1875-XX Century), was the first to describe the carcinogenic effect of X-ray on humans in 1902. An increased incidence of leukemia and other forms of cancer was subsequently reported after radiotherapy for various conditions such as *ankylosing spondylitis* (a form of arthritis causing pain and stiffness of the back).[2]

1.1.2.5.3. Viral Carcinogenesis

In 1908 two Danish researchers, Vilhelm Ellerman (1871-1924) and Olaf Bang (1881-1937),[9] were the first to demonstrate that leukemia in the chicken was caused by a filterable agent: a virus. Francis Peyton Rous (1879-1970) from the Rockefeller Institute in New York, in 1910 demonstrated that sarcoma, a solid cancer, is the result of a virus infection in the chicken. He was awarded the Nobel Prize for his work in 1966, and the virus is still known as the Rous sarcoma virus. Ludwik Gross (1905-1999) of the Veterans Administration Hospital in the Bronx (New York) showed in 1951 that leukemia in mice is caused by a virus. Sarah Stewart and Bernice Eddy at the National Cancer Institute (Bethesda, MD) showed a new type of virus, the polyoma virus (parotid tumor virus), it is currently classified as a papovavirus. The EBV, Epstein-Barr virus, also known as human herpesvirus 4, was discovered in 1964 by Michael Epstein and Yvonne Barr (London) in tissue from a lymphoma of the children's jaw, sent to them by Denis Burkitt (Kampala, Uganda). The tumor came to be known as *Burkitt's lymphoma*.[2] EBV is a DNA virus with versatile properties, it was found to silently infect people from an early age in most countries; it turned out to be the agent of infectious mononucleosis, which is most common among adolescents and young adults; and also has been reported to be

present in many patients with nasopharyngeal carcinomas; and in the laboratory it became a tool for "immortalizing" lymphoid cell lines, making them continue to grow indefinitely. The initial focus on EBV also prompted research on the most frequently occurring tumor of viral origin in women, in developing countries: cancer of the uterine cervix.[10]

Harald Zur Hausen (1936-), professor of Virology at the University of Freiburg, Germany, revealed in 1983 that cervical cancer is caused by human papillomavirus type 16 and 18. Zur Hausen received the Nobel Prize for his work in 2008. Both statistical and experimental studies have demonstrated that various other viruses induce cancer in humans or act as cocarcinogens to promote the disease. These include the hepatitis-B virus, which can cause hepatocellular carcinoma, and the retrovirus HTLV-1 that has been found to give rise to T-cell leukemia in adults in southern Japan.[2] During the 90's, was established the scientific basis for the production of preventive vaccines acting against virus-like particles of HPV. The vaccines approved for use in human populations were available by the pharmaceutical industry in 2006.[10]

In order to create some kind of order in the large number of viruses that have been discovered, both oncogenic and non-oncogenic viruses are currently classified on the basis of their nucleic-acid content. A distinction is drawn between viruses that contain DNA, such as papovaviruses, adenoviruses and herpesviruses, and those that contain RNA like retroviruses. The retroviruses were discovered in 1970 by Howard Temin (1934-1994) from the University of Wisconsin-Madison, and David Baltimore (1938) from Massachusetts Institute of Technology, these viruses after infection, transcribe their RNA into DNA with the aid of the enzyme reverse transcriptase. Temin and Baltimore shared the Nobel Prize for Medicine in 1975 with Renato Delbucco for their discoveries concerning "*the interaction between tumor viruses and the genetic material of the cell*".[2]

When proto-oncogenes mutate, like src, myc, myb, ras and erb, they can cause cancer. They occur not only in humans but also in animals, and have been in

existence for hundreds of millions of years. They have survive because they have evolutionary value. The src gene, plays a role in the regulation of the normal process of cell division, by coding for the production of a protein that has a key function in the transmission of growth signals in a cell. As soon as the necessary growth factors have adhered to the outer surface of the cell, this protein starts up the cell division process, when there are changes in the protein, cell division occur even in the absence of growth factors.[2]

1.1.2.5.4. Heredity and Cancer

Cancer has been defined as a genetic disease because gene alterations are key steps in the processes that transform a normal cell into a cancer cell capable of propagating to the stage of clinical cancer. Genes can also predispose to cancer when particular variants occur in the germ cells (sperm and ova) of parents. For example, a rare hereditary mutation of TP53 (tumor suppressor gene) is transmitted from parents to offspring as a dominant gene, conferring a very high risk of cancer in one or more of several organs: the breast, soft tissue and bone, the brain, and bone marrow.[10]

The first known human malignant tumor with an autosomal dominant inheritance pattern is the retinoblastoma. This is a malignant tumor of the pigment layer of the eye, which is seen in children; in 40% or the cases, the tumor is family-related.

Physicians in ancient Rome documented the fact that breast cancer occurs more often in some families than in others. The French surgeon and anatomist Pierre Paul Broca (1824-1880), described the occurrence of ten cases of breast cancer in four generations of his wife's family; four other women in the family died of liver tumors, which were probably metastases of breast cancer. In 1984 Wick Williams and David Anderson form the University of Texas provided statistical evidence of the existence of a gene that caused this higher risk of breast cancer. In 1990, Mary-Claire King described the occurrence of the BRCA1 gene on chromosome 17q21 in familial breast cancer, if the gene is mutated, the risk of getting breast cancer is 60-80%. In

1995, Michael Strattton and Richard Wooster discovered the BRCA2 gene that also plays a role in familial breast cancer. Mutations in one or both of these genes also lead to a predisposition to ovarian cancer (30-60% for BRCA1 and 5-20% BRCA2).

Epidemiologic investigation suggests that at least 15% of colorectal carcinomas have a dominant inheritance pattern. The two best defined forms of these complaints are familial adenomatous polyposis (FAP) and hereditary non-polyposis colorectal cancer (HNPCC).[2]

1.1.2.6.　　Classifications of Tumors

1.1.2.6.1.　Benign Tumors:

- Adenoma: Is a benign epithelial tumor with a glandular organization; the corresponding type of malignant tumor is and adenocarcinoma (Fig. 1.3).
- Chondroma: Is a benign tumor or cartilage, chondrosarcoma is the malignant tumor.

1.1.2.6.2.　Malignant Tumors

Cancers are classified according to the tissue and cell type from which they arise.

- Carcinomas: Are cancers arising from epithelial cells, and they are by far the most common cancers in humans.
- Sarcomas: Arise from connective tissue or muscle cells.
- Leukemias and lymphomas: Derived from white blood cells and their precursors (hemopoietic cells), as well as cancers derived from cells of the nervous system.
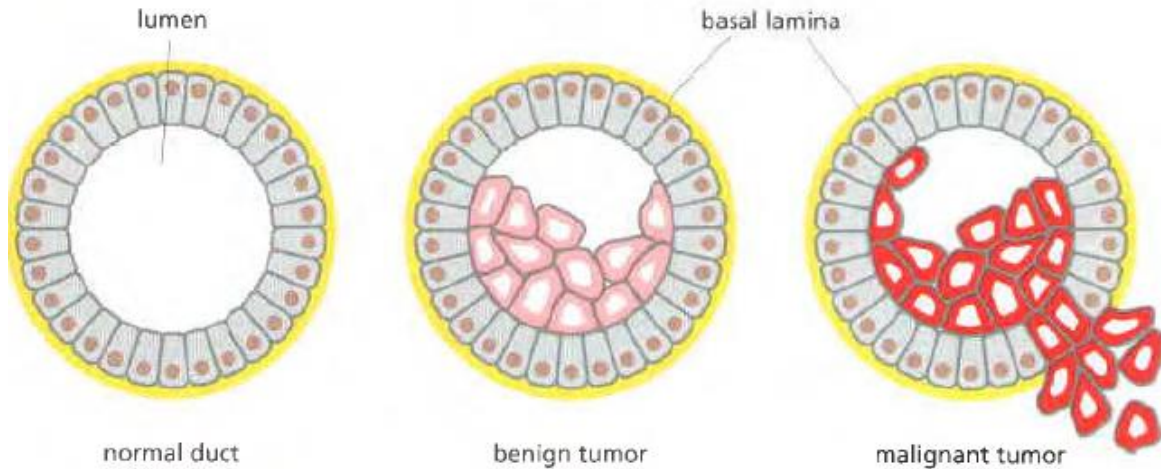
Figure 1.3. Benign versus malignant tumors. A benign glandular tumor (an adenoma) remains inside the basal lamina that marks the boundary of the normal structure, whereas a malignant glandular tumor (an adenocarcinoma) destroys duct integrity as shown.[1]

About 80% of human cancers are carcinomas, because most of the cell proliferation in adults occurs in epithelia or because epithelial tissues are most frequently exposed to the various forms of physical and chemical damage that favor the development of cancer.[1]

1.1.3. Diagnostics

In the seventeenth and eighteenth centuries, cancer was believed to be as infectious as tuberculosis. The development of microbiology led to the intensive microbiological study of tumors. Practically every new micro-organism that could be detected was also found in tumorous tissue, and some authors claimed that inoculation with these organisms could lead to the development of cancer. It was subsequently found, however, that all the germs observed came from secondary infections.[2]

The Greek physician George Papanicolaou (1883-1962), refined the smear test and introduced it as a screening method for cervical carcinoma, the "Pap test", as positive result is an indication that cancer may be present, but a biopsy is almost always required before a definite diagnosis can be made.[2] Technique for growing tissue and cell culture were developed at the beginning of the twentieth century. Thanks to the use of suitable nutrient media and the availability of antibiotics, it became possible to grow cells in an artificial environment. This gave researchers a powerful tool for the study of the biology of cancer cells. After this the believed that cancer was a disease of the whole body was dismissed. Nowadays, it is know that Cancer is a essentially a disease of the genes, the cause of cancer lies in the DNA of the cell nucleus, to be precise, in the genes that undergo mutated genes.[2]

Clinical genetics was born in 1956, when Joe Hin Tjio (1919-2001) and Albert Levan (1905-1998) published an article in which they demonstrated that human cells have 46 chromosomes. Theodor Boveri (1862-1915), a professor of Biology at Würzburg in Germany, was the first in establish a link between chromosomes defects and cancer. In sea-urching eggs he observed that an uneven distribution of the chromosomes during cell division led to malformations. The first important cytogenetic defect to be discovered was described by Peter Nowell (1928-), a pathologist from Philadelphia, and David Hungerford (1927-1993) in 1960. This "*Philadelphia chromosome*" is an abnormally small chromosome found in the blood and bone-marrow cells of 95% of patients with chronic myelogenous leukemia.[2]

1.1.4.   Treatments

1.1.4.1.   Laser in Medicine

If laser radiation strikes biological tissue, various effects can be observed. All are caused primarily by the interaction of photons with the molecules and the molecular compounds of the tissue. The resulting actions depend mainly on the application parameters, which, in turn, can be characterized by the wavelength of the applied laser, the exposure time and the power density. The action mechanisms may be divided approximately into:

- Photochemical processes: For low power densities and long exposure times.
- Thermal responses: For average power densities and exposure times.
- Non-linear actions: For power densities exceeding 10^7 W/cm² and ultra-short exposure times, in the ns range.[11]

The optical tissue properties, like absorption, scattering and refraction, determines the primary distribution of the laser light inside the therapeutic volume, while its actions is determined only by the absorption of the radiation energy by the tissue. The tissue volume absorbing the radiation depends, for a given spot size, on the penetration depth of the laser radiation. The penetration depth is characterized approximately by a *1/e* decrease in its intensity below the irradiated tissue surface. It also depends on the laser's wavelength and on the type of tissue involved. The Table 1.1 indicates typical values for the penetration depth into selected tissues for the most popular laser radiations used in medicine.

The exposure time of the laser radiation and the laser power also determine the laser-tissue reactions, lasers can affect soft and hard tissues. The Fig. 1.4 summarizes the therapeutic and diagnostic applications of lasers.[11]

Table 1.1. Depth of penetration (*1/e* intensity) into selected tissue types for various medical lasers. The numbers indicate the order of magnitude.[11]

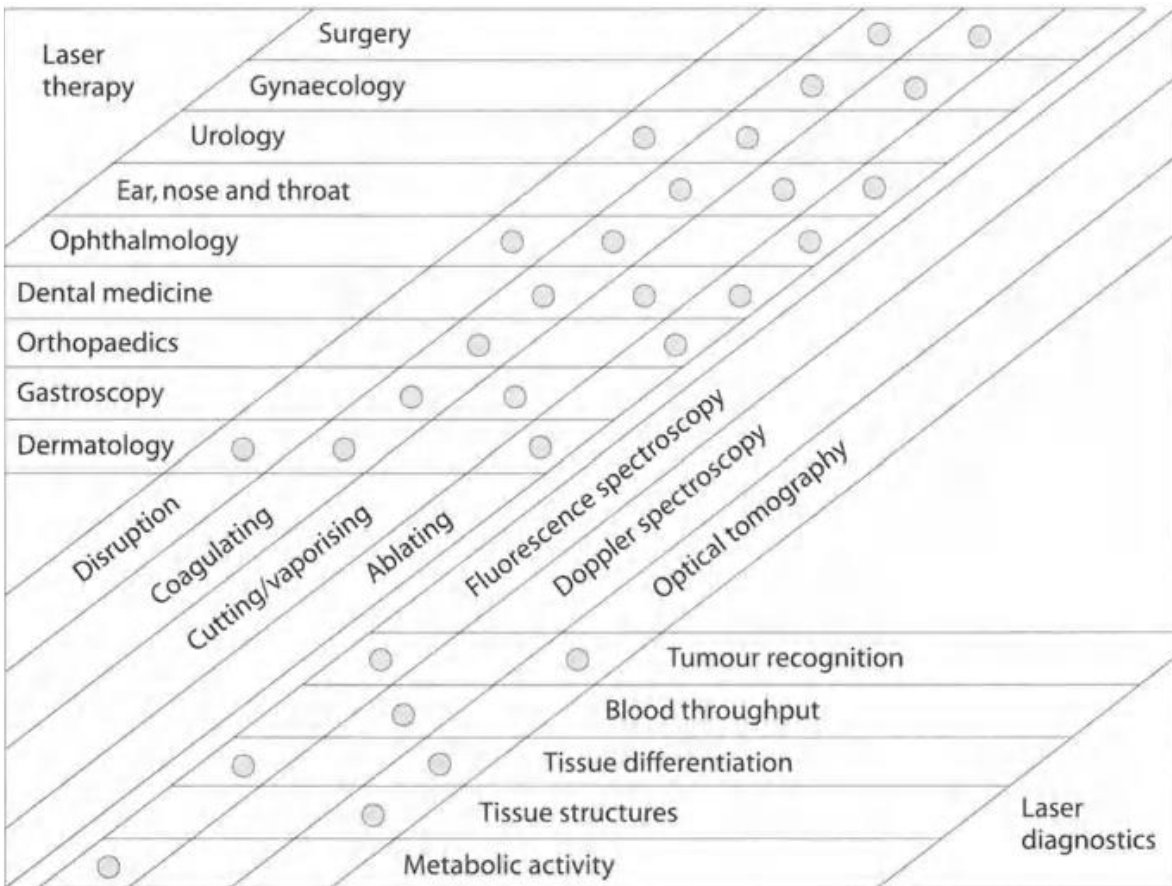| Laser	λ (mm)	Depth of penetration (mm)			
		Skin	Liver	Muscle	Blood
CO_2	10600	0.01	0.01	0.01	0.01
Er:YAG	2940	0.001	0.001	0.001	0.001
Nd:YAG	1064	4	5	4	0.8
Ar	514	2	0.5	1	0.3

Figure 1.4. Therapeutic and diagnostic applications of lasers in medicine. The applications are ordered according to the laser actions.

1.1.4.1.1. Optical Properties of Tissues

If a laser beam strikes biological tissue, a specific distribution of the laser light inside the irradiated volume is observed. Part of the radiation is absorbed by the tissue and, consequently, may be therapeutically active. Depending on the layer thickness, another part will be transmitted either directly at or after multiple scattering. A further fraction of the photons will be scattered in the tissue and leave it as reemission radiation (Fig. 1.5).
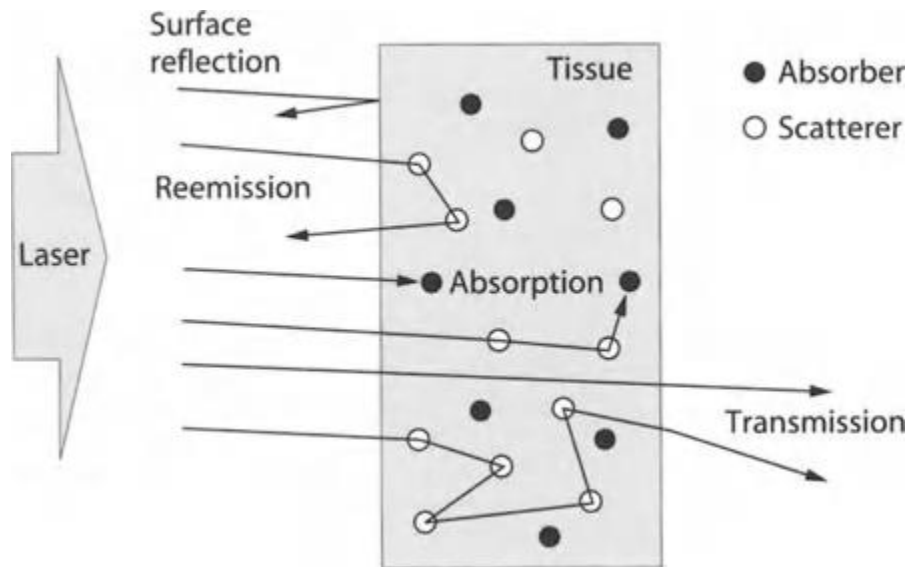

Figure 1.5.   Optical behavior of a tissue layer during irradiation with laser light.

The absorption of photons can, in principle, take place in all molecular components of the tissue. In the UV-Vis regions these components will be tissue-specific chromophores like porphyrin, hemoglobin (Fig. 1.7), melanin, flavin, retinol, ribonucleic acid, where electronic transitions are excited. In the NIR and MIR, tissue absorption is dominated mainly by the absorption in water (Fig. 1.6). The absorption coefficient μ_a (cm^{-1}) characterizes the absorption. It is the product of absorber concentration c_a (cm^{-3}) and absorption cross-section σ_a [cm^2]. The inverse value $1/\mu_a$ is called the mean free path of the photons. In general, different absorbers contribute at one wavelength, consequently μ_a must be considered the sum of all substances involved:

$$\mu_a = \sum c_a \sigma_a \qquad\qquad \text{Eq. 1.1}$$

Biological tissues typically display absorption coefficients in the range 0.01 cm^{-1} < μ_a < 100 cm^{-1}. The intensity of the part transmitted, I_T, through a layer of thickness d (cm) can be easily calculated according to Bouger-Lambert law. If I_o is the intensity on entry into the substrate, then:

$$I_T = I_0 exp(-\mu_a d) \qquad\qquad \text{Eq. 1.2}$$
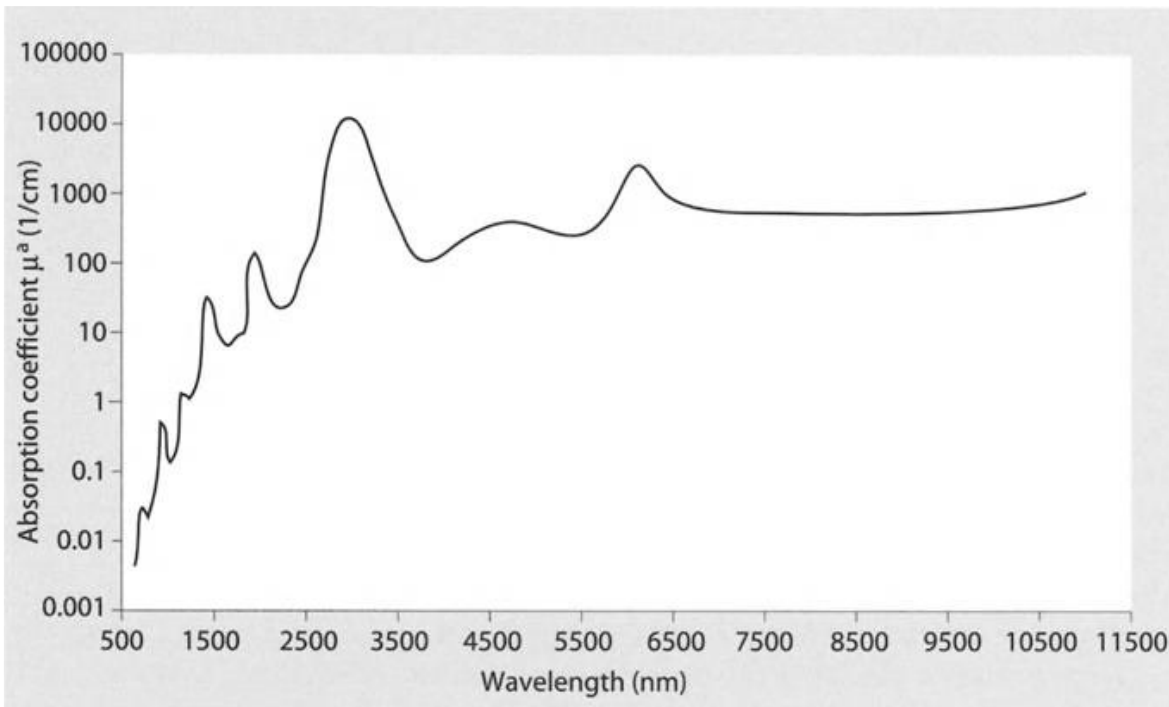

Figure 1.6.   Absorption coefficient of pure water.

Frequently, especially in chemistry, the following terms are employed: absorber concentration c (mol dm^{-1}) and decimal molar extinction coefficient (dm mol^{-1} cm^{-1}). The latter term is defined by the Bouger Lambert law and utilizes the decimal logarithm:

$$I_T = I_0 \times 10^{-\varepsilon cd} = I_0 \times 10^{-A} \qquad\qquad \text{Eq. 1.3}$$

The exponent is called extinction coefficient or absorbance A of a substance, and mostly refers to a layer thickness d of 1 cm.
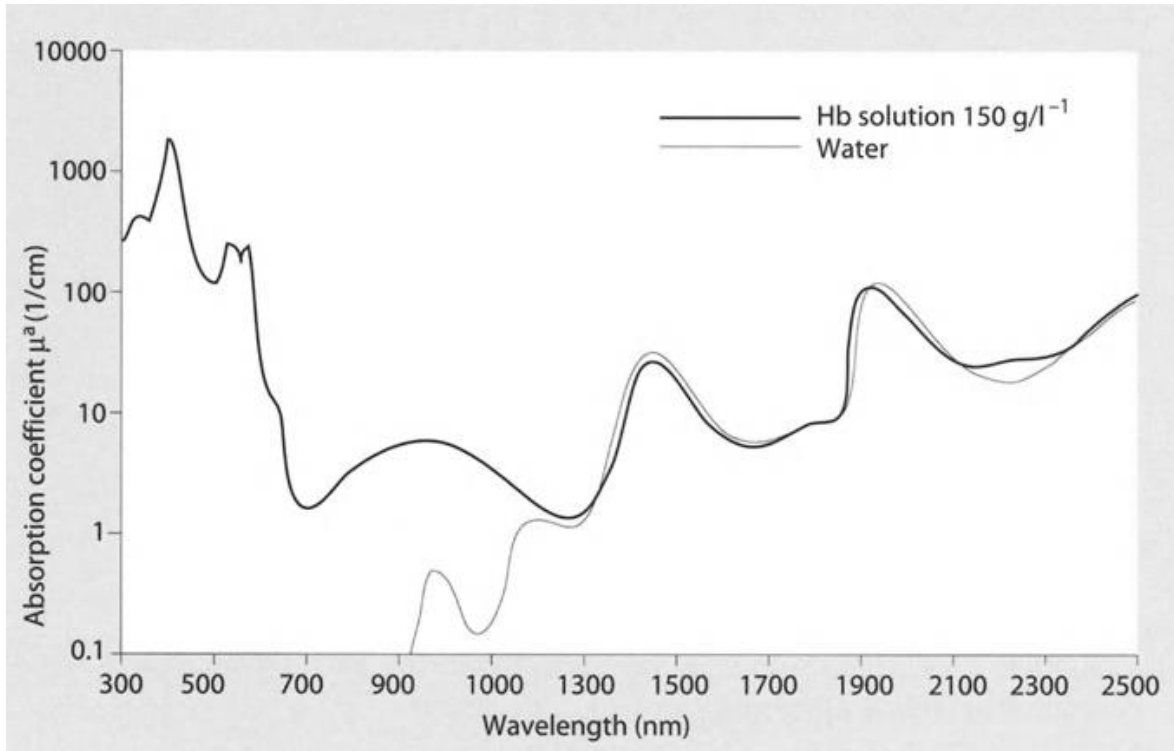
Figure 1.7. Absorption coefficient of oxygenated human hemoglobin (Hb) without cellular components. The physiological concentration is 150 g/L. For comparison, the absorption coefficient of water is also displayed.

The following relations holds:

$$\mu_a = 2.303 \, c \, \varepsilon \qquad \text{Eq. 1.4}$$

The scattering coefficient μ_s is determined by the scattering of photons in biological tissues, at sites of inhomogeneity of the refractive index, *e.g.* at membranes, cell nuclei, mitochondria, lipids etc. The μ_s it is defined, in analogy with the absorption coefficient, as the product of the concentration c_s (cm⁻³) of the scattering centers and the scattering cross-section σ_s (cm²). It is summed over the various types of scattering centers:

$$\mu_s = \sum c_s \, \sigma_s \qquad \text{Eq. 1.5}$$

Biological tissues typically display scattering coefficients in the range 10 cm⁻¹ < μ_s < 1000 cm⁻¹. In tissue optics the scattering coefficient is frequently expressed in mm⁻¹.

29

μ_s is a direct measure for the number of scattering events per unit path length covered by a photon. Over a wide range of wavelengths, the scattering coefficient is significantly larger than the absorption coefficient. For wavelengths in the far region of the optical window (800-1100 nm), the scattering exceeds absorption by 1 to 2 order of magnitude. For wavelengths showing extreme absorption, scattering can be neglected.

If laser beam proceeds from an optically less dense medium (*e.g.* air) into an optically denser medium (*e.g.* water or tissue), it will be partially reflected at the boundary. This partial reflection depends on the wavelength and differs from reemission. The transmitted fraction of the laser beam changes its direction of propagation. Both effects depend on the refractive indices *n* of both media. The refractive index of many biological materials is correlated with that of water because for many tissues this is the main component.

In the visible spectral range the photons will be repeatedly scattered before absorption. In this case, the scattering will not be isotropic but show a distinctly forward component. This anisotropy is expressed by the anisotropy factor *g*, having values between 0 and 1. The value 0 indicates isotropic scattering, all scattering angles are of equal probability; 1 indicates forward scattering. For soft tissues the values for *g* range from 0.7 to 0.98. For theoretical considerations the reduced scattering coefficient, defined as $\mu_{s'}$ = (1-*g*) μ_s, describes the influence of anisotropy.[11]
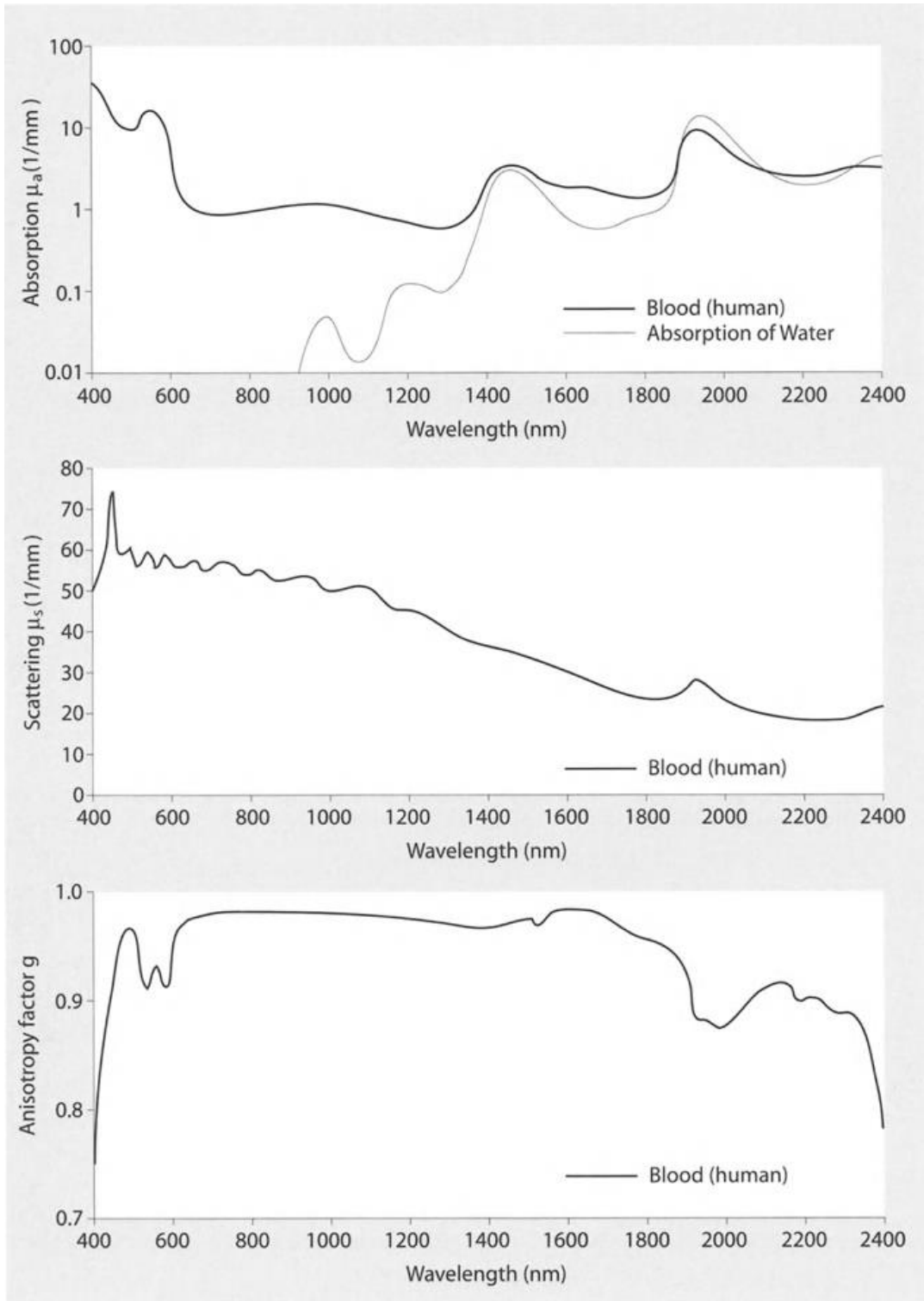
Figure 1.8. Optical properties of human blood. Mean values from three measurements, thickness of optic cell 94 μm.

To characterize the domination of the scattering or absorption, the ratio of scattering coefficient to the sum of scattering and absorption coefficients (albedo) is utilized. Photons are scattered, for example, inside the dermis on average 100 times before they are absorbed. The optical constants completely characterizing a tissue are summarized and listed below (Table 1.2).

Table 1.2. List of optical constants.[11]	
Absorption coefficient	μ_a (cm^{-1})
Scattering coefficient	μ_s (cm^{-1})
Anisotropy factor	g
Reduced scattering coefficient	$\mu_{s'} = (1 - g)\, \mu_s$
Effective attenuation	$\mu_{aff} = (\mu_a + \mu_s)$
Albedo	$q = \mu_s/(\mu_s + \mu_a)$

The light intensity directly below the tissue surface is enhanced by a factor of 2 to 4 as compared with the intensity of the incident beam. The increased intensity is caused by backscattered photons overlapping with the incident photons. Another observation is that, due to the scattering effect, the penetration depth depends on the irradiated area. Consequently, the penetration depth will double if, for the same irradiance, the beam diameter increases from 1 to 5 mm.

The penetration depth of laser light into tissues is greatest in the wavelength range of 700 – 900 nm (Fig. 1.9).
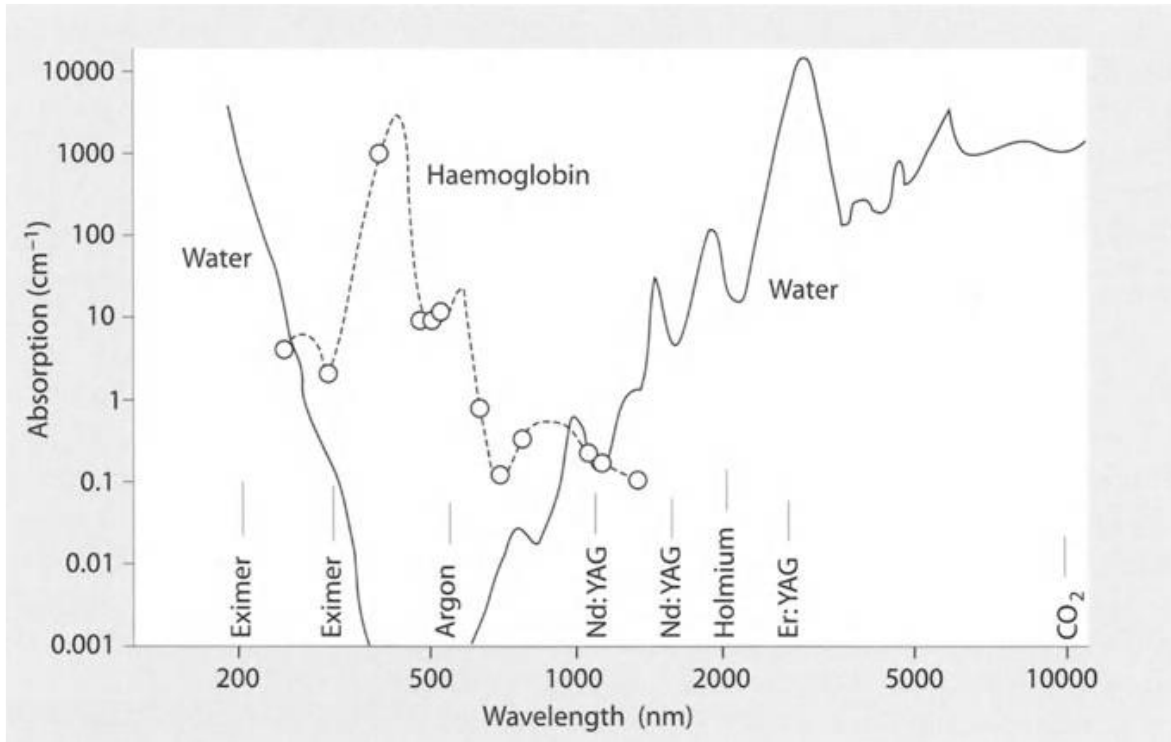
Figure 1.9. Absorption spectra of water and of hemoglobin.

To initiate a thermal reaction, the photons must be absorbed. Beer's law states that the light intensity in tissues is attenuated exponentially with depth, as described by the absorption coefficient μ_a (cm^{-1}), examples are in the Table 1.3.[11]

Table 1.3. Penetration depth of laser as a function of the absorption coefficients μ_a and $\mu_{eff} = \mu_a + \mu_s$, the sum of absorption and scattering coefficients.[11]

Wavelength (nm)	Penetration depth 1 μ_a (µm)	Eff. Opt. penetration 1 μ_{eff} (µm)
193	ca. 10	ca. 1
309	50	240
532	830	240
1 064	2500	1900
2060	286	250
2940	3	3
10600	17	17

1.1.4.1.2. Thermal Properties of Tissues

The action of the laser beam in surgery, as a tool for cutting or coagulation, is based on the conversion of electromagnetic energy into thermal energy. The thermal action is characterized by the absorption of radiation by specific tissue chromophores and its subsequent conversion into thermal energy, the temperature increase, consequently induce thermal changes in the tissue.

The heat source density q, (W m⁻³) inside an irradiated tissue volume is a function of the absorption coefficient μ_a and the total radiation density L. L is composed of the directly contributing part of the collimated laser beam (L_c) and of contributions scattered in from the surrounding tissues (L_s):

$$q(r,t) = \mu_a[L_c(r,t) + L_s(r,s)]$$ Eq. 1.6

Where r is a position vector, and t is the time.

The light energy, converted into heat, causes a local temperature increase inside the irradiated volume. As long as there are no phase transitions, the temperature T will increase proportionally the heat source density q. Part of the heat will diffuse by thermal conduction into the cooler surroundings: This process depends on the temperature gradient. For a given beam intensity this will limit the achievable maximum temperature of the irradiated region. On the other hand, there is for each tissue, a specific intensity threshold which must be exceeded in order to reach a desired local temperature.

Since part of the energy is transported by thermal conduction and other processes into adjacent regions, not only the irradiated volume is heated, but also its surroundings. In vivo the local blood circulation will also transport heat away from the irradiated tissue. The thermal properties of living tissues are dominated by the conductivity, storage and dissipation of heat.[11]

1.1.4.1.2.1.Heat Conductivity

The heat flow *dQ/dt*, is directly proportional to the temperature gradient. For a one-dimensional ideally homogeneous tissue sample of length *s* and uniform cross-sectional area *A*, the heat energy *ΔQ* is conducted within time *Δt* from a position of higher temperature T1 to a position with lower temperature T2, according to the following equation:

$$\frac{\Delta Q}{\Delta t} = \lambda A \frac{T_1 - T_2}{\sigma}$$

Eq. 1.7

Table 1.4. Thermal conductivity of various materials and substances measured in W(m^{-1}K^{-1}) under standard conditions.[11]	
Material	**λ (W m^{-1}K^{-1})**
Air	0.02
Ethanol	0.16
Fatty tissue	≈ 0.3
Watery tissue	≈ 0.5
Water	0.58
Blood	0.62
Steel	46.02
Cooper	418.00

The factor λ is called thermal conductivity [W (m^{-1}K^{-1})]. In general, it is low for gases and highest for metals. The Table 1.4 summarizes typical values.

The heat conductivity for tissues ranges depending on water content. To a good approximation, the following formula holds:

$$\lambda = (0.06 + 0.57 \, w/\rho)[w(m^{-1}K^{-1})]$$

Eq. 1.8

Where *ρ* is the tissue density in kg/m³ and w the water content of the tissue in kg/m³.[11]

1.1.4.1.2.2. Heat Storage

The specific heat c characterizes the ability of a tissue to store heat. This material constant describes the amount of heat needed to increase the temperature of a mass unit by 1 K. Typical values are summarized in Table 1.5.

Table 1.5. Specific heat c of some materials and substances (for gases c_p).[11]

Material	kJ $(kg^{-1}K^{-1})$
Copper	0.385
Steel (V2A)	0.477
Air	1.005
Fat	1.930
Ethanol	2.430
Blood	3.22
Water	4.183

The heat-penetration coefficient b combines thermal conductivity and specific heat. It is a measure of the amount of heat penetrating, during a given duration, into a tissue volume after a sudden increase of the surface temperature:

$$b = \sqrt{\lambda \rho c}$$

Eq. 1.9

It is also possible to characterize the temperature behavior of a tissue sample by:

$$X = \frac{\lambda}{\rho c}$$

Eq. 1.10

This temperature conductivity X as defined by the above equation, has the same value for most tissues (about 1.2×10^{-7} m²s^{-1}). The reason is that a decreasing thermal conductivity due to a lower water content in general is compensated by a decrease of the specific heat.[11]

1.1.4.1.2.3. Heat Dissipation by Blood Flow and Other Mechanisms

Thermal energy dissipates from an irradiated tissue region not only by thermal conduction but also via the vascular system. During continuous irradiation, it is possible that heat transport via blood flow will be the dominating factor in maintaining a stationary temperature distribution. Without any blood flow the temperature during thermal equilibrium will decrease inversely with distance from the local heat source ($T \propto 1/r$). Furthermore, the irradiated volume can lose heat by metabolic processes, by water evaporation at the surface and by convection in cases of laser radiation.

The influence of the vascular region can be estimated by multiplying the inverse of the product of the rate of blood throughput v_B (Table 1.6) and the ρ density of the tissue. The resulting perfusion time t_B represents the time during which the entire blood of a unit volume of tissue is exchanged. The influence of the vascular region must be taken into account if the irradiation time is of the same order of magnitude, or larger, than t_B.[11]

Table 1.6. Rate of blood throughput v_B for various human organs.[11]	
Tissue	**v_B (mL min^{-1}g^{-1})**
Fatty tissue	0.012…0.015
Muscle (arm)	0.02 …0.07
Skin	0.15…0.5
Brain	0.46…1.0
Kidney	3.4

1.1.4.1.3. Interactions of Laser Light with Tissues

The exposure time together with the laser power determine the particular reaction mechanisms (Fig. 1.10). During continuous irradiation (> 0.25 s) of 30 J/cm² in total 1; tissues are easily coagulated. After shortening the interaction time to 10^{-3} s, the

heat produced cannot diffuse into the tissue, so local overheating occurs and the tissue vaporizes at temperature > 300°C. If the exposure time is reduced to several hundred microseconds then the time is insufficient even to vaporize the tissue and it will ablate explosively into fragments. If the time is shortened into the ns range (10^{-9} s), optical breakdown will occur, *i.e.* within the laser focus a plasma will be created and will expand and produce a cavitation bubble which subsequently collapses.
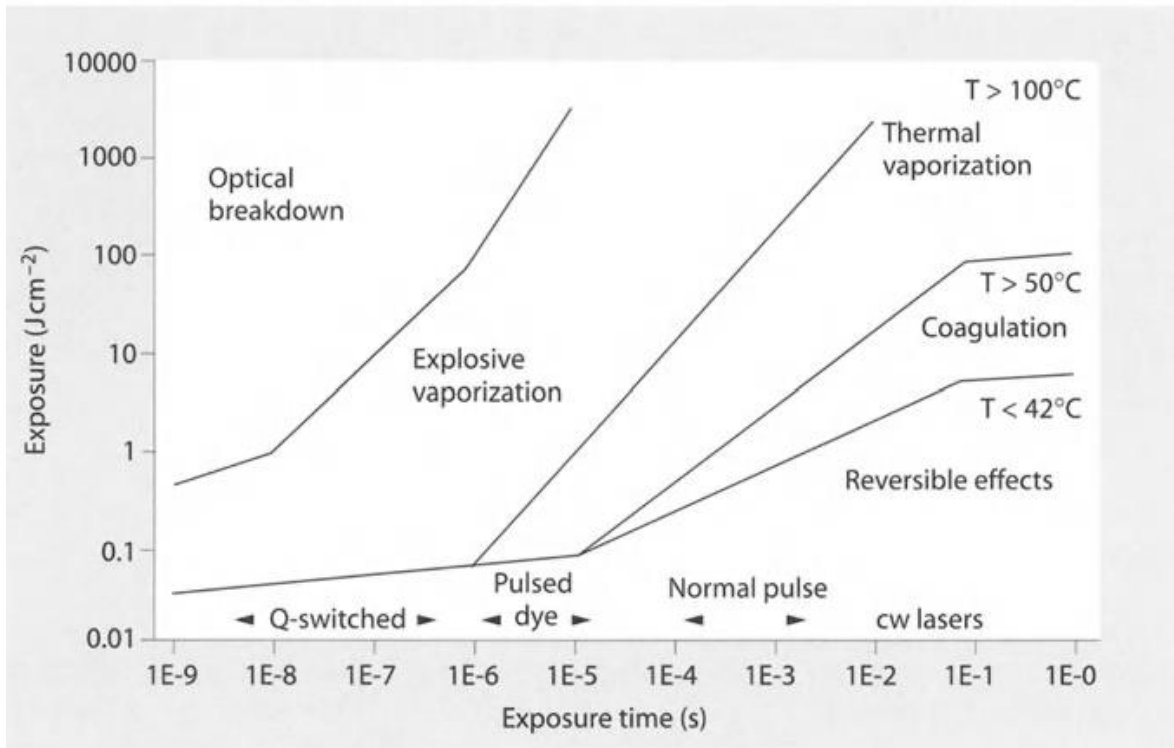

Figure 1.10.   Interactions of laser light depending on the exposure time.
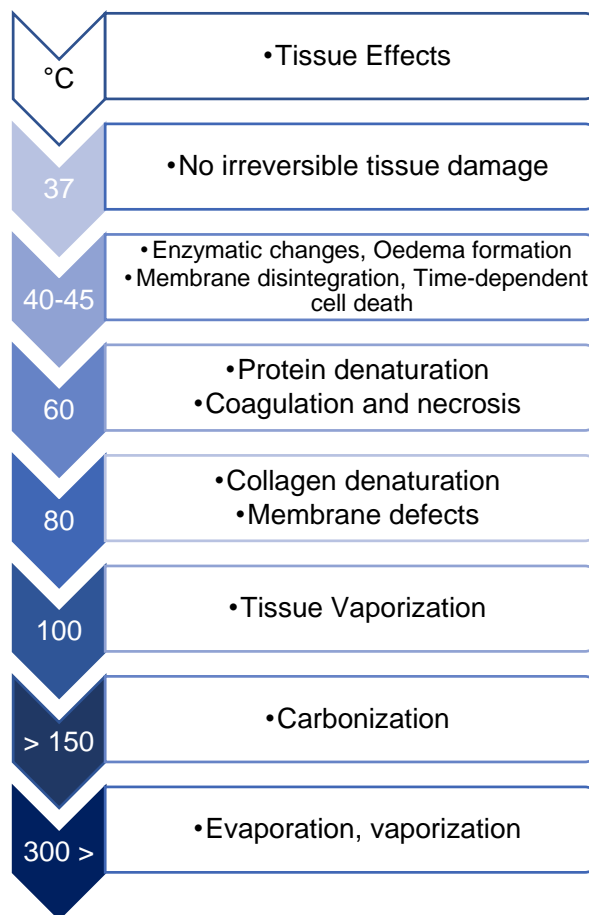
1.1.4.1.3.1.   No thermal Reactions

During no thermal reactions the quantum energy of the laser photons is utilized to excite certain specific molecules. These mechanisms is the basis of photodynamic laser therapy (PTT). So-called sensitizers, *i.e.* dye molecules which predominantly accumulate in tumorous tissues, will be excited by the absorption of the laser light. After an internal energy transfer, this excitation energy will be transmitted to oxygen molecules. Singlet-oxygen of radicals are formed which are a cell toxin. In this case, a purely phototoxic effect is utilized.[11]

1.1.4.1.3.2. Thermal Reactions

Medical lasers are utilized for cutting or coagulating tissues. During coagulation the tissues pass through various stages of thermal damage until vaporization occurs at several hundred °C. The various thermal reactions of tissues are summarized in the Table 1.7.

Table 1.7. Thermal effects at different temperatures during laser irradiation.[11]

°C	Tissue Effects
37	• No irreversible tissue damage
40-45	• Enzymatic changes, Oedema formation • Membrane disintegration, Time-dependent cell death
60	• Protein denaturation • Coagulation and necrosis
80	• Collagen denaturation • Membrane defects
100	• Tissue Vaporization
> 150	• Carbonization
300 >	• Evaporation, vaporization

If radiation enter homogeneous tissues, its power will decrease with increasing depth. It will be partly scattered and absorbed; accordingly, a temperature gradient will develop inside the tissue. In the region where the temperature exceeds 300 °C the tissue will vaporize. This will be followed by a zone with a temperature exceeding 150 °C where the tissue will be carbonized; the next tissue layer will be coagulated.

39

Even further out there will be a region with tissue very slightly warmed, hence suffering no irreversible damages. In the Figure 1.11 indicates schematically the thermal effects caused by decreasing temperatures as a function of depth and lateral extension.
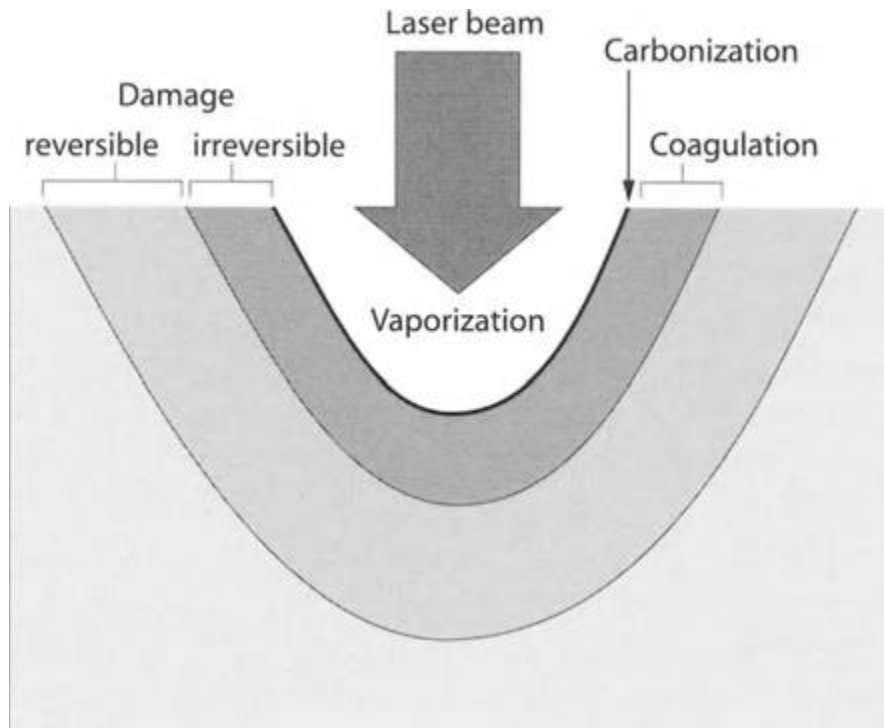
Figure 1.11.   The various action zones during the cutting of tissues.

Hyperthermia is not a therapy by itself because no cells are damage. As opposed to microwave hyperthermia, laser hyperthermia is locally limited to tissue heating. Temperatures between 40 and 60 °C result in disorder of cellular metabolism and membrane function. The result is a thermodynamic reaction which may result in apoptosis of the affected regions. Definite coagulation necrosis occur between 60 and 100 °C (Table 1.7).[11]

1.1.4.1.3.3.   Ablative Effects of Laser Light

For the ablation of soft and hard tissues, high absorption of the laser light in the tissue is needed, in order to reach the ablation threshold with the initial fraction of the pulse energy alone. The shorter the pulse, higher the power density of the laser beam, then lower the ablation threshold. The remaining energy will heat the tissue in the region of the penetration depth of the laser light (a few μm) and can even propagate by thermal diffusion. For this reason, the necrotic zone is wider than the theoretical penetration depth of the light. Since during vertical laser irradiation the tissue fragments are ejected towards the laser beam, the radiation may be significantly absorbed by the ablation products (Fig. 1.12).[11]

1. Coupling of the laser beam to the tissue surface (absorption inside tissue, absorption inside vapour)
2. Tissue conversion by the incident radiation (heating, vaporization, ionization, mechanical destruction)
3. Ejection of tissue materials (convection, heat conduction, condensation)

Laser beam

(Wavelength, power, cw, pulsed, pulse shape, repetition rate)

Burn-up
(Temperature, properties of flow, absorption coefficient, focusing properties)

Surrounding medium
(air, water, blood)

Tissue
(absorption coefficient, heat conductivity)

Figure 1.12.   The various parameters influencing the tissue reactions during laser irradiation.

1.1.4.1.4. Instruments for Laser Therapy

Laser therapy needs transmission systems and applicators to transfer the radiation safely, and with losses as low as possible, to the point of application. Transmission systems are optical fibers, bending light guides and articulated arms. They transport the radiation from the laser's resonator to the point of application. Light guides are made up of flexible, transparent fibers. They are mostly composed of quartz glass, usable with laser radiation in the visible range as well as in the NIR and UV. The light guide can be composed by single optical fiber or random bundles. While fibers bundles are well suited for the transfer of diffuse and incoherent light, single fibers offer the possibility to transfer the concentrated light of the laser and to conserve its special quality to a large degree. There are not light guides available for many wavelength ranges, such as the IR region around 10 µm. In these cases, the beam transport from laser to hand pieces, or to an operating microscope or endoscope takes place via an articulated arm equipped with mirrors that guide the radiation through interconnecting tubes. The Table 1.8 presents a list of the advantages and disadvantages of different beam handling systems.[11]

Table 1.8. Beam-handling systems.[11]

	Advantages/disadvantages	Wavelength range
Directing coupling	Good beam quality, conservation of coherence and polarization. Only for compact laser systems	Arbitrary
Articulated arm	Good beam quality, conservation of coherence and polarization. Inflexible, expensive, difficult to adjust.	Arbitrary, used in UV and 10 µm range

Light guide	Flexible, inexpensive. Restricted for coherence, polarization and focus control	Near UV-Vis and NIR

1.1.4.1.5. Range of Applications for Medical Lasers

There are a number of laser applications for medical procedures, *e.g.* retina coagulation in ophthalmology, thermotherapy and laser angioplasty. Dosimetry is the method to determine the laser radiation parameters necessary for achieving a predetermined action, then determines laser power, power density and energy of a suitable wavelength to achieve the desired response. Applying radiation energy over various times leads to very different tissue reactions. It is necessary to distinguish between the direct physical results of irradiation and the desired medical-biological consequences, often manifesting themselves long after the end of irradiation. The Fig. 1.13 gives a breakdown of the processes and times involved.[11]

Laser radiation	
↓	
Absorption of a photon	10^{-15} s
↓	
Energy transfer molecular, intermolecular	$10^{-12} - 10^{-8}$ s
↓	
Change of the irradiated tissue: chemical, mechanical and temperature	$10^{-8} - 10^{-5}$ s
↓	
Changing of the surroundings of the irradiated tissue	$10^{-3} - 10^{-1}$ s
↓	
Biological changes	s - h
↓	
Medical changes	days
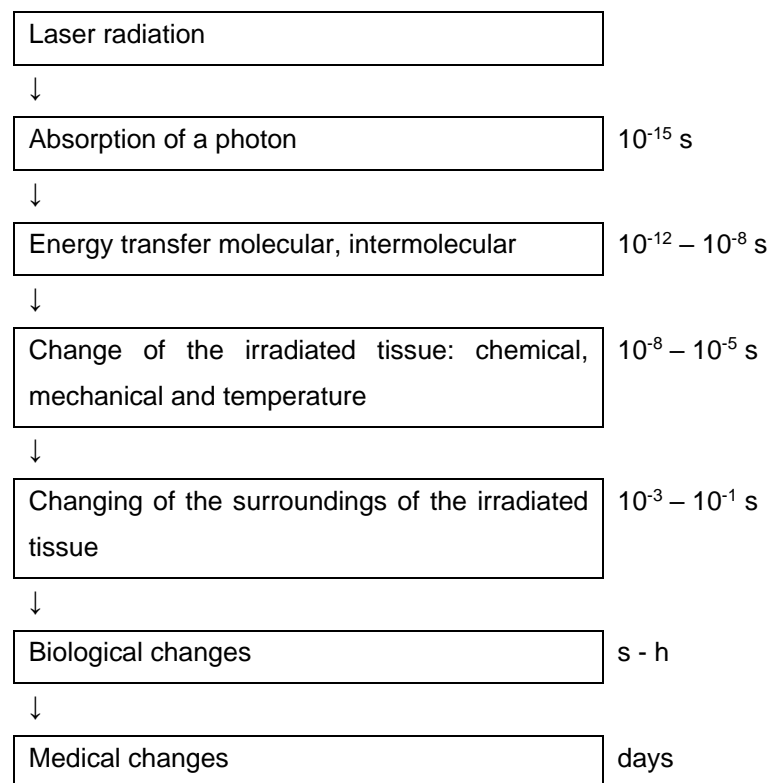
Figure 1.13. Time scales during laser treatment.

The next table, gives an overview of further action principles based on different physical tissue reactions during medical application of lasers.

Table 1.9. Classes of action principles.[11]

Photochemical effects	Action principle
Photoinduction	Biostimulation
Photoactivation of drugs	POD
Photoirradiation	
Photochemotherapy	Photodynamic therapy (PDT)
	Black light therapy (PUVA)
Photoresonance	
Photothermal effects	
Photohyperthermia	37°C – 43 °C
	Reversible damage of normal tissue.
	45 – 60 °C: Cell oedema, tissue welding; protein coagulation
Photothermolysis	Thermodynamical effects microscopically small sites of overheating
Photocoagulation	60 – 100 °C: Coagulation, necrosis
Photocarbonization	100 – 300 °C: Drying out, vaporization of water, carbonization
Pyrolysis	> 300 °C
Photoionization of photofission	
Photoablation	Rapid thermal explosion (angioplasty)
Photodisruption	Optical breakdown
Photofragmentation	Mechanical shockwave (lithotripsy)

The methods for laser therapy of tumors comprises tumor resection, endoscopic recanalization of tumor resection and of tumor stenosis, interstitial laser coagulation of liver metastases, colorectal and mammary carcinoma, thoracoscopic coagulation of lung metastases and local recurrence of breast carcinoma, melanomas and of Kaposi's sarcoma.

1.1.4.1.6. Laser Safety in Medicine

Safety has always been important for any laser application in surgery and medicine, and several issues dominate. These issues include: wearing eye protectors, dealing with the plume of vaporized tissue, and controlling potential fire hazards. The first, second and third-degree skin burns can be induced by visible and infrared laser beam exposure, producing thermal injury, and the same irradiances that can produce a severe thermal burn can also ignite fabrics and burn plastics.

1.1.5.   The International Agency for Research on Cancer, IARC (Statistics Data)

Cancer is among the leading cause of worldwide deaths, every sixth death in the world is due to cancer.[12] Lung, prostate, colorectal, stomach, and liver cancer are the most common types of cancer in men, while breast, colorectal, lung, uterine cervix, and stomach cancer are the most common among women (Fig. 1.14-1.15). More than 30% of cancer deaths could be prevented by modifying or avoiding key risk factors, especially tobacco use, having a healthy diet, being physically active and moderating the ingestion of alcohol. Early detection, accurate diagnosis, and effective treatment, including pain relief and palliative care, help increase cancer survival rates and reduce suffering. Treatment options include surgery, chemotherapy and radiotherapy, tailored to tumor stage, type and available resources.[13]
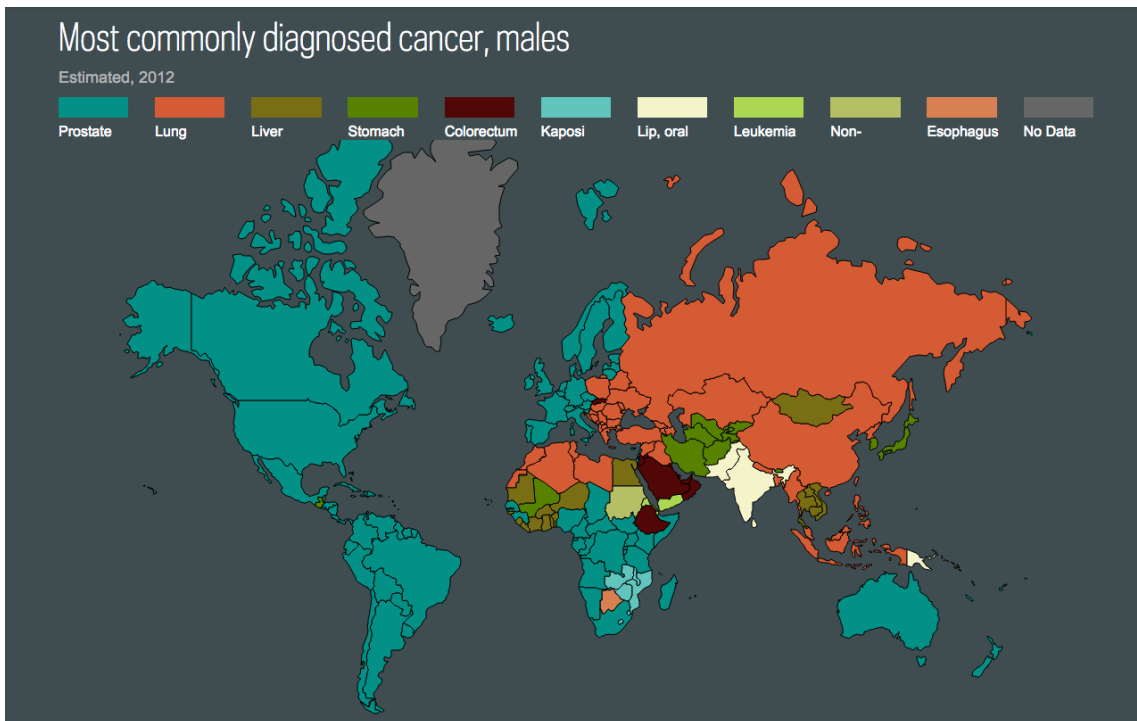
Figure 1.14.   Most commonly diagnosed cancer in males. All incidence and mortality rates are age-standardized to the 1960 world population. All survival estimates are age-standardized to the international Cancer Survival Standard weights.[13]
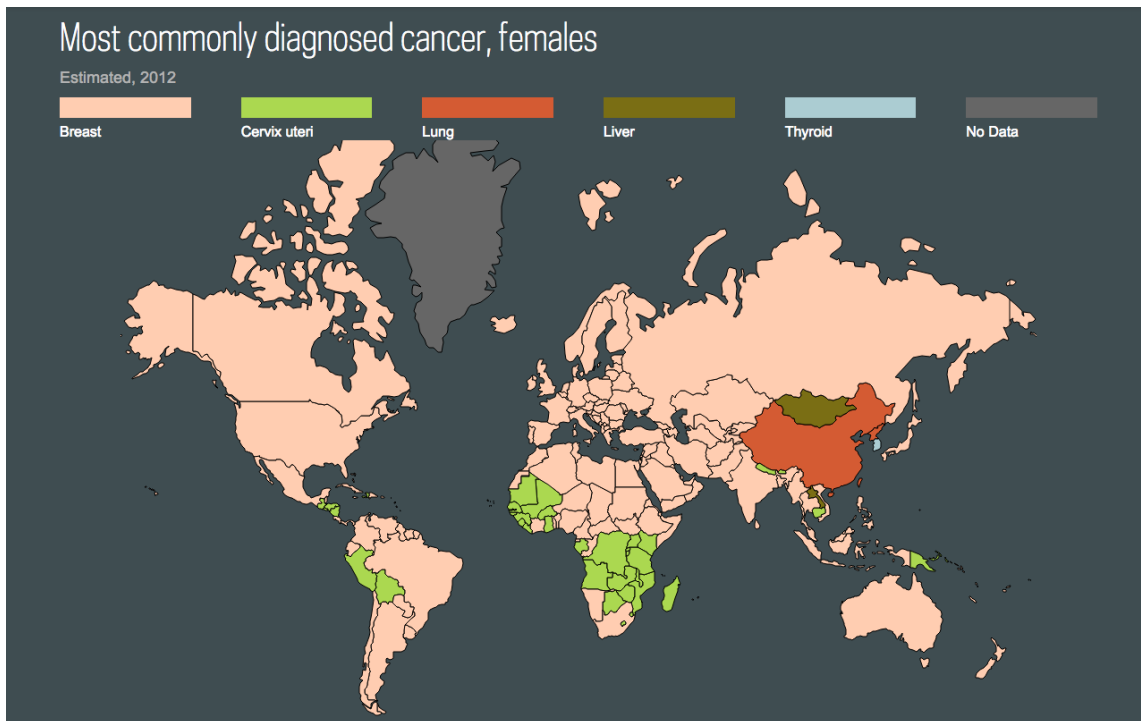
Figure 1.15. Most commonly diagnosed cancer in females. All incidence and mortality rates are age-standardized to the 1960 world population. All survival estimates are age-standardized to the international Cancer Survival Standard weights.[13]

In 20 May of 1965 the World Health Assembly created an agency for international cooperation in the field of health, the International Agency for Research on Cancer, IARC. The agency begun to function on 15 September 1965 with five participating states: the Federal Republic of Germany, France, Italy, the United Kingdom, and the USA. The Soviet Union was not among the founders of IARC, but was one of the countries that soon joined.

Since 1966, the IARC set many of their priorities, including a firm commitment to the need for a strong interdisciplinary approach to understanding the causes and prevention of cancer.

At 1965 was already known about several cancer-causing factors, all belonging to the environment in its broadest sense (Table 1.10). The health effects, acute and chronic, of local, home, and occupational environments have long been known and continue to be described and investigated. Lung cancers caused by air pollutants,

like diesel exhaust or asbestos fibers, and skin cancers caused by solar ultraviolet radiation are just two examples among many.[10]

Type	Factor
Table 1.10. The cancer-causing factors that had been established by 1967.[10]	
In the general environment	Ionizing radiation
	Ultraviolet radiation
In the local and occupational environment	Asbestos
	Nickel refining
	Chromate manufacture
	Inorganic arsenic compounds
	Mustard gas manufacture
	Fumes from gasworks
	Isopropylene
	Alpha- and beta- naphthylamine
	Benzidine
	Xenylamine
	Benzene
	Tar and other coal combustion products
	Ointments containing coal tar
Personal behaviors	Chewing of tobacco, betel, and lime
	Tobacco smoking
	Alcohol consumption
Pharmaceutical drugs	Chlornaphazine
Infections	*Clonorchis sinensis* (Chinese liver fluke)
	Virus inducing Burkitt lymphoma
Predisposing conditions	Tropical ulcers

	Ulcerative colitis

Since 1965, there have been medical improvements in all fields. Such as, the body imaging limited to X-ray techniques, now includes a variety of ultrasound methods, computed tomography (CT) scans, magnetic resonance imaging (MRI), and positron emission tomography (PET) scans. Organ transplants, then confined to corneal transplants and very tentative early attempts for other organs, now have become routine. Minimally invasive and robotic methods are changing the practice of surgery. The advances in cancer medicine have translated into benefits for the population: survival rates of all cancer patients in defined areas, irrespective of care and treatment (Table 1.11).

Table 1.11. Progress in cancer treatment: percentage survival (relative to normal life expectancy) of patients at 5 years after initial diagnosis, for main cancer sites in the United States.[10]

Site	Period		
	1947–1951	1975–1977	2003–2009
Oesophagus	4	5	19
Stomach	7	15	29
Colon	36	51	65
Rectum	32	48	68
Pancreas	2	2	6
Larynx	47	66	63
Lung	5	12	18
Breast (women)	54	75	90
Cervix uteri (women)	62	69	69
Ovary (women)	28	36	44
Prostate (men)	28	68	100
Bladder	38	72	80

Over the decades, IARC has supported the systematic development of cancer registries throughout the world, in cooperation with the International Association of Cancer Registries. This has enabled the scope of cancer incidence analyses to expand in three directions: (i) a more complete coverage of countries, for many of which no data had been available in the first rounds of the exercise; (ii) more reliable estimates of incidence rates based on larger numbers of cancers recorded, a feature of special importance for the less frequent types of malignancies; and (iii) the possibility of observing, for the first time, trends in cancer incidence in the medium and long term, over periods of up to several decades.[10]

With the increasingly reliable data flowing in to IARC from registries all over the world; and the evolution of computerized data processing GLOBOCAN database (globocan.iarc.fr) was created. GLOBOCAN contains incidence, mortality, and prevalence estimates for 27 site-specific cancers and for all sites combined in 184 countries worldwide.[10]

According to IARC (Globocan 2012)[13], there were 14.1 million new cancer cases (Fig. 1.16), 8.2 million cancer deaths and 32.6 million people living with cancer (within 5 years of diagnosis), in 2008 were 7.6 million; an estimated of 13 % from all deaths worldwide. And it is expected an increase of 70 % in new cases of cancer over the next 2 decades.[14]

Cancer cases, all ages (total 14'067,894)

Cervix uteri 3.8%
Oesophagus 3.2%
Bladder 3.1%
Liver 5.6%
Stomach 6.8%
Prostate 7.8%
Other 35.3%
Colorectum 9.7%
Breast 11.9%
Lung 13.0%

Cancer deaths, all ages (total: 8'201,575)

Pancreas 4.0%
Prostate 3.7%
Cervix uteri 3.2%
Oesophagus 4.9%
Breast 6.4%
Stomach 8.8%
Colorectum 8.5%
Liver 9.1%
Other 32.0%
Lung 19.4%
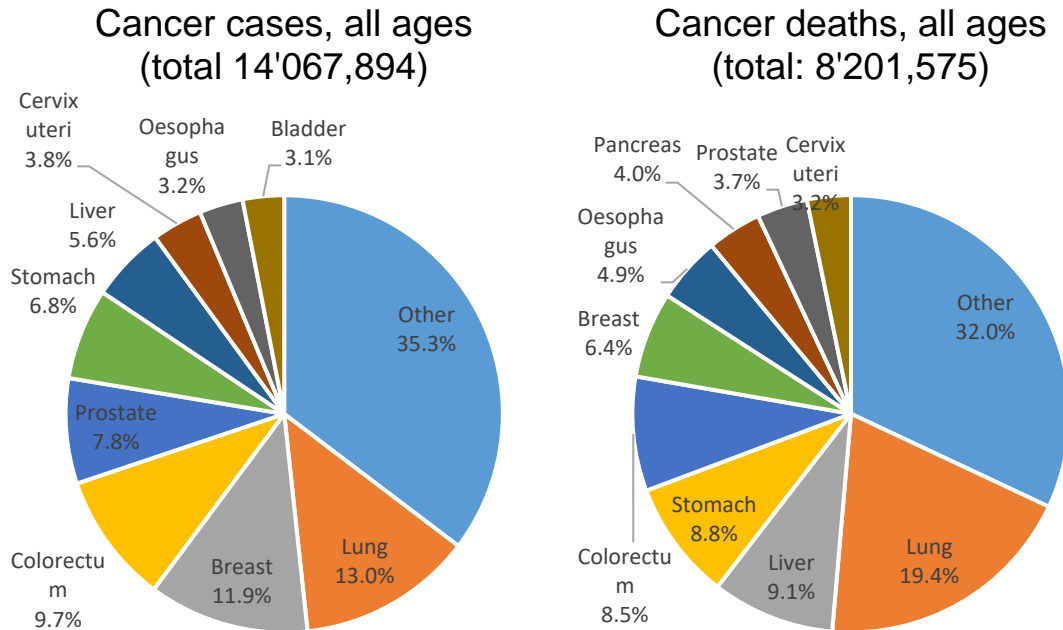
Figure 1.16. Estimated number of cancer cases and deaths worldwide, both sexes.[13]

> 219.1
168.3 - 219.1
139.9 - 168.3
111.6 - 139.9
< 111.6

No data   Not applicable

The boundaries and names shown and the designations used on this map do not imply the expression of any opinion whatsoever on the part of the World Health Organization concerning the legal status of any country, territory, city or area or of its authorities, or concerning the delimitation of its frontiers or boundaries. Dotted and dashed lines on maps represent approximate border lines for which there may not yet be full agreement.

Data source: GLOBOCAN 2012
Map production: IARC
World Health Organization

World Health Organization

Figure 1.17. Estimated cancer incidence worldwide in 2012, females. All incidence and mortality rates are age-standardized to the 1960 world population. All survival estimates are age-standardized to the international Cancer Survival Standard weights.[13]

> 281.2
178.3 - 281.2
135.2 - 178.3
89.8 - 135.2
< 89.8

No data   Not applicable
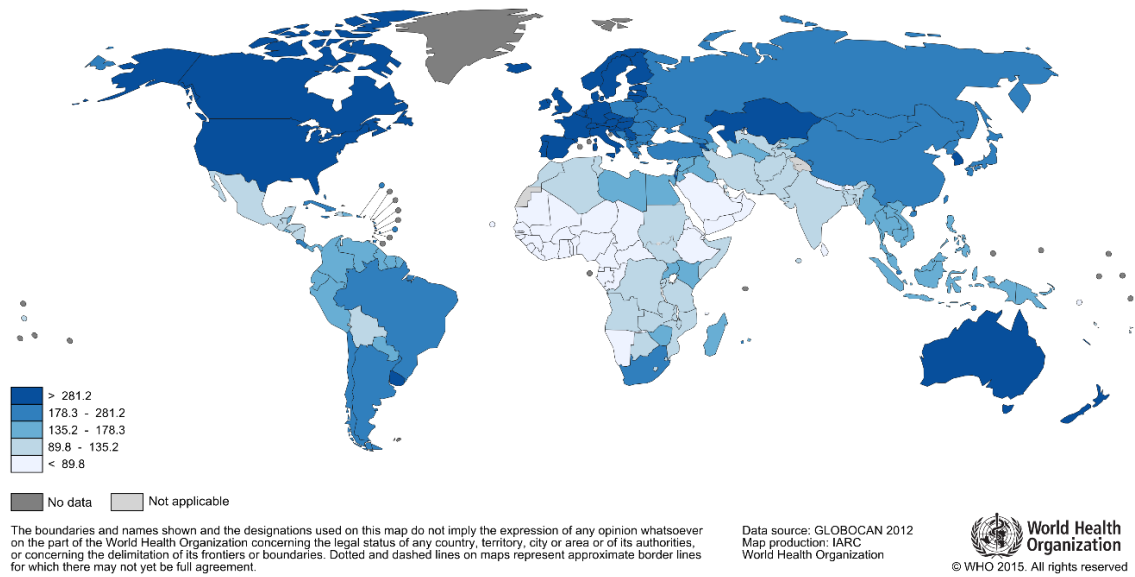
Figure 1.18.   Estimated cancer incidence worldwide in 2012, men. All incidence and mortality rates are age-standardized to the 1960 world population. All survival estimates are age-standardized to the international Cancer Survival Standard weights.[13]

> 96.4
88.4 - 96.4
78.2 - 88.4
69.2 - 78.2
< 69.2

No data   Not applicable
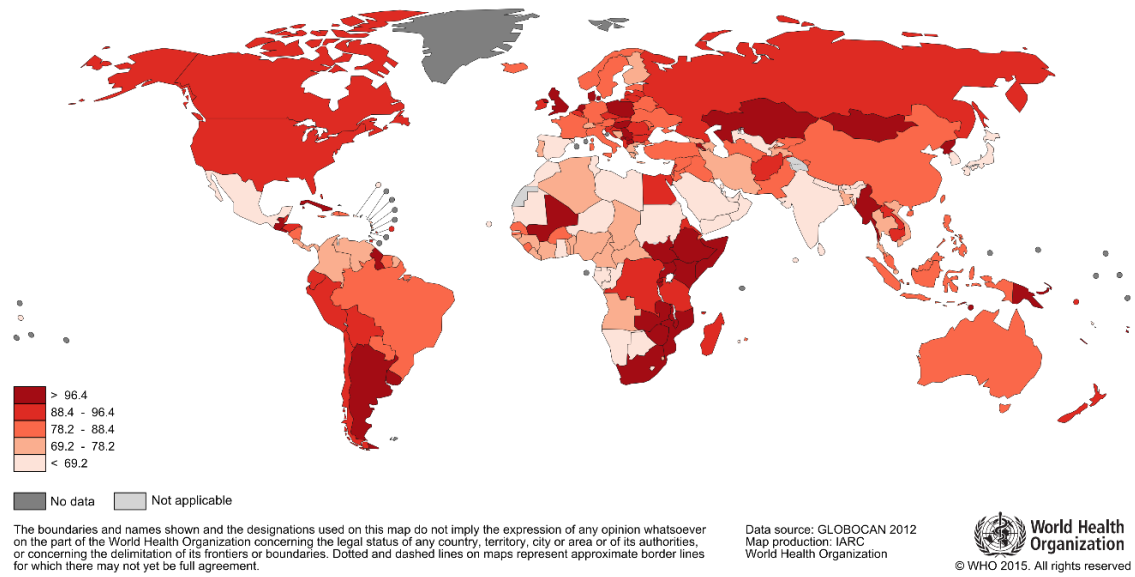
Figure 1.19.   Estimated cancer mortality worldwide 2012, females. All incidence and mortality rates are age-standardized to the 1960 world population. All survival estimates are age-standardized to the international Cancer Survival Standard weights.[13]
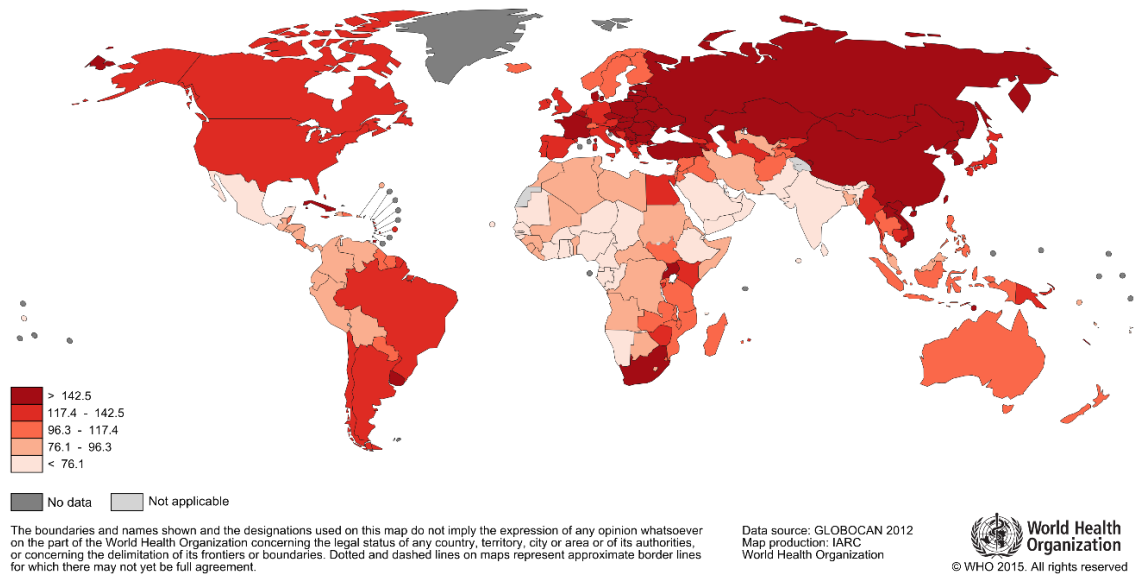
Figure 1.20.   Estimated cancer mortality worldwide 2012, males. All incidence and mortality rates are age-standardized to the 1960 world population. All survival estimates are age-standardized to the international Cancer Survival Standard weights.[13]

The overall age standardized cancer incidence rate is almost 25 % higher in men than in women, with rates of 205 and 165 per 100,000, respectively. Male incidence rates vary almost five-fold across the different regions of the world, with rates ranging from 79 per 100,000 in Western Africa to 365 per 100,000 in Australia/New Zealand (Fig. 1.18). In terms of mortality, there is less regional variability than for incidence, the rates being 15% higher in more developed than in less developed regions in men, and 8 % higher in women (Fig. 1.19-1.21). In men, the rates is highest in Central and Eastern Europe (173 per 100,000) and lowest in Western Africa (69). In contrast, the highest rates in women are in Melanesia (119) and Eastern Africa (111), and the lowest in Central America (72) and South-Central (65) Asia.[13]

Tobacco use is the single largest preventable cause of cancer in the world causing 22 % of cancer deaths. And 20 % of all cancer worldwide are caused by a chronic infection, for example human papillomavirus (HPV) causes cervical cancer and hepatitis B virus (HBV) causes liver cancer.[14]

53

Table 1.12. Estimated Incidence, Mortality and Prevalence of all Cancers (excluding non-melanoma skin cancer) in 2012

Estimated numbers (thousands)	Cases	Men Deaths	5-year prev.	Cases	Women Deaths	5-year prev.	Cases	Both sexes Deaths	5-year prev.
World	7410	4653	15296	6658	3548	17159	14068	8202	32455
More developed regions	3227	1592	8550	2827	1287	8274	6054	2878	16823
Less developed regions	4184	3062	6747	3831	2261	8885	8014	5323	15632
Africa (AFRO)	265	205	468	381	250	895	645	456	1363
Americas (PAHO)	1454	677	3843	1429	618	4115	2882	1295	7958
East Mediterranean (EMRO)	263	191	461	293	176	733	555	367	1194
Europe (EURO)	1970	1081	4791	1744	852	4910	3715	1933	9701
South-East Asia (SEARO)	816	616	1237	908	555	2041	1724	1171	3278
Western Pacific (WPRO)	2642	1882	4493	1902	1096	4464	4543	2978	8956
IARC (24 countries)	3689	1900	9193	3349	1570	9402	7038	3470	18595
United States of America	825	324	2402	779	293	2373	1604	617	4775
China	1823	1429	2496	1243	776	2549	3065	2206	5045
India	477	357	665	537	326	1126	1015	683	1790
European Union (EU-28)	1430	716	3693	1206	561	3464	2635	1276	7157
GLOBOCAN 2012 Cancer Fact Sheets[14]									
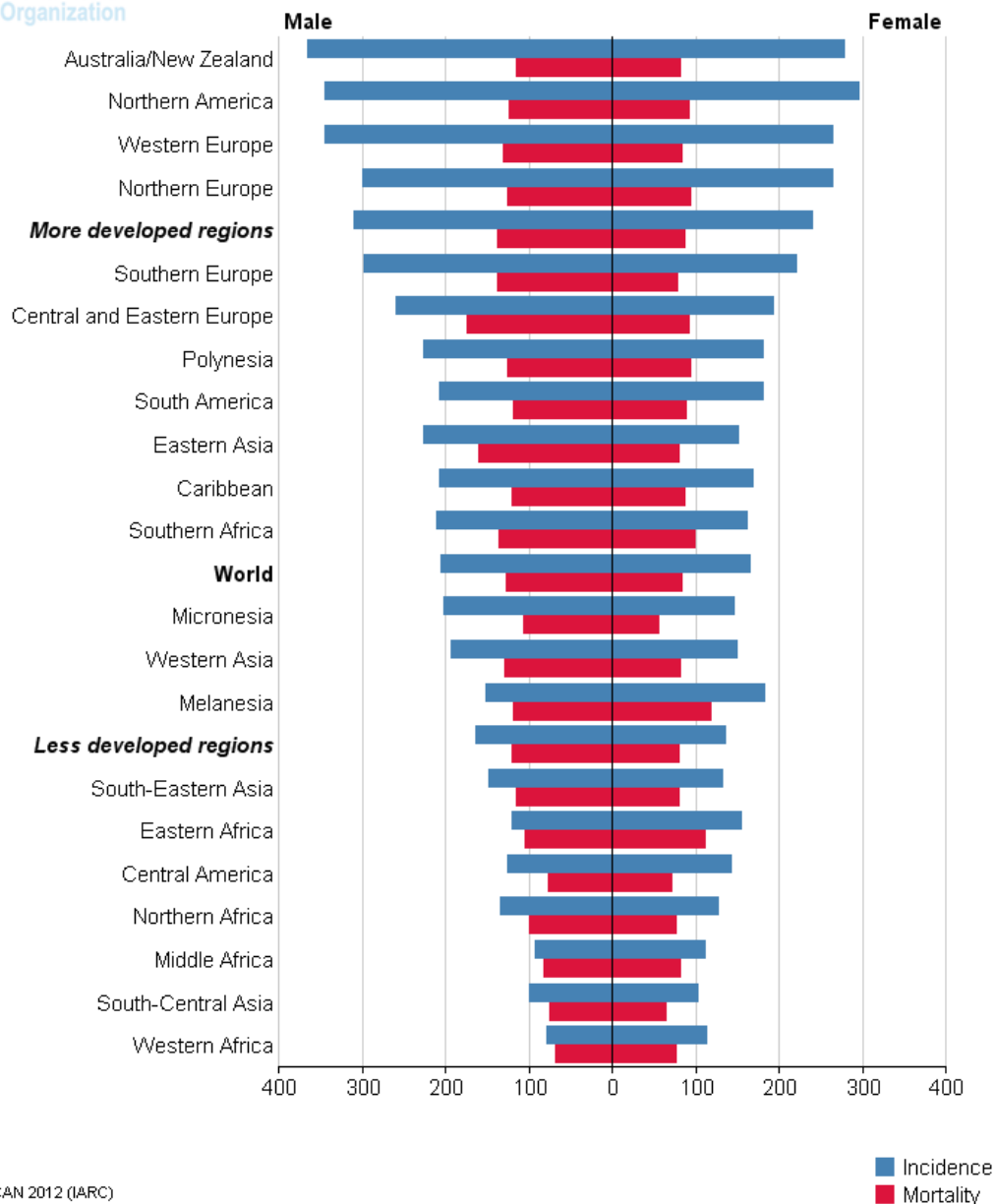
Figure 1.21. Estimated incidence and mortality of all cancers, age-standardized rates (World) per 100,000.

In the third edition of IARC's World Cancer Report (in 2014), a categorization in terms of Human Development Index (HDI) has been introduced. HDI captures three dimensions of human development: life expectancy at birth, educational level attained, and purchasing power. With this new categorization, close to 8 million new

cases of cancer occur per year in countries with high or very high HDI, whereas the annual burden on countries with low or medium HDI is about 6 million. In countries with low or medium HDI, a quarter of cancers are infection-related, and in countries with high or very high HDI, more than one third of cancers are related to industrialized lifestyles (Fig. 1.22).
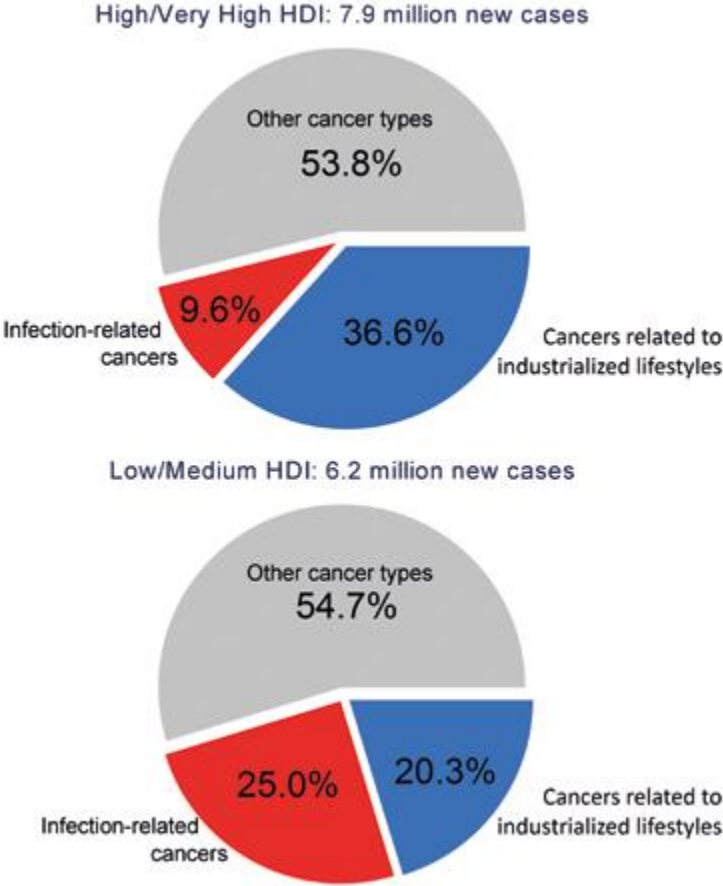
Figure 1.22. Estimated number of new cases of cancer in 2012 by categories of Human Development Index (HDI). Within each HDI category are shown the percentages of cancer attributable to infections (cervical, liver, and stomach cancers and Kaposi sarcoma) and related to industrialized lifestyles (colorectal cancer, female breast cancer, and prostate cancer).

1.1.5.1. Regional Diversity, Cancer in Latin America and the Caribbean

About 1.1 million new cancer cases and 600,000 cancer deaths are estimated to occur annually in Latin America and the Caribbean. Prostate cancer is the leading cause of cancer death among males, with about 51,000 deaths annually, followed by lung cancer and stomach cancer (Fig. 1.23). Among females, breast cancer is the leading cause of cancer death, with about 43,000 deaths annually, followed by cervical and lung cancer. There is considerable variation in cancer rates and trends within Latin America. For example, cervical cancer incidence rates in 2012 ranged from 11.4 cases per 100,000 population in Costa Rica to 47.7 cases per 100,000 in Bolivia, with the highest rates generally found in low-income countries.

Cervical cancer rates are decreasing in many countries due to increased screening, while breast cancer rates are increasing due to increased prevalence of hormonally-linked factors such as delayed childbearing and lower parity, as well as lifestyle risk factors. Gallbladder cancer rates are exceptionally high in many Latin American countries, especially Chile and Bolivia, for unknown reasons. Lung cancer mortality rates have begun to stabilize or decrease among males in many middle-income countries of the Americas, such as Argentina and Brazil, because of decreased smoking prevalence. Notably, lung cancer mortality rates among females continue to increase in most countries of the Americas, reflecting the lag in smoking reduction.[15]

Total Estimated Cases
1'096,000

13.9%
13.9%
8.0%
7.7%
36.5%
6.3%
5.6%
2.8%
2.2%
2.7%

- Prostate
- Breast
- Colorectal
- Lung
- Cervix
- Stomach
- Liver
- NHL
- Leukemia
- Other
- Pancreas
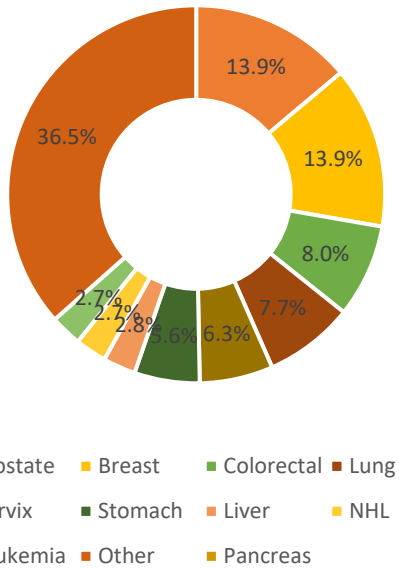
Total Estimated Deaths
603,000

12%
8%
9%
8%
37%
7%
5%
5%
5%
4%
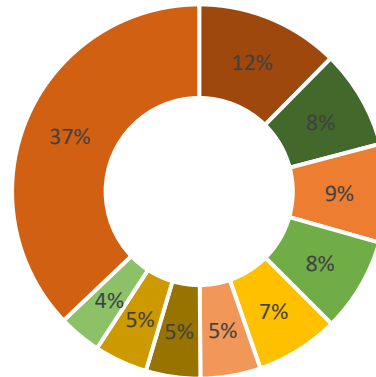
Figure 1.23.   Estimated numbers of new cancer cases and deaths, both sexes, 2012. Lung cancer is the leading cause of cancer death for both sexes combined.[15]

1.1.5.2.   Global Cancer Country Profiles 2014 (México)

The aim of the WHO Global Cancer Country Profiles, is to synthesize in one reference document, the global status of cancer prevention and control. Each Profile includes data on cancer mortality and incidence; risk factors; availability of cancer country plans; monitoring and surveillance; primary prevention policies; screening; treatment and palliative care. The Fig. 1.24 correspond to Mexico's profile, the graphic presents the percentage of incidence and deaths in the country for both sexes.

Cancer cases (total: 147,985)

Cancer deaths (total: 78,719)
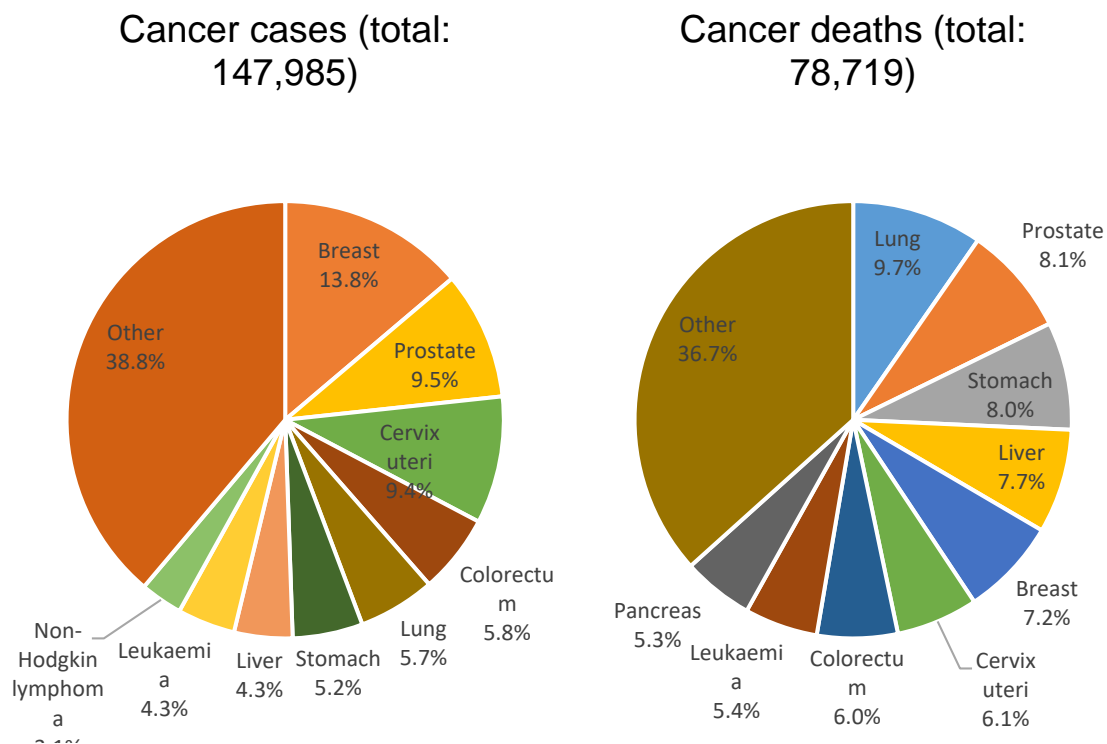
Figure 1.24. Estimated number of cancer incidence and deaths, all ages and both sexes in Mexico.[13]

Cancer can be caused by a variety of known risk factors, many of them preventable. The Table 1.13 list the main risk factors considered for adults in Mexico. In the Table 1.14 are listed the cancer treatment and palliative care in the country.

Table 1.13. Adult risk factors.			
	Males	**Females**	**Total**
Current tobacco smoking (2011)	27 %	8.2 %	17.4 %
Total alcohol per capita consumption, in liters of pure alcohol (2010)	12.4 %	2.6 %	7.2 %
Physical Inactivity (2010)	18.9	31.2 %	25.4 %
Obesity (2014)	22.1 %	32.7 %	27.6 %
Household solid fuel use (2012)	-	-	14.0 %

Table 1.14. Cancer treatment and palliative care.

Radiotherapy	Generally available in the public health system
Total high energy teletherapy units / million inhabitants	0.5
Number of radiotherapy centers	91
Number of radiation oncologists	212
Chemotherapy (medicines not specified)	Generally available in the public health system
Oral morphine (formulation not specified)	DK
Non-methadone morphine equivalent consumption per cancer death (mg)	…
Community/home care for people with advanced stage cancer and other NCDs	Generally available
… = No data vailable	
DK = Country responded "don't know"	

Table 1.15. Cancer screening and early detection

Cervical cancer	
Cervical cytology (PAP)	Generally available at the public primary health care level
Acetic acid visualization (VIA)	DK
Breast cancer	
Breast palpation/clinical breast exam (CBE)	Generally available at the public primary health care level

Mammogram	Generally available at the public primary health care level
Colorectal cancer	
Fecal occult blood test of fecal immunological test	DK
Bowel cancer screening by exam or colonoscopy	DK
DK = Country responded "don't know"	

1.1.6. Nanomedicine

Nanoparticles (particles in the size range 1 – 100 nm) are emerging as a class of therapeutics for cancer. Nanoparticles can be made from several materials, including polymers, metals, and ceramics. Based on their manufacturing methods and materials used, these particles can adopt diverse shapes and sizes with distinct properties.

The most common cancer treatments are limited to chemotherapy, radiation, and surgery. Frequent challenges encountered by current cancer therapies include nonspecific systemic distribution of antitumor agents, inadequate drug concentrations reaching the tumor, intolerable cytotoxicity, and limited ability to monitor therapeutic responses.[16] Poor drug delivery to the target site leads to significant complications, such as a multidrug resistance. Greater *targeting selectivity* and better *delivery efficiency* are the two major goals in the development of therapeutic agents or imaging contrast formulations.[17] Several ligand-targeted therapeutic strategies, including immunotoxins, radio-immuno-therapeutics and drug immuno-conjugates, are being developed to overcome the problems associated with conventional chemo-therapeutics drugs. Although these conjugated agents have shown promising efficacy compared with conventional chemotherapy drugs, limitations in their delivery still remains a major problem.[16] Early clinical results suggest that nanoparticle therapeutics can show enhanced efficacy, while simultaneously reducing side effects, owing to properties such as more targeted localization in tumours and active cellular uptake.[12]

Drug resistance is one of the major obstacles limiting the therapeutic efficacy of chemo-therapeutic or biologic agents. In the clinic, *chemo-resistance* is defined as a lack of tumor-size reduction of the occurrence of clinical relapse after an initial positive response to antitumor treatment. Drug resistance can be caused by:

- No cellular-base mechanisms: Physiological barriers, which protect cancerous cells from drug-induced cytotoxicity. The blood-brain barrier

restricts the entry of anticancer agents to the brain from the periphery. The acidic environment in tumors can also result in resistance to basic drugs through neutralization.

- Cellular mechanisms: Alterations in the biochemistry of cancer cells, such as altered activity of specific enzyme systems, altered apoptosis regulation, or increased drug efflux in malignant cells.

Given the enormous capacity of cancer cells to deploy various mechanisms to ensure their survival in the face of treatment with anticancer drugs, it is not surprising that promising strategies to inhibit drug resistance have proven difficult to translate into clinical success. Strategies for overcoming drug resistance should be based on new drug delivery systems, which will allow selective drug accumulation in tumor tissues, tumor cells, or even compartments of tumor cells. Nanoparticles are examples of such delivery systems.[17]

Tumor imaging plays a key role in clinical oncology, with radiological examinations able to detect solid tumors, determine recurrence, and monitor therapeutic responses. Conventional tumor imaging approaches such as CT and MRI focus mainly on delineating morphological features of the tumor, tissue, and organs, such as the anatomic location, extent, and size of the tumor, at various levels of spatial resolution and contrast. Despite continuous improvements in spatial resolution with advanced imaging equipment, imaging modalities using no targeted contrast agents such as CT and MRI have limited sensitivity and ability to provide specific and functional information on the disease, which is increasingly recognized to be an obstacle to earlier diagnosis and the monitoring of treatment responses. Recent advances have stimulated the emergence of the new field of "molecular imaging," which focuses on visualizing or imaging biological events and processes in living systems, including patients.[17]

Nanomedicine (the medical application of nanotechnology) has incredible potential for revolutionizing cancer therapeutics and diagnostics by developing ingenious biocompatible nanosystems. Cancer nanomedicine is a field of interdisciplinary

research, between the disciplines of biology, chemistry, physics, engineering and medicine. Is expected to lead major advances in cancer detection, diagnosis and treatment.[16]

The term "Nanomedicine" can be traced back to the late 1990's and first appeared in research publications in the year 2000. Its definition varies among experts in this area. For example, the European Science Foundation in 2004 defined nanomedicine as "the science and technology of diagnosing, treating, and preventing disease and traumatic injury, of relieving pain, and of preserving and improving human health, using molecular tools and molecular knowledge of the human body."[19]

Nanoparticles of specific sizes can be synthesized under controlled conditions to obtain the desired properties and characteristics.[17] The nanosystems have unique properties that distinguish them from traditional cancer therapies:

- Nanosystems can themselves have therapeutic or diagnostic properties and can be designed to transport a large therapeutic payloads.
- Nanosystems can be attached to multivalent targeting ligands, which yield high affinity and specificity for target cells.
- Nanosystems can be made to accommodate multiple drug molecules that simultaneously enable combinatorial cancer therapy.
- Nanosystems can bypass traditional drug resistance mechanisms.

1.1.6.1.   Theranostics Nanosystems

Theranostics is an emerging biomedical method that refers to a combination between diagnosis and therapy in one process.[16] The primary goal of theranostics is to selectively target-specific (diseased) tissues or cells to increase diagnostic and therapeutic accuracy. Biocompatible nanoparticles are currently under development as cancer theranostic agents that would enable noninvasive diagnosis and precise cancer therapy. Examples of theranostics materials are the magnetic nanoparticles, it can simultaneously act as diagnostic molecular imaging agents, as drug carriers and for localized magnetotherapy.[16]

1.1.6.2. Therapeutic Applications of Gold Nanoparticles

Over the past two decades, there has been a renewed interest in applying gold nanoparticles (AuNPs) to biological studies and biomedicine (Fig. 1.25).[20] Some of these applications are based on the well-controlled sizes, shapes and surface properties of AuNPs synthesized. Other applications are built upon the unique, highly tunable optical properties of AuNPs, which extend from the photoluminescence of Au clusters to the plasmonic properties.
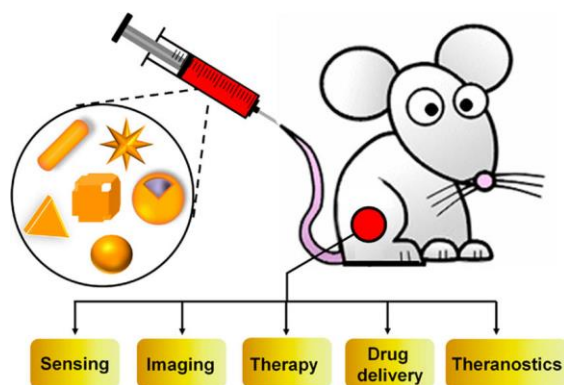
Figure 1.25. Summary of some biomedical applications enabled by different types of AuNPs.

Gold nanoparticles can serve as optical probes for sensing as well as contrast agents for optical imaging. For Au clusters, their superior photostability allows them to be irradiated over long periods of time with the use of laser at a high intensity. For AuNPs, their absorption and scattering cross sections are typically 5−6 orders of magnitude greater than those of organic dyes, making them ideal contrast agents. Significantly, the photothermal conversion capability inherent to Au nanostructures can be utilized to trigger and manage the release of drugs and thus help achieve on-demand release with high spatial and temporal resolutions. Even Au nanostructures themselves can be directly used for the ablation of tissues and killing of cancer cells owing to the photothermal effect.[20]

Gold is one of the least reactive known metals, is one of the few exceptional metals known for incredible resistance against oxidation and corrosion. After exposure to air, not even a single atomic layer of gold oxide(s) can be detected on the surface of

65

a gold substrate. As a result, gold is the only known elemental metal that is both colored and can maintain its unique luster indefinitely. This nonreactive and thus bio-inert nature of gold therefore makes it an excellent candidate for both *in-vitro* and *in-vivo* applications.[20] Despite its extraordinary inertness under most conditions, gold is well-known for its ability to form a relatively strong (about 184 kJ/mol) gold−thiolate (Au−S) bond with compounds containing the thiol (−SH) or disulfide group (S−S). This well-characterized binding has been widely investigated to add functionality to the surface of gold nanostructures, as active targeting. Because a rich variety of proteins can adsorb onto the surface of Au nanostructures during *in-vitro* or *in-vivo* studies, this type of binding will be an important factor to consider when examining the interaction between Au nanostructures and a biological system. The adsorbed proteins can significantly alter the surface properties of Au nanostructures and thus their interactions with the biological system, including cellular uptake and blood circulation.[20]

The first report on the use of gold compounds to treat arthritis appeared in 1934. It was found that gold salts could reduce inflammation and slow disease progression in patients with rheumatoid arthritis through a procedure known as "gold treatment". In some patients, the treatment helped relieve joint pain and stiffness, reduce swelling and bone damage, and diminish the chance of joint deformity and disability. Since the 1990s, however, the clinical use of "gold treatment" has dropped significantly due to its numerous side effects and limited efficacy. In the 1950s, gold colloids were evaluated as radiotracers for sentinel lymph node biopsies in humans. In addition, gold nanoparticles have been used extensively in immunochemistry since 1971, when Faulk and Taylor reported a method that involved the conjugation of AuNPs with an antibody for the direct visualization of the surface antigens of *salmonellae* through electron microscopy.[20]

1.1.6.2.1. Photothermal Therapy (PTT)

Photothermal therapy (PTT) employs photoabsorbing agents to generate heat from light, leading to thermal ablation of cancer cells and the subsequent cell death. Ideal

photothermal agents should exhibit strong absorbance in the NIR region, which is a transparency window for biological tissues, and could efficiently transfer the absorbed NIR optical energy into heat. Inorganic nanomaterials including different gold nanostructures, carbon nanomaterials, palladium nanosheets, copper sulfide nanoparticles, and few other newly reported ones, as well as organic nanoparticles such as NIR-absorbing conjugated polymers, porphysomes, and nanomicelles encapsulated NIR dyes, have been widely explored by many research groups as photothermal agents for PTT ablation of cancer cells *in-vitro* and *in-vivo*.[21]

With their ability to accumulate at the tumor site through passive targeting and/or active targeting enabled by ligands, AuNPs have much higher tumor specificity for PTT compared to the traditional heating methods.[20] With a much higher absorption cross-section than small organic dyes, AuNPs usually exhibit strong visible absorption with the capability of been tuned. Photothermal ablation of cancer can be achieved using AuNPs under irradiation by visible lasers. The use of continuous wave (CW) laser during PTT has its advantage in terms of effective heat accumulation to induce tumor ablation in a large area.[21] AuNPs can serve as contrast agents for various imaging techniques, making it possible to achieve imaging-guided therapy. The high photothermal conversion efficiency of AuNPs minimizes the required particle dosage for PTT.[20]

A CW laser provides a steady rise in temperature upon irradiation, leading to local hyperthermia. Pulsed laser irradiation is also used for PTT with AuNPs, and in this case, a second cell killing mechanism could take place, the phenomenon termed *cavitation effect*. The cavitation occur under pulse laser irradiation, when a high photon density is present, and the repetitive absorption of photons by AuNPs can exceed the rate of heat dissipation, leading to an extremely rapid rise in local temperature (*i.e.*, superheating).[20] The cavitation in cells cause the perforation of plasma membranes, leading to an influx of extracellular Ca^{2+}, and finally causing cell death. This enhanced cell killing performance is observed for AuNPs attached to the cells surface, then is considered the AuNPs targeted to cell surface receptors.[20] In the chapter 3 we review this topic with more detail, and the table 3.3 resumes some

of the last decade published results in evaluation of thermal response of gold nanoparticles and photothermal therapy with cultured cells and *in-vivo* models.

There are some complications that have to be resolved before this noninvasive therapeutic method can find a clinical application. First, the laser power used in most cases (W/cm²) for AuNPs are far exceed the *skin tolerance threshold* of ~0.33 W/cm² at 808 nm set by the American National Standards Institute (ANSI). Second, although the penetration depth of PTT has been greatly improved through the use of NIR lasers, it still needs to be further refined, in order to reach deep-buried tumors. This issue renders PTT less attractive than magnetic hyperthermia, for which there is no limitation on the penetration depth from the alternating magnetic field. Third, the *cell killing* mechanism of PTT with AuNPs needs to be systematically investigated. And finally, the *high cost* of Au may remain a major limitation to the real-world applications of these nanomaterials.[20]

Figures Index

Tables Index

References

(1)   Alberts, B.; Johnson, A.; Lewis, J.; Raff, M.; Roberts, K.; Walter, P.; Science, G.; Group, F. *Molecular Biology of The Cell*; Fifth Edit.; Garland Science: New York, 2008.

(2)   Wagener, D. J. T. *The History of Oncology*; Springer: Netherlands, 2009.

(3)   Aufderheide, A. C.; Rodríguez-Martín, C. *The Cambridge Encyclopedia of Human Paleopathology*; Cambridge University Press, 1999.

(4)   The History of Cancer http://www.cancer.org/acs/groups/cid/documents/webcontent/002048-pdf.pdf (accessed Oct 29, 2015).

(5)   Triolo, V. A. Nineteenth Century Foundations of Cancer Research Advances in Tumor Pathology, Nomenclature, and Theories of Oncogenesis. *Cancer Res.* **1965**, *25*, 75–106.

(6)   Pervan, V.; Cohen, L. H.; Jaftha, T. *Oncology for Healt-Care Professionals*; Juta & Co. Ltd., 1995.

(7)   Knowles, M. A.; Selby, P. J. *Introduction to the Cellular and Molecular Biology of Cancer*; Fourth Edi.; Oxford University Press: New York, 2005.

(8)   Cook, J. W.; Duffy, E.; Schoental, R. Primary Liver Tumours in Rats Following Feeding with Alkaloids of Senecio Jacobaea. *Br. J. Cancer* **1950**, *4*, 405–410.3.

(9)   Moore, P. S.; Chang, Y. Why Do Viruses Cause Cancer? Highlights of the First Century of Human Tumour Virology. *Nat Rev Cancer* **2010**, *10*, 878–889.

(10)   Saracci, R.; Wild, C. P. *International Agency for Research on Cancer: The First 50 Years, 1965–2015*; International Agency for Research on Cancer: Lyon, France, 2015.

(11)   Berlien, H. P.; Müller, G. J. *Applied Laser Medicine*; Springer, 2003; Vol. 1.

(12)   Our World in Data https://ourworldindata.org/ (accessed Apr 20, 2018).

(13)   International Agency for Research on Cancer http://globocan.iarc.fr/Default.aspx (accessed Oct 29, 2015).

(14)   WHO. World Health Organization http://www.who.int/en/ (accessed Oct 29, 2015).

(15)   *The Cancer Atlas*; Jemal, A.; Vineis, P.; Bray, F.; Torre, L.; Forman, D., Eds.; Second Edi.; American Cancer Society: Atlanta, Georgia, 2014.

(16)   Misra, R.; Acharya, S.; Sahoo, S. K. Cancer Nanotechnology: Application of Nanotechnology in Cancer Therapy. *Drug Discov. Today* **2010**, *15*, 842–850.

(17)   Wang, X.; Yang, L.; Chen, Z. G.; Shin, D. M. Application of Nanotechnology in Cancer Therapy and Imaging. *CA. Cancer J. Clin.* **2008**, *58*, 97–110.

(18)   Davis, M. E.; Chen, Z. G.; Shin, D. M. Nanoparticle Therapeutics: An Emerging Treatment Modality for Cancer. *Nat. Rev. Drug Discov.* **2008**, *7*, 771–782.

(19)   Min, Y.; Caster, J. M.; Eblan, M. J.; Wang, A. Z. Clinical Translation of Nanomedicine. *Chem. Rev.* **2015**, *115*, 11147–11190.

(20)   Yang, X.; Yang, M.; Pang, B.; Vara, M.; Xia, Y. Gold Nanomaterials at Work in Biomedicine. *Chem. Rev.* **2015**, *115*, 10410–10488.

(21)   Cheng, L.; Wang, C.; Feng, L.; Yang, K.; Liu, Z. Functional Nanomaterials for Phototherapies of Cancer. *Chem. Rev.* **2014**, *114*, 10869–10939.

2 Hypothesis and Objectives

General Background

The cancer is among the leading causes of death in the world. According to IARC,[1] in 2012, there were 14.1 million new cancer cases, 8.2 million cancer deaths and 32.6 million people living with cancer (within 5 years of diagnosis). About 1.1 million new cancer cases and 600,000 cancer deaths are estimated to occur annually in Latin America and the Caribbean.[2] The Mexico Cancer Profile of 2014, estimates 147 thousands cancer incidence and 78 k cancer deaths.[1]

The lack of prevention, early detection and efficient treatments makes of Cancer, the main reason to design new materials for its treatment. The theranostic materials, combine detection, diagnosis and therapy, are able of sensing and targeting to the tumor site and once there, been activated locally. Therefore, these new therapies leaves intact the healthy sites of the organism and reduce the adverse effect on patient recovery.

The anisotropic gold nanoparticles absorbs light in the NIR region. When the gold nanoparticles are irradiated with a laser to a determined frequency, they are able to heat the surrounding media, and this property is shape dependent.

The human serum albumin has a 30mg/mL concentration in the blood, and it is the main vehicle of nutrients, ions, meds, fatty acids and wastes, among others blood components.

The gold nanoparticles can be conjugate with human serum albumin to improve its stability, dispersion and biocompatibility.

The endothelial cells express albumin receptors that helps to accumulate albumin complex in the interstitial tumors space.

Hypothesis

The complex of anisotropic gold nanoparticles conjugated with serum albumin is able of interact with endothelial cells, and thus been internalized and accumulated in tumor extracellular regions. Therefore, these complex can be activated with proper electromagnetic irradiation for the generation of enough heat, and promote cells death.

General and Specific Objectives

❖ **Synthesis of gold nanoparticles with anisotropic geometry by diverse wet chemical methods.**

- Structural characterization by electron microscopy and X-ray diffraction.
- Measurement of localized surface plasmon resonance of gold nanoparticles with UV-Vis spectroscopy.
- Measurements of Z-potential for evaluation of colloidal stability.

❖ **Evaluation of thermal response of anisotropic gold nanoparticles.**

- Fabrication of equivalent tissue phantoms for evaluation of thermal response.
- Evaluation of thermal response of gold nanoparticles by dynamic thermography.

❖ **Conjugation of gold nanoparticles with bovine serum albumin.**

- Evaluation of localized surface plasmon resonance shift by UV-Vis spectroscopy.
- Raman characterization of the conjugated complex.
- Stability evaluation of the conjugated complex.

❖ **Evaluation of cytotoxicity of nanoparticles in cultured cells.**

- Evaluation of cell growth impact by nanoparticles.
- Evaluation of mitochondrial activity and cell membrane integrity.

References

(1)   International   Agency   for   Research   on   Cancer
      http://globocan.iarc.fr/Default.aspx (accessed Oct 29, 2015).
(2)   *The Cancer Atlas*; Jemal, A.; Vineis, P.; Bray, F.; Torre, L.; Forman, D., Eds.;
      Second Edi.; American Cancer Society: Atlanta, Georgia, 2014.

3. Properties, Synthesis and Characterization of Gold Nanoparticles

Chapter Contents

3.1. Introduction

Gold is a transition metal and one of the least reactive chemical elements; its historical popularity in the jewelry industry can be attributed to its long lasting metal luster and its relative material rarity and value. Owing to its malleability, gold can be easily formed into different shapes, and even hammered into very thin sheets or stretched into fine threads. Also, gold can be processed into sub-100 nm (1nm = 1 × 10^{-9} m) structures by synthetics methods. The sub-100 structures, are classified as nanomaterials (NMs) because one of their dimensions is between 1 and 100 nm. A particular type of NMs are the metallic nanoparticles (NPs), that might have all their dimensions in the nanometric range, and because of this, they have more surface atoms than core atoms. Because of the atomic surface to volume ratio, NPs can have different physical and chemical properties than those of bulk material.

Because all the properties of NMs, they are one of the main topics in research projects, with the purpose of develop new technologies.[1,2] The recent advances in design of NMs have allowed the achievement of structures with complicated geometric forms and the uses of non-toxic chemicals for synthesis. Gold have had a particular role in the NPs synthesis with controlled factors such as size and shape, and because of their special properties, those NPs are studied to be applied in technologies for different areas as renewable energies, catalysis, medicine, photonics and others. *In this project we focused on the optic and low-reactive properties of gold nanoparticles (AuNPs), for the development of an efficient heat antenna, that can be applied in localized photo-thermal therapy (PTT) of malignant cells.*

The principal character of this chapter are the AuNPs, presented from their use since ancient civilizations to their more technological applications in present days (section 3.1). For a good understanding of the AuNPs properties, specific topics are reviewed. In section 3.2 is given a resume of the synthesis methods that we based on for this project, and the main results published for others groups. The first experimental work of the project subject in this thesis, is treated starting from section

3.3. This chapter comprise the work developed for the achievement of the first two general objectives of the project: i) **Synthesis of gold nanoparticles with anisotropic geometry by diverse wet chemical methods,** and ii) **Evaluation of thermal response of anisotropic gold nanoparticles**. The topics are divided into methods, results and the discussion of the experimental data obtained from AuNPs synthesis and evaluation of their thermal response.

3.1.1. History of Gold

The history of gold starts long before the invention of writing and the establishment of the first cities of Mesopotamia and Egypt. It starts around 4500 B.C. (before Christ) with "old Europe" civilization, that was at that time among the most sophisticated and technologically advanced regions in the world. The most ancient gold artifacts were found in 1972, in a necropolis with 294 graves dating to 4600-4200 B.C., in Varna on the Black Sea coast, nowadays modern Bulgaria. The Egyptians mined gold before 2000 B.C. in Nubia. Large mines were also present across the Red Sea in where today is Saudi Arabia. By 325 B.C. the Greeks had mined in areas from Gibraltar to Asia Minor and Egypt. Also, the Romans mined gold extensively throughout the empire, developing mining by divert streams of water in order to mine hydraulically, and even pioneered "roasting", the technique for separating gold from rock.[3]

The first use of gold nanoparticles (AuNPs) is intimately related to the history of red-colored glass. The production of red glass starts with the very beginning of glassmaking in Egypt and Mesopotamia back in 1400-1300 B.C. The origin of the red color is debated, with some scientists stating that it is due to metal copper nanoparticles, while others state that it is due to cuprous oxide (cuprite) nanoparticles or both. The production of copper red glass is a challenge from the technological point of view, since it requires a reducing atmosphere; for this reason, red glasses are less frequent than other colors. There is written evidence that the alchemists of the middle ages knew how to produce red-colored glass with gold, although samples of such glass have yet to be found. It should be noted that some textbooks and websites state that the red color of stained glasses of medieval church windows is given by gold. However, in all cases analyzed so far, the colorant found is copper.

The first milestone in the history of gold ruby glass is a Roman opaque glass cup dated to the fourth century, the Lycurgus cup, which is exhibited at the British Museum in London (Fig. 3.1). The cup's decoration represents a mythological scene

about the triumph of Dionysus over Lycurgus, a king of the Thracians (circa 800 B.C.), when Ambrosia a Dionysus maenad, was transformed into a vine by Mother Earth, and holds Lycurgus captive while Dionysus instructs his followers to kill him. This cup shows a green jade color due to the diffusion of light when it is illuminated from outside, and a deep ruby red one in transmission when it is illuminated from inside. A detailed analysis of the Lycurgus cup (Fig. 3.1), published in 1965 by Brill[4], revealed the presence of minute amounts of gold (~40 ppm) and silver (~300 ppm) in the glass. In 1980, an electron microscopy analysis by Barber and Freestone[5], probe the presence of silver-gold alloy nanoparticles of 50-100 nm in diameter, with a ratio of silver to gold of about 70:30. Later, Hornyak *et al.* confirmed through a theoretical study that the deep red color of the Lycurgus cup due to light absorption around 515 nm, is consistent with the presence of Ag:Au alloy with ratio of 70:30.

(a)   (b)

Figure 3.1.   The Lycurgus cup, late Roman period (IV century). From the British Museum free image service. (a) Illuminated from outside. (b) Illuminated from inside.[3]

According to most of the textbooks and technical encyclopedias on gold, glass and ceramics, the production of the so-called "gold ruby glass" (Fig. 3.2) did not take place until the end of the seventeenth century, by Johann Kunckel (c.1637-1703, Brandenburg). The gold preparation that is added to melted glass to give it the ruby red color is attributed to Andreas Cassius of Leyden (1645-1700) who described in 1685 at his work "*De Auro*".[3,6] This is the so-called *Purple of Cassius*, which is a

precipitate obtained from the mix of two dissolutions in *aqua regia*, one of English tin and other of gold metal; followed by the precipitation of metallic gold, exhibiting the three cardinal colors found in gold, yellow, blue and black which turn into a beautiful reddish purple.[6]

Figure 3.2. Kunckel produced ruby glass in great quantities at Potsdam between 1679 and 1689, and many pieces survive today. This silver mounted tea-pot show the red color obtained by Kunckel using the purple preparation of gold chloride and stannous hydroxide, later to be associated with the name of Andreas Cassius.[6]

Since the discovery of gold, its medical application was because people considered it of an immortal nature, and have associated it with longevity, probably because of its resistance to chemical corrosion. Many ancient cultures, such as those in India and Egypt, used gold in medicine but mainly for its magic-religious power. In fact, gold played almost no role in rational therapeutics. An exception is China around 2500 B.C., with the earliest application of gold as a therapeutic agent. In Rome at the first century, Pliny the elder (23 - 79 A.D.), reported gold for healing fistulas and hemorrhoids.

The uses of gold were limited because at that time people did not know how to dissolve it and make it soluble. Until the medieval period, the European chemists became gold a prominent medicinal element, with the idea that the elixir of life,

Aurum potabile, can restore youth. *Aurum potabile* contained "little" gold[7] and was closely related with the discovery of *aqua regia* (a mixture of hydrochloric and nitric acids), the "royal" solvent of gold. A gold cordial was advocated by Nicholas Culpeper (1616-1654), in the seventeenth century for the treatment of aliments caused by a decrease in the vital spirits, such as melancholy, fainting, fevers and falling sickness. Later, in the nineteenth century, a mixture of gold chloride and sodium chloride $Na[AuCl_4]$, "muriate of gold and soda", was used to treat syphilis.[3,7]

Metal colloid science (as opposed to alchemical and aesthetic investigations) begun with the experiments of Michael Faraday on gold solutions in the mid-nineteenth century. Deep red solutions of colloidal gold were prepared by the reduction of chloroaurate ($AuCl_4^-$) solutions using phosphorus as reducing agent.[8]

The Ayurvedic medicine or Ayurveda[9] date back from India, thousands of years ago. Ayurveda relates the medical use of herbal compounds, metals and minerals, involving gold as medicine. For instance, *Swarna Bhasma* comprises globular gold nanoparticles with an average size of 60 nm. Gold is considered to be a rejuvenator and, because of that, is taken by millions of Indians each year. A typical daily dose corresponds to one or two milligrams of gold incorporated into a mixture of herbs.[3]

The use of gold compounds in modern medicine began in 1890, with the German bacteriologist Robert Koch who discovered that gold cyanide $K[Au(CN)_2]$ was bacteriostatic towards the tubercle bacillus. Gold therapy for tuberculosis was subsequently introduced in the 1920s, but soon proved to be ineffective. The suggestion that the *tubercle bacillus* was a causative agent for rheumatoid arthritis, led to the use of gold therapy for this disease and in 1985, and then was introduced the oral drug Auranofin, a gold complex for the treatment for rheumatoid arthritis.[7] Since then, gold drugs have also been used to treat a variety of other rheumatic diseases including juvenile arthritis, palindromic rheumatism, discoid lupus erythematosus and various inflammatory skin disorders such as pemphigus, urticarial and psoriasis.[3] The future for the medical chemistry of gold may be in other therapeutic areas than rheumatoid arthritis, the new research projects are into the

anticancer and antimicrobial activity of gold compounds.[7] The project that lead to this thesis is classified within the Nanomedicine of Cancer.

Pure metallic gold is non-toxic and non-irritating when it is ingested. Metallic gold has been approved as a food additive in the EU (European Union, E175 in the *Codex Alimentarius*). As gold leaf, it is sometimes used as food decoration in China, Japan, and India; also in Europe (France) on "*palet d'or*" chocolate. Gold leaves are also used as a component of alcoholic drinks, such as "Goldschläger", "Gold Strike" and "Goldwasser".[3]

The malleability and resistance to corrosion make gold perfect for dental use, although its softness requires to be alloyed, most commonly with platinum, silver or copper. So gold in alloys is used in tooth restorations, such as crowns and permanent bridges.[3] In order to go throw the design of desirable response of the AuNPs, for a selected application, the next section will resume the properties of interest for this project.

3.1.2. The Properties of Gold Nanoparticles

In the XXI century there has been a breakthrough in the nanoscale science and technology, which involves the ability to fabricate, characterize, and manipulate artificial structures, whose features are controlled at the nanometer level. The nanoscale materials show properties different from those of a single atom, and because of the number of atoms on the surface, also present different properties as those from bulk solid, as higher chemical reactivity or probably lower melting point,[8] among many others.

Gold is the third member of eleven group of the Periodic Table, lying below copper and silver. Gold possesses a unique combination of physical and chemical properties in both the macro and nano scale; on the macroscopic scale gold is known for its unique yellow color, for its chemical stability, high redox potential, considerable malleability and high density. On the nanoscale, gold has an unusual electronic configuration, combined with other effects due to the extremely small dimensions:[3]

- Electromagnetic confinement when an optical wave interacts with a gold nanoparticle giving rise to their specific color through a localized plasmon resonance.
- Quantum effects that explain the change from metallic to semiconducting character of NPs.

The crystal structure of gold is face-centered cubic (*fcc*), and its metallic radius is fractionally smaller than that of silver (Table 3.1); this structure is responsible for its malleability. It has a non-zero nuclear spin quantum number ($I = 3/2$) and its nucleus is therefore "magnetic", but its receptivity relative to the proton is only 2.77×10^{-5}, so it's a hard nucleus to study.[3]

Table 3.1. Physical properties of elements of column 11 in periodic table.[3]

Property	Cu	Ag	Au
Atomic number	29	47	79
Atomic mass, amu	63.55	107.868	196.9665
Electronic config.	$[Ar]3d^{10}4s^1$	$[Kr]4d^{10}5s^1$	$[Xe]4f^{14}5d^{10}6s^1$
Structure	Fcc	fcc	fcc
Metallic radius, nm	0.128	0.14447	0.14420
Density, gcm^{-3}	8.95	10.49	19.32
Melting temp, K	1356	1234	1337
Sublimation enthalpy, $kJ\ mol^{-1}$	337 ± 6	285 ± 4	343 ± 11
1st ionization energy, $kJ\ mol^{-1}$	745	731	890
Electrical resistivity at 293 K/micro-ohm cm	1.67	1.59	2.35
Interband transition threshold,	$3d \rightarrow 4s$	$4d \rightarrow 5s$	$5d \rightarrow 6s$
/eV	2.1	3.9	1.84
/nm	590	318	674

The optical absorption of gold in the visible region of the spectrum is due to the relativistic lowering of the gap between the center of the *5d* band and the Fermi level (Fig. 3.3). The interband threshold is the energy required to excite electrons from the top of the *5d* band into the *6sp* conduction band. In the case of gold, an optical wave of 1.84 eV that corresponds to a red wavelength, is able to excite this transition.[3]

The electronic structure of gold atoms in the massive (bulk) state, however is not exactly that of the free atom, because a weak white line on the leading edge of the L_{III} X-ray absorption edge signifies a small number of vacancies in the *d*-band because of *d-s* hybridization. The chemistry of gold ($5d^{10}6s^1$) is determined by the easy activation of the *5d* electrons and its propensity for acquiring a further electron to complete the $6s^2$ level and not to lose the one it has; that is the reason of more electron affinity and higher first ionization potential than copper or silver (see Table 3.1), and accounts for the formation of the Au^{-1} state. The Au^{III} state is the more common, which has the $5d^8$ configuration. The Au^V state ($5d^6$) is present in molecules as AuF_5, the Au^I state is uncommon. Gold's electronegativity (2.4 in

Pauling units) is equals to one of selenium and approaches to the one of sulfur and iodine (2.5); also its electrode potential (E^0 = +1.691 V) is high for a metal. Its electronic structure determines its nobility, and its inability in the massive form to interact with oxygen or sulfur compounds. The sulfides Au_2S and Au_2S_3 are known, but are of limited stability and importance. The dissolution of gold requires both an oxidant and a ligand to stabilize the resulting cation. Thus it dissolves in *aqua regia* to form $AuCl_4$, and in the presence of oxygen in aqueous CN^- to form the $[Au(CN)_2]^-$ anion.[3]

When the size of a gold particle is progressively decreased, significant changes in physical properties and chemical reactivity are observed; they become especially noticeable when size falls below about 10 nm.[3] As an example of how drastically the number of surface atoms increases with decreasing particle size, consider a cube or 1 cm of edge, the percentage of surface atoms would be only 10^{-5}%. Dividing the same cube into smaller cubes with an edge of just 10 nm, results in a percentage of surface atoms of 10% and in a cube with an edge of 1 nm every atom would be a surface atom. Because of this, changes in the size range of a few nanometers are expected to lead to great changes in the physical and chemical properties of the nanoparticle.[10]

Changes in the electronic structure also affect the optical response of particles, then with the reduction of size down to the nanometer scale AuNPs colloids, matrix and films exhibits various colors.[3]
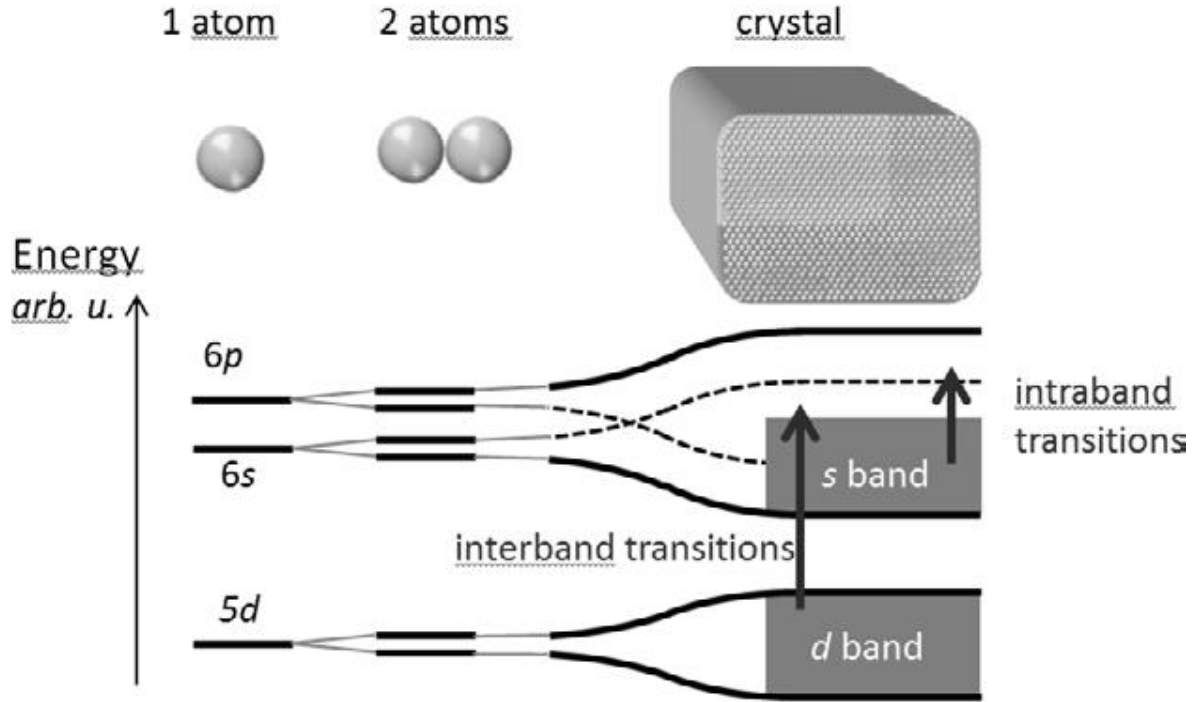
Figure 3.3. Sketch of the evolution of the electronic structure of gold; for a single atom, the electronic levels are discrete. For a gold dimer Au-Au, the levels tend to split. For a crystal, this lifting of degeneracy widens and forms a continuum of levels: the d band emerges from the d electrons of all the gold atoms and is completely filled with electrons. The conduction band is formed from the 6s and 6p orbitals and is partially filled. With this structure, light can excite two kinds of transitions: intraband transitions and interband transitions.[3]

3.1.2.1.1. Localized Surface Plasmon Resonance (LSPR)

When electromagnetic radiation interacts with matter at nanoscale, there arise interesting phenomena and properties that are used and applied in diverse applications. Particularly, the optical properties of NPs are presented in the Appendix I. In this section, we will introduce the localized surface plasmon resonances (LSPR), which is a significant phenomenon for the understanding of this work.

In dealing with plasmon resonance, a certain confusion reigns in the terms used. Opposite to the propagation of surface plasmon polaritons (SPPs) in a flat metallic surface, the closed geometrical boundaries in a metal nanoparticle, can sustain a localized oscillation of the surface charge density.[3,11] The modes belong to resonant

oscillations of the surface charge density at the boundaries of the metal nanoparticle (see Fig. 3.4).[11]

Propagating Surface Plasmon
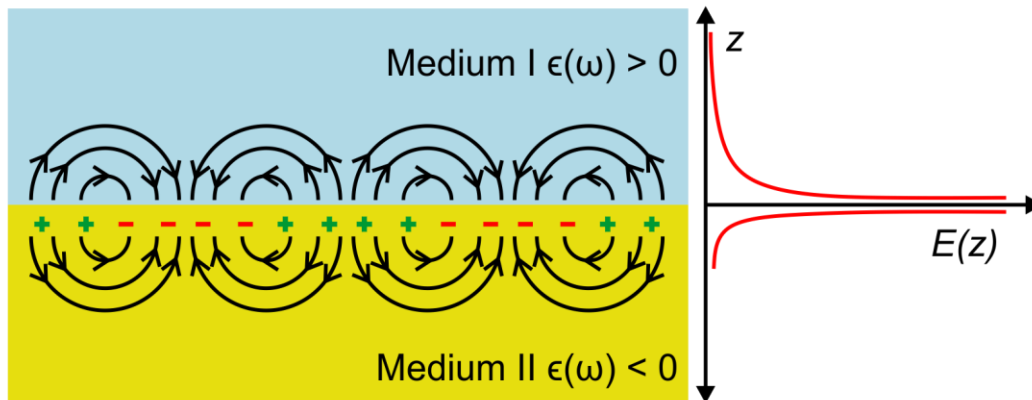
Localized Surface Plasmon
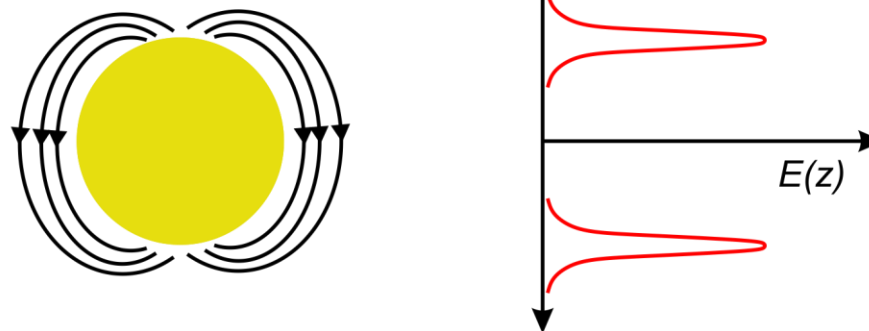
Figure 3.4.   Top, schematics of the surface charge density of a propagating surface plasmon polariton. Bottom, schematics of the surface charge density of a localized surface plasmon. In the geometric boundaries of a NPS, there are produced surface charge density oscillations, and once they are irradiated with light at proper wavelength, they become coupling resonantly giving rise to an enhanced LSPR.

The optical response of the LSPR in a metallic particle can be described through the particle polarizability. The net electric field E_{tot} around a dielectric particle is composed of the superposition of an external applied field E_0 and the induced (dipole) field in the particle (see Fig. 3.4(b)). For a polarizable spherical particle with radius r_m and dielectric constant ε, placed in a medium with dielectric constant ε_m, the following expression is found for the field gain, G:

$$G(\omega) = \frac{E_{tot}(\omega)}{E_0(\omega)} \approx 1 + \frac{\varepsilon(\omega)-\varepsilon_{\mathrm{m}}}{\varepsilon(\omega)+2\varepsilon_m}\left(\frac{r_m}{r+r_m}\right)^3 \qquad \text{Eq. 3.1}$$

In the condition for the excitation of a surface plasmon in the metallic nanoparticle, *G* can reach enormous values, with ε close to *-2ε_m*; in a "normal" dielectric medium where $\varepsilon_m>0$; in a metal, ε can be negative; additionally, the imaginary part of ε should be as small as possible.[12]

3.1.2.2. Dependency of Optical Properties on Size and Shape

The physical and chemical properties of NPs depend on the type of motion its electrons can execute, which is dictated by the degree of their spatial confinement and enhancement of light field, intrinsic to LSPR modes in metal NPs. The characteristic features of the LSPR, such as absorption and peak width, depend on the shape, size, composition, surface charge, interparticle interactions, surface-adsorbed species, and the refractive index of the surrounding medium.[13] By changing the morphology of AuNPs, their LSPR peak can be tuned to the NIR region (Fig. 3.5).[14]
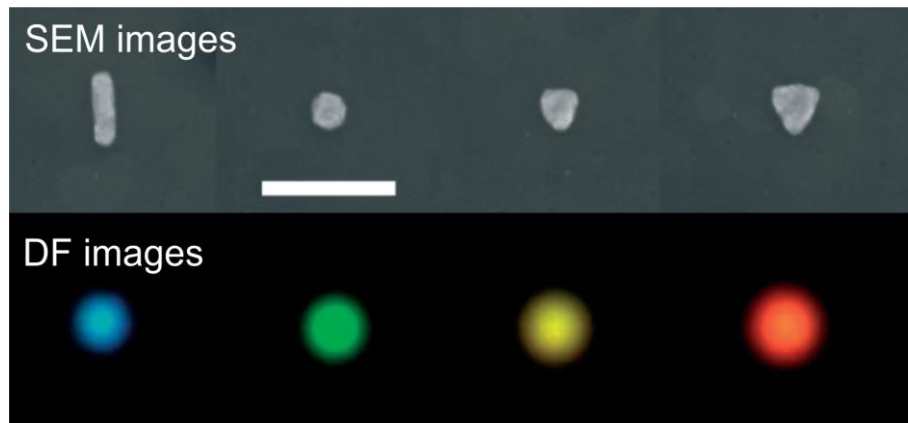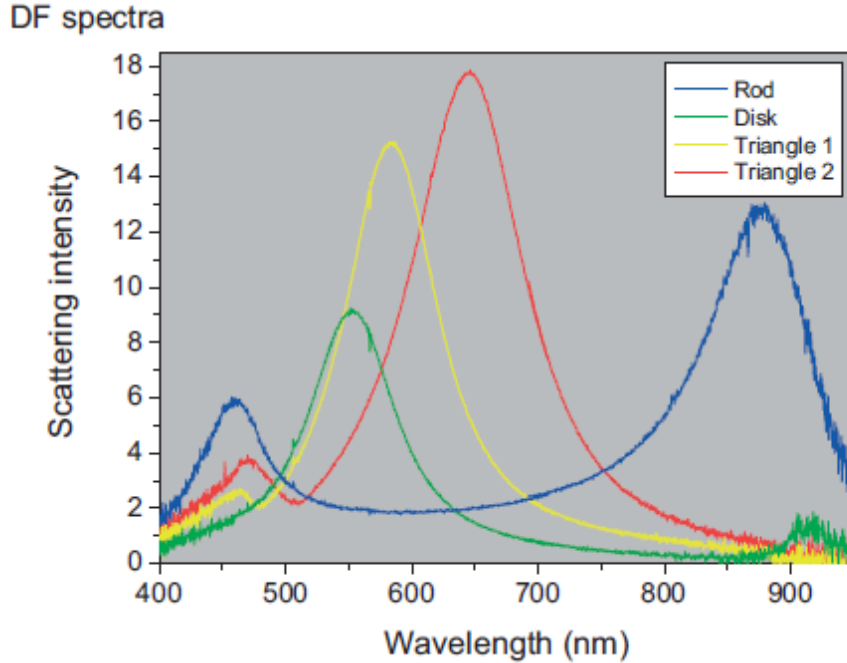
DF spectra

Figure 3.5. Scanning electron micrographs (top), dark-field images (middle), and dark-field spectra of several metallic nanoparticles made by e-beam lithography. From left to right the shapes are, a rod, a disc, and two triangles (the right hand one being the larger of the two). The thickness of these particles were 30 nm and the substrates were silica glass coated with 20 nm of ITO. (The scale bar in the top figure is 300 nm.)[15]

For nanoparticles much smaller than the wavelength of light ($2r \ll \lambda$, or roughly $2r < \lambda_{max}/10$) only the dipole oscillation contributes significantly to the extinction cross-section. Thus, in the case for spherical AuNPs larger than 20 nm radii, the dipole approximation is no longer valid, the plasmon resonance depends explicitly on the particle size. The larger the particles become, the more important are the higher-order modes as the light can no longer polarize the nanoparticles homogeneously. These higher-order modes peaks at lower energies and therefore the plasmon band red shifts with increasing particle size (Fig. 3.6). At the same time, the plasmon bandwidth increases with increasing particle size.[10]

92
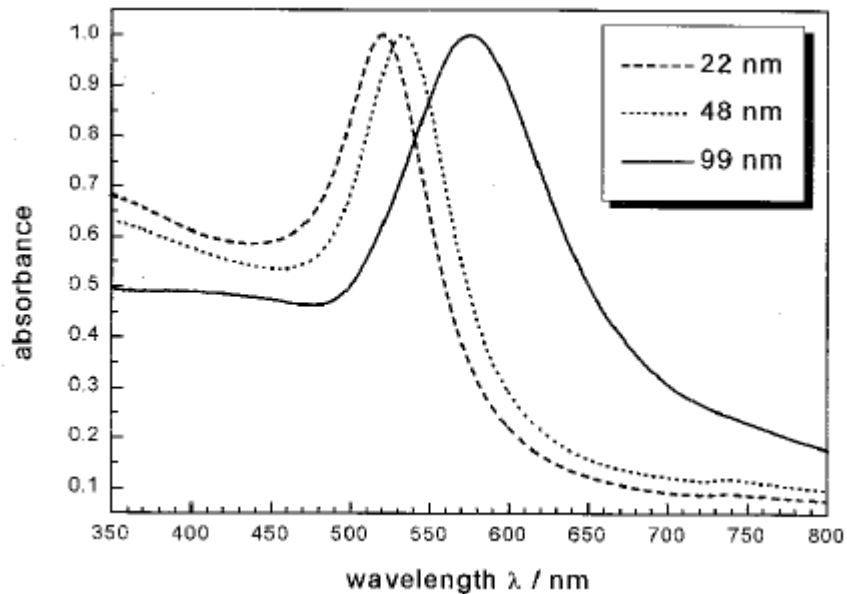
Figure 3.6. Optical absorption spectra of 22, 48 and 99 nm spherical gold nanoparticles. The broad absorption band corresponds to the surface plasmon resonance.[10]

As in the Fig. 3.6, the plasmon bandwidth can be associated with the dephasing of the coherent electron oscillation. Large bandwidth corresponds to rapid loss of the coherent electron motion. For 5 nm particles, the plasmon oscillation is strongly damped and its absorption becomes weak and broad, and it completely disappears for nanoparticles less than about 2 nm in diameter. This is because the electron density in the conduction band becomes very small.[10]

Geometries with sharp corner such as triangular, rod-like, or star-like can lead to a much stronger concentration of the electromagnetic field at the apex of their tips as compared to spherical particles.[11]

3.1.2.2.1. NIR Absorbing Nanoparticles

Spherical AuNPs usually show the LSPR peak at ~520 nm, with slightly red-shifted absorbance as the nanoparticle diameter increases (see Fig. 3.7 and Table 3.2).
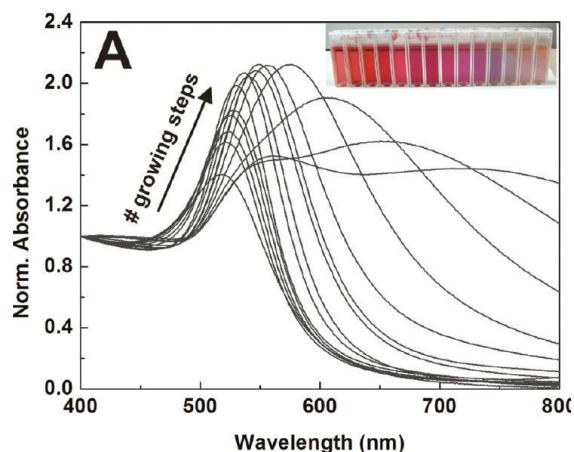
Figure 3.7. UV-Vis spectra of spherical AuNPs of different size. All spectra are normalized at 400 nm to facilitate comparison.[16]

Table 3.2. Summary of sizes and optical response of spherical AuNPs.[16]	
Diameter (nm)	**SPR peak (dipolar, nm)**
8.4 ± 1.0	518
17.6 ± 1.2	521.5
22.3 ± 2.2	523.5
31.1 ± 2.8	525.5
36 ± 2.4	527.5
42.2 ± 2.3	530.5
54.4 ± 3.3	535
64.8 ± 3.4	540
69.3 ± 4.5	542.5
80.1 ± 5.4	546.5
96.1 ± 5.6	555.5
109.2 ± 7.6	574.5
123.6 ± 10.6	606
150.0 ± 9.9	649
180.5 ± 10.7	720

New resonances can be achieved with interacting particles,[15] *e.g.*, in a dimer geometry a strong field concentration is achieved (optical gap antenna).[11] Upon linearly polarized illumination along the particle alignment, a strong gradient of surface charge is created across the gap, leading to a concentration of light in

between the two particles. For example in the Fig. 3.8, the distribution of the electric field intensity in the equatorial plane of a dimer formed by two gold cylinder lying upon a glass substrate and separated by a 10 nm air gap. Both the magnitude and confinement of the "*hot spot*" increase as the gap becomes smaller and the near-field coupling becomes stronger.[11]
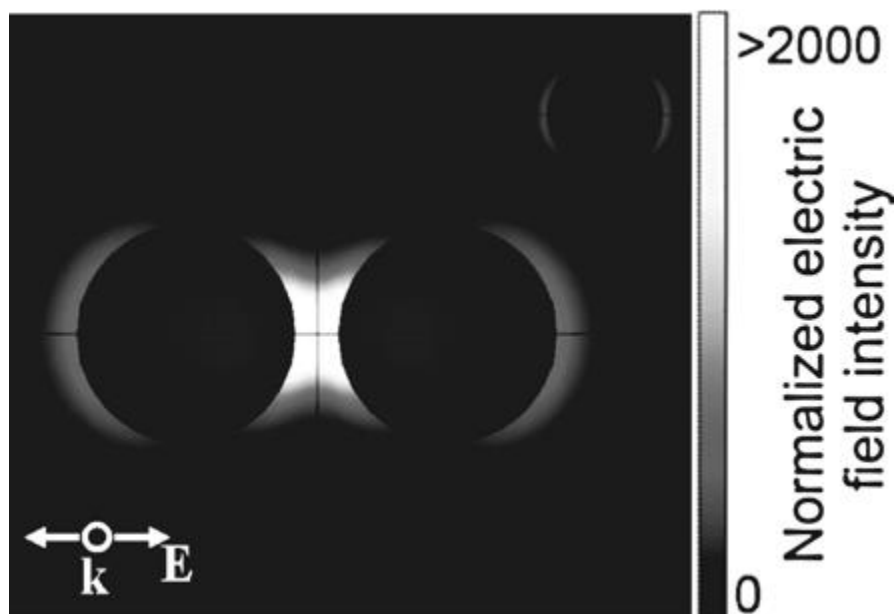
Figure 3.8. Plasmonic dimer formed by two gold cylinders of 50 nm diameter and 20 nm height, separated by a 10 nm air gap. Normalized electric field intensity distribution computed (in the equatorial plane of the particles) at the plasmon resonance (659 nm) upon a plane wave illumination (normal incidence) linearly polarized across the particle alignment. For reference, the near-field distribution for a single gold disk at resonance is shown in the inset (upper right).[11]

Independently of the gap size, the geometry of the particles has a considerable influence on the optical properties of the antenna, both on its spectroscopy and on the distribution of the local field. Using triangular particles or rods instead of a cylinder tends to broaden the resonance bandwidth and increase the ratio between the field within the gap and at the outer edges.[11]

As mentioned in Sect. 3.1.2.2, the shape and size can influence the frequency of LSPR. Typically, this is achieved by designing structures that have an inhomogeneous geometry, such as core/shell nanoparticles, or with sharp

geometrical features such as nanoprisms, nanocubes, and star-shaped particles (Fig. 3.5).[15] Gold nanorods (AuNRs) typically have two LSPR peaks, one for the transverse mode around 520 nm and the other for the longitudinal mode whose position strongly depends on the aspect ratio of the nanorod and can be tuned from visible to NIR region. The gold nanoshells (AuNSs), are a core-shell NP composed of a dielectric core, typically silica, coated with an ultrathin Au layer.[17] The optical absorption of AuNSs can be tuned to the NIR range by varying the relative size of the core and shell. Gold nanocages (AuNCs), are hollow cubic Au nanostructures with ultrathin porous walls and truncated corners. The LSPR peaks of AuNCs can be tuned to any wavelength in the range of 600-1200 nm by controlling the size or wall thickness. Gold nanostars or multibranched gold nanoparticles (MB-AuNPs), contain multiple peaks with absorbance tunable in the NIR region, depending on the width and length of peaks. The extinction spectra of MB-AuNPs exhibits broad visible and NIR absorbance due to the overlapping of spectra.[14] Depending on the characteristics of the branches, these kind of nanoparticles can present three plasmonic resonances. Two out of the three NIR plasmonic resonances depend strongly on the length:width ratio of the branches.[18,19] The other band, is hypothesized that corresponds to the geometrical arrangement between peaks, in this case, co-linear branches, then the longitudinal oscillation of the electrons along these aligned branches is responsible for the long LSPR and the rest of branches contribute to the intermediate LSPR.[20]

3.1.2.3.   Applications of Gold Nanoparticles

Gold nanostructures have proved to be a versatile system for a broad range of biomedical applications, for cancer diagnosis and therapies, based on the tuning of the optical phenomena of LSPR.[14] Particularly, plasmonic nanostructures reveal a wide range of phenomena, including unusual directionality of the light-scattering properties, tunable Fano resonances, the enlightenment of new modes that arise due to conductive overlap and charge transfer between adjacent individual nanoparticles.[21] In practice, plasmonic excitations decay into combined effects. One part of the absorbed light concentrates at the particle surface and its scattering, so

the far field is enhanced. The remaining absorbed energy is converted into heat, creating a nanoscale photo-thermal transducer.[11] When plasmonic nanoparticles are excited with high-power nanosecond laser pulses in a fluid environment, a rapid generation of heat forms a transient vapor bubble around the nanoparticle that grows to only hundreds of nanometer in diameter and lives only hundreds of nanoseconds before collapse.[21]

3.1.2.3.1. Heat Generation

Living cells are highly sensitive to the temperature and rises of few degrees can lead to cell death. The NIR absorption and related photothermal effect made the anisotropic nanoparticles ideal for both imaging and therapy agents. It has been demonstrated the NIR absorbing capacity of several anisotropic nanomaterials such as nanorods, nanocages, nanoshells, and nanostars can be used for the photothermal therapy. Such therapy is less invasive than chemotherapy or surgery and holds strong promise as a new form of cancer treatment. By varying the power density, the laser exposure time, and the time of responde after irradiation, it is possible to optimize the treatment conditions to achieve effective destruction of the cancer cells.[13]

3.1.2.3.1.1. Nanoscale Heat Generation in Metal Nanoparticles

Upon suitable illumination matching the resonance conditions, the light is efficiently coupled to the nanoparticle. Part of the coupled light is efficiently scattered in the near field, leading to an enchanced field at the particle surface, and to the far field, the NP acting as an efficient optical antenna. The remaining part of the energy is absorbed and dissipated into heat, creating an increase of the particle environment temperature.[3]

The ability of a bulk material to heat up upon laser illumination is mostly dictated by its structural properties and in particular by the imaginary part of its dielectric function at the illumination wavelenght. Heating in plasmonic metallic nanoparticles is a

process that, directly depends on their optical response as reflected in the expression of the heat source density *q(r)*:

$$q(r) = \frac{n^2 \omega}{2 \mathrm{T}(\epsilon(\omega)) |E(r)|^2}.$$

Where *n* and *ε(ω)* stand for the refractive index of the surrounding medium and the dielectric function of the metal at the light frequency ω, respectively. The quantity of generated heat is governed by the electric field intensity $\mathrm{T}(\epsilon)|E(r)|^2$ within the metal. Consequently, the drastic influence of particle geometry on the plasmon mode distribution offers some degree of control for designing efficient nano heat-sources, remotely controllable by laser illumination.[11]

The Green Dyadic Method (GDM) has been used to quantify the influence of the geometry of a AuNP on its heating efficiency. The GDM makes it possible to map the spatial distribution of the heat power density inside the nanoparticles, providing further insight into the influence of the particle shape and the illumination conditions on the origin of heat. Fig. 3.9 displays calculation of heating power (*q(r)* integrated over the particle volume) spectra for different geometries of gold nanoparticles surrounded by water and illuminated by a plane wave, with intensity of 1 mW/µm² = 10^5 W/cm², corresponding to the typical value found in the literature for biological applications.[11]
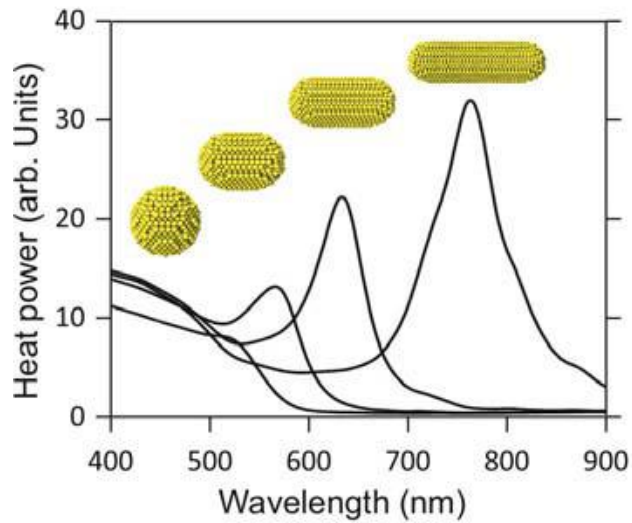
Figure 3.9.　Heat generation in gold nanoparticles. Evolution of the heat power spectrum with the particle aspect ratio at a constant gold volume, calculated by the Green Dyadic Method (GDM).[3]

A red-shift of the LSPR is expected for nanorods compared with spheres, and a substantial increase in the heating efficiency, by a factor of 5 from the sphere is expected. By means of the GDM, in the Fig. 3.10 is shown the distribution of the heat power density *q(r)* around and across each of the geometries. For a sphere excited at the SPR, the heat generation arises mainly from the outer part of the particles facing the incoming light. Consequently, the major part of the nanoparticle presents a weak electric field intensity and thus does not contribute to heating. For elongated nanorods, the field can further penetrate the inner part of the particle thus making the whole metal volume more efficiently involved in the heating process. The heat generation mainly arises from the central part of the nanorods because the extremities undergo charge accumulation that leads to a weaker electric field inside the structure.[11]
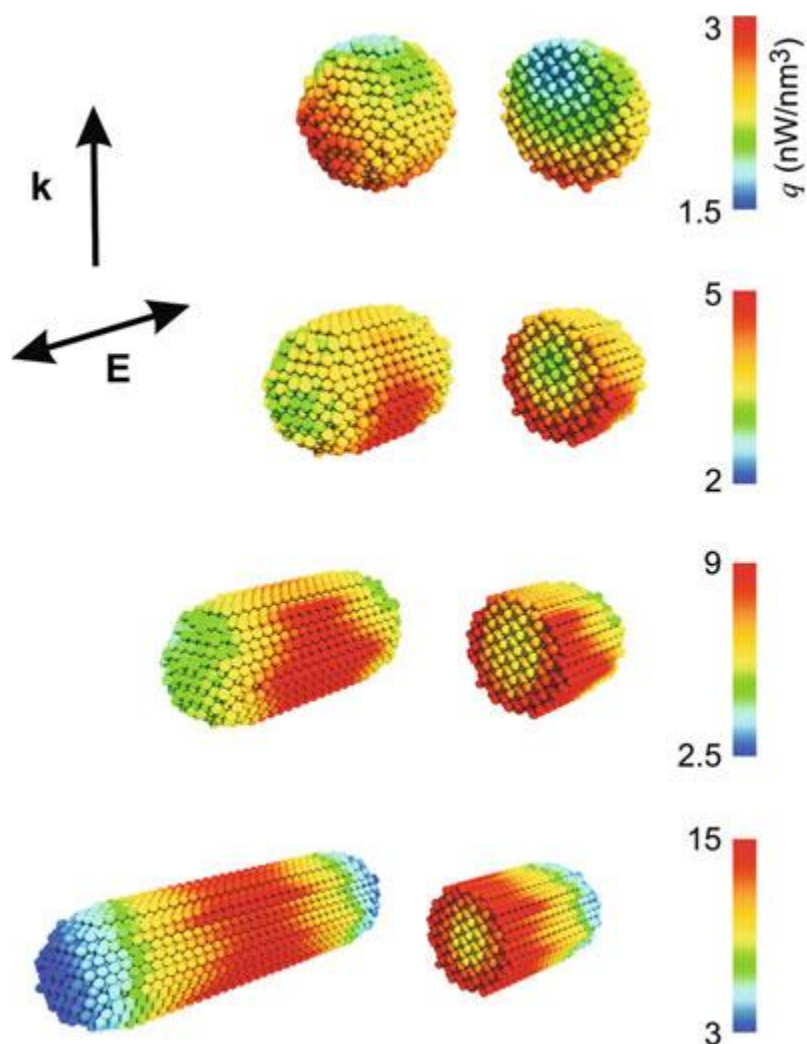
Figure 3.10. 3D mapping of the heat power density computed for the four nanoparticles of Fig. 3.9 at their respective plasmon resonance. The *k* and *E* vectors give the illumination conditions.[11]

An example of the transient regime of the heating of surrounding medium is mapped in the Fig. 3.11. It shows the temperature field around a core-shell nanoparticle consisting of a 40 nm silica bead coated with a 0.5 nm thick gold layer. The nanoshell is irradiated with a 7 ns Gaussian light pulse with a peak power absorbed of $5 \times 10^{17} Wm^{-3}$ (typical for nanosecond lasers). The surrounding medium is silica, but the method could be used for any medium. Such mapping can be useful for biomedical applications, for selecting the irradiation power or the molecular spacer length between the NP heat source and the biological objet to be targeted.[3]

100
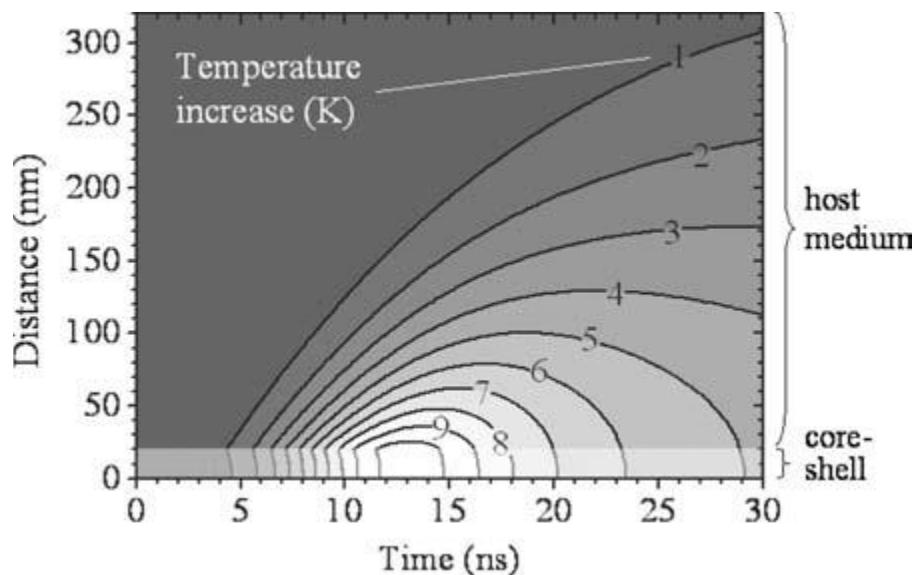
Figure 3.11.   Isothermal plot of the medium (silica) surrounding a core-shell NP consisting of a 40 nm silica bead coated with a 0.5 nm thick gold layer, irradiated with a nanosecond laser pulse.[3]

When light interacts with an ensemble of randomly dispersed particles, as in a fluid environment, the light can be either scattered or absorbed, or both, depending on the properties of the particles. When the average distance between particles in a solution is smaller than the wavelength of light, the wave nature of light must be explicitly considered, and multiple scattering events can lead to phenomena such as weak localization or Anderson localization of light. Multiple scattering events control the spatial distribution of absorbed photons (Fig. 3.12), which directly determines the thermal response.[22] Because of these series of energy exchanges, the internal energy of the electron gas subsequent to light pulse absorption undergoes *(i)* a sudden and strong rise, *(ii)* an inner redistribution within the electron gas (athermal regime), *(iii)* a fast decrease (*e-ph* scattering) and *(iv)* a slow return back to equilibrium (thermal transfer to the host medium.

The next figure presents a Monte Carlo simulation of temperature evolution on a NP's colloid excited with an incident laser at the top of the solution. This result shows that the temperature increases at the top of the nanoshells solutions for 10°C more than in nano-matryoshka solutions of equal concentration (Fig. 3.13).[22]

101
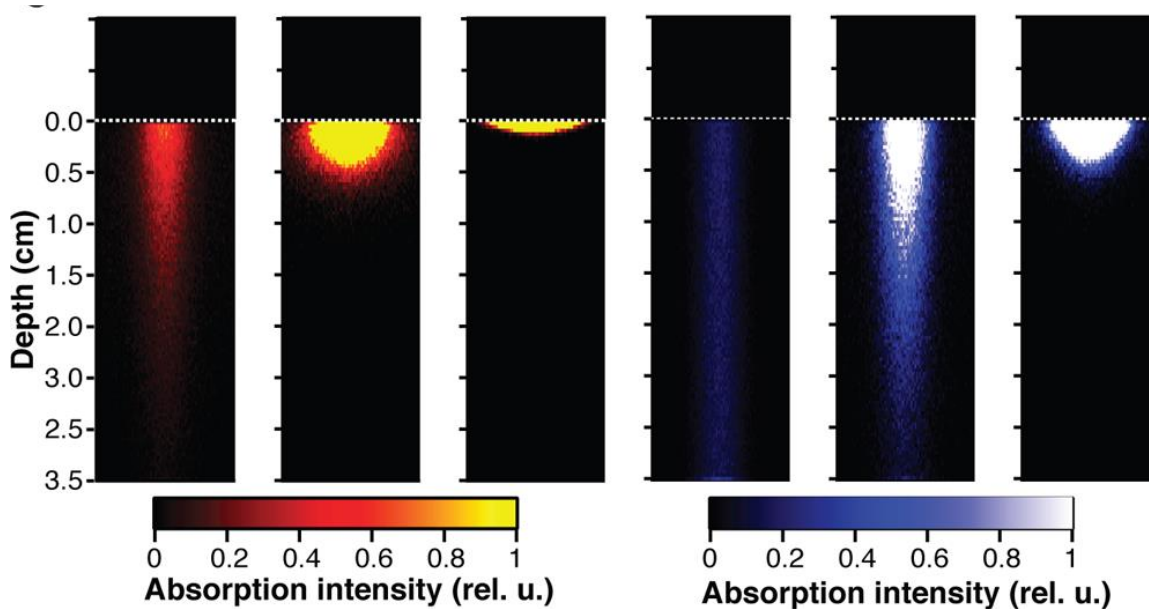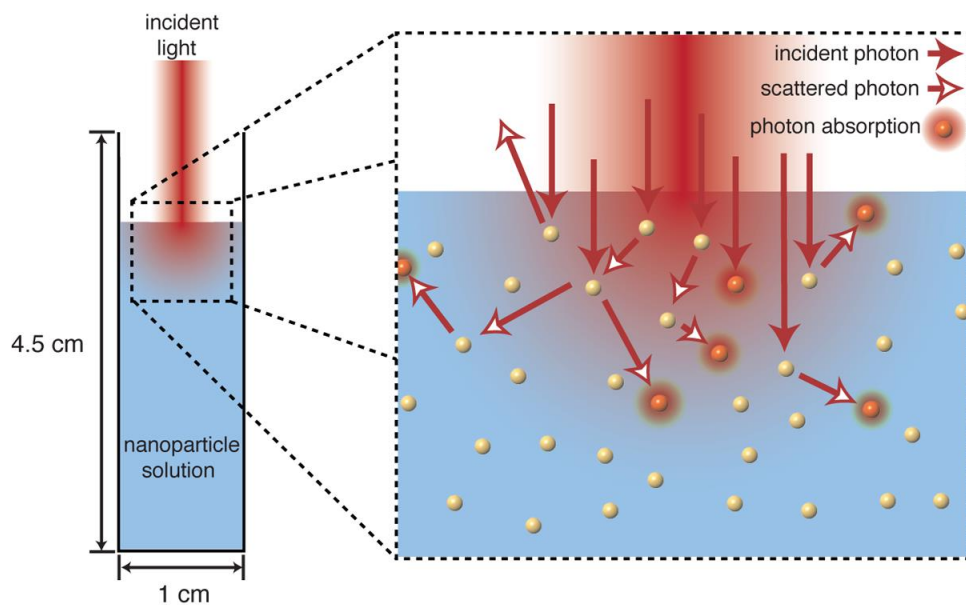
Figure 3.12. (Top) Scheme for a dense solution of nanoparticles contained in a cuvette illuminated with 808 nm laser light; showing multiparticle optical interactions in such nanofluids where photons are scattered and/or absorbed. (Down) A Monte Carlo simulation of absorption intensity of photons corresponding to Nanoshells (red) and Nanomatryoshkas (blue) at 5 ×10^{8-10} per mL.[22]
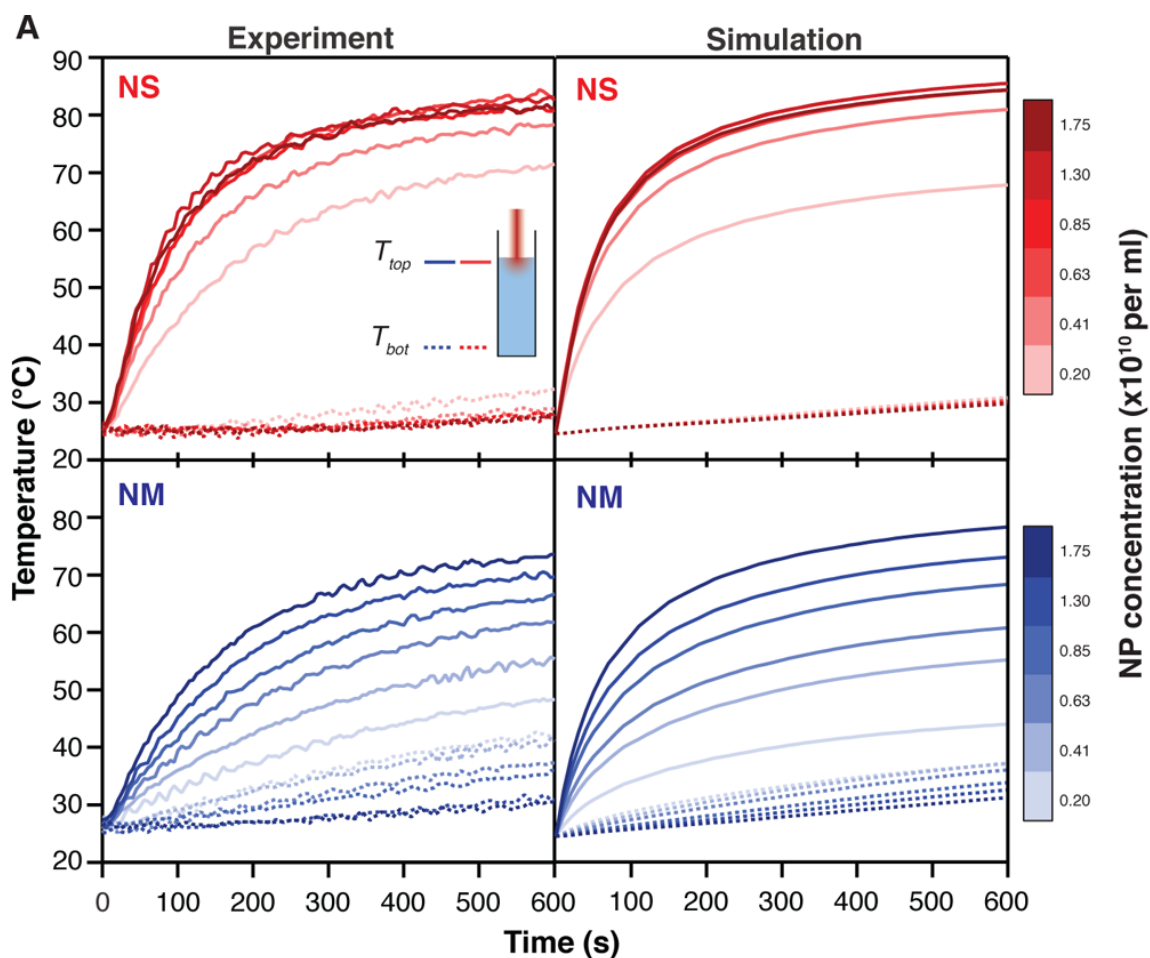
Figure 3.13. Experimental and simulated temperature evolution of illuminated nanoparticle solutions, nanoshells (NS) and nanomatryoshkas (NM).[22]

It has been also reported that a complex of AuNPs can melt ice, when laser light of weak intensity is applied. By itself, the laser could not melt the ice. A group of AuNPs can generate more heat than single arrangements (4.5×10^9 NPs/mL, $0.2 - 50$ mW), agglomerates of AuNPs can generate craters in the ice around the 200 μm in diameter, at velocities of 2500 μm/s.[23]

3.1.2.3.1.2. Photothermal Therapy with AuNPs

When AuNPs are exposed to electromagnetic waves of same wavelength at the SPR of the AuNPs, occurs a coupled oscillation of the conduction electrons that produce dispersion and absorption of light.[24] This phenomenon implies that part of the

incident energy is converted into heat (by means of the electron-phonon interaction), and because of this, it is possible to reach the necessary temperature to ablate cancer cells. It is known that around 85-90 °C there is enough temperature for to induce conformational changes in RNA and DNA, and above 40 °C cellular death is induced due to protein's denaturation (see Chap. 1).

The physical mechanism of heating by thermal ablation therapies provides obvious advantages over other cancers resistant to treatments such as chemotherapy. Therefore, by using this method, it only remains to carefully design the size, shape and surface chemistry of the AuNPs; so that the proportion of scattered light relative to the absorbed light is optimum for this particular application.

The continuous research in this area has generated significant advances in the field of synthesis of metal nanoparticles that can absorb in the NIR region with appropriate intensity and wide band. In the present, hyperthermic therapy by using AuNPs been studied in clinical trials phase II.[25]

As we mentioned in previous topics, not only the material and size of the NPs influenced its response to laser irradiation, also the shape influences the efficiency of light conversion into heat. There is reported for nanohexapods a rapid increase in temperature during the first 3 min of laser irradiation, and a total temperature increase of 26.5 °C, that it was slightly major than in the case of gold nanorods and minor than gold nanocages at the same extinction intensity (see Fig. 3.14).[26]
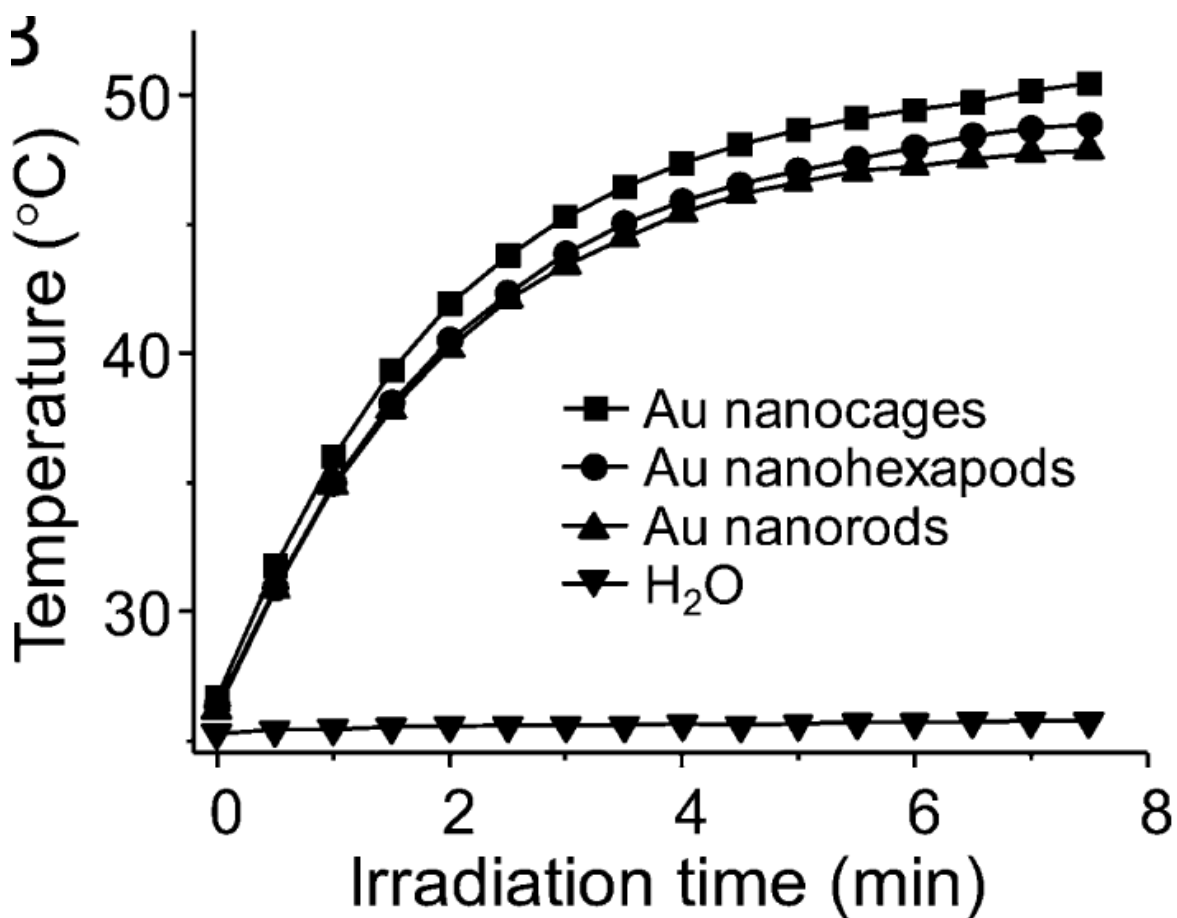
Figure 3.14. Plots of temperatures as a function of irradiation time for suspension of Au nanohexapods, nanorods, and nanocages. The concentration of each suspension was adjusted to give an extinction intensity of 1 at 805 nm. The laser power density was 0.8 W/cm².[26]

If the results of Fig. 3.14 are analyzed in terms of photothermal conversion efficiency per Au atoms, at the same extinction intensity, the concentrations of Au atoms for the nanostructures were 34.4 µg/mL for nanohexapods, 36.4 µg/mL for nanorods, and 9.6 µg/mL for nanocages. Then the nanocages are more efficient systems.[26] Besides their photothermal conversion efficiency, several reports have shown that the gold nanorods lose their shape during continuous laser irradiation in much less time than other structures. Within In-vivo models, the gold nanohexapods also have shown better response besides gold nanorods and nanocages (see Fig. 3.15).
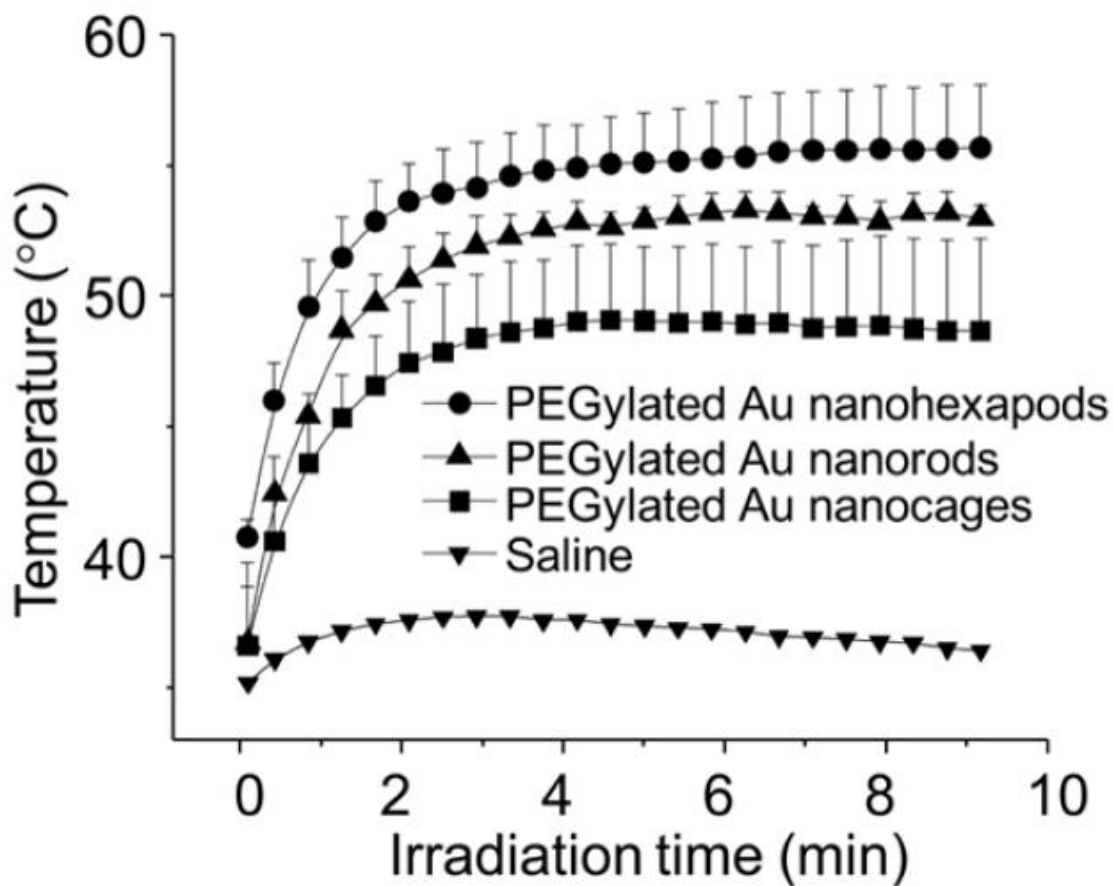
Figure 3.15. Plots of average temperature increase within the tumor region as a function of irradiation time. The laser power density was 1.2 W/cm².[26]

Penta-branched NPs (0.6 mg/mL) with three LSPR have shown to have photothermal activity on both the intermediate (NIR) and long (SWIR) LSPR, under CW laser irradiation. The maximum ΔT depends linearly on the power of the laser source reaching ΔT of 14°C for 150 mW, for irradiation at the intermediate band. When the irradiation laser has de wavelength near to the far band, the ΔT is bigger (12 °C for 100 mW) due to this linear dependency of ΔT and the power laser.[20]
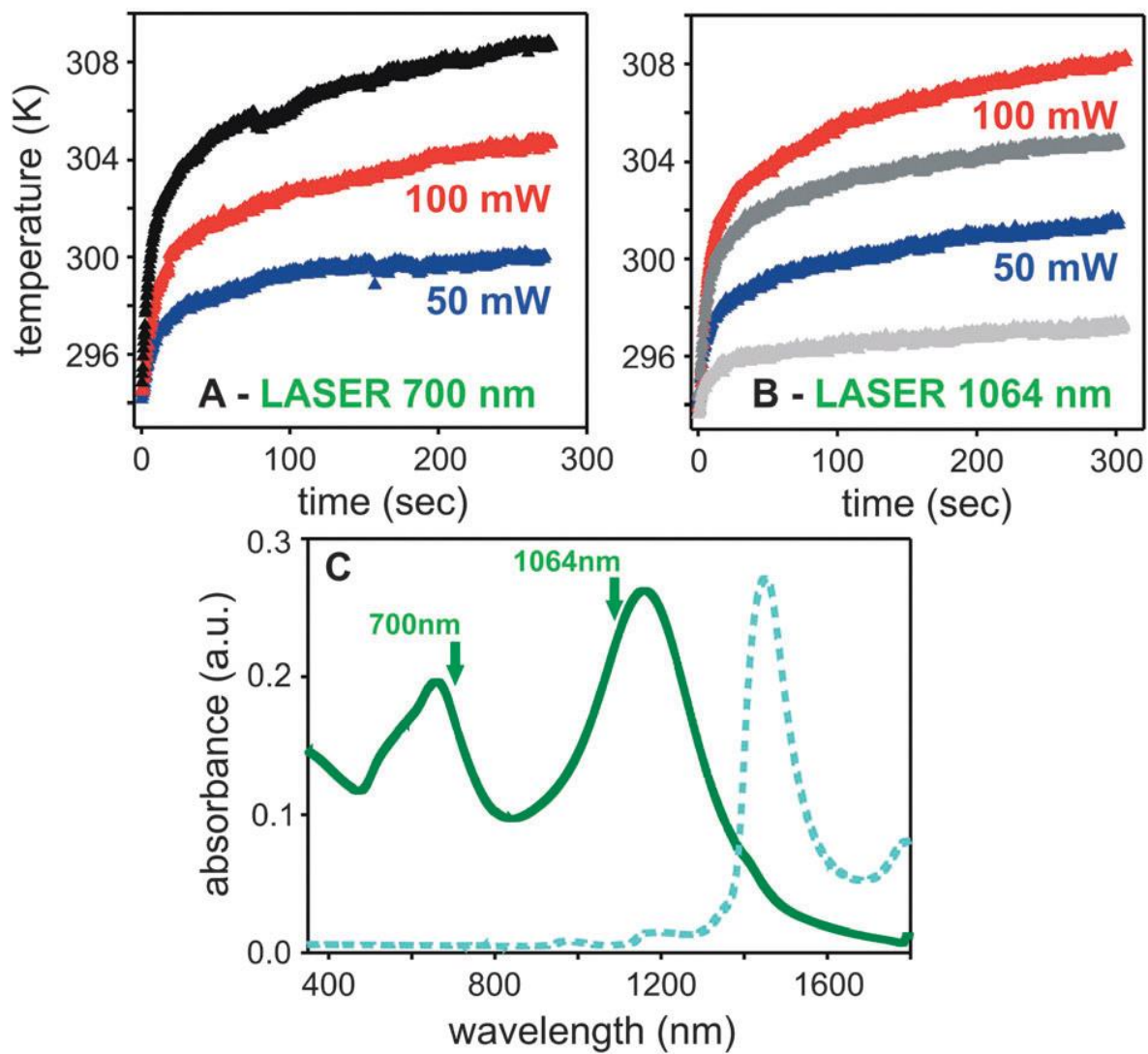
Figure 3.16. Plot of T vs time for branched NPs irradiated at (A) 700 nm; (B) 1064 nm; and (C) absorption spectrum of the NPs (green solid line) and water (dashed line). The green arrows show the laser wavelength used for solution.[20]

Table 3.3. Thermal response of AuNPs *in-vitro* and *in-vivo*, under laser irradiation.

Nanoparticle Type	Concentration	Medium	Exposure	Temperature Analyses	Ref.
Au nanoshells 110 ± 11 nm 10 nm shell $\lambda_{máx}$ = 820 nm	4.4×10^9 NPs/mL 1 h	Human breast epithelial carcinoma SK-BR-3 cells 12-well plates 10 % FBS 37 °C	Coherent light 820 nm 35 W/cm² 7 min	Photothermal destruction within the laser spot	27
	20 – 50 µL 25 min	Tumor bearing mice D = 1 cm	4 W/cm² 5 mm spot diameter < 6 min	MRI ΔT = 37.4 ± 6.6 °C $\Delta T_{control}$ = 9.1 ± 4.7 °C	
Au nanoshells 120 nm 8-10 nm shell $\lambda_{máx}$ = 805-810 nm	100 µL 2.4×10^{11} NPs/mL Injected via tail vein	Female albino BALB/cAnNHsd Inoculation: CT26.WT murine colon carcinoma tumor cells Ø = 3-5.5 mm	Diode laser 808 nm 600 µm 4 W/cm² 3 min	IR thermometer $T_{máx}$ = 30 seg T = 50°C	28
Au nanocages 48 ± 3.5 nm $\lambda_{máx}$ ≈ 800 nm	9×10^{12} particles/mL	Solution	IR camera 10 s per frame CW 808 nm 1 W/cm² 10 min	$\Delta T10^{12}$ = 43.9 °C $\Delta T10^9$ = 10.2 °C $\Delta T_{control}$ = 3.5 °C	29
	100 µL 15 nM 72 h	Athymic mice U87wtEGFR cells 200 – 400 mm³	0.7 W/cm² 10 min	$T_{máx}$ = 2 min 54 °C $T_{control}$ = 37 °C 10 min stable	
Gold nanorods 67 × 10 nm $\lambda_{máx}$ = 1050 nm	Local delivery: 0,1 day 30 µL 3.6 × 10^{12} particles/mL	MXH10/Mo/lpr mice Tumor in lymph nodes 3 days 9.76 ± 0.35 mm	Nd YVO4 Optical fiber Functional thermography Resolution 0.05 °C	$T_{control}$ = 46 °C T_{local} = 51 °C $T_{systemic}$ = 50 °C ΔT = 36 °C	30

	Systemic delivery: 0,1 day 100 µL 14.4 × 10^{12} particles/mL			1064 nm 0.6 mm 1.5 W/cm² 180 s	
Au nanohexapods 25.3 ± 0.8 nm Arms 16.3 ± 2.2 nm, 13.6 ± 1.8 nm λ$_{máx}$ = 540, 805 nm	100 µL 34.4 µg/mL ε = 1 at 805 nm	Solution	Diode laser 808 nm 0.8 W/cm² Thermal stability 15-35 mW/cm² 15 min	NIR camera Distance 25 cm Recorded 15 s ΔT$_{ε4}$ = 36.5 °C ΔT$_{control}$ = 0.5 °C Thermal stable < 25 mW/cm²	26
	40 µL 1 nM	Tumor-bearing mice	1 W/cm² 5 min	ΔT = 23.1 °C ΔT$_{control}$ = 4.2 °C	
	200 µL ≈0.8 mg/mouse 3 days	MDA-MB-435 tumor model Athymic nude-foxn1nu nude mice	1.2 W/cm² 10 min	55.7 ± 2.4 °C	
Au nanocages 47.4 ± 4.5 nm Thickness 5.2 nm λ$_{máx}$ = 802 nm	36.4 µg/mL	Solution	15-35 mW/cm²	Thermal stable < 25 mW/cm²	
	200 µL ≈0.8 mg/mouse 3 days	MDA-MB-435 tumor model	1.2 W/cm² 10 min	48.7 ± 3.5 °C	
Au nanorods 36.2 ± 2.3 nm 9.1 ± 1.7 nm λ$_{máx}$ = 800 nm	9.6 µg/mL	Solution	15-35 mW/cm²	Thermal stable < 15 mW/cm²	
	200 µL ≈0.8 mg/mouse 3 days	MDA-MB-435 tumor model	1.2 W/cm² 10 min	53 ± 0.5 °C	
Au nanostars λ$_{máx}$ = 670 and 1150 nm	0.25 mL 0.6 mg/mL	Solution	IR thermocamera 0.5 m distance CW 1.2 mm 700 nm, 50, 100, 150 mW 1064 nm, 25, 50, 75, 100 mW	T$_{máx}$ = 250 s ΔT$_{700\_50}$ = 6 °C ΔT$_{700\_100}$ = 10 °C ΔT$_{700\_150}$ = 14 °C ΔT$_{1064\_50}$ = 7 °C ΔT$_{1064\_100}$ = 12 °C	20
Au nanostars 58 ± 4 nm λ$_{máx}$ = 806 nm	50 µL 184 µg 26 µg	Solution	IR camera Laser diode 808 nm	ΔT = ~ 30 °C ΔT$_{control}$ = 4.2 °C T$_{184}$ = 54.9 °C	31

	3 mm diameter		1.2 mm 11.28, 4.84, 1.95 W/cm² 10 min	$T_{184\_4.84}$ = 40.7 °C $T_{184\_1.95}$ = ~27 °C T_{26} = ~ 42 °C	
Au-Cu$_9$S$_5$ AuNPs = 10 nm $\lambda_{máx}$ = 520 nm Plus Cu$_9$S$_5$ = ~20 nm $\lambda_{máx}$ = 550 nm, 1100 nm	0.6 mL 50 ppm	Solution	1064 nm 0.5 W/cm² 5 min	Thermocouple probe Accuracy of 0.1 °C Recorded every 20 s ΔT = 12.3 °C Thermal stable vs GNRs	32
	50 µg/mL	HeLa cells 96-well plate 7 ×10³ cells/well	0.7 W/cm² Control = 1 W/cm² 7 min	Cell viability, WST assay ~ 10 % survival Control = viable	
	100 µL 100 µg/mL	CT26 tumor-bearing mice, female ~ 5 mm Intratumoral injected	0.6 W/cm² 5 min	Thermal imaging camera T_{2min} = 54 °C ΔT = ~20 °C ΔT_{PBS} = ~ 5 °C	
Gold Nanorods $\lambda_{máx}$ = 1070 nm			1 W/cm² 30 min	$\lambda_{máx}$ blue shifted and decreased in intensity > 20 %	
Gold Nanospheres 50-100 nm $\lambda_{máx}$ = 660 nm	1 mL 10 mg	PBS	808 nm 1 W/cm² 420 s	Probe-type thermometer ΔT = ~ 32 °C ΔT_{PBS} = ~ 10 °C	33
	2.5 mg/kg 8 h	MDA-MB-231 Tumor-bearing nude mice model Intravenously injected into tail vein	6 min	Thermal imaging camera ~ 50 °C $T_{control}$ = 29 °C	
Gold Nanocages $\lambda_{máx}$ = 750 nm	Sol = 1 mL, 50 µg/mL Cells = 100 µg/mL 5 h	MDA-MB-231 Breast cancer cells 96-well plate 1×10⁴ cells/well DMEM 10 % FBS 37 °C	CW 750 nm 650 mW t_{sol} = 20 min t_{cell} = 7.5, 10 min	Digital thermometer 0, 2, 5, 10, 15, 20 min T_0 = 24 °C ΔT_{sol} = 24 °C Cell death MTT assay 12 h after: 7.5 min = 62.92 ± 3.25 % 10 min = 96.41 ± 3.04 %	34

				ΔT$_{sol}$ = 18 °C Cell death: 7.5 min = 43.35 ± 1.91 % 10 min = 79.89 ± 4.74 %	
Gold Nanosells λ$_{máx}$ = 750 nm					
pH-sensitive gold nanospheres 10 nm Vehicle: Tumor-tropic mesenchymal stem cells (MSCs)	90 µg/mL	MSCs 6-well plate 1×10^5 cells/well 24 h	Diode laser 660 nm 0.5 W/cm² 100 s	Real-time IR thermal imaging Recorded every 20 s ~ 49.3 °C ΔT = ~ 20 °C	35
	50 µg/mL × 3			ΔT$_{x1}$ = ~ 16 °C ΔT$_{x3}$ = ~ 43 °C	
	100 µL MSC - AuNPs	Tumor-bearing mice 7 mm 3 days	1 cm diameter 60 s	ΔT = ~ 23.3 °C	
Gold Nanostars 77.5 ± 3.2 nm λ$_{máx}$ = 762 nm NH2-PEG-SH: COOH-PEG-SH 4:1 94.3 ± 4.3 nm λ$_{máx}$ = 780 nm	80 × 10^{-12} M GNSs/C 4 h	HeLa cells 6-well plate DMEM, 10% FBS 37°C, 5 % CO$_2$	808 nm 2 W/cm² 3 min	~ 43 °C ΔT = ~ 20 °C	36
	GNS-N/C 4 100 µL of 200 × 10^{-9} M 10.19 % accumulation of injected dose per gram (ID%/g) of tumor 24 h	Female Balb/c mice Orthotopic mouse model of breast cancer ≈ 60 mm³	1 W/cm² 5 min	56 °C ΔT = ~ 23 °C ΔT$_{PBS}$ = ~ 8 °C	

Gold Nanostars $\lambda_{máx}$ = 890 nm Size = 60 nm Core ø = 20-25 nm	1mL of 0.2 nM of NPs	SKBR3 breast cancer cells McCoy 5A, 10% v/v FBS 35 mm Petri dishes 1 h	980 nm diode laser 15 W/cm² 8 mm² spot size 1, 3 and 5 mins	Thermal ablation was evaluated by fluorescence microscopy. No thermal damage is observed after 1 min. But, after 5 mins, thermal damage is observed even in the control sample.	37
	50 µL of 50 nM PEGylated AuNPs	CD-1 nude mice 48 h post injection	785 nm CW 1.1 W/cm² 33.5 mm² spot size 10 mins	Thermal damage was observed in the ablate region.	
	1nM and 0.1 nM of AuNPs	Water	980 nm 1.2 W 1 min	T 1nM = 80°C T 0.1 nM = 60°C	
Gold Nanostars 25 – 150 nm	0.75 × 10⁻³ M of Au	Water	680, 808 and 1064 nm 1 W/cm²	IR thermal camera ΔT_{max} = 5-10min $\Delta T25nm,680nm_{1min}$=19°C $\Delta T25nm,1064nm_{1min}$=3°C $\Delta T25nm,680nm_{plateau}$=44°C $\Delta T85nm,680nm_{1min}$=13°C $\Delta T85nm,808nm_{1min}$=18°C $\Delta T85nm,1064nm_{1min}$=5°C $\Delta T150nm,680nm_{1min}$=10°C $\Delta T150nm,808nm_{1min}$=13°C $\Delta T150nm,1064nm_{1min}$= 16°C	38
		PC3 Human prostate cancer cell line DMEM, 10% FBS 16 h Irradiated as pellet		$\Delta T25nm,680nm_{1min}$=15°C $\Delta T25nm,808nm_{1min}$=17°C $\Delta T25nm,1064nm_{1min}$=13°C $\Delta T85nm,1064nm_{1min}$= 13°C $\Delta T150nm,1064nm_{1min}$= 11°C	

		PC3 tumors induced in mice Intratumoral injection 0-3 days post injection		$\Delta T_{control}$= 3-4°C $\Delta T_{25nm,680nm_{1min}}$=12°C $\Delta T_{25nm,808nm_{1min}}$= 8°C $\Delta T_{25nm,1064nm_{1min}}$= 5°C $\Delta T_{85nm,680nm_{1min}}$=10°C $\Delta T_{85nm,808nm_{1min}}$= 14°C $\Delta T_{85nm,1064nm_{1min}}$= 5°C $\Delta T_{1064nm,680nm_{1min}}$=6°C $\Delta T_{1064nm,808nm_{1min}}$= 10°C $\Delta T_{1064nm,1064nm_{1min}}$= 9°C	
Gold Nanostars Ø = 52.2 ± 14.2 nm $\lambda_{máx}$ ~ 890 nm	1, 5, 10, 15 and 20 × 10^{-3} M of Au	Water	808 nm 1.2 W/cm² 300s	ΔT 1mM = 20°C ΔT 5mM = 28.6 ΔT 10mM = 33.3 ΔT 15mM = 45.7 ΔT 20mM = 55°C Photothermal conversion efficiency of 79%	39

3.1.2.3.2. Surface Enhanced Raman Spectroscopy, SERS

Consider Raman-active molecules near a metal nanoparticle. The detected Raman intensity $I(\omega,\omega_{sc})$ can be expressed as:

$$I_{Raman}(\omega, \omega_{sc}) = \gamma E_{exc}^2 \cdot E_{sc}^2 = \gamma G^2(\omega) G^2(\omega_{sc}) I_0(\omega) I_{0,sc}(\omega_{sc}) \qquad \text{Eq. 3.3}$$

Where E_{exc} is the total excitation electric field to which the molecule is exposed and E_{sc} is the total Raman-scattered field. The constant γ is an experimental constant that is unimportant in the present discussion.[12]

By choosing an angular frequency ω that excites surface plasmons in the metal (usually gold or silver) and detecting scattering frequencies ω_{sc} not too far from the excitation frequency, both the excitation and the scattered field are enhanced by the presence of the metal particle. It has been found experimentally that a surface-enhanced Raman spectroscopy (SERS) enhances Raman signals from 10^{12}—10^{14} times compared with those obtained from non-surface enhanced experiments.[12]

The stellated or multi-branched nanoparticles, can be used as substrates for surface enhanced Raman scattering (SERS)[40] due the local concentration of electromagnetic field on the several tips of the nanostructure.[41]

3.2. Synthesis of Anisotropic Gold Nanoparticles

The engineering of nanosystems pursues the enhancement of particular properties of nanomaterials for specific applications. In recent years has become important to design the synthesis protocols, in order to control the size, shape, composition, self-assembly, etc., and obtain noble metals nanoparticles with anisotropic complex shapes that can have several applications, *e.g.,* in catalysis, owing to high densities of edges, and crystalline defects (twinned atomic planes, stepped atoms, high-index crystalline facets, etc.).[42]

Anisotropic nanomaterials are a class of materials in which their properties are direction-dependent and more than one structural parameter is needed to describe them. Systematic efforts have been made to find various parameters that directly affect the intrinsic properties of materials at the nanoscale. Among these, shape was found to play an important role in determining the properties of nanomaterials. Restricted motion of electrons, holes, excitons, phonons, and plasmons with respect to the physical shape of an object is the reason for the change in properties of typical nanosystems. The most important change that is manifested is the color, due to the confinement of electrons and consequent changes in electronic energy levels. A pictorial representation of isotropic and anisotropic nanomaterials, categorized based on the dimensionality, is shown in Fig. 3.17.[13]
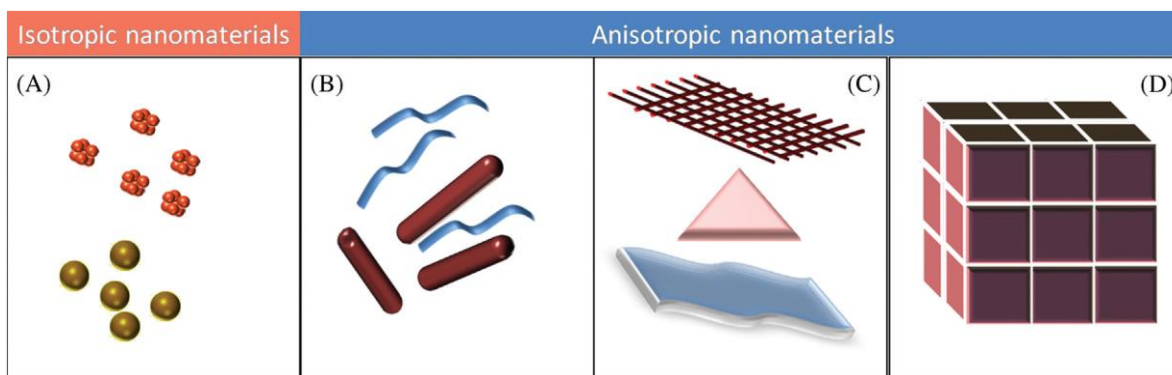
Figure 3.17.   Various kinds of nanomaterials. (A) 0D spheres and clusters. (B) 1D nanofibers, wires, and rods. (C) 2D films, plates, and networks. (D) 3D nanomaterials or hierarchically nanostructure ensembles.[13]

Particle shape anisotropy offers features and functions that are difficult to obtain simply by size-tuning of spherical nanoparticles. A slight change in particle geometry can produce great changes in the surface plasmon peak position of a metallic nanoparticle, which can hardly be achieved in the spherical nanosystems through a similar change in diameter.[13] Anisotropic nanoparticles have higher surface to volume atoms ratio than spheres and, consequently, higher energy per atom.

Taking into consideration atomic packing in a tiny nanoparticle surface, low Miller index facets such as {100}, {111}, and {110} are more stable than other facets due to their high density of atomic packing, and these facets tend to form the surface of polyhedral structures. Among the low index facets, the surface energy is in the order of $\gamma\{111\} < \gamma\{100\} < \gamma\{110\}$, where the {111} facets have the largest surface density and the lowest number of dangling bonds of the surface atoms. Consequently, the particles tend to have {111} facets on the surface without any kinetic adjustment.[3] Among three-dimensional polyhedrons, a decahedron is one of the most stable structures, having only {111} surfaces, although it has strain energy originating from twin boundaries. A single-crystalline cuboctahedron is a common structure for the larger particles, because lattice strain rapidly increases with particle sizes enlargement. The surface shape agents can selectively bound to specific facets and alter the relative surface energies and the resulting particle morphology.[3]

Localized electric fields generated near these nanoparticles[41] have been exploited for the chemical and biological detection of molecules and SERS.[40] The strong electromagnetic fields at the surfaces of anisotropic metallic nanostructures make them useful for non-linear optical (NLO) applications in photonics as well as chemical and biological detection.

In order to prepare monodisperse anisotropic NPs, pre-synthesized gold single-crystalline and twinned nanoparticles are used as seeds for the growth of tips or branches,[43,44] which seem to grow along preferential crystallographic directions of the metallic core, and can be single or poly crystalline.[45] According to previous reports, the capping agents[46] have a preferential adsorption by specific crystalline

faces of the metal seed;[47] and this promotes an accelerated growth rate along a specific crystallographic direction.[40,48–51]

Since sphere is the lowest-energy shape, simple reduction of metal salts generally results in the formation of spherical nanoparticles. Generally, nanoparticle growth can happen either in a thermodynamically controlled or kinetically controlled manner. Thermodynamic growth often results in uniform growth of all crystal facets and subsequent formation of spherical or near-spherical structures. In the case of kinetically controlled growth, preferential and directional growth happens that it turn results in the anisotropic growth. Preferential adsorption of capping molecules to specific facets can hinder o enhance the crystal growth in some direction. The anisotropic interactions of different facets with surfactant and solvents will result in the formation of twinned morphology with lower energy.[13]

The AuNPs can be obtained by controlled growth of atomic species in various ways: *(i)* by condensation of vaporized metal atoms under UHV conditions to form gaseous clusters having relatively few atoms (<20); *(ii)* by reduction of a solution of a gold compound, usually $HAuCl_4$, to form a colloidal dispersion; and *(iii)* by deposition of a gold compound followed by decomposition of reduction to the metallic state or vaporized gold atoms onto a support.[3] The method followed in this thesis is the reduction of tetrachloroauric(III) acid ($HAuCl_4$) in a liquid phase.

3.2.1. One-Pot Synthesis Method

Reduction of gold salts is a simple process that only requires mixing of the reagents under well-controlled external conditions. Besides the strength of the reductant, the action of a stabilizer is critical in liquid phase synthesis. The reaction temperature is one of the main factors to determine particle size, because the oxidation potential and related kinetics of the reductant are normally dependent upon the temperature (see Table 3.4). Representative examples are the Brust method, an organic phase synthesis involving a two-phase process; the Turkevich method, a single-phase water based reduction of gold salt by citrate, which produces almost spherical particles over a tunable range of 10-20 nm diameter; and the Polyol method, an alcohol phase synthesis over a tunable range of 20-300 nm diameter.[3]

Table 3.4. Various well-known synthetic methods of gold nanoparticles in liquid phase.[3]

Reduction method	Reaction media	Reductant	Surface protecting agent	Particle size (nm)	Reaction temperature (°C)
Brust-Shciffrin	Organic	NaBH4	Organothiol	2-10	R.T.
Turkevich	Aqueous	Citrate	Citrate	10-20	100
Murphy	Aqueous	Ascorbic Acid	CTAB	10-50	R.T.
Perrault		Hydroquinone	Citrate	50-200	R.T.
Polyol	Alcohol	Diols	PVP	20-200	20-300

For producing monodisperse gold nanoparticles of 10-20 nm diameter in an aqueous solution, the citrate-reduction method of $HAuCl_4$ has been widely adopted and improved. This method was pioneered by Turkevich *et al.* in 1951 and refined by Frens in the 1970s. In this reaction, sodium citrate behaves both as a reducing agent and as a capping agent that stabilizes the nanoparticles. Reduction of the sodium citrate concentration diminishes the citrate ion concentration available for particle stabilization, which causes aggregation of small particles into larger ones.[3] During the synthesis, the citrate (Ctr^{3-}) is oxidized to acetone dicarboxylate ($ACDC^{2-}$),[52] a ligand that complexes Au^{III}, thus facilitating nanoparticle growth. Following AuNPs

nucleation ACDC^{2-} is thought to be rapidly degrade to acetate at the synthesis temperature of ~100°C:

$$2AuCl_4^- + Ctr^{3-} + 2H_2O \xrightarrow{100°C} 2Au + 3CH_2O + 3CO_2 \uparrow + 8Cl^- + 3H^+ \text{Eq. 3.4}$$
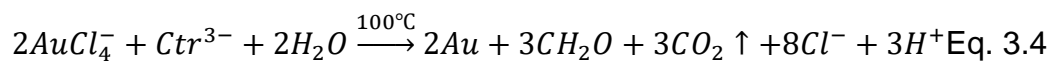
The polyol method is a low-cost method for the synthesis of metal nanostructures in a large scale. In this method is used a long-chain Diol such as ethylene glycol, that acts both as a solvent and as reductant. After the reduction, the resulting particles are monodisperse and non-agglomerated in a relatively large size range, form several nano to micrometers. The products are not spherical, but rather polyhedrons or plates with stable surface facets. PVP (Polyvinylpyrrolidone) is a representative surface regulating reagent that kinetically controls the growth rates of various facets for the formation of anisotropic gold nanostructures, on the basis of its excellent adsorption ability.[3]

Alternative synthetic processes to chemical reduction methods are the electrochemical, photochemical, sonochemical, and microwave-assisted methods, these processes do not require the use of chemical reducing agents, and the reduction of the gold precursors is assisted by various energy sources, with or without surface stabilizing agents.[3]

The microwave dielectric heating is useful for effective and uniform heating, and thus is applied for rapid synthesis of gold nanostructures. Microwaves are in the electromagnetic spectrum with a frequency range of 300 MHz to 300 GHz. In these wavelengths, polar solvents such as water, alcohols, dimethylformamide (DMF), and ionic liquids continuously orientate under an alternating electric field, and lose energy in the form of heat by molecular friction. The microwave heating is rapid and homogeneous, and can even provide superheating beyond the boiling point of the solvent. Therefore, it provides uniform nucleation and growth conditions, shorter reaction times, and reduced energy consumption for gold nanoparticle synthesis. Many studies have explored the synthesis of gold nanoparticles by microwave

assisted methods, and it is known that the reaction time, temperature, and ramping rate are important factors in the enhancement of particle monodispersity.[3]
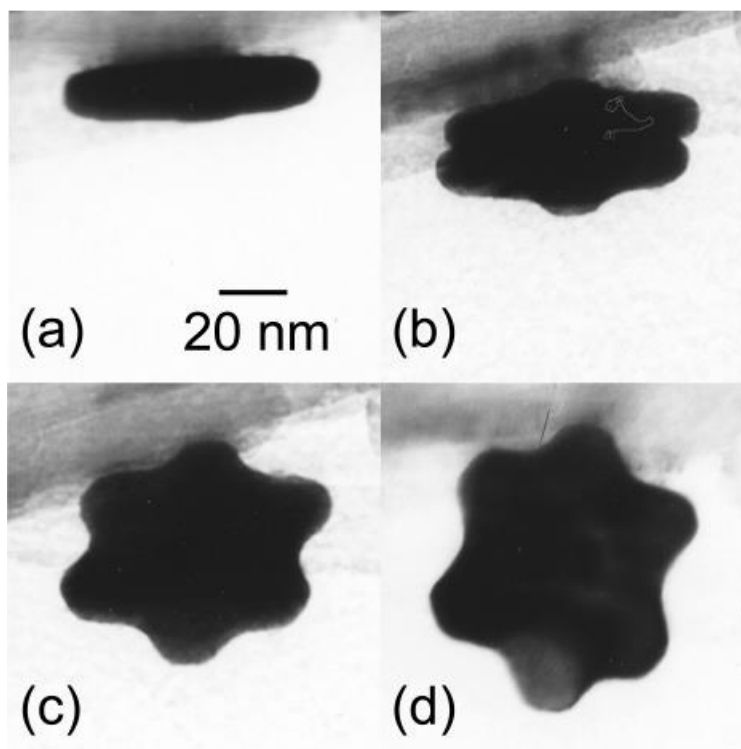
Figure 3.18.   TEM images of a star-shaped nanoplate taken from different angles. The relative angles are (a) 0°, (b) 20°, (c) 45°, and (d) 83°.[53]

By the one-pot method, the star-shaped gold nanoplates of Fig. 3.18, were synthesized using PVP as shape agent. The star-shaped nanoplates were prepared via the reduction of $HAuCl_4$ by L-ascorbic acid at room temperature in the presence of PVP. The preferential growth occurred on the {112} plane.[53]

3.2.2. Seeded-Growth Synthesis Method

The growth mechanism of metal nanoparticles involves nucleation and growth steps. In the seed-growth method, tiny seeds or clusters serve as nucleation centers for surface growth, and both steps can be separate effectively and successfully control the dispersitiy of the NPs.[3] The seed-growth process is a widely used method that can yield various nanostructures such as rods, wires, triangles, stars, flowers, and so on. This method involves two steps, the first step is the synthesis of seed nanoparticles with reducing agents by a one-pot route. Growth of seed nanoparticles into the desired shape is the second step. The growth solution contains surfactant or shaping agent and a mild reducing agent, so the metal salts will get reduced on the surface of the seed nanoparticles. Following this route, the growth direction can be influenced by the seed.

The seeded-growth method was originally applied to synthesize gold nanorods. Recently, numerous gold nanostructures (Fig. 3.19), such as rods, platonic crystals, triangles, branched structures and high index surface structures, have been synthesized using CTAB-based synthetic methods, where the morphology and dimension of the Au nanocrystals can be controllably varied by manipulation of the synthetic parameters.[3,54]

Murphy *et al.* synthesized nanorods with a tunable aspect ratio using decahedral gold seeds, through optimization of the Cetyl-trimethyl-ammonium bromide (CTAB) and ascorbic acid concentrations and by applying a step seeding process.[55] Mann *et al.* confirmed that the electron diffraction patterns of the resulting nanorods were consistent with a pentagonally twinned prism with five {100} side faces capped with five {111} faces at both ends, with the growth again being observed to be along the [110] direction.[3]
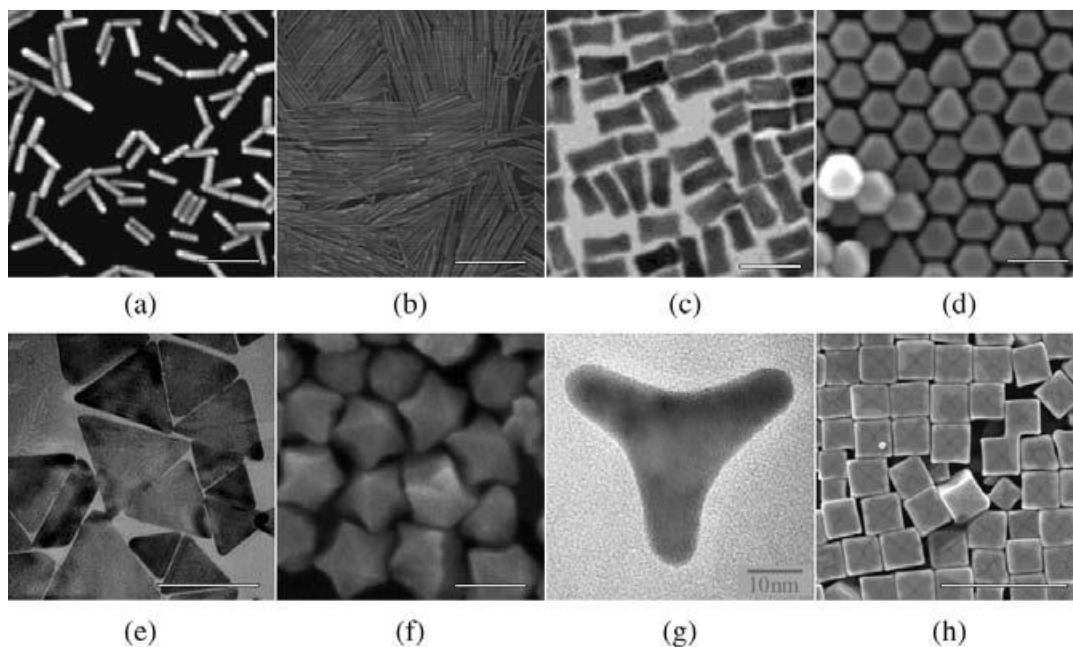
Figure 3.19. (a, b, d, f, h) SEM, and (c, e, g) TEM images of gold nanostructures of various kinds of morphology synthesized with CTAB as a surfactant in aqueous solutions. The bars represent: (a, c, d, f) 100 nm; (b, h) 500 nm; and (e) 166 nm.[3]

The formation mechanism of one-dimensional rods was proposed to entail preferential binding of the CTAB head group to {110} and {100} faces of gold existing along the sides of twinned rods, as compared to {111} faces at the tips. This is based on the finding that CTAB absorbs onto gold nanorods in a bilayer fashion with the trimethylammonium headgroups of the first monolayer facing the gold surface.[56]

The optical properties of anisotropic gold or silver nanorods are tunable throughout the Vis-NIR-IR regions of the spectrum, as a function of their aspect ratios.[13]

3.2.3. Green Methods

AuNPs synthesized in a biological buffer, can allow unambiguous manipulation for biochemical and biomedical applications without the need for tedious ligand or solvent exchange for biocompatibility. The organic molecule HEPES, 2-[4-(2-hydroxyethil)-1-piperazinyl]ethanesulfonic acid, has been used as reducing and shape agent[57,58] in the synthesis of nanoparticles by wet chemical[59–61] and hydrothermal synthesis.[62] Besides, is one of the good's Buffers used in cell culture[63], due to its pKa=7.55 near to physiological pH and its low permeability into cellular membrane. Other reason for their use in cells culture is that was thought to had high chemical stability and low affinity to metal ions like Mg^{2+}, Ca^{2+}, Mn^{2+} o Cu^{2+}. Using electron spin resonance spectroscopy (RSE) was proved that piperazine ring has the ability to generate free cationic nitrogen-centered radicals,[57] which provides the molecule the property of reduce from Au(III) to Au(II)/Au(I) and finally to Au(0) among other metallic ions (see Eq. 3.5).

Also, the shape directing property promotes the growth of anisotropic nanoparticles, mainly directing the growth of multiple tips.[57,58]

$$Au(III) + HEPES \rightarrow Au(II) + Cationic\ free\ radical\ of\ HEPES$$
$$2Au(II) \rightarrow Au(III) + Au(I)$$
$$Au(I) + HEPES \rightarrow Au(0) + Cationic\ free\ radical\ of\ HEPES$$
$$nAu(0) \rightarrow \left(Au(0)\right)_n, AuNPs$$
$$Cationic\ free\ radicals\ of\ HEPES + O_2 \rightarrow Degraded\ products$$
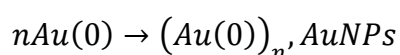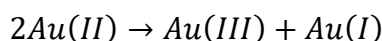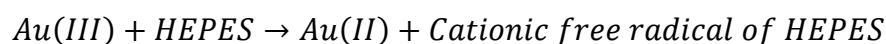
Eq. 3.5

The HEPES-mediated multibranched gold nanoparticles (MB-AuNPs), generate relatively narrow peak widths giving rise to extraordinary LSPR sensing capabilities. Have been reported a 373 nm/RIU refractive index sensitivity, which is relatively high for similarly sized branched nanostructures of this class.[64]

The hydroxylamine is capable of reducing Au^{3+} to bulk metal (see Eq. 3.6),[65] but the reaction is dramatically accelerated by Au surfaces.[66] Recently Jiang *et al.*[51] report

the synthesis of stellated gold polyhedral[51] by exposition of {110} faces promoted by a six times excess of hydroxylamine. Also it has been reported a high-pH dependence[48,65] of hydroxylamine reducing capability, *i.e.,* at pH above 11 hydroxylamine can reduce Au^{3+} to Au^0 without the presence of seeds. At pH below 11 the Au^{3+} reduction did not take place.

$$2Au(Cl)_4^- + 6NH_2OH \rightarrow 3N_2 + 6H_2O + 6H^+ + 2Au^0 + 8Cl^- \qquad \text{Eq. 3.6.}$$
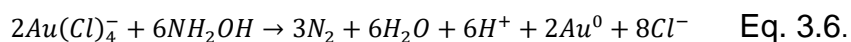
3.2.3.1. HEPES-based One-Pot Synthesis Method

At 2005 Habib *et al.*[57] reported the wet chemical synthesis of AuNPs using HEPES as reducing agent, obtaining aggregates of 32 and 40 nm average size, and with -23 and -27 mV respectively of Z-potential (ζ), they determined a medium reducing power of HEPES and the obtaining of second products of nitrogen species absorbing at ~346 nm. Later, J. Xie *et al.*[58,40,67] reported the one-pot synthesis of heterogeneous sample of 92% of gold multipods from one to eight branches with average length of 25 nm and LSPR in 658 nm, and multibranched nanoparticles with tips of ~10 nm using molar rates of HEPES/$AuCl_4^-$ of 20-700/1. They reported a nucleation and branches growth in a time of 10-20 min, indicating an accelerating reaction rate when the branches are growing, moreover at lower molar rates of HEPES, 45:1, a decrease in the reaction rate spherical NPs were produced, taking an hour to complete the reaction.[40] Recently Dam *et al.*[49] reported a modification of Xie's method with an increase rate of HEPES, and this increase produce gold multipods with LSPR at 780 nm.

There is a comparison study between similar molecules with the idea of elucidate the functional group of the HEPES that promotes the branching formation, and the conclusion was that piperazine ring should be the most accountable for the formation of branched gold nanocrystals.[58] The HRTEM analysis show that branches grow in [111] and [200] direction, due to adsorption or lack of HEPES molecules in the {111}, assuming a growth competition of (111) and (100).

The multipods[58] show to be unstable under boiling conditions, turning into spheres, and for one week at 4°C. On the other hand, recently articles report one-pot synthesis of ~26 nm spheres an polygon NPs with boiling gold salt solution and HEPES/Au ratios of 1-20:10, at 4:10 ratio more homogenous sample than comparative citrate synthesis obtained, and report a ζ value of -31.7 mV. The reported FT-IR spectra (Fig. 3.20) of pure HEPES and powders of HEPES-prepared AuNPs exhibited two IR bands at 3,134 and 1,338 cm⁻¹, which could be attributed to the stretching bands of C–H and C–O, respectively. This figure also shows the difference of νS–H vibration band at 2,538 cm⁻¹ between the AuNPs and HEPES, the groups suggested that the S–H bond is broken upon binding to the gold particle surface to form the bond of S–Au.[61]
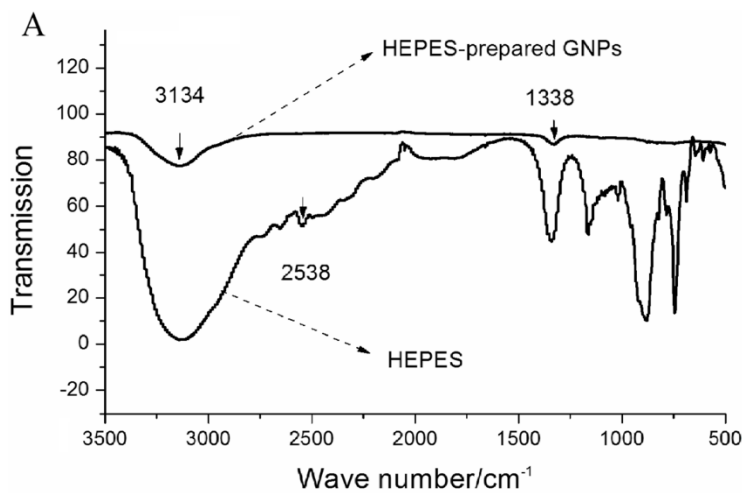
Figure 3.20. FT-IR spectra of the HEPES-prepared AuNPs powder and pure HEPES.

There is another report of 70 min one-pot synthesis by immersion method, with 30-360 MM of HEPES at pH 7.4, and 0.2 mM of gold salt solution. For 30 mM of HEPES solution, the nanoparticles absorbs near 600 nm, but for 300 mM is near to 800 nm (Fig. 3.21).[64]
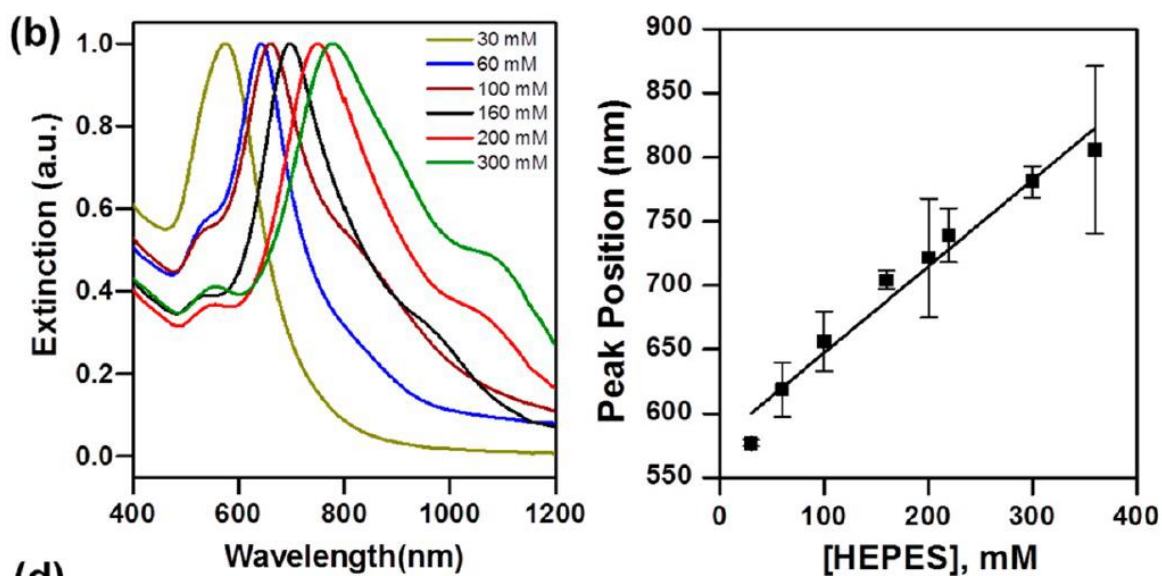
Figure 3.21. Peak position of MB.AuNPs synthetized by one-pot method.[64]

3.2.3.2. HEPES-based Seeded-Growth Synthesis Method

Maiorano *et al.*[43] reported the seeded-growth synthesis of MB nanoparticles using HEPES as shape directing agent and hydroxylamine (NH$_2$OH·HCl) as surface reducing agent. By this approach, mono-disperse products were obtained, with branches growth due to an affinity of HEPES for twins in the nanoparticles used as seeds. It has been reported that excess of hydroxylamine and therefore an acceleration in reaction rate promote also the branching growth.[48] Reports of anisotropic nanoparticles using hydroxylamine as reducing agent have shown the main of kinetics growth in the formation of thorny nanoparticles[50] with a slightly dendritic growth along the tips.

3.3. Experimental Procedure of Gold Nanoparticles Synthesis

3.3.1. Gold Nanorods (AuNRs)

In one of the first reports of the synthesis of gold nanorods (AuNRs),[55] the key factor for the modulation of growth of the AuNRs is the ratio between amount of seeds and gold salt in the growth solution. The first reports show results with non monodispersed AuNRs, the synthesis product has secondary products as AuNSs and gold nanoplates. The improvement of these synthesis come with the implementation of CTAB as directing agent, and silver ions.[68] It is suspected that silver ions are adsorbed at the gold surface as AgBr, these restrict the growth of the rod in one direction. Also is hypothesized the preferential adsorption of the CTA+ for some crystal faces of the gold seed, so the faces with major energy are stabilized and is avoided the growth.

Materials and Methods

Deionized water was used for all experiments. The reagents used for AuNRs synthesis were obtained from Sigma-Aldrich: $HAuCl_4 \cdot 3H_2O$, CTAB, sodium borohydrade ($NaBH_4$), ascorbic acid (AA) and silver nitrate ($AgNO_3$). All reagents were used as received without further treatment or purification and all glassware was cleaned with *aqua regia* and rinsed with plenty deionized water. For morphological studies, the samples were washed and redispersed in deionized water and a drop was deposited in a copper grid and left to dried for characterized by electron microscopy in a SEM (HITACHI) and TEM (JEOL 2010). For UV-Vis spectra, the colloids were measured without modifications in a Cary 50 spectrometer.

Synthesis of 33 nm Gold Nanorods by Seeded-Growth Method

Gold seeds were prepared by the reduction of 5 mL of gold salt [0.5 mM], in 5 mL of [0.2 M] CTAB solution by 0.6 mL of fresh cooled solution of $NaBH_4$ [0.01 M], under magnetic stirring. The stirring was stope after 2 minutes, and the seeds were left to react during two hours inside the fume hood. The growth solution for the AuNRs was

prepared as follow, to 4.5 mL of [0.1M] CTAB, was added 0.2 mL of [0.01 M] of gold salt and 0.03 mL of [0.01 M] $AgNO_3$, finally 0.3 mL of [0.1 M] AA and the immediate addition of 100 µL of seeds solution without modifications. The growth step was carried out by manual immersed agitation, and the AuNRs were left to growth overnight at ambient temperature, avoiding the solidification of CTAB.

Synthesis of 66 nm Gold Nanorods by Seeded-Growth Method

Gold seeds were prepared by the same procedure and concentrations of reactants as for 33 AuNRs seeds. The growth solution for the AuNRs was prepared as follow, to 9.5 mL of [0.1M] CTAB, was added 0.5 mL of [0.01 M] of gold salt and 0.1 mL of [0.01 M] $AgNO_3$, finally 0.05 mL of [0.1 M] AA and the immediate addition of 12 µL of seeds solution without modifications. The growth step was carried out by manual immersed agitation, and the AuNRs were left to growth overnight at ambient temperature, avoiding the solidification of CTAB.

Results and Discussion

By these protocol mostly monodispersed AuNRs of 33 and 66 nm large were obtained, the size histograms of Fig. 3.23, were obtained by the analysis of electron micrographs and measurement of ~100 NPs. Both samples were prepared from same size and shape seeds, the final length and shape, particularly the extra tips in the rod ends (see Fig. 3.24) depend on growth solution, gold salt availability and silver catalysis effect. Was observed the casual presence of NPs with cuboid shape, they were also considered for histograms analysis.[69]
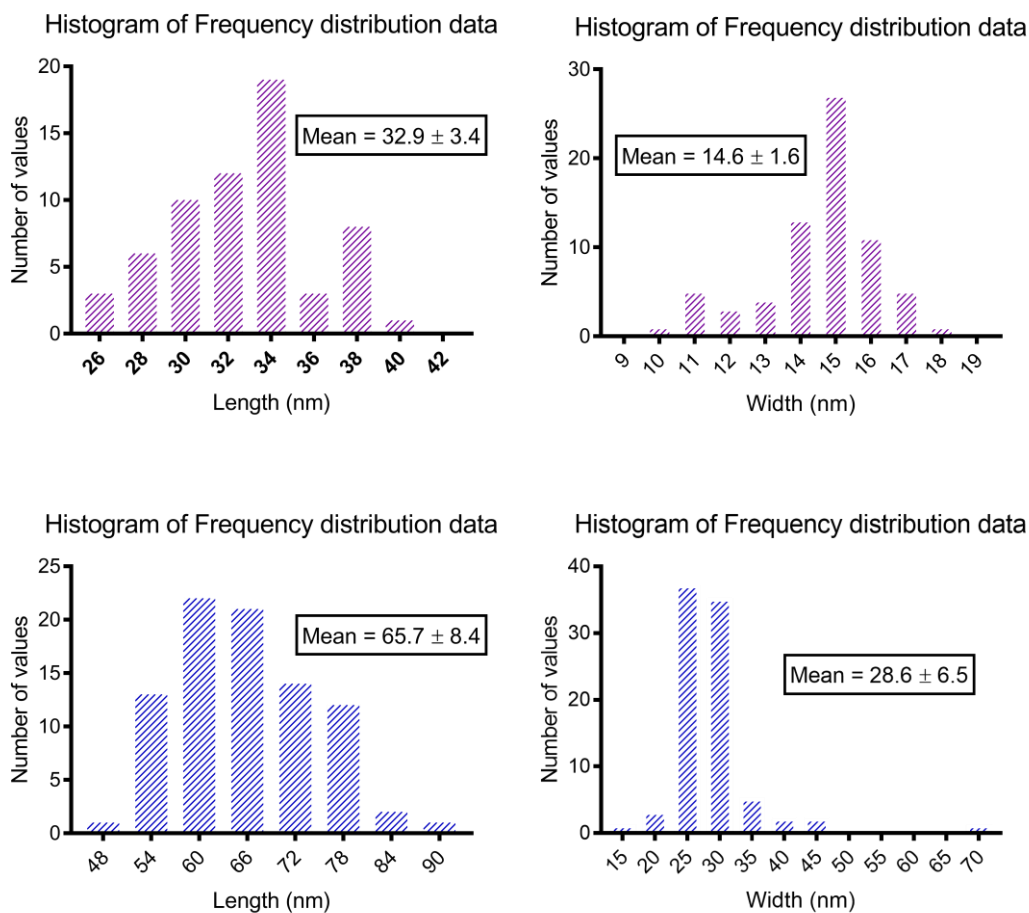
Figure 3.22. Frequency histograms of length and width of of 33 AuNRs (**Top**) and 66 AuNRs (**Down**).

As can be observed in the UV-Vis spectra of AuNRs (see Fig. 3.23), the final length and aspect ratio of the rods play a critical role in the final LSPR of the AuNRs.
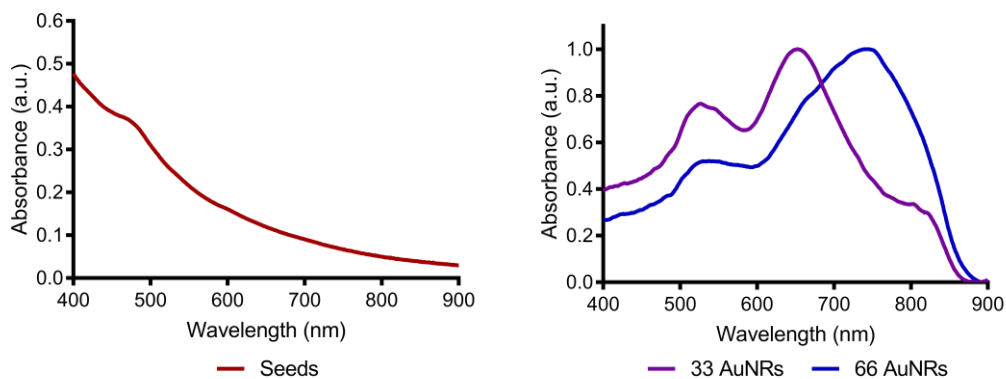
Figure 3.23. UV-Vis spectra of gold seeds (**left**) and 33-AuNRs (653 nm) and 66-AuNRs (745 nm) (**right**).
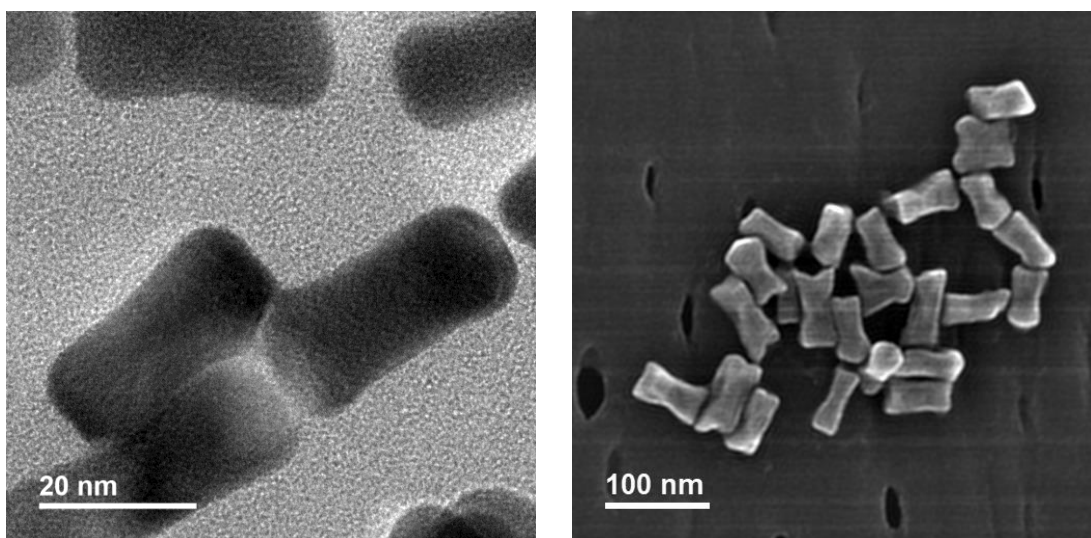
Figure 3.24. (Left) TEM micrograph of 33 nm AuNRs and (Right) SEM micrograph of 66 AuNRs.

3.3.2. Gold Nanostars (AuNSts)

With the propose of synthesized gold nanoparticles with star shape, we modified the AuNRs protocols, mainly the growth step was carried out from silver seeds. For the synthesis of the seeds, silver nitrate ($AgNO_3$) was reduced with sodium borohydrade ($NaBH_4$) in the presence of CTAB. The gold nanostars (AuNSts) were prepared at ambient temperature by manual immersion of the reactants, as solution CTAB was used, and silver ions, gold salt, ascorbic acid and silver seeds were added in that order. The solution was left over night for the reaction to be completed.

Materials and Methods

We use the same reactants from AuNRs synthesis without modifications. The sodium tricitrate was obtained from Sigma-Aldrich. Also, the same conditions and equipment for morphological and UV-Vis characterization were used. For acquired of Raman spectra the samples were prepared with a drop of washed and concentrated AuNSts, deposited on silicon substrates and left to dried, later was added a drop of R6G solution. For comparison, a substrate without AuNSts was prepared. The samples were analyzed with a 785 nm laser.

Synthesis of Gold Nanostars by Seeded-Growth Method

Silver seeds were prepared as follow, under magnetic agitation to 18 mL of deionized water was added 0.5 mL of sodium tricitrate [0.01 M], and 1.25 mL of silver nitrate [0.004 M] and finally 0.6 mL of fresh cooled solution of $NaBH_4$ [0.01 M]. The stirring was stope after 2 minutes, and the seeds were left to react during two hours inside the fume hood. The growth solution for the AuNSts was prepared as follow, to 5 mL of [0.2 M] CTAB, was added 0.9 mL of [0.004 M] of silver nitrate and 5 mL of [7.8 mM] gold salt, finally 0.6 mL of [0.1 M] AA and the immediate addition of 200 μL of seeds solution without modifications. The growth step was carried out by manual immersed agitation, and the AuNSts were left to growth overnight at ambient temperature, avoiding the solidification of CTAB.

Results and Discussion

The morphological characterization shows a monodisperse sample, with estimation of NPs diameter of 200 ± 23 nm (see Fig. 3.25).
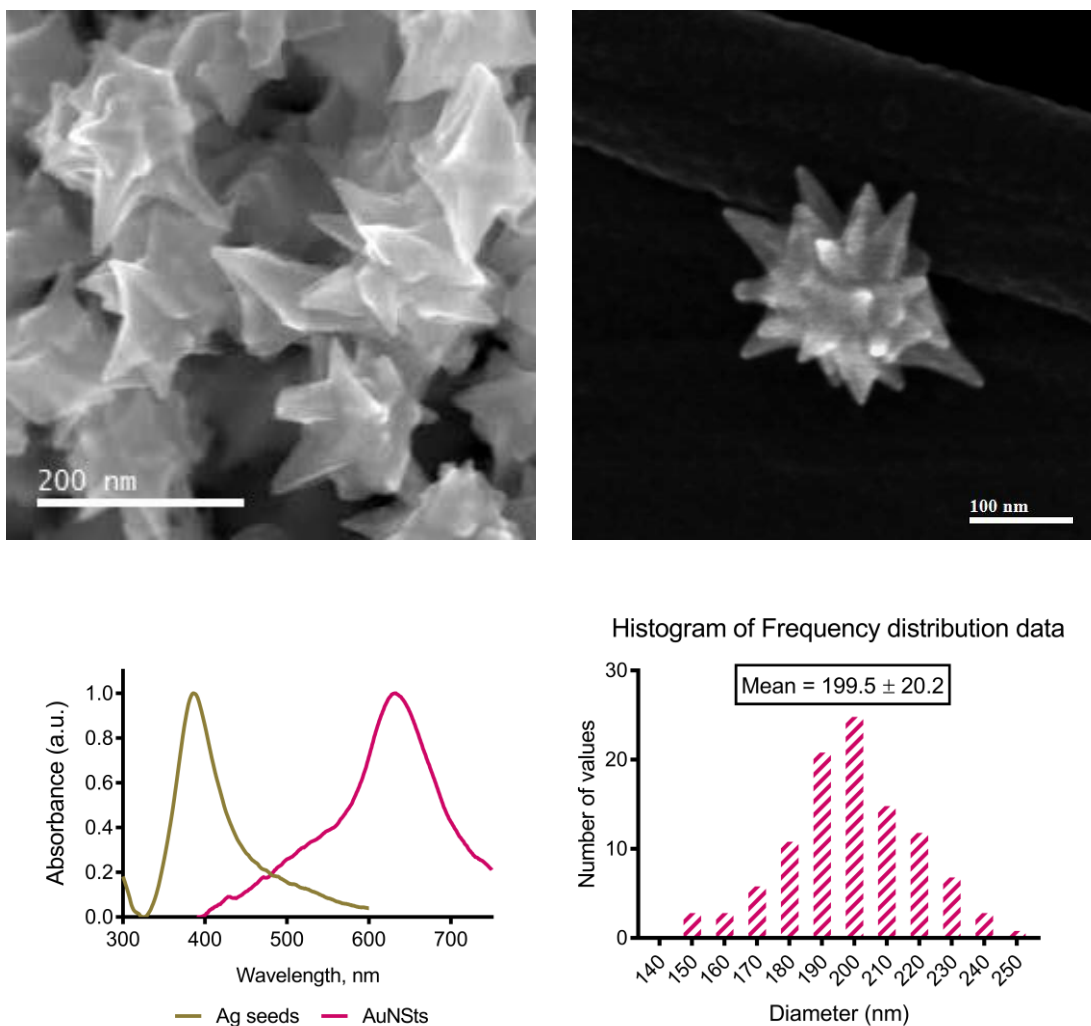
Figure 3.25. (**Up**) SEM micrographs of AuNSts synthesized by seeded-growth method. (**Down left**) UV-Vis spectra of AgNPs used as seeds and the final product AuNSts. (**Down right**) Histogram of AuNSts diameter measured from tip to tip.

AuNSts due to their irregular shape are candidates as substrates for SERS, in particular for their multiple hot-spots. For the evaluation of AuNSts, the Raman spectra of rhodamine (R6G) was obtained. The next table list the main R6G vibrations presents in Raman spectra.

Table 3.5.	Peaks of vibrations in Raman spectra of R6G
cm⁻¹	**Vibrations**
610	C-C-C ring in one plane
770	
1123	C-H bending
1178	
1309	C-O-C stretching
1361	
1507	
1571	C-C stretching in aromatics
1597	
1645	

In the Raman spectra is observed the enhancement of signal intensity of the main vibrations of R6G, and the apparition of 1645 cm⁻¹ peak indicates a major sensibility.
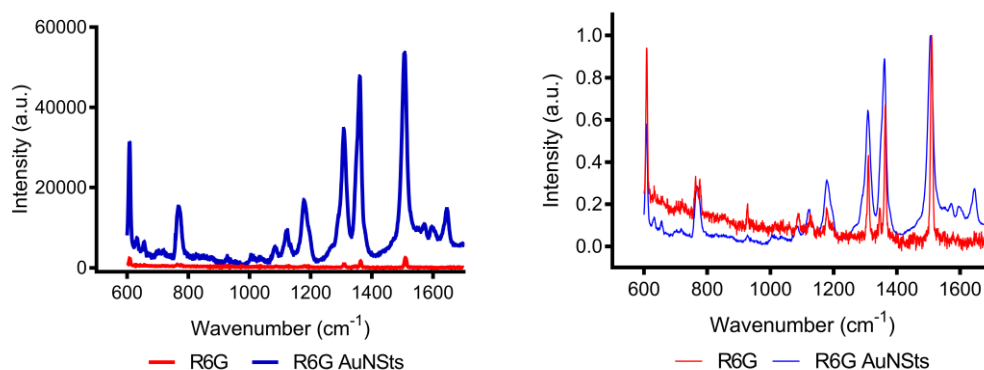
Figure 3.26. Raman spectra (**Left**) and normalized Raman spectra (**Right**) of R6G molecule and the enhancement of the spectra acquired on a AuNSts film.

3.3.3. Multibranched Gold Nanoparticles (MB-AuNPs)

Materials and Methods

Deionized water was used for all experiments. The reagents used for NPs synthesis were obtained from Sigma-Aldrich: $HAuCl_4 \cdot 3H_2O$, HEPES, $NH_2OH \cdot HCl$, and sodium citrate. For the preparation of skin-equivalent-phantom, polyethylene powder (PEP) was obtained from Baker, Agar from Sigma-Aldrich, and TX-151 from Oil Center, and all reagents were used as received without further treatment or purification. All glassware was cleaned with *aqua regia* ($HCl:HNO_3$, 3:1), and rinsed with plenty deionized water. The samples were characterized with UV-Vis absorption spectroscopy, acquired on a Cary 60 UV-Vis-NIR spectrophotometer at room temperature. ICP elemental quantification was performed on Variant 730-ES spectrometer. The electron micrographs were acquired in a transmission electron microscope JEOL 2100, and scanning electron micrographs in a FEI-Helios Nanolab. The x-ray diffractograms were obtained in a Bruker DX-8 system at CuKα source of wavelength 1.54056 Å. The dynamic thermographs were taken at a distance of 0.3 m from the skin-equivalent phantom,[70,71] using a high-resolution infrared camera with thermal sensitivity better than 40 mK and a 480x360 focal plane array of VOx microbolometers (FLIR T600, FLIR Systems Inc., Wilsonville, OR). The phantoms were evaluated with a 785 nm laser diode with a spot size of 3.5 mm and optical power of 0.15 W. Temperature measurements of the skin-like phantom were taken with and without MB-AuNPs. Data was analyzed with FLIR-IR Research software.

Synthesis of Multi-branched Gold Nanoparticles (MB-AuNPs) using a Seed-Growth Method. The 16 and 18 gold nanospheres (AuNSs) used as seeds, were prepared by a reverse-modified Turkevich method[72] by citrate reduction of gold salt. Shortly, in a three-neck round-bottom flask with a condenser mounted, a citrate solution was brought to boiling by a heating mantle for 5 mins, then a gold solution of initial concentration of 25 mM was added, and after a light red ruby color appeared the system was left to react for half hour. For the synthesis of 16 nm AuNSs, the total

concentration of sodium citrate and gold salt were 1.8 mM and 0.16 mM respectively; and for 18 nm AuNSs were 0.75 mM and 0.25 mM. After the reaction was completed, the seeds solution was left to cold down at ambient temperature, and used without modifications.

For the MB-AuNPs synthesis we used three concentrations of HEPES buffer [25, 50, 75 mM] as solution. Briefly, under slowly stirring within an ice bath (~4°C) to 12.5 mL of HEPES there were added 50 µL of AuNSs (16 or 18 nm), as well as 30, 60 or 120 µL of hydroxylamine [0.1 M], and finally the dropwise addition of gold salt solution with rate of 0.375 mL/min to a final concentration of [0.07 or 0.13 mM]. For the reaction to be complete it is necessary to leave the sample to rest 8 h in the fridge. The samples were washed three times by centrifugation and a drop of the concentrated colloid was deposited on an aluminum pin for SEM, and on a lacey carbon copper grid for HRTEM. For UV-Vis measurements, the samples were analyzed as synthesized. The samples for ICP quantification were centrifuged and the NPs concentrated was dissolved in aqua regia.

3.4. Phantom Gel Model for Photothermal Response

Facing the photo-thermal treatment of cancer (local heating for killing cancer cells) as possible application, the evaluation of thermal nanoheaters using tissue samples, may be impractical due to the restrictions of accessibility and storage of fresh samples; and reproducibility of results may also be poor because of the difficulty in finding identical specimens. As a consequence, tissue-equivalent models (gel phantoms) were developed to simulate tissue dynamic and static optical properties, and to study the effects of laser irradiation,[71,73–75] as absorption and propagation of light and subsequent temperature rise in tissue. We have to consider that phantoms are usually homogeneous, and therefore do not normally possess the complex structures that exist throughout tissue such as the vasculature, and because of that do not necessarily reflect the true complexity and hence the proper response of tissue during laser therapy. Previous reports used agar phantoms with intralipid® (fat emulsion) as scattered agent,[76] to evaluate the thermal response of gold nanorods (AuNRs),[55] and suggested to be effective for tumor irradiation of 10 mm depth from the illuminated tissue surface.

Infrared (IR) imaging is based on the fact that any object at a temperature above absolute zero (-273 °C) will emit IR radiation, even if only weakly. The human body has a low thermal emittance, radiating in a wavelength range that starts at around 3 mm, and peaks in the vicinity of 10 mm, and trails off from this point into the extreme IR and negligibly, beyond it. On the other hand, the emissivity of human skin has a constant value of 0.98 ±0.01 between wavelengths of 2 and 14 mm for black skin and 0.97±0.02 for white skin;[77] thus, human skin has a known and almost invariant emissivity in this wavelength region that makes IR imaging an ideal procedure to evaluate surface temperature of the human body.[78,79] The emittance of the skin-equivalent phantoms previously reported is 0.62 ± 0.01.[75]

3.4.1. Gold Nanoantennas and Skin-Equivalent Phantom Reports

In previous reports, a concentrated solution of MB-AuNPs were excited with 1 W near-infrared laser diode at 808 nm, and 1.2 mm spot size. An aqueous 50 µL (184 µg), 3mm droplet of NPs suspension placed on glass slide were heated by light illumination, the maximum temperatures were monitored for 15 min, using an IR camera and software from FLIR systems (T440). The results show an increment of ~5 °C for power densities of 1 W/cm².[64]

3.4.2. Experimental Fabrication of Skin-Equivalent Phantom with Embedded MB-AuNPs

For the fabrication of the control phantom was used a previously reported protocol, and the reagents concentration was maintained.[80] The procedure is as follows: a Buchner flask with 20 mL of deionized water and 620 mg of agar was heated until ~ 80°C under slow magnetic stirring and vacuum. Once the agar was dissolved and the boiling point was reached, the vacuum and heating was turned off, 500 mg of TX-151 was added and mixed gently with a stirring rod until its complete incorporation, and then 2 gr of PEP was added to decrease the real and imaginary parts of the permittivity. After complete PEP incorporation the vacuum was turned on for a moment to avoid bubbles in the final phantom. Finally, the mix was placed into a petri box (ø=55 mm) and left to solidify at ambient temperature. When phantoms with nanoparticles were prepared, a 1x concentrated of pre-washed MB-AuNPs colloid was added and completely incorporated before TX-151 addition. For comparison, other phantoms with AuNSs were prepared, at the same NPs concentration of MB-AuNPs. The dynamic thermographs were taken at a distance of 0.3 m from the skin-equivalent phantom,[70,71] using a high-resolution infrared camera with thermal sensitivity better than 40 mK and a 480x360 focal plane array of VOx microbolometers (FLIR T600, FLIR Systems Inc., Wilsonville, OR). The phantoms were evaluated with a NIR laser of 785 nm with 3 W/cm² power density. Temperature measurements of the skin-like phantom were taken with and without MB-AuNPs. Data was analyzed with FLIR-IR Research software.

3.5. Assembly of Results and Discussion of Multibranched Gold Nanoparticles (MB-AuNPs)

3.5.1. Growth Mechanism

In order to prepare monodisperse MB-AuNPs, pre-synthesized gold single-crystalline and multi-twinned nanoparticles are used as seeds for the growth of peaks,[43,44] which grow along preferential crystallographic directions of the metallic core.[45] According to previous reports, the capping agents[46] have preferential adsorption by specific crystalline faces of the metal seeds,[47] and this promotes an accelerated growth rate along specific crystallographic directions.[40,48–51]
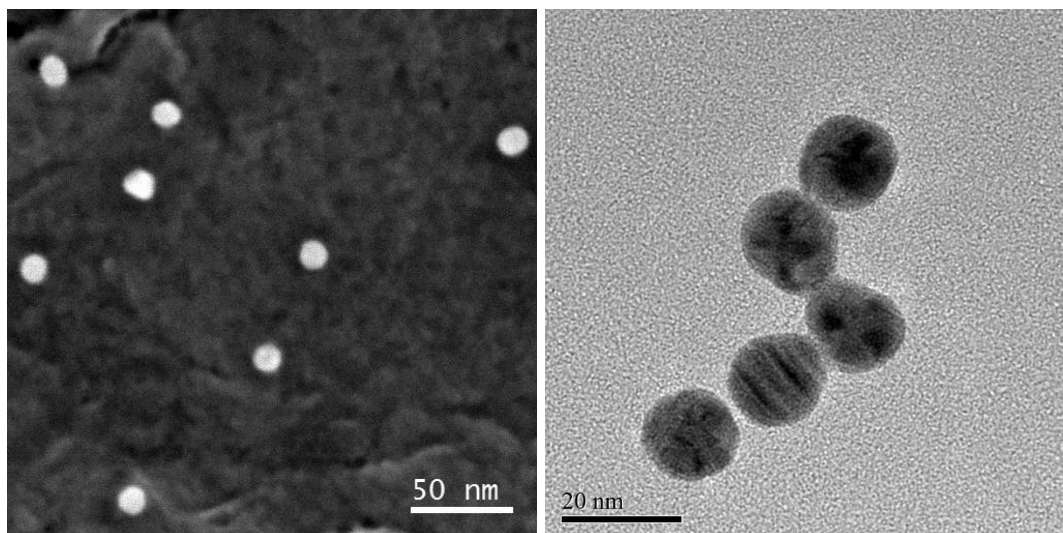
Figure 3.27. **Left.** SEM Micrograph of 16 ± 1.69 nm of spheres gold nanoparticles (16-AuNSs). **Right.** TEM micrograph of 18.18 ± 2.33 nm sphere gold nanoparticles (18-AuNSs) used as seeds.

The AuNSs obtained by the reverse Turkevich method, were monodisperse in size (see Fig. 3.27 and Fig. 3.28), by ICP spectroscopy was determined the concentration of 2.39×10^{11} and 3.66×10^{11} NPs/mL for 16 and 18 nm AuNSs respectively. These was calculated according the Eq. 3.7, where N_A is the Avogadro's number, ρ is the gold density in g/cm³ and M is the molecular weight of gold, then an estimated of the number of atoms present in a AuNPs can be made if the diameter is known and later of the density of NPs according the ICP results.

$$Nat = \frac{N_A \pi \rho D^3}{6M}$$

We will see later that the structural characteristics of the AuNSs will influenced the growth process of peaks, as can be seen in Fig. 3.27 (left), the 16-AuNSs present more symmetrical shape and monocrystalline structure, being different from 18-AuNSs samples (Fig. 3.27, right) that show multi-twinned structure and non-spherical multi-faceted shapes.
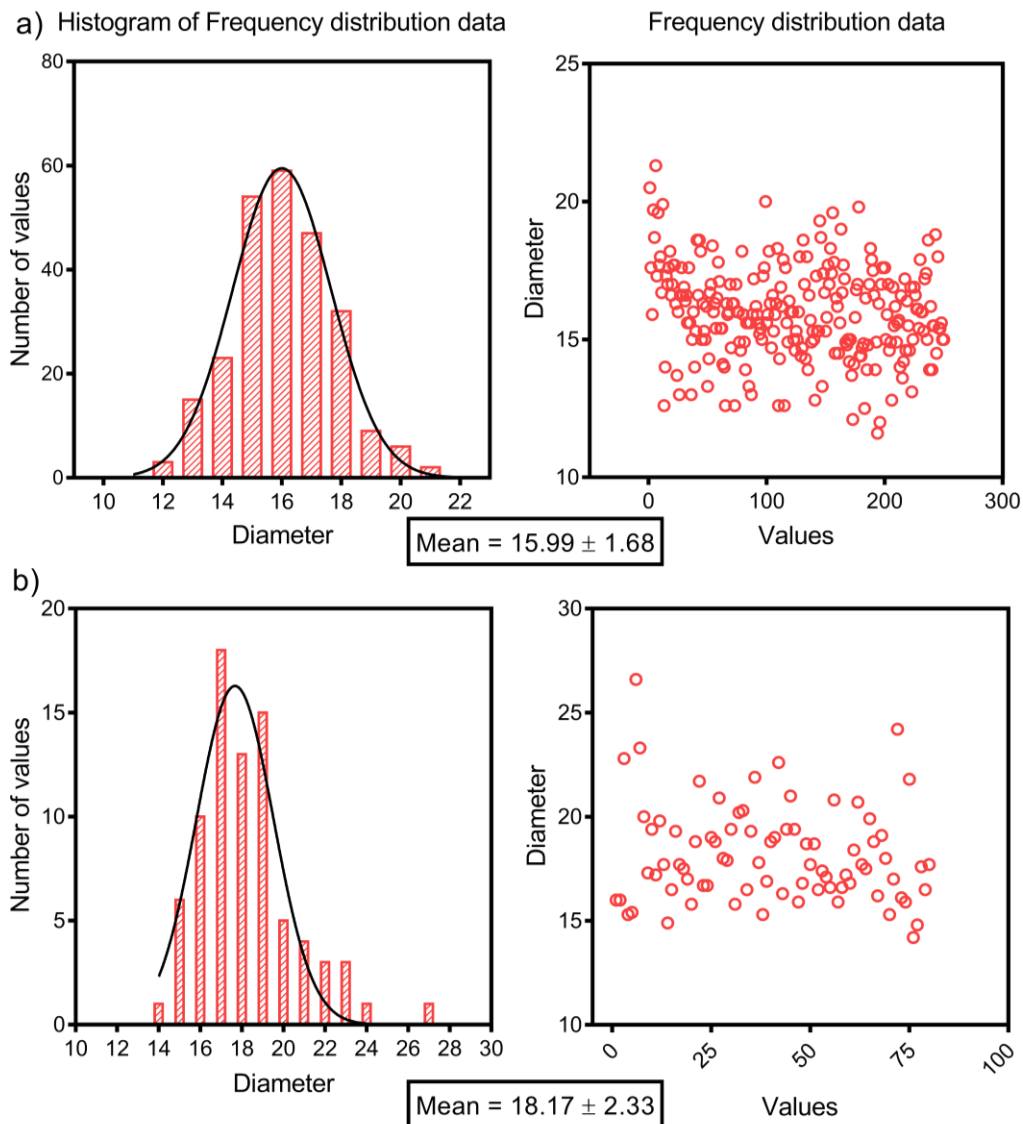
Figure 3.28. Histograms of diameters and frequency distribution data of populations of a) 200 AuNSs for 16-AuNSs and b) 100 for 18-AuNSs.

During the stage of peaks formation, the promotion of second-order branching (Fig. 3.34) is up to the seed structure[81] and the stabilizer agent protection[40] at the nanoparticle surface, observed in the MB-AuNPs synthesized from 18 nm nanospheres (18MB-AuNPs), with 0.13 mM of gold salt. Also, we observed that the growth mechanism of the MB-AuNPs is influenced by the chemical characteristics of the reagents present in the growth solution and by its molar ratio with respect to gold ions.
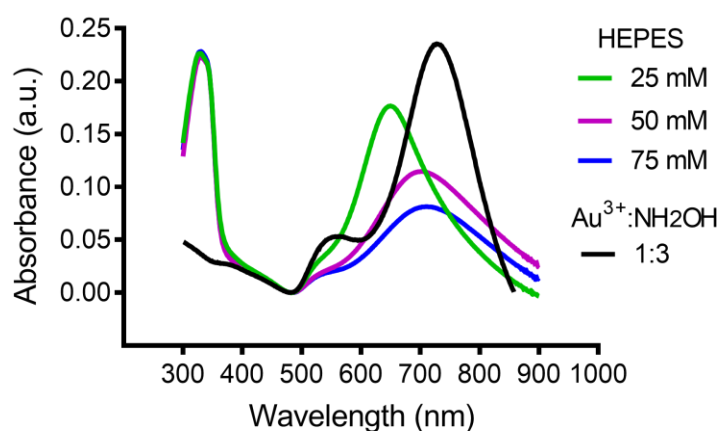
Figure 3.29.   The increase of the molar concentration of HEPES promotes strong anisotropic formation of the MB-AuNPs. The UV-Vis spectra compares the SPR band of MB-AuNPs synthetized without hydroxylamine and with an increment of concentration of HEPES, it can be observed that the SPR band shifts to the infrared (compare HEPES 25, 50 and 75 mM in the 600-800 nm region). During the reaction, nitrogen species results from HEPES degradation, as can be seen in the spectra at 346 nm. After the use of hydroxylamine (black line), can be observed in this same spectra region that there is not degradation of HEPES, and a better optical response is obtained. Thus the role of HEPES is to promote the anisotropic formation while hydroxylamine is dedicated to the reduction of Au^{3+} salt ions.

Therefore, both hydroxylamine and HEPES are dual agents, with reducing and shape capabilities. Manipulation of the role played by each reactive is made through experimental conditions such as temperature (*e.g.*, to slow the HEPES reducing action) and concentration of hydroxylamine (using the necessary to reduce the gold ions). Within the molar rates used in this work, the hydroxylamine governs the reaction kinetics and the final shape of the peaks and the HEPES modulate the

peaks growth. A simple way to know if the HEPES has been or not contributing as reducing agent, is by means of UV-Vis spectroscopy (see Fig. 3.29), since the nitrogen species from degraded HEPES can be detected by its absorption at ~346 nm.[57]
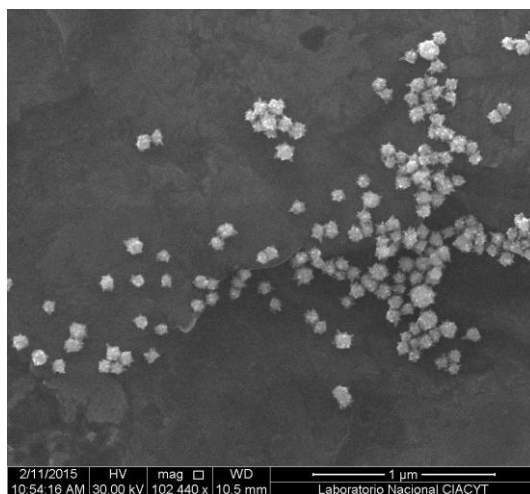
Figure 3.30.   Scanning electron microscopy micrograph of 16MB-AuNPs, it can be observed the monodispersity and non-agglomeration of the NPs.

Is important to mention that in the reaction where no hydroxylamine is used, the color changes of the colloid takes place slowly, evidencing that HEPES is a slow reductor. Increasing the concentration of HEPES (from 25 to 50mM), the growth of narrow peaks is promoted while the cores remain small. Then the addition of hydroxylamine is necessary to modulate the kinetics without excess of HEPES and will help to obtain better definition on the peaks and a monodisperse size and shape sample (see Fig. 3.30). From the mechanism reduction of Au^{3+} by hydroxylamine proposed by Minati et al.[65], the molar ratio of Au^{3+}:NH_2OH (1:3) was used to synthesized the sample with 16 nm nanospheres (16MB-AuNPs), in order to avoid the intervention of HEPES reducing action (see Fig. 3.29). We observed that, when hydroxylamine is present and increases its molar rate, the change of colors gets faster indicating the necessary use of a mild reducing agent (hydroxylamine) simultaneously with a directing shape agent (HEPES) for better anisotropic growth. We also have determined that an excess of hydroxylamine promotes the second-order branching

in 18MB-AuNPs, which was synthesized with molar rate of Au^{3+}:NH_2OH of 1:6 (see Fig. 3.31).
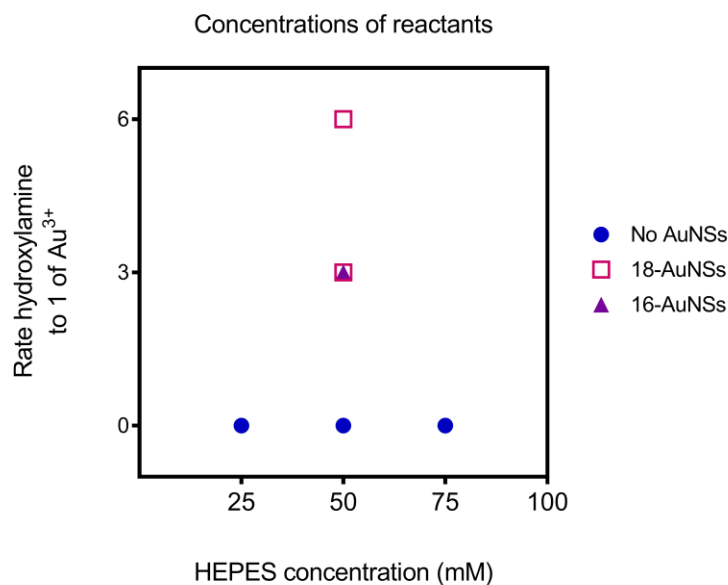
Figure 3.31. Diagram of the concentrations of reactants used for the samples analyzed.

It had been reported that the size of the NPs used as seeds influences the shape of final products.[82,83] In our results we observed that from 16-AuNSs can be obtained MB-AuNPs of 80 nm of diameter, synthesized with 0.07 mM of gold salt (16MB-AuNPs, see Fig. 3.32), and the colloid present a maximum absorbance at 728 nm (Fig. 3.33). On the other hand, dendritic growth is only perceptible in 18MB-AuNPs (Fig. 3.34), even if the concentration of gold ions is increased in the samples synthesized from 16-AuNSs (see Fig. 3.35). The increase in gold ions leads to bigger cores and smaller length of peaks, due to an addition of gold atoms between peaks for minimization of energy, instead of the growth of longer peaks.[84,85]
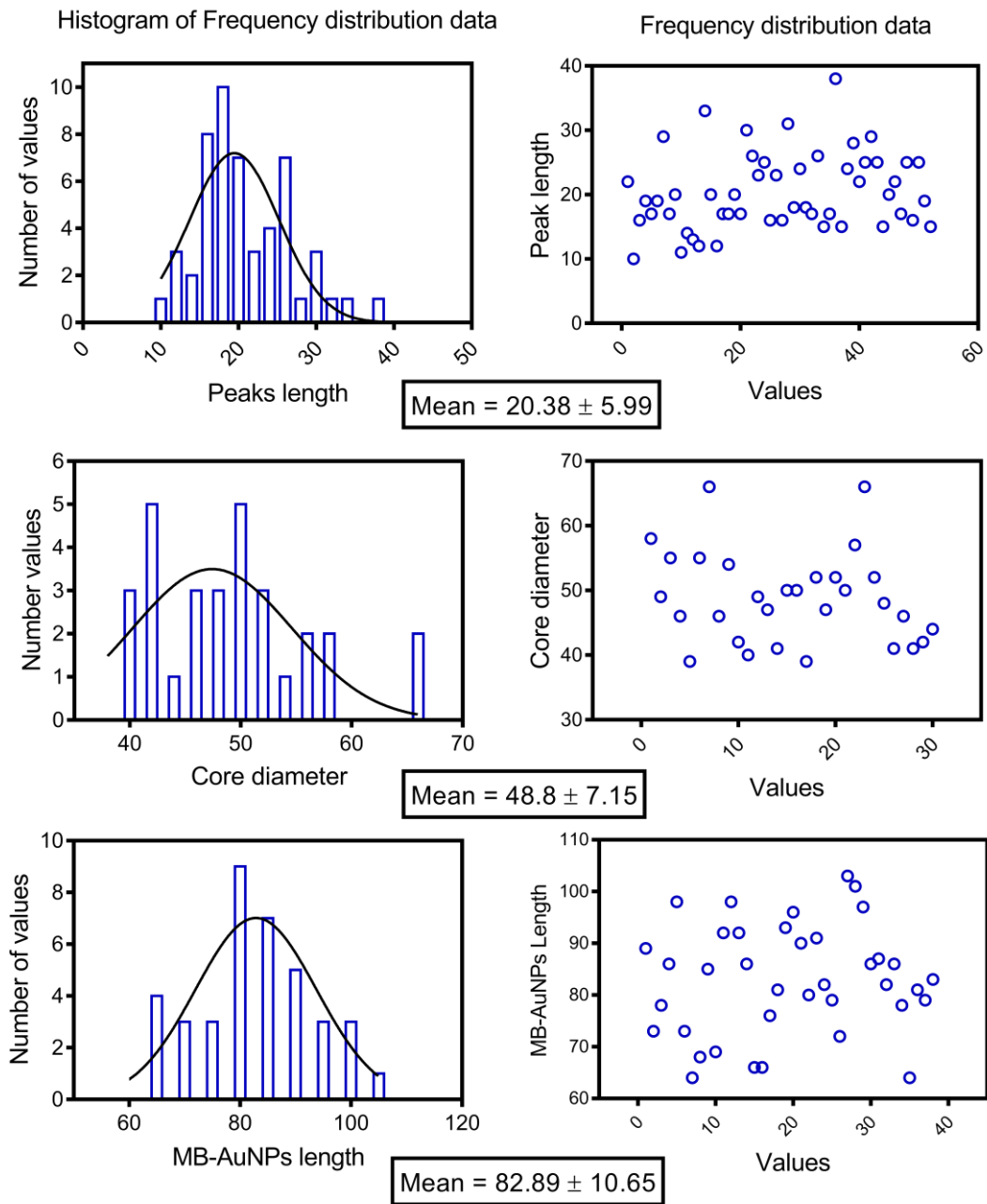
Figure 3.32. Histograms of diameters and frequency distribution data of populations of 50 16MB-AuNPs.
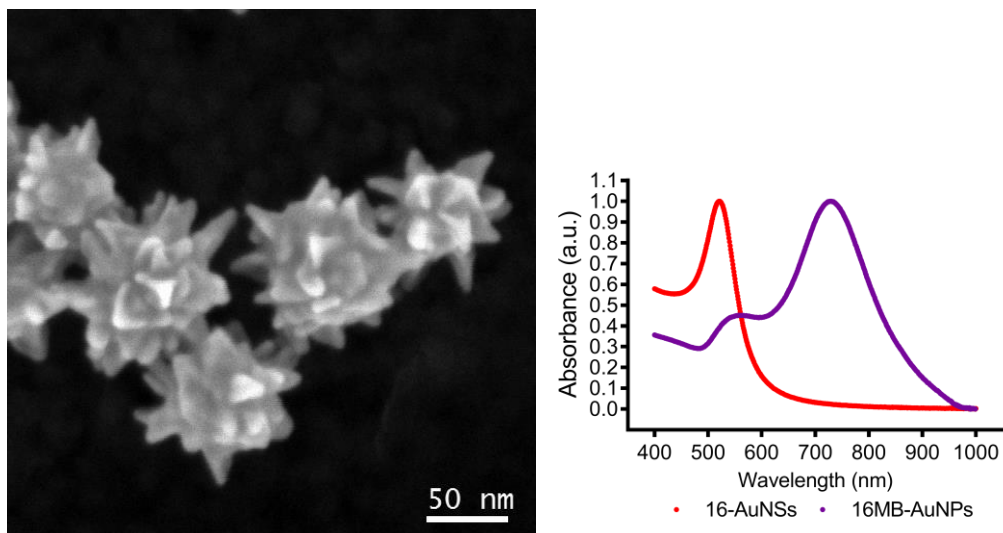
Figure 3.33.   **Left.** SEM micrograph of 16MB-AuNPs synthetized with 16-AuNSs. **Right.** UV-Vis Spectra of 16-AuNSs and 16MB-AuNPs with a band centered at 520 nm and 729 nm respectively.
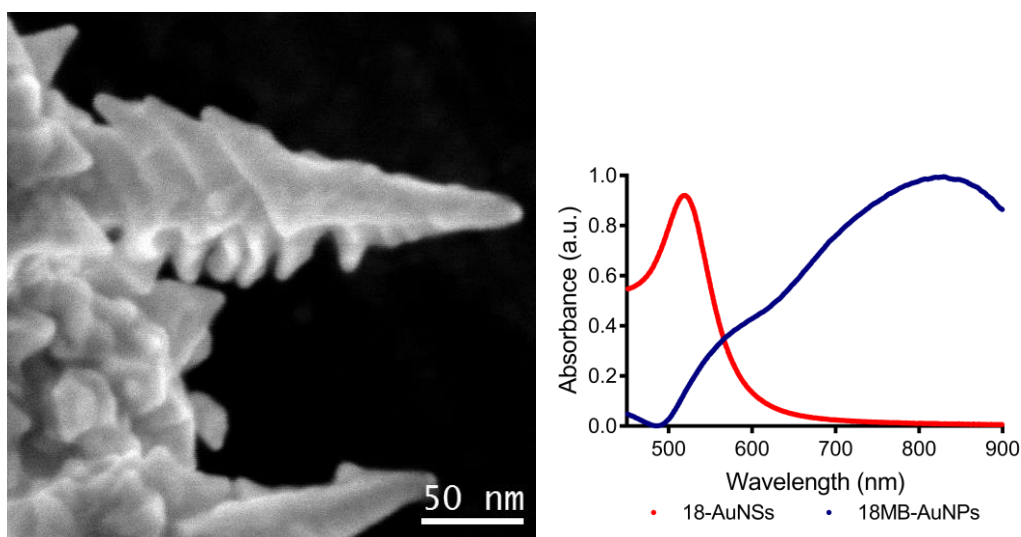
Figure 3.34.   SEM Micrographs (**left**) of 18MB-AuNPs with second order branches and UV-Vis spectra (**right**) of 18-AuNSs and 18MB-AuNPs, they have a band centered at 524 nm and 830 nm respectively.

At this stage we have shown that both sets of samples (16 and 18MB-AuNPs) present good optical response for been used as nano-heaters. The next criteria for choose a sample is the critical size for being used in an in-vitro or in-vivo environment. Thus, we decided the use of 16MB-AuNPs for being tested as nano-

heaters, however the optical response of 18MB-AuNPs in the 830 nm (Fig. 3.34) is suitable for applications in nanostructured system for SERS[86].
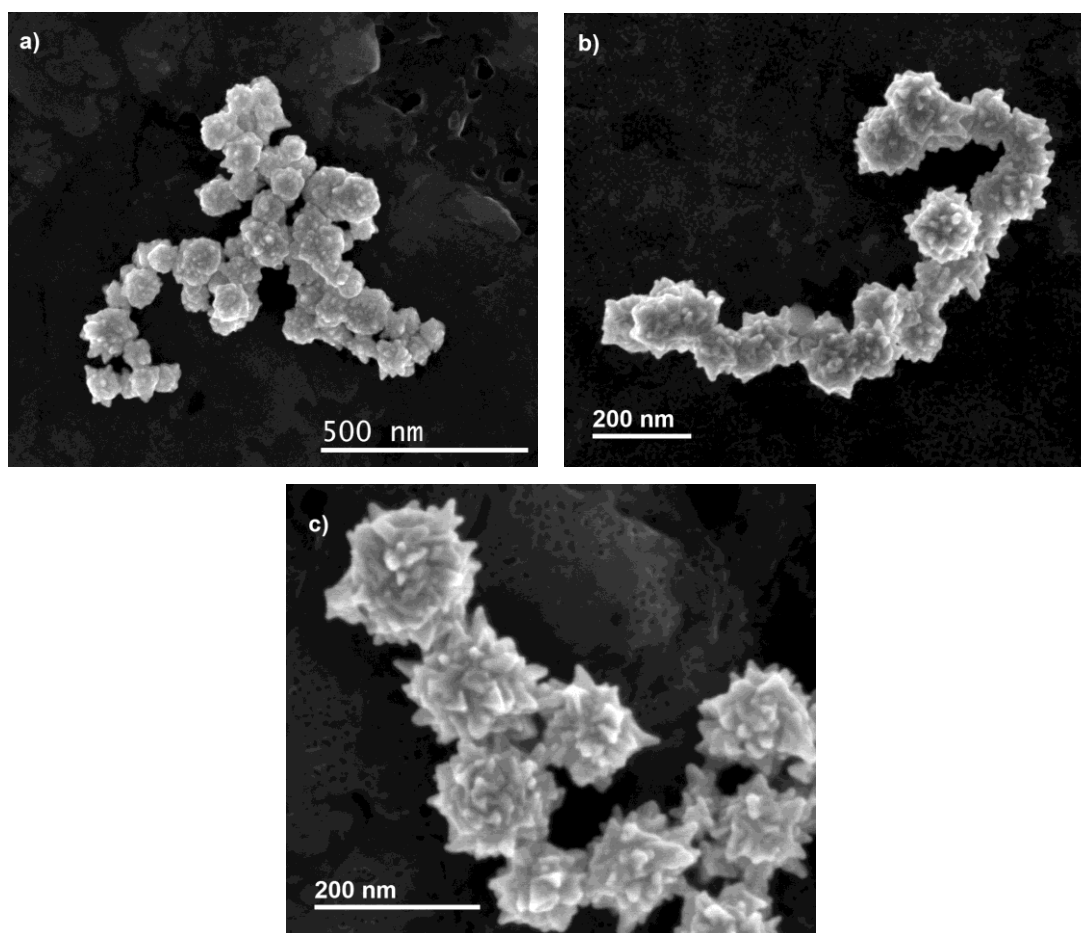
Figure 3.35. SEM micrographs of MB-AuNPs synthesized in a medium of HEPES [50mM], with a molar ratio Au^{3+}/NH_2OH of 1:3, with a) 16-AuNSs and b-c) 18-AuNSs. The difference between sample b) and the 16MB-AuNPs is the size of the AuNSs and with sample a,c) is the addition of double amount of gold ions. The sample a) does not present increment in length peaks.

3.5.2. Thermal response of MB-AuNPs

Infrared (IR) imaging is based on the fact that any object at a temperature above absolute zero (-273 °C) will emit IR radiation, even if only weakly. The human body has a low thermal emittance, radiating in a wavelength range that starts at around 3 µm, and peaks in the vicinity of 10 µm, and trails off from this point into the extreme IR and negligibly, beyond it. The emissivity of human skin has a constant value between wavelengths of 2 and 14 µm of 0.98 ±0.01 for black skin and 0.97±0.02 for white skin;[77] thus, human skin has a known and almost invariant emissivity in this wavelength region that makes IR imaging an ideal procedure to evaluate surface temperature of the human body.[78,79] Because above arguments, the skin-equivalent phantoms with 0.62 ± 0.01 reported emittance,[75] is a well suited model for IR thermal evaluation.
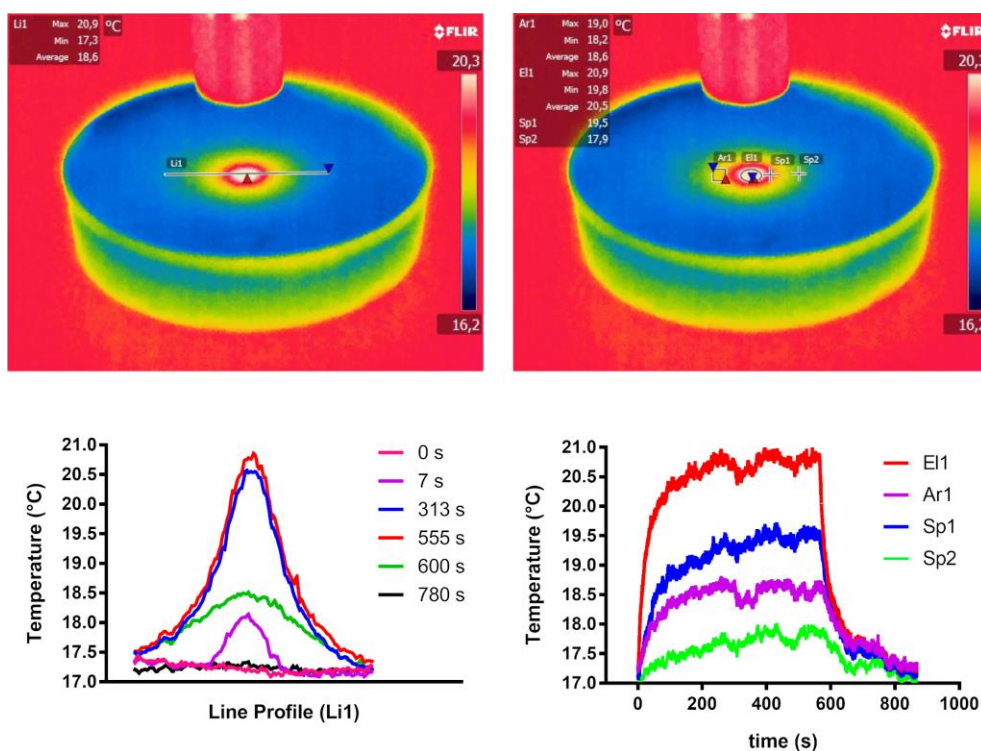
Figure 3.36. The thermography corresponds at the 555 s of laser irradiation. **Left.** Temperature profiles of the heating area at different times. The profile analized is designed as Line 1 (Li1) in the thermography. **Right.** Temporal analysis of temperature variations of different points and regions marked in the thermography as area (Ar1), elipsoide (El1), singles points (Sp1, Sp2).

146

The thermal response of 16-AuNSs and 16MB-AuNPs was evaluated inside the skin-equivalent phantoms by dynamic thermography. The samples were irradiated at 0.15 W power laser by 3 cycles of 10 mins, and recorded with an IR camera, and the thermographs shown at

The Figs. 3.36 were extracted at 555 s using the FLIR-RIR software, which allows the analysis of single points, line profiles and averages of circle/rectangular areas. The plot in

The Fig. 3.36 (left) shows data from a line profile analyzed at different times, and clearly can be observed that not only the incident laser area is been heated, there is a radial propagation by diffusion of the generated heat, thus there is energy transmitted to the adjacent regions due to the immersed NPs. This effect is also observed in the control phantom analysis, but over a smaller area and with more uniform temperature as can be seen in Fig. 3.37. The

The Fig. 3.36 (right) reports the information on how fast the system absorbs the energy, achieving constant temperature at early irradiation times (60 s). This was also performed for evidence the continuity of the thermal response of immersed 16MB-AuNPs in the phantom as a function of time.
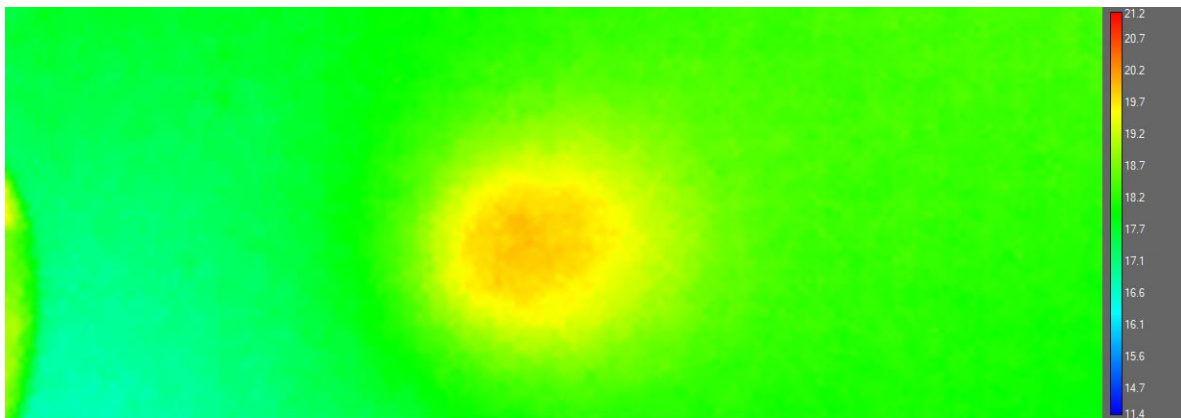
Figure 3.37.   Thermography of skin-equivalent phantom used as control. The thermography was extracted from the video at 200 s after light irradiation starts. It can be observed that the incident light transmits energy to the adjacent regions, but in small area and with not strong gradient temperature.

The plot in the Fig. 3.38 corresponds to a dynamic thermal analysis, and from it we can appreciate the difference in the temperature reached by the three phantoms: the largest increase of localized temperature is measured in the sample prepared with 16MB-AuNPs, compared to the phantom with 16-AuNSs and the one without the addition of NPs, used as a control.
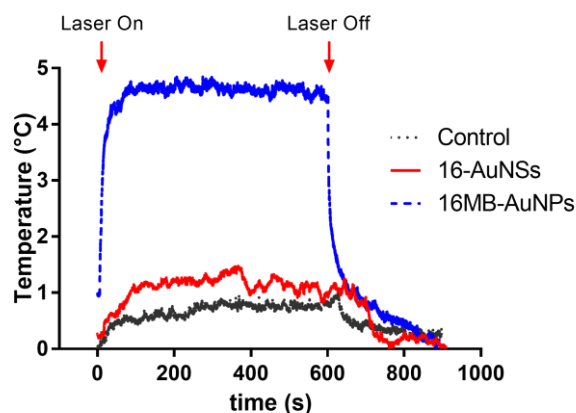
Figure 3.38. Thermal response of skin-equivalent phantoms with: 16-AuNSs, 16MB-AuNPs and control.

A red-shift of the LSPR is present for anisotropic MB-AuNPs compared with spheres (see Fig. 3.27), and a substantial increase in the heating efficiency with respect the sphere is expected. In our results, the maximum temperature increment in 16MB-AuNPs phantom was achieved in 60 s and maintained during all the laser irradiation. This temperature increment is $\Delta T=4.5$ °C and when the light source is turned off, a fast decay is observed. The comparison between the AuNSs and MB-AuNPs at the same concentration, shows the evident increase of thermal response due to the anisotropic shape of MB-AuNPs and the localized SPR's synergy, because the MB-AuNPs absorbs closer to the wavelength of laser irradiation. In the case of the phantom with 16-AuNSs, the increment in temperature can be adscribed for the excitation of hot-spots created in the interaction among spherical NPs.[87,88] Importantly to mention is that there were not physical changes observed in the phantoms under laser irradiation, as leaking or deformation, even after the three cycles evaluation.

3.5.3. Discussion

We have shown that the control on the width, the length, the number of peaks, and the degree of dendritic growth, give rise to an easy tuning of the plasmon resonance spectra[89] and their corresponding higher transduction of light into heat, and therefore gold nano-heaters are good candidates for IR absorption for efficient photothermal therapy of malignant cancer cells.

The structural characteristics of the AuNSs influenced the degree of ramification of the nanoparticle tips, resulting in second-order branches for MB-AuNPs synthesized from 18-AuNSs, which present crystalline defects promoting directed anisotropy. From 16-AuNSs we could obtain monodisperse samples. After analyzing the impact of HEPES and hydroxylamine on the final tips shape, we estimated that the optimal molar ratio of hydroxylamine:Au ions is 3:1, being this amount enough to avoid the intervention of HEPES in the reduction. Even if an excess of hydroxylamine may result in a better definition of tips, it can also cause the agglomeration of MB-AuNPs, due to the resulting high ionic force of the solution, that could not be used for clinical applications, and the same argument is valid for higher concentration of HEPES (75mM). On the other side, the increase on the molar concentration of Au ions (and necessary hydroxylamine) leads to bigger cores and smaller length of tips, thus it shifts the SPR to lower wavelengths making them not practical for PTT.

Regarding the dynamic thermography results for 16MB-AuNPs, we found that not only the incident laser area is being heated, but there is also a radial propagation of the released heat, which means there is transmission of energy around the adjacent region of the spot due to the immersed NPs. Therefore, the addition of MB-AuNPs results in the production of more efficient centers for scattering and re-emission of energy.

The temperature increment achieved by the nanoheaters in this work ($\Delta T \sim 5\ ^{\circ}C$) is good enough for effective and minimally harmful gold nanoparticles based photo-thermal therapy techniques.[90] This temperature increment from multibranched gold

nanoparticles immersed in a phantom gel (as a model approach for the real environment in bio-applications), satisfies biomedical requirement for the treatment of superficial diseases (mycoses, fungal infections and many different types of skin cancer).[18]

Figures Index

Tables Index

References

(1)   Rana, S.; Kalaichelvan, P. T. Ecotoxicity of Nanoparticles. *ISRN Toxicol.* **2013**, *2013*, 1–11.

(2)   Moran-López, J. L.; Rodríguez-López, J. L. *Los Materiales Nanoestructurados: Sus Propiedades Y Aplicaciones En La Revolución Científica Y Tecnológica Del Siglo XXI*; Fondo de Cultura Económica, 2012.

(3)   Louis, C.; Pluchery, O. *Gold Nanoparticles for Physics, Chemistry and Biology*; Imperial College Press, 2012.

(4)   Brill, R. H. The Chemistry of the Lycurgus Cup. In *Comptes rendus/ Congrés international du verre*; 1965; p. 2:223.

(5)   BARBER, D. J.; FREESTONE, I. C. AN INVESTIGATION OF THE ORIGIN OF THE COLOUR OF THE LYCURGUS CUP BY ANALYTICAL TRANSMISSION ELECTRON MICROSCOPY. *Archaeometry* **1990**, *32*, 33–45.

(6)   Hunt, L. B. The True Story of Purple of Cassius. *Gold Bull.* **1976**, *9*, 134–139.

(7)   Fricker, S. P.; Pricker, S. P. Medical Uses of Gold Compounds: Past, Present and Future. *Gold Bull.* **1996**, *29*, 53–60.

(8)   Schmid, G. *Nanoparticles, from Theory to Application*; Wiley-VCH Verlag GmbH & Co., 2004.

(9)   Health, N. C. for C. and I. https://nccih.nih.gov/health/ayurveda/introduction.htm https://nccih.nih.gov/health/ayurveda/introduction.htm (accessed Feb 10, 2016).

(10)   Link, S.; El-sayed, M. A. Shape and Size Dependence of Radiative, Non-Radiative and Photothermal Properties of Gold Nanocrystals. *Int. Rev. Phys. Chem.* **2000**, *19*, 409–453.

(11)   Enoch, S.; Bonod, N. *Plasmonics, From Basics to Advanced Topics*; Springer-Verlag Berlin Heidelberg GmbH, 2012; Vol. 167.

(12)   Schasfoort, R. B. M.; Tudos, A. J. *Handbook of Surface Plasmon Resonance*; Royal Society of Chemistry: Cambridge, UK, 2008.

(13)   Sajanlal, P. R.; Sreeprasad, T. S.; Samal, A. K.; Pradeep, T. Anisotropic Nanomaterials: Structure, Growth, Assembly, and Functions. *Nano Rev.* **2011**, *2*, 5883.

(14)   Cheng, L.; Wang, C.; Feng, L.; Yang, K.; Liu, Z. Functional Nanomaterials for Phototherapies of Cancer. *Chem. Rev.* **2014**, *114*, 10869–10939.

(15)   Murray, W. A.; Barnes, W. L. Plasmonic Materials. *Adv. Mater.* **2007**, *19*, 3771–3782.

(16)   Bastús, N. G.; Comenge, J.; Puntes, V. Kinetically Controlled Seeded Growth Synthesis of Citrate-Stabilized Gold Nanoparticles of up to 200 Nm: Size Focusing versus Ostwald Ripening. *Langmuir* **2011**, *27*, 11098–11105.

(17)   Ye, J.; Van Dorpe, P.; Van Roy, W.; Lodewijks, K.; De Vlaminck, I.; Maes, G.; Borghs, G. Fabrication and Optical Properties of Gold Semishells. *J. Phys. Chem. C* **2009**, *113*, 3110–3115.

(18)   Chirico, G.; Pallavicini, P.; Collini, M. Gold Nanostars for Superficial Diseases: A Promising Tool for Localized Hyperthermia? *Nanomedicine* **2014**, *9*, 1–3.

(19)   Alfonso, L. D.; Falqui, A.; Pallavicini, P.; Chirico, G.; Collini, M.; Dacarro, G.; Dona, A.; Donà, A.; D'Alfonso, L.; Falqui, A.; *et al.* Synthesis of Branched Au Nanoparticles with Tunable near-Infrared LSPR Using a Zwitterionic Surfactant. *Chem. Commun.* **2011**, *47*, 1315–1317.

(20)   Pallavicini, P.; Donà, A.; Casu, A.; Chirico, G.; Collini, M.; Dacarro, G.; Falqui, A.; Milanese, C.; Sironi, L.; Taglietti, A. Triton X-100 for Three-Plasmon Gold Nanostars with Two Photothermally Active NIR (near IR) and SWIR (Short-Wavelength IR)

Channels. *Chem. Commun.* **2013**, *49*, 6265–6267.

(21)   Hafner, J. H.; Nordlander, P.; Weiss, P. S. Virtual Issue on Plasmonics. *ACS Nano* **2011**, *5*, 4245–4248.

(22)   Hogan, N. J.; Urban, A. S.; Ayala-Orozco, C.; Pimpinelli, A.; Nordlander, P.; Halas, N. J. Nanoparticles Heat through Light Localization. *Nano Lett.* **2014**, *14*, 4640–4645.

(23)   Richardson, H. H.; Hickman, Z. N.; Thomas, A. C.; Kordesch, M. E.; Govorov, A. O. Thermo-Optical Properties of Nanoparticles and Nanoparticle Complexes Embedded in Ice: Characterization of Heat Generation and Actuation of Larger-Scale Effects. *MRS Proc.* **2006**, *964*.

(24)   Glomm, W. R. Functionalized Gold Nanoparticles for Applications in Bionanotechnology. *J. Dispers. Sci. Technol.* **2005**, *26*, 389–414.

(25)   Pilot Study of AuroLase Therapy in Refractory and/or Recurrent Tumors of the Head and Neck http://clinicaltrials.gov/ct2/.

(26)   Wang, Y.; Black, K. C. L.; Luehmann, H.; Li, W.; Zhang, Y.; Cai, X.; Wan, D.; Liu, S.-Y.; Li, M.; Kim, P.; *et al.* Comparison Study of Gold Nanohexapods, Nanorods, and Nanocages for Photothermal Cancer Treatment. *ACS Nano* **2013**, *7*, 2068–2077.

(27)   Hirsch, L. R.; Stafford, R. J.; Bankson, J. a; Sershen, S. R.; Rivera, B.; Price, R. E.; Hazle, J. D.; Halas, N. J.; West, J. L. Nanoshell-Mediated Near-Infrared Thermal Therapy of Tumors Under Magnetic Resonance Guidance. *Proc. Natl. Acad. Sci. U. S. A.* **2003**, *100*, 13549–13554.

(28)   O'Neal, D. P.; Hirsch, L. R.; Halas, N. J.; Payne, J. D.; West, J. L. Photo-Thermal Tumor Ablation in Mice Using near Infrared-Absorbing Nanoparticles. *Cancer Lett.* **2004**, *209*, 171–176.

(29)   Chen, J.; Glaus, C.; Laforest, R.; Zhang, Q.; Yang, M.; Gidding, M.; Welch, M. J.; Xia, Y. Gold Nanocages as Photothermal Transducers for Cancer Treatment. *Small* **2010**, *6*, 811–817.

(30)   Okuno, T.; Kato, S.; Hatakeyama, Y.; Okajima, J.; Maruyama, S.; Sakamoto, M.; Mori, S.; Kodama, T. Photothermal Therapy of Tumors in Lymph Nodes Using Gold Nanorods and near-Infrared Laser Light. *J. Control. Release* **2013**, *172*, 879–884.

(31)   Webb, J. a.; Erwin, W. R.; Zarick, H. F.; Aufrecht, J.; Manning, H. W.; Lang, M. J.; Pint, C. L.; Bardhan, R. Geometry-Dependent Plasmonic Tunability and Photothermal Characteristics of Multibranched Gold Nanoantennas. *J. Phys. Chem. C* **2014**, *118*, 3696–3707.

(32)   Ding, X.; Liow, C. H.; Zhang, M.; Huang, R.; Li, C.; Shen, H.; Liu, M.; Zou, Y.; Gao, N.; Zhang, Z.; *et al.* Surface Plasmon Resonance Enhanced Light Absorption and Photothermal Therapy in the Second near-Infrared Window. *J. Am. Chem. Soc.* **2014**, *136*, 15684–15693.

(33)   Lee, U. Y.; Youn, Y. S.; Park, J.; Lee, E. S. Y-Shaped Ligand-Driven Gold Nanoparticles for Highly Efficient Tumoral Uptake and Photothermal Ablation. *ACS Nano* **2014**, *8*, 12858–12865.

(34)   Rengan, A. K.; Kundu, G.; Banerjee, R.; Srivastava, R. Gold Nanocages as Effective Photothermal Transducers in Killing Highly Tumorigenic Cancer Cells. *Part. Part. Syst. Charact.* **2014**, *31*, 398–405.

(35)   Kang, S.; Bhang, S. H.; Hwang, S.; Yoon, J.-K.; Song, J.; Jang, H.-K.; Kim, S.; Kim, B.-S. Mesenchymal Stem Cells Aggregate and Deliver Gold Nanoparticles to Tumors for Photothermal Therapy. *ACS Nano* **2015**, *9*, 9678–9690.

(36)   Wang, S.; Teng, Z.; Huang, P.; Liu, D.; Liu, Y.; Tian, Y.; Sun, J.; Li, Y.; Ju, H.; Chen, X.; *et al.* Reversibly Extracellular pH Controlled Cellular Uptake and Photothermal Therapy by PEGylated Mixed-Charge Gold Nanostars. *Small* **2015**, *11*, 1801–1810.

(37)   Yuan, H.; Khoury, C. G.; Wilson, C. M.; Grant, G. A.; Bennett, A. J.; Vo-Dinh, T. In Vivo Particle Tracking and Photothermal Ablation Using Plasmon-Resonant Gold

Nanostars. *Nanomedicine Nanotechnology, Biol. Med.* **2012**, *8*, 1355–1363.

(38)   Espinosa, A.; Silva, A. K. A.; Sánchez-Iglesias, A.; Grzelczak, M.; Péchoux, C.; Desboeufs, K.; Liz-Marzán, L. M.; Wilhelm, C. Cancer Cell Internalization of Gold Nanostars Impacts Their Photothermal Efficiency In Vitro and In Vivo: Toward a Plasmonic Thermal Fingerprint in Tumoral Environment. *Adv. Healthc. Mater.* **2016**, n/a-n/a.

(39)   Wei, P.; Chen, J.; Hu, Y.; Li, X.; Wang, H.; Shen, M.; Shi, X. Dendrimer-Stabilized Gold Nanostars as a Multifunctional Theranostic Nanoplatform for CT Imaging, Photothermal Therapy, and Gene Silencing of Tumors. *Adv. Healthc. Mater.* **2016**, *5*, 3203–3213.

(40)   Xie, J.; Zhang, Q.; Lee, J. Y.; Wang, D. I. C. The Synthesis of SERS-Active Gold Nanoflower Tags for In Vivo Applications. *ACS Nano* **2008**, *2*, 2473–2480.

(41)   Liu, X.-L.; Wang, J.-H.; Liang, S.; Yang, D.-J.; Nan, F.; Ding, S.-J.; Zhou, L.; Hao, Z.-H.; Wang, Q.-Q. Tuning Plasmon Resonance of Gold Nanostars for Enhancements of Nonlinear Optical Response and Raman Scattering. *J. Phys. Chem. C* **2014**, *118*, 9659–9664.

(42)   Guerrero-Martínez, A.; Barbosa, S.; Pastoriza-Santos, I.; Liz-Marzán, L. M. Nanostars Shine Bright for You. Colloidal Synthesis, Properties and Applications of Branched Metallic Nanoparticles. *Curr. Opin. Colloid Interface Sci.* **2011**, *16*, 118–127.

(43)   Maiorano, G.; Rizzello, L.; Malvindi, M. A.; Shankar, S. S.; Martiradonna, L.; Falqui, A.; Cingolani, R.; Pompa, P. P. Monodispersed and Size-Controlled Mmultibranched Gold Nanoparticles with Nanoscale Tuning of Surface Morphology. *Nanoscale* **2011**, *3*, 1–6.

(44)   Plascencia-Villa, G.; Bahena, D.; Rodríguez, A. R.; Ponce, A.; José-Yacamán, M. Advanced Microscopy of Star-Shaped Gold Nanoparticles and Their Adsorption-Uptake by Macrophages. *Metallomics* **2013**, *5*, 29–32.

(45)   Zhu, M.; Lei, B.; Ren, F.; Chen, P.; Shen, Y.; Guan, B.; Du, Y.; Li, T.; Liu, M. Branched Au Nanostructures Enriched with a Uniform Facet: Facile Synthesis and Catalytic Performances. *Sci. Rep.* **2014**, *4*, 5259.

(46)   Ahmed, W.; Kooij, E. S.; van Silfhout, A.; Poelsema, B. Controlling the Morphology of Multi-Branched Gold Nanoparticles. *Nanotechnology* **2010**, *21*, 125605.

(47)   Senthil Kumar, P.; Pastoriza-Santos, I.; Rodríguez-González, B.; Javier García de Abajo, F.; Liz-Marzán, L. M. High-Yield Synthesis and Optical Response of Gold Nanostars. *Nanotechnology* **2008**, *19*, 15606.

(48)   Zhao, L.; Ji, X.; Sun, X.; Li, J.; Yang, W.; Peng, X. Formation and Stability of Gold Nanoflowers by the Seeding Approach: The Effect of Intraparticle Ripening. *J. Phys. Chem. C* **2009**, *113*, 16645–16651.

(49)   Dam, D. H. M.; Lee, J. H.; Sisco, P. N.; Co, D. T.; Zhang, M.; Wasielewski, M. R.; Odom, T. W. Direct Observation of Nanoparticle-Cancer Cell Nucleus Interactions. *ACS Nano* **2012**, *6*, 3318–3326.

(50)   Yuan, H.; Ma, W.; Chen, C.; Zhao, J.; Liu, J.; Zhu, H.; Gao, X. Shape and SPR Evolution of Thorny Gold Nanoparticles Promoted by Silver Ions. *Chem. Mater.* **2007**, *19*, 1592–1600.

(51)   Jiang, L.; Tang, Y.; Liow, C.; Wu, J.; Sun, Y.; Jiang, Y.; Dong, Z.; Li, S.; Dravid, V. P.; Chen, X.; *et al.* Synthesis of Fivefold Stellate Polyhedral Gold Nanoparticles with {110}-Facets via a Seed-Mediated Growth Method. *Small* **2013**, *9*, 705–710.

(52)   Leng, W.; Pati, P.; Vikesland, P. J. Room Temperature Seed Mediated Growth of Gold Nanoparticles: Mechanistic Investigations and Life Cycle Assesment. *Environ. Sci. Nano* **2015**, *2*, 440–453.

(53)   Yamamoto, M.; Kashiwagi, Y.; Sakata, T.; Mori, H.; Nakamoto, M. Synthesis and

Morphology of Star-Shaped Gold Nanoplates Protected by Poly(N-Vinyl-2-Pyrrolidone). *Chem. Mater.* **2005**, *17*, 5391–5393.

(54) Sau, T. K.; Murphy, C. J. Room Temperature, High-Yield Synthesis of Multiple Shapes of Gold Nanoparticles in Aqueous Solution. *J. Am. Chem. Soc.* **2004**, *126*, 8648–8649.

(55) Jana, N. R.; Gearheart, L.; Murphy, C. J. Wet Chemical Synthesis of High Aspect Ratio Cylindrical Gold Nanorods. *J. Phys. Chem. B* **2001**, *105*, 4065–4067.

(56) Murphy, C. J.; Sau, T. K.; Gole, A. M.; Orendorff, C. J.; Gao, J.; Gou, L.; Hunyadi, S. E.; Li, T. Anisotropic Metal Nanoparticles: Synthesis, Assembly, and Optical Applications. *J. Phys. Chem. B* **2005**, *109*, 13857–13870.

(57) Habib, A.; Tabata, M.; Guang Wu, Y.; Wu, Y. G. Formation of Gold Nanoparticles by Good's Buffers. *Bull. Chem. Soc. Jpn.* **2005**, *78*, 262–269.

(58) Xie, J.; Lee, J. Y.; Wang, D. I. C. Seedless, Surfactantless, High-Yield Synthesis of Branched Gold Nanocrystals in HEPES Buffer Solution. *Chem. Mater.* **2007**, *19*, 2823–2830.

(59) Chen, R.; Wu, J.; Li, H.; Cheng, G.; Lu, Z.; Che, C. M. Fabrication of Gold Nanoparticles with Different Morphologies in HEPES Buffer. *Rare Met.* **2010**, *29*, 180–186.

(60) Bao, Y.; Yeh, H.-C.; Zhong, C.; Ivanov, S. a.; Sharma, J. K.; Neidig, M. L.; Vu, D. M.; Shreve, A. P.; Dyer, R. B.; Werner, J. H.; *et al.* Formation and Stabilization of Fluorescent Gold Nanoclusters Using Small Molecules. *J. Phys. Chem. C* **2010**, *114*, 15879–15882.

(61) Xia, D.-L.; Wang, Y.-F.; Bao, N.; He, H.; Li, X.; Chen, Y.-P.; Gu, H.-Y. Influence of Reducing Agents on Biosafety and Biocompatibility of Gold Nanoparticles. *Appl. Biochem. Biotechnol.* **2014**, *174*, 2458–2470.

(62) Li, H.; Lu, Z.; Wu, J.; Yu, H.; Yu, X.; Chen, R. Hydrothermal Synthesis of Transition Metal Oxide Nanomaterials in HEPES Buffer Solution. *Mater. Lett.* **2010**, *64*, 1939–1942.

(63) Good, N. E.; Izawa, S. Hydrogen Ion Buffers. *Methods Enzymol.* **1972**, *24*, 53–68.

(64) Webb, J. a.; Erwin, W. R.; Zarick, H. F.; Aufrecht, J.; Manning, H. W.; Lang, M. J.; Pint, C. L.; Bardhan, R. Geometry-Dependent Plasmonic Tunability and Photothermal Characteristics of Multibranched Gold Nanoantennas. *J. Phys. Chem. C* **2014**, *118*, 3696–3707.

(65) Minati, L.; Benetti, F.; Chiappini, A.; Speranza, G. One-Step Synthesis of Star-Shaped Gold Nanoparticles. *Colloids Surfaces A Physicochem. Eng. Asp.* **2014**, *441*, 623–628.

(66) Brown, K. R.; Natan, M. J. Hydroxylamine Seeding of Colloidal Au Nanoparticles in Solution and on Surfaces. *Langmuir* **1998**, *14*, 726–728.

(67) Su, Q.; Ma, X.; Dong, J.; Jiang, C.; Qian, W. A Reproducible SERS Substrate Based on Electrostatically Assisted Aptes-Functionalized Surface-Assembly of Gold Nanostars. *ACS Appl. Mater. Interfaces* **2011**, *3*, 1873–1879.

(68) Nikoobakht, B.; El-Sayed, M. A. Preparation and Growth Mechanism of Gold Nanorods (NRs) Using Seed-Mediated Growth Method. *Chem. Mater.* **2003**, *15*, 1957–1962.

(69) Jiao, Z.; Xia, H.; Tao, X. Modulation of Localized Surface Plasmon Resonance of Nanostructured Gold Crystals by Tuning Their Tip Curvature with Assistance of Iodide and Silver(I) Ions. *J. Phys. Chem. C* **2011**, *115*, 7887–7895.

(70) Ito, K.; Furuya, K.; Okano, Y.; Hamada, L. Development and Characteristics of a Biological Tissue-Equivalent Phantom for Microwaves. *Electron. Commun. Japan Part I Commun.* **2001**, *84*, 67–77.

(71) Mazzara, G. P. A.; Briggs, R. W.; Wu, Z.; Steinbach, B. G. Use of a Modified

Polysaccharide Gel in Developing a Realistic Breast Phantom for MRI. *Magn. Reson. Imaging* **1996**, *14*, 639–648.

(72) Sivaraman, S. K.; Kumar, S.; Santhanam, V. Monodisperse Sub-10nm Gold Nanoparticles by Reversing the Order of Addition in Turkevich Method – The Role of Chloroauric Acid. *J. Colloid Interface Sci.* **2011**, *361*, 543–547.

(73) Driver, I.; Feather, J. W.; King, P. R.; Dawson, J. B. The Optical Properties of Aqueous Suspensions of Intralipid , a Fat Emulsion. *Phys. Med. Biol.* **1989**, *34*, 1927–1930.

(74) Iizuka, M. N.; Sherar, M. D.; Vitkin, I. A. Optical Phantom Materials for Near Infrared Laser Photocoagulation Studies. *Lasers Surg. Med.* **1999**, *25*, 159–169.

(75) Okano, Y.; Ito, K.; Ida, I.; Takahashi, M. The SAR Evaluation Method by a Combination of Thermographic Experiments and Biological. *IEEE Trans. Microw. Theory Tech.* **2000**, *48*, 2094–2103.

(76) Didychuk, C. L.; Ephrat, P.; Chamson-Reig, A.; Jacques, S. L.; Carson, J. J. L. Depth of Photothermal Conversion of Gold Nanorods Embedded in a Tissue-like Phantom. *Nanotechnology* **2009**, *20*, 195102.

(77) Jones, B. F. A Reappraisal of the Use of Infrared Thermal Image Analysis in Medicine. *IEEE Trans. Med. Imaging* **1998**, *17*, 1019–1027.

(78) Teich, J. S. Digital Infrared Imaging for Medicine Recent Advances in I.R. Focal Plane Array Imaging Technology. *IEEE Eng. Med. Biol. Soc.* **1996**, *5*, 2079–2080.

(79) Gore, J. P.; Xu, L. X. Thermal Imaging for Biomedical and Medical Diagnostics. In *Biomedical Photonics Handbook*; Vo-Dinh, T., Ed.; CRC Press: Boca Raton, FL, 2003.

(80) Chahat, N.; Zhadobov, M.; Alekseev, S.; Sauleau, R. Human Skin-Equivalent Phantom for On-Body Antenna Measurements in 60 GHz Band. *Electron. Lett.* **2012**, *48*, 67.

(81) Bibikova, O.; Popov, A.; Bykov, A.; Fales, A.; Yuan, H.; Skovorodkin, I.; Kinnunen, M.; Vainio, S.; Vo-Dinh, T.; Tuchin, V. V.; *et al.* Plasmon-Resonant Gold Nanostars With Variable Size as Contrast Agents for Imaging Applications. *IEEE J. Sel. Top. Quantum Electron.* **2016**, *22*, 13–20.

(82) Gole, A.; Murphy, C. J. Seed-Mediated Synthesis of Gold Nanorods: Role of the Size and Nature of the Seed. *Chem. Mater.* **2004**, *16*, 3633–3640.

(83) Tian, F.; Conde, J.; Bao, C.; Chen, Y.; Curtin, J.; Cui, D. Gold Nanostars for Efficient in Vitro and in Vivo Real-Time SERS Detection and Drug Delivery via Plasmonic-Tunable Raman/FTIR Imaging. *Biomaterials* **2016**, *106*, 87–97.

(84) Weiner, R. G.; Skrabalak, S. E. Metal Dendrimers: Synthesis of Hierarchically Stellated Nanocrystals by Sequential Seed-Directed Overgrowth. *Angew. Chemie Int. Ed.* **2015**, *54*, 1181–1184.

(85) Bakshi, M. S. How Surfactants Control Crystal Growth of Nanomaterials. *Cryst. Growth Des.* **2016**, *16*, 1104–1133.

(86) Zoppi, A. . B.; Trigari, S. .; Margheri, G. .; Muniz-Miranda, M. .; Giorgetti, E. . Gold Nanostars as SERS-Active Substrates for FT-Raman Spectroscopy. *RSC Adv.* **2015**, *5*, 8523–8532.

(87) Farcau, C.; Astilean, S. Mapping the SERS Efficiency and Hot-Spots Localization on Gold Film over Nanospheres Substrates. *J. Phys. Chem. C* **2010**, *114*, 11717–11722.

(88) Pasquale, A. J.; Reinhard, B. M.; Dal Negro, L. Engineering Photonic-Plasmonic Coupling in Metal Nanoparticle Necklaces. *ACS Nano* **2011**, *5*, 6578–6585.

(89) Espinosa, A.; Silva, A. K. A.; Sánchez-Iglesias, A.; Grzelczak, M.; Péchoux, C.; Desboeufs, K.; Liz-Marzán, L. M.; Wilhelm, C. Cancer Cell Internalization of Gold Nanostars Impacts Their Photothermal Efficiency In Vitro and In Vivo: Toward a Plasmonic Thermal Fingerprint in Tumoral Environment. *Adv. Healthc. Mater.* **2016**, *5*, 1040–1048.

(90)   Zhu, X.; Feng, W.; Chang, J.; Tan, Y.; Li, J.; Chen, M.; Sun, Y.; Li, F. Temperature-Feedback Upconversion Nanocomposite for Accurate Photothermal Therapy at Facile Temperature. *Nat. Commun.* **2016**, *7*, 10437.

4. Bioconjugation of Gold Nanoparticles with Bovine Serum Albumin

Chapter Content

4.1. Introduction

When a synthesized system is intended to be applied for biological purposes, it is necessary to carefully design the surface layer. The molecules at the surface of nanometric systems, as nanoparticles (NPs,) will provide the signals to its long term circulation, biocompatibility and selectivity to target sites. Also, it can be considered to create a full coverage of NPs to avoid toxic responses, but the coverage may not affect the principal property of the NPs, for which was selected and the increased size still has to allow the long term body circulation. Along this chapter, we will introduce the main concepts and topics of conjugation of NPs, and we review the published work in this subject. With the intention to provide documented background to the hypothesis sustained in this project, at section 4.3 we analyses the biological function and properties of serum albumin, characteristics for which has been subject of interest in the preparation of conjugated nanosystems. Besides, we briefly review the reported work of serum albumin as vehicle and signal agent of metal nanoparticles.

The experimental work starting from section 4.4, corresponds to the fulfillment of the general objective Conjugation of gold nanoparticles with bovine serum albumin, for which, we performed a spectroscopic quantification of serum albumin for the proper ratio conjugation with MB-AuNPs, to obtain a stable protein shell. We follow with the analysis of the bonding of albumin to the NP surface by UV-Vis spectroscopy to monitor changes of the refractive index in the near vicinity of the metal surface and with Raman spectroscopy we study the different surface functional groups that may interact to form the bioconjugated system, and the evaluation of conjugate stability by bonding to cibacron blue agar spheres. Also, we characterized the shell thickness by TEM.

4.2. Design of Surface Chemistry of Gold Nanoparticles

In the design of bioconjugated nanosystems (nanoparticles and proteins) for their use as therapeutic agents, the stability is an important factor to consider since these conjugated systems must maintain its structure under harsh conditions, *e.g.*, the bloodstream or the environment in the living cells. In this work we present the conjugation of multibranched gold nanoparticles (MB-AuNPs) with bovine serum albumin (BSA) in order to exploit the primary physiological role of this protein for transport hydrophobic molecules through the bloodstream, and take advantage of the great potential of these spiky nanoparticles to obtain local electromagnetic field enhancement (hot-spots) due to local surface plasmon resonances (LSPR).

4.2.1. Stabilizers

In some of the methods of synthesis, the as synthesized NPs have capping molecules that, not always supports the temporal stability of NPs, in sense of shape and dispersion, in other cases, the capping molecules are not suitable for their applications, as the melting point or the biotoxicity of molecules, also cannot be soluble in the medium used for preparation of models, as organic solvents.[1] Therefore, ligand exchange reactions or surface modifications (conjugation) have been used for adapting the NPs to their application.

The conjugation of AuNPs with other molecules can be achieved by direct covalent linkage or non-covalent interactions. The most direct covalent approach is using strong Au-S bonds with organothiols, disulfides, and cysteine groups. Non-covalent interaction approaches use physisorption and electrostatic interactions of surface ionized ligands.[2]

For biological applications, AuNPs must be stable and thoroughly dispersed in aqueous media. The most common AuNPs have been synthesized with CTAB or citrate, the CTAB AuNPs have been shown to be toxic mostly for its positive charge. Thiol groups containing carboxylate or poly(ethylene oxide) units are commonly

incorporated in water-soluble, biocompatible gold nanoparticles, but relatively poor long-term stability of gold-sulfur bonds limits their biomedical and catalytic applications.[2] Alternative ligands of choice are polymers with polar groups such as poly(vinyl pyrrolidone) (PVP), poly(vinyl alcohol) (PVA), poly(acrylic acid) (PAA), and their copolymers. In the methods of synthesis called polyol methods, a random copolymer containing a vinyl pyrrolidone unit can be utilized for the synthesis of NPs. Secondary modification is also commonly employed when the surface functionality on AuNPs has activated groups such as carboxylates and hydroxyls. The secondary reaction on the surface is accomplished using chemical coupling, polymerization, electrostatic interaction, and selective interaction between biomolecules. The most well-established methods are coupling and esterification.[2]

For the conjugation of AuNPs with biological molecules, may be two possible approaches, the first involves the surface modification of prepared NPs using ligand exchange and secondary modification.[2] The second entails the use of biological materials as synthetic agents including reductants and surfactants. Biological materials such as enzymes and peptides, plant extracts, and fungi have been used for the reduction of metal ions and the formation of NPs. The biosynthetic method has the potential to be clean, non-toxic, and environmentally friendly, although, the exact mechanism for the NPs synthesis are not clear, cysteine rich, metal binding polypeptides, phytochelatins and metallothioneins have been relatively well characterized.

One of the important surface treatments is coating with other components, silica coating can enhance stability against aggregation and provide tuneable solubility in various solvents. Each NPs isolate by a silica shell provides a relatively homogeneous environment around the particle surface. The outer shell structure also hinders the aggregation of neighboring particles, even under harsh reaction conditions. Another way to generate stable NPs is through the use of polyethylene glycol (PEG) ligands. Although, this approach has limitations, because PEG is

uncharged, it has been challenging to engineer the desired electrostatic and hydrophobic interactions.[3]

The approach of interest for this thesis is the conjugation of NPs with proteins,[4] there are some reports of conjugation of AuNPs with bovine serum albumin (BSA) in order to improve the stability. The BSA has been chosen due to the biological relevance of albumin as the most abundant protein in blood plasma.

4.2.2. Selectivity

Nanoparticle delivery of anticancer drugs to tumor tissues can be achieved by either passive or active targeting. The passive targeting takes advantage of the inherent size of NPs and the unique properties of tumor vasculature, such as the enhanced permeability and retention effect.[5] Angiogenic blood vessels in tumor tissues, unlike those in normal tissues, have gaps as large as 600 to 800 nm between adjacent endothelial cells. This defective vascular architecture coupled with poor lymphatic drainage induces the permeability and retention, which allow NPs to extravasate through these gaps into extravascular spaces and accumulate inside tumor tissues (Fig. 4.1).[5,6]
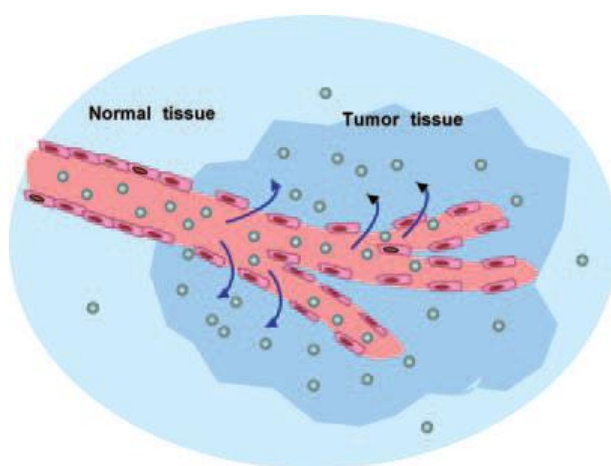
Figure 4.1. Passive tumor targeting with nanoparticle drugs. Long-circulating therapeutic nanoparticles accumulate passively in solid tumor tissue by the enhanced permeability and retention effect.

Dramatic increases in tumor drug accumulation, usually of 10-fold or greater, can be achieved when a drug is delivered by a NP rather than as a free drug. However, the localization of NPs within the tumor is not homogeneous. An alternative strategy to overcome these limitations is to conjugate a targeting ligand or an antibody to NPs. By incorporating a targeting molecule that specifically binds an antigen or receptor that is either uniquely expressed or overexpressed on the tumor cell surface, the ligand-targeted approach is expected to selectively deliver drugs to tumor tissues with greater efficiency (Fig. 4.2).[5]

Figure 4.2.   Internalization of nanoparticles via receptor-mediated endocytosis. Nanoparticle-conjugated tumor-specific ligand/antibodies bind to surface receptors, triggering nanoparticle internalization through an endosome-dependent mechanism. As the interior of the endosome becomes more acidic, drugs are released from the nanoparticle into the cytoplasm.

4.3. Targeting the Serum Albumin Receptor in Endothelial Cancer Cells
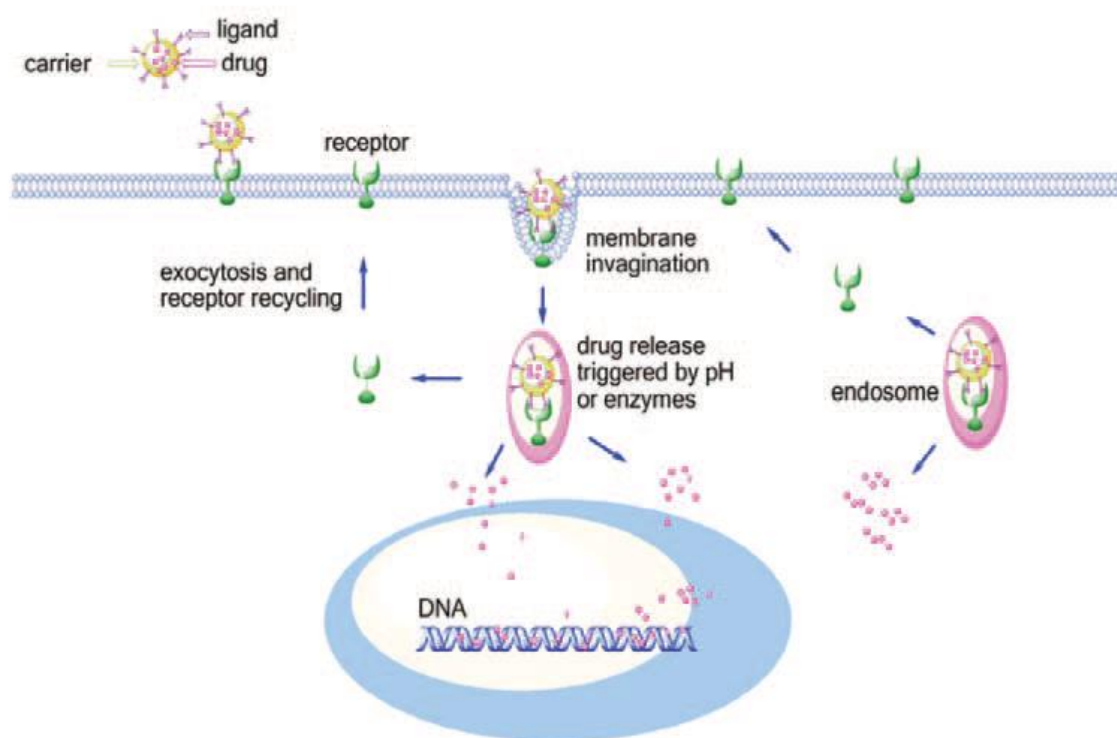
Selection of the appropriate receptor or antigen on cancer cells is crucial for the optimal design of vehicle NPs. The ideal targets are those that are abundantly and uniquely expressed on tumor cells, but have negligible or low expression on normal cells.[5]

Recent research during the last decade have proved that in tumor external environment there are albumin deposits,[7,8] and is well known that inside the human body, albumin is the main carrier of insoluble molecules like vitamins, hormones and fatty acids.

Endothelial cells express the specific receptor (gp60) to albumin, called albondin. This receptor increases the albumin's absorption probability and its releasing at sub endothelial space after been directed throw the endothelium via transcytosis.[9] Once at the tumors interstice, the albumin accumulation is facilitated by SPARC, a secreted glycoprotein acidic rich in cysteine, which presents albumin affinity and its homologue to gp60. The increase concentration of SPARC in tumors external space it is due to characteristic modulation of extracellular proliferation and migration of cells. Almost all the solid tumors difficult to treat secret SPARC, including tumors like mama, lung, pancreas, ovary, brain, stomach, esophagus and cervix.[10,11]

On the other hand, when NPs go into the blood stream, they are covered with a protein corona, which forms from the nonspecific interactions between the NPs and the plasma proteins.[12] This protein corona modifies the uptake of the nanoparticle by cells and organs. Thus, one strategy for optimizing therapeutic NPs is creating a crown of albumin on the surface of the NP (see Fig. 4.3), to reduce their potential toxicity due to the chemistry of the surface and inhibit the adsorption of other molecules that can activate plasma complementary signals, a fact that would influence both the specificity of the NP properties, and affect or minimize the time

circulating in the blood.[12] In the area of medicine applications, gold NPs (AuNPs) have been extensively studied and applied in medical trials since these systems can be used as contrast agents, for hyperthermic therapy and delivery of drugs.[13]
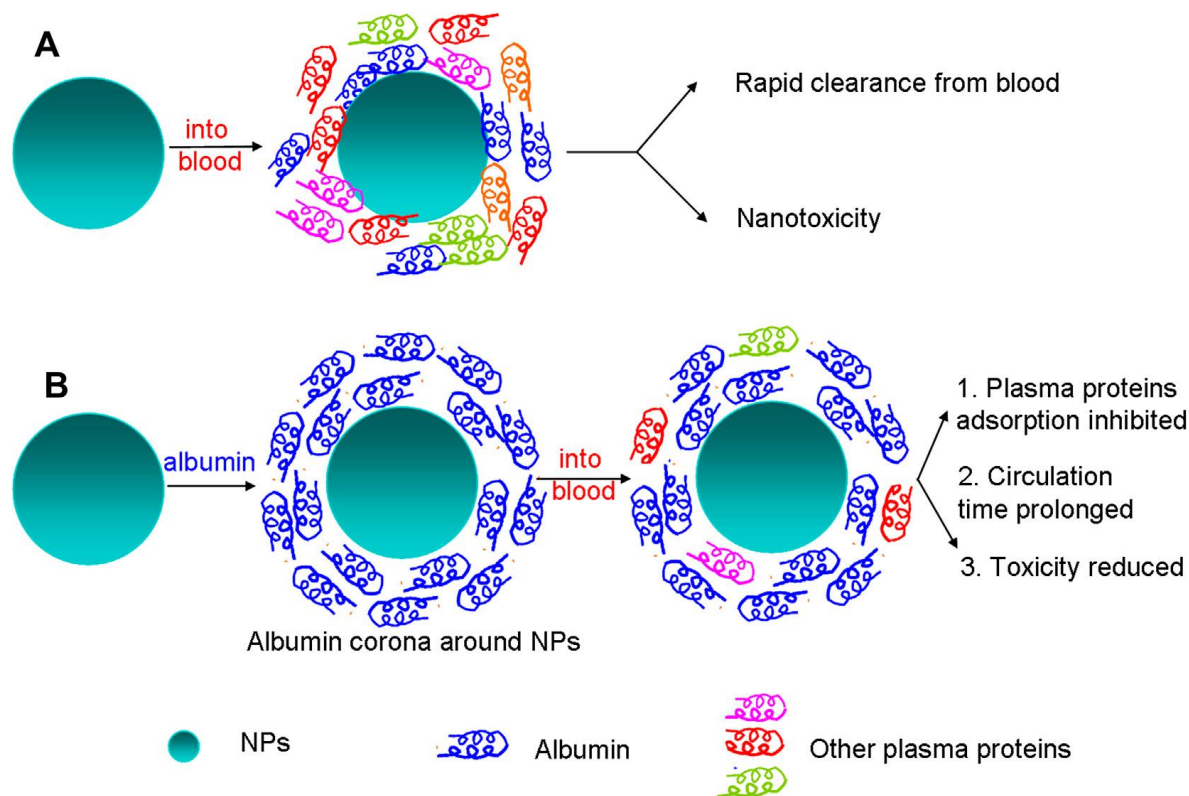
Figure 4.3. Schematics of the biological responses to NPs in the absence or presence of albumin corona. **a)** Various plasma proteins are adsorbed onto the naked NPs immediately after its entry into the blood, resulting in the rapid clearance and toxicity. b) The preformed albumin corona around NPs is able to inhibit the plasma proteins adsorption and thus prolong the circulation time and reduce the toxicity of NPs.[12]

4.3.1. Serum Albumin Conjugates

Peptides and proteins are composed of amino acids polymerized together through the formation of peptide (amide) bonds. Each amino acid is composed of an amino group and a carbocyl group bound to a central carbon, termed de α-carbon. Also bound to the α-carbon is a hydrogen atom and a side chain unique to each amino acid (Fig. 4.4).There are 20 common amino acids found throughout nature, each

containing an identifying side chain of particular chemical structure, charge hydrogen bonding capability, hydrophilicity (or hydrophobicity), and reactivity. The side chains do not participate in polypeptide formation and are thus free to interact and react with their environment.[14] Those side chains are used to conjugate the proteins, and can be conjugated with organic molecules (fluorescent dyes), drugs[15] and metallic clusters or NPs.[16]
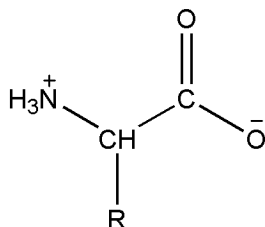
Figure 4.4.   Individual amino acids consist of a primary (α) amine, a carboxylic acid group, and a unique side chain structure (R). At physiological pH the amine is protonated and bears a positive charge, while the carboxylate is ionized and possesses a negative charge.

The peptide bonded polymer that forms the backbone of polypeptide structure is called de α-chain.[14] The peptide bonds of the α-chain are rigid planar units formed by the reaction of the α-amino group of one amino acid with de α-carboxyl group of another (Fig. 4.5). The peptide bond possesses no rotational freedom due to the partial double bond character of the carbonyl-amino amide bond. The bonds around de α-carbon atom, however, are true single bonds with considerable freedom of movement.[14] The sequence and properties of the amino acid constituents determine protein structure, reactivity, and function.

Figure 4.5.   Rigid peptide bonds link amino acid residues together to forma proteins. Other bonds within the polypeptide structure may exhibit considerable freedom of rotation.

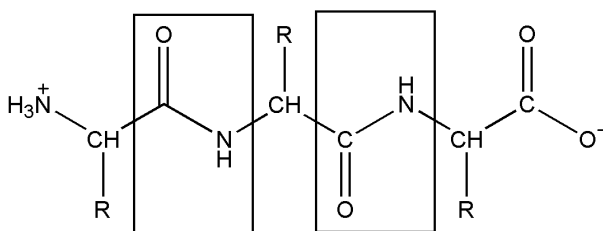All the aliphatic and aromatic hydrophobic residues often are located at the interior of protein molecules or in areas that interact with other nonpolar structures such as lipids. They usually form the hydrophobic core of proteins and are not readily accessible to water or other hydrophilic molecules.

Protein molecules may contain up to nine amino acids that are readily at their side chains: aspartic acid, glutamic acid, lysine, arginine, cysteine, histidine, tyrosine, methionine, and tryptophan. These nine residues contain eight principal functional groups with sufficient reactivity for modification reactions: primary amines, carboxylates, sulfhydryls (or disulfides), thioethers, imidazolyls, guanidinyl groups, and phenolic and indolyl rings. All of these side chain functional groups in addition to the N-terminal α-amino and the C-terminal α-carboxylate form the full complement of polypeptide reactivity within proteins.[14]

Phenylalanine and tryptophan contain aromatic side chains that, like the aliphatic amino acids, are also relatively nonpolar and hydrophobic (Fig. 4.6). Phenylalanine is unreactive toward common derivatizing reagents, whereas the indolyl ring of tryptophan is quite reactive, if it is accessible. The presence of tryptophan in a protein contributes more to its total absorption at 275-280 nm on a mole-per-mole basis than any other amino acid. The phenylalanine content, however, adds very little to the overall absorbance in this range.
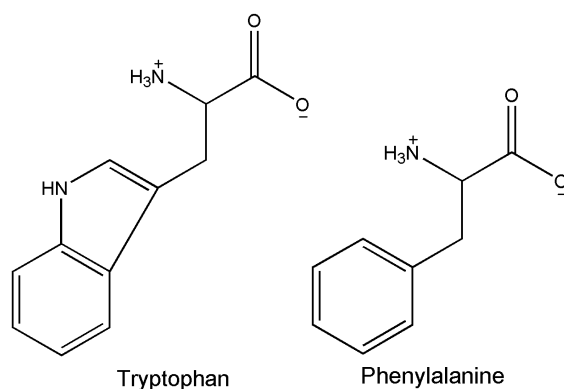

Tryptophan   Phenylalanine

Figure 4.6.   The two nonpolar aromatic amino acids.

The most significant amino acids for modification and conjugation purposes are the ones containing ionizable side chains: aspartic acid, glutamic acid, lysine, arginine, cysteine, histidine, and tyrosine (Fig. 4.7). In their unprotonated state, each of these side chains can be a potent nucleophile to engage in addition reactions. Carboxylate groups in proteins may be derivatized through the use of amide bond forming agents or through active ester or reactive carbonyl intermediates. The carboxylate actually becomes the acylating agent to the modifying group. Amine containing nucleophiles can couple to an activated carboxylate to give amide derivatives. Hydrazide compounds react in a manner similar to that of amines. Sulfhydryls, while reactive and resulting in a thioester linkage, form unstable derivatives that hydrolyze in aqueous solutions.

Lysine, arginine, and histidine have ionizable amine containing side chains that, along with the N-terminal α-amine, contribute to a protein's overall net positive charge. Lysine contains a straight four-carbon chain terminating in a primary amine group. The ε-amine of lysine differs in pK_a from the primary α-amines by having a slightly higher ionization point (pK_a of 9.3-9.5 for lysine versus pK_a of 7.6-8.0 for α-amines). At pH values lower that the pK_a of these groups, the amines are generally protonated and possess a positive charge. At pH values greater that the pK_a, the amines are unprotonated and contributed to net charge.
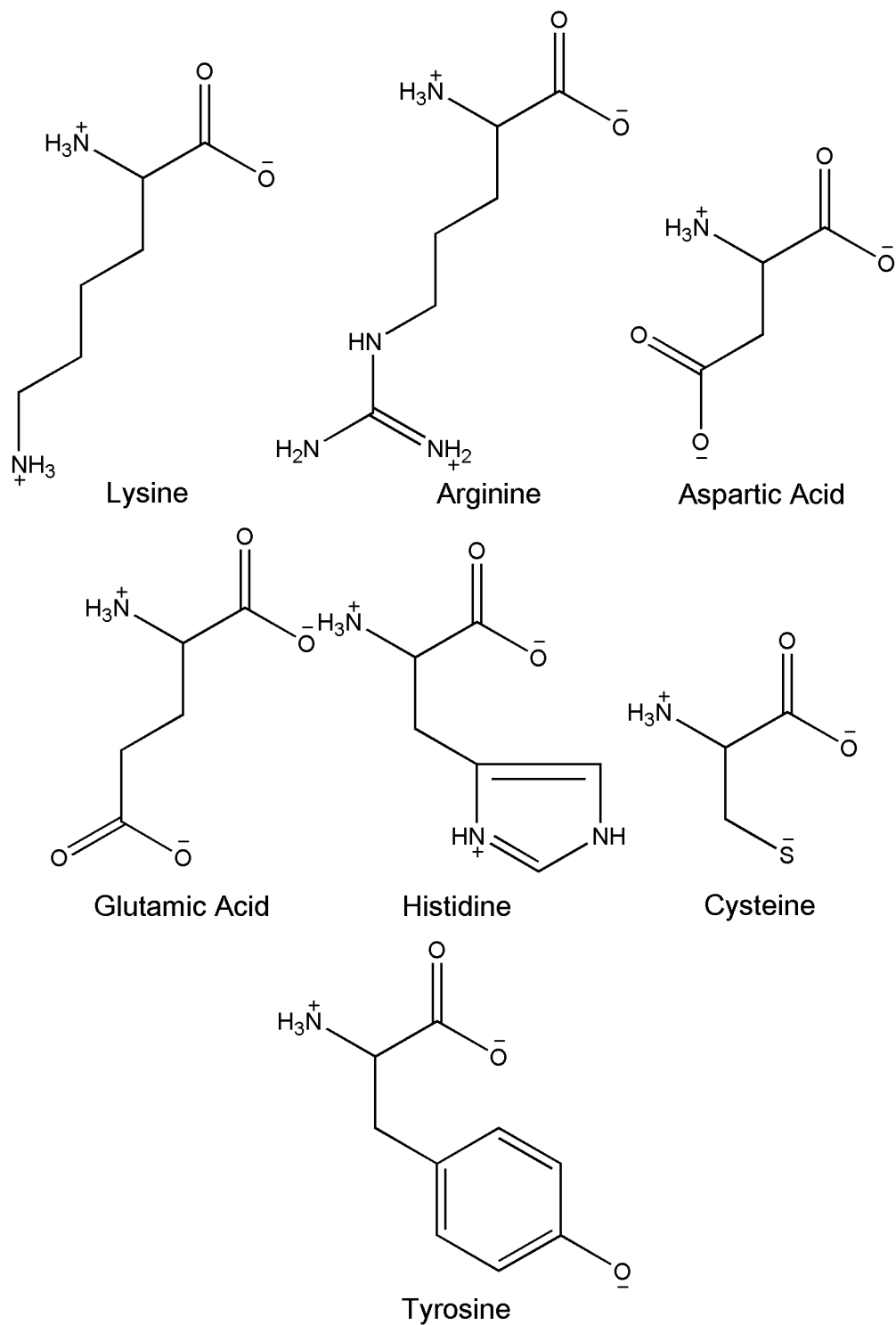
Figure 4.7. The ionizable amino acids possess some of the most important side-chain functional groups for bioconjugated applications.

The side chain of histidine is an imidazole ring that is potentially protonated at slightly acid pH values (pK$_a$ 6.7-7.1). Thus, at physiological pH, these residues contribute to the overall net positive charge of an intact protein molecule. The amine-containing side chains in lysine, arginine, and histidine typically are exposed on the surface of proteins and can be derivatized easily. The most important reactions that can occur with these residues are alkylation and acylation. In alkylation, an active alkyl group is transferred to the amine nucleophile with loss of one hydrogen. In acylation, an active carbonyl group undergoes addition to the amine.[14]

Cysteine is the only amino acid containing a sulfhydryl group. At physiological pH, this residue is normally protonated and possesses no charge. Ionization only occurs at high pH (pK$_a$ 8.8-9.1) and results in a negatively charged thiolate residue. The most important reaction of cysteine groups in proteins is the formation of disulfide crosslinks with another cysteine molecule. Cysteine disulfides (called cystine residues) often are key points in stabilizing protein structure and conformation. They frequently occur between polypeptide subunits, creating a covalent linkage to hold two chains together.[14] Cysteine and cystine groups are relatively hydrophobic and usually can be found within the core of a protein. For this reason, it is often difficult to reduce fully the disulfides of large proteins without a deforming agent present to open up the inner structure and make them accessible. Derivatization of the side chain sulfhydryl of cysteine is one of the most important reactions of modification and conjugation techniques for proteins.[14] Has been reported that the cysteine residues are likely to interact with AgNPs via direct chemical bonding and provide steric stabilization due to the bulky protein molecules. Additionally, metal NPs, such as silver and gold are likely to interact with amine groups of proteins due to its large complexation for noble metal amines.[17]

4.3.1.1. Conjugation to Gold Nanoparticles

Human serum albumin (HSA) has a molecular weight of ~64-66 kDa and a concentration on blood serum of ~35-50 mg/mL,[9] it has the property to improve the

173

pharmacokinetic profile of meds of low molecular weight and peptides of therapeutic importance due its labeling to specific antibodies situated on swollen tissue o malignant cells. In the present is been used in clinical trials as a vehicle of therapeutic agents that threat several diseases as cancer, rheumatoid arthritis, diabetes and hepatitis (Table 4.1).[9]

Table 4.1. Albumin therapeutic agents			
Product	Diseases	Therapeutic agent	Clinical studies
Victoza	Diabetes	Derivatives of myristic acid	Approved in 2004
Abraxane®	Metastatic breast cancer	Paclitaxel	Approved in 2005
INNO-206	Sarcoma	Doxorubicin	Phase II
ATN-103, Ozoralizumab	Rheumatoid arthritis	Neutralizes TNF-α	Phase II
MTX-HSA	Renal cell carcinoma	Methotrexate	Phase II
MM-111	Inhibition of cancer cell proliferation	Bonding antibodies to ErbB2 y ErbB3	Phase II
Albuferon	C Hepatitis	Interferon-α-2b	Phase III
Compiled information from the reference [9]			

Along with increase interest in AuNPs as therapeutic agents, have been proposed several approaches to stabilized the AuNPs in biological environment, and to improve its biocompatibility. In this chapter we revised the stabilization throw conjugation to albumin. Previously, AuNPs have been conjugated with bovine serum albumin (BSA), the results concluded that BSA binding to Au surfaces occurs by an electrostatic mechanism.[18] Also, a greater degree of BSA association with the NPs was suggested, as the formation of multilayers. The studies reveal that nonspecific binding to self-assembled monolayers is favored in the following order: hydrophobic

> COO⁻ > NH₃⁺ > OH > ethylene glycol. The preferential binding of BSA to negatively charge surfaces is somewhat puzzling because the isoelectric point of BSA is 4.6, and therefore BSA is negatively charged at pH 7.0, and here is where the protonated lysine residues are important to notice, because these residues can have electrostatic interactions with negatively charged moieties.[19]

Due to the structural and functional similarity of human serum albumin (HSA) with bovine serum albumin (BSA), for the development of this project we have chosen to obtain the bioconjugated complex of the BSA and AuNPs, in order to direct them to endothelial cells and hence to the malignant tumors.

Basic monitoring of NP conjugation to the BSA has been reported as the UV-Vis spectral shift, and in some cases also the broadening of the absorption spectrum at pH 7 (see Fig. 4.8).[19,20]
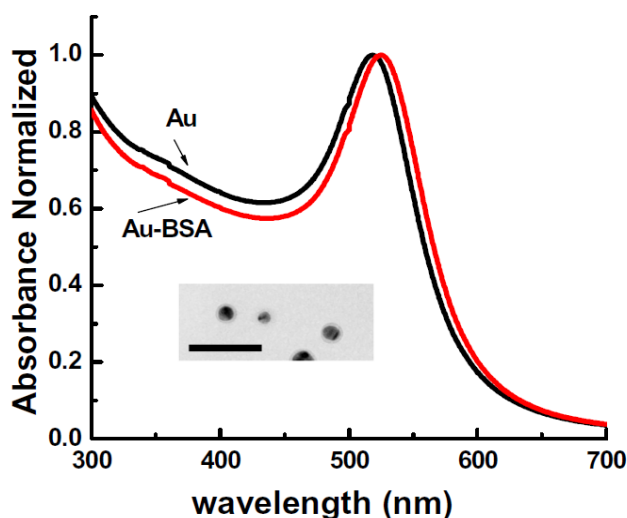

Figure 4.8.   UV-VIS spectra of colloidal AuNPs (black line) and BSA-AuNPs (red line). Inset: TEM image of BSA-AuNPs, scale bar is 50 nm.[20]

Far UV Absorbance

The peptide bond absorbs strongly in the far UV with a maximum about 190 nm, and is because of this very strong absorption that this method has been used in protein

determination. Various side chains, including those of tryptophan (Trp), phenylalanine (Phe), tyrosine (Tyr), histidine (His), cysteine (Cys), methionine (Met) and arginine (Arg), in the descending order, make contributions to the absorbance at 205 nm (A_{205}).[21]

Because of the difficulties caused by absorption by oxygen and the low output of conventional spectrophotometers at this wavelength, measurements are more conveniently made at 205 nm, where the absorbance is about half that at 190 nm. Most proteins have extinction coefficients at 205 nm for a 1 mg/mL solution of 30-35 and between 20 and 24 at 210 nm.[21]

The advantages of this method include simplicity and sensitivity, the sample is recoverable and in addition, there is little variation in response between different proteins, permitting near-absolute determination of protein. Disadvantages of this method include the necessity for accurate calibration of the spectrophotometer in the far UV, and the fact that many buffers and other components, such as heme or pyridoxal groups, absorb strongly in this region.[21]

Near UV Absorbance (280nm)

Quantitation of the amount of protein in a solution is possible in a simple spectrometer. Absorption of radiation in the near UV by proteins depends on the Tyr and Trp content, and a very small contribution of Phe and disulfide bonds. Therefore, the A_{280} varies greatly between different proteins (for a 1 mg/mL solution most values are in the range 0.5-1.5). The extinction of nucleic acid in the 280 nm region may be as much as 10 times that of protein at their same wavelength, and hence, a few percent of nucleic acid can greatly influence the absorption. The advantages of this method are that it is simple, and the sample is recoverable; the disadvantages, include interference from other chromophores, and the specific absorption value for a given protein must be determined.[21]

For proceed with the quantitation, the protein solution must be diluted in the buffer to a concentration that is well within the accurate range of the instrument. Measure A_{280} of the protein solution, using quartz cuvets, microcuvets or microplate. The value obtained will depend on the path length of the cuvet. Then, it must be adjusted by the appropriate factor with the Beer-Lambert law states that:

$$A = \varepsilon\, c\, l$$ Eq. 4.1

where ε = extinction coefficient, c = concentration in mol/L and l = optical path length in cm. Therefore, if ε is known, measurement of A gives the concentration directly; ε is normally quoted for a 1 cm path length. The actual value of UV absorbance for a given protein must be calculated form the amino acid composition, which can be determined by amino acid analysis. The UV absorbance for a protein is then calculated according to the following formula:

$$A_{280}(1\,mg/mL) = \left(5690_{n_w} + 1280_{n_y} + 120_{n_c}\right)/M$$ Eq. 4.2

where n_w, n_y, and n_c are the numbers of Trp, Tyr, and Cys residues in the polypeptide of mass M and 5690, 1280 and 120 are the respective extinction coefficients for these residues.[21]

It is best to measure absorbance in the range 0.05-1.0 (between 10 and 90% of the incident radiation). At around 0.3 absorbance (50% absorption), the accuracy is greatest. Bovine serum albumin (BSA) is frequently used as a protein standard; 1 mg/mL has an A_{280} of 0.66. The presence of non-protein chromophores can increase A_{280}. If nucleic acids are present (which absorb strongly at 260 nm), the following formula can be applied. This gives an accurate estimate of the protein content by removing the contribution to absorbance by nucleotides at A_{280} nm, by measuring the A_{260} which is largely owing to the latter.[21]

$$Protein(mg/mL) = 1.55A_{280} - 0.76A_{260}$$ Eq. 4.3

It has been reported that the conjugation mechanism on citrate stabilized NPs is accomplished by non-specific interactions of the 60 lysine residues that may have electrostatic interaction with a negatively charged medium. Other studies report that the protein loses its secondary structure portion when conjugated at the border of the surface of the NP, but also it has been shown that after the conjugation much of the structure of the protein is conserved and presenting no loss of their function.

The Raman scattering spectroscopy have been used to obtain information on structures and the properties of molecules from their vibrational transitions. The Raman shift is a two-photon event, and the property involved is the change in the polarizability of a molecule with respect to its vibrational movement. The interaction of the incident radiation polarizability creates an induced dipole moment in the molecule, and the radiation emitted by this process contains the Raman shift observed. The light scattered by the dipole molecules consist of both Rayleigh and Raman scattering. Rayleigh scattering corresponds to the scattered light at the frequency of the incident radiation, while the Raman radiation shifts in frequency (and therefore in energy), with respect to the frequency of the incident radiation by means of the vibrational energy that is gained or lost by the molecule. If the molecule gains vibrational energy, this scattering is called Raman-Stokes, whereas if the molecule loses vibrational energy, the process is known as Raman anti-Stokes scattering (Fig. 4.9).[22]
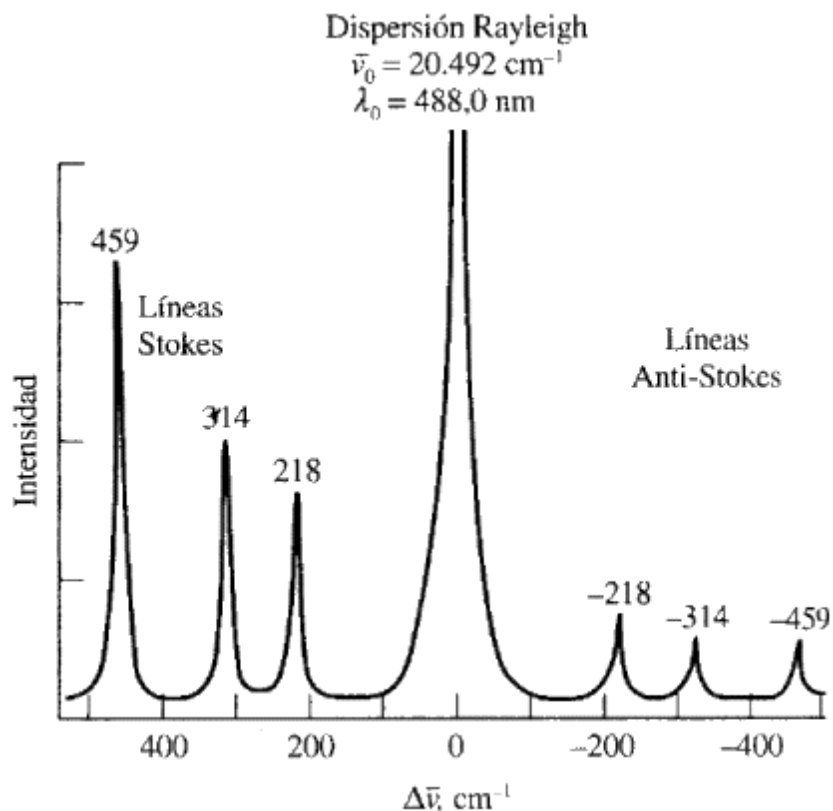
Figure 4.9. Raman spectra of carbon tetrachloride (CCl_4), irradiated with laser of λ_0= 488 nm o $\bar{v}_0$ = 20.492 cm^{-1}. The peaks number correspond to Raman shift $\Delta\bar{v} = (\bar{v}_s - \bar{\mu}_0)$ cm^{-1}.[23]

Vibrational spectroscopy contributes to the study of structures and the physicochemical properties of conjugated systems. Stability studies of proteins are based on the comparison between the native conformational and denatured states. In the natural state, the conformation of the protein changes upon interaction with other molecules, so there are different conformations with relevant functionality. The different conformations possess intrinsic stabilities as they differ in their Gibbs free energy. Even when there is not a significant conformational change in the native state, there are local events such as changes in interactions that result in sub-states by the energy differences between previous intramolecular interactions and the new formed.

The formation of stable complexes between proteins and AuNPs can be accomplished by different mechanisms and combinations: a) the electronic charge attraction between the gold nanoparticles and the charges of the different protein residues, b) the adsorption phenomenon involving the formation of hydrophobic environment at the interface of the conjugate, and c) the affinity of gold to covalently bind with free sulfhydryl groups (Fig. 4.10).
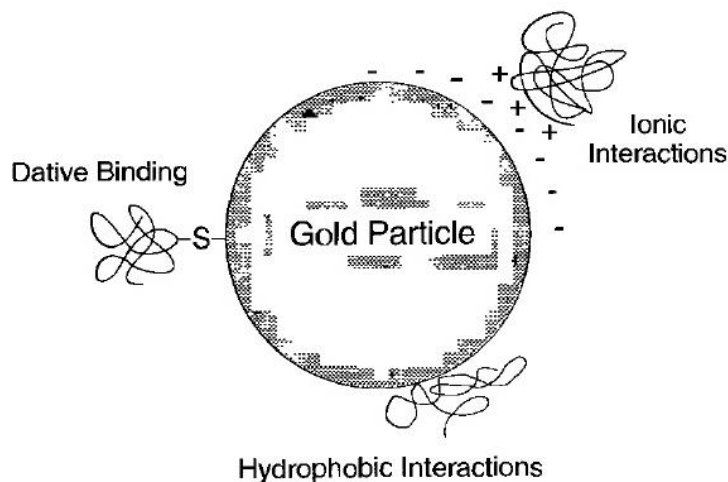

Figure 4.10.   Possible interactions between proteins and the AuNPs surface.

In an aqueous environment proteins fold to expose their hydrophilic part by intramolecular interactions of different chemical groups, and hence the disappearance of other interactions.
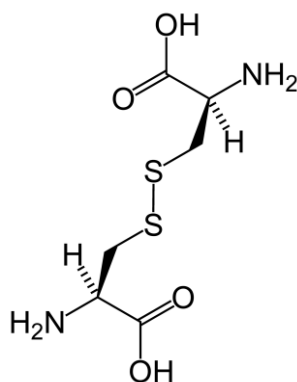

Figure 4.11.   Cysteine arises by forming a disulfide bridge at the junction of two cysteines.

The formation and breaking of disulfide bonds (S-S) that arise by oxidation of two cysteines (Fig. 4.11), plays an important role in the stability of protein structure.[17] Disulfide bridges are located between the segments of the helixes, *i.e.*; they are part of the tertiary structure of proteins and are responsible of their folding.[18] Serum albumin has 17 disulfide bridges or bonds and a cysteine residue.

In Raman spectroscopy the band of S-S bond vibration appears near the 490 cm^{-1} and arises from a rotation between C-C and S-C bonds.[17] It is expected that if this vibration is not present, the state of the protein is denatured; but in the conjugates, it is considered the possibility that the thiol group from the cysteine residues involved previously in disulfide bonds, are now interacting with the surface of the AuNPs.[19]

Because the amino acids composition, the vibrations most commonly present in a Raman spectrum are characteristic of the amides, C-O and N-H bond, which are similar to those present in secondary amides. The position of the *amide bands I, II and III* is affected by the conformational state of the protein, in particular by changes in the secondary structure: spiral form (α-helix), extended form (β) and random form.[17] The band *amide II* (1200-1320 cm-1) is a shift towards lower frequencies in the protein denatured state.[20] Because the signal of the *amide II* band has low intensity and the signal from the amide I for the conformation of helix- α can be inhibited by absorption of water,[17] is common to choose for analysis the signals from the *amide III* band. This band is formed by a superposition of stretching signals of the C-N bond and in-plane bending of the NH bond. The α-helix conformation appears in the 1260-1300 cm^{-1} range, the β-conformation at 1230 to 1235 cm^{-1} and the random conformation appears near the 1240-1250 cm^{-1} band. It has been estimated that the BSA contains relative amounts of alpha and random conformation in a percentage of 55-60% and 45-40%, respectively,[21,22] which can be detected by the amide band peaks corresponding to the random shape and not necessarily indicating protein denaturation.

After solvation of the protein in water, these molecules penetrate the interior of the protein and induce a conformation with hydrophobic regions, because the side chains of hydrocarbons are approaching one another and some of the polypeptide chains are forced to the β-conformation.[21] An increase in the band intensity at 1247 cm^{-1} is indicative of an increase in the percentage of disordered structure.

Other vibrations indicate the presence of α-helical conformation, the band at 941 cm^{-1} due to stretching vibration of the bond between C-C atoms, and its intensity indicates a high percentage of this protein conformation, and characteristically stretching vibration of the S-S bond at frequency 500-515 cm^{-1}, for the gauche-gauche-gauche configuration of BSA.[18]

The six disulfide bridges located between protein domains, restrict the compact arrangement between subdomains, and are responsible in conformational state transitions (α→β), as well as the isomerization of domains I and II without losing the helix conformation, and also for the unfolding of domain III in the cooperative process.[18] The largest contribution to the intensity of the stretching vibration in the range 650-750 cm^{-1}, is provided by the C-S bond vibration of the cysteine residues, since there are only three methionine residues per BSA molecule. Also it has to be considered that vibrations of the C-S bond do not show sharp, defined bands in the spectrum.

4.4. Experimental Procedure of Conjugation with Bovine Serum Albumin

Materials and Methods

Deionized water was used for all experiments. The bovine serum albumin (BSA), HEPES and cibacron blue CL6 was obtained from Sigma Aldrich, the salts used for phosphate buffers were obtained from Baker, K_2HPO_4, KH_2PO_4, Na_2HPO_4 and NaH_2PO_4. All reagents were used as received without further treatment of purification. All glassware was cleaned with *aqua regia* (HCl:HNO3, 3:1), rinsed with plenty deionized water and sterilized before use. The UV-Vis spectra was acquired on a Cary 60 UV-Vis-NIR spectrophotometer and fluorescence spectra on a Cary Eclipse at excited λ = 280 nm, both at ambient temperature. The electron micrographs were acquired in the transmission electron microscopes (Jeol JSPM-5200 and Tecnai F30), the scanning electron micrographs in a Quanta SEM. The z-potential and hydrodynamic diameter were determined by dynamic light dispersion Nano Zetratrac. The protein quantification was acquired in a 2 μL microplate UV-Vis spectromether, Epoch from BioTek. The Raman spectra was acquired in the region 100-2000 cm^{-1} on a two lasers (534, 633 nm, the last was used) equipped Renishaw spectrophotometer, the spectra were processed by deconvolution techniques, applying a Lorentzian function, using the QtiPlot software.

Spectroscopic Analysis of Conjugated. MB-AuNPs freshly synthesized were centrifuged and washed three times and finally re suspended at the same volume, in HEPES buffer 25 Mm with BSA concentration of 10 mg/mL. For UV-Vis measurements, samples were left to rest overnight and the spectra were capture before and after the conjugation. For Raman analysis, conjugated samples were washed three times by centrifugation and de concentrated of NPs was deposited in a clean cover glass and left to dry at ambient temperature avoiding dust contamination. Also were acquired Raman spectra of MB-AuNPs and solutions of

HEPES and BSA. For fluorescence curves, the solutions for conjugation were mixed at the moment prior the measurements.

Spectrometry Quantification of Protein. For calibration curves, HEPES buffer solution at 25 mM and pH 7.4 was used to prepare solutions with BSA concentration of 0.2 to 10 mg/mL at ambient temperature. For the quantification of conjugated protein, MB-AuNPs freshly synthesized were centrifuged and washed three times and finally re suspended in HEPES buffer 25 Mm at the same volume, then an increase concentration of BSA was added from 0.2 to 10 mg/mL and left to rest overnight. Later, the samples were washed three times by centrifugation and re suspended. The absorbance at 280 nm was acquired with the multi plate microreader in triplicate for condition.

Analysis of efficacy of conjugated MB-AuNPs@BSA throw interaction of conjugated BSA with cibacron blue. For this assay we use, spheres of blue sepharose CL-6B of 45-165 µm and with an albumin bond capability of 5mg/mL in phosphate buffers 0.1M, pH 7.0 were used. Shortly, 100 mg of dry frozen CL-6B were hydrated with 0.4 mL of Milli Q water, after 30 min were washed in a sintered glass filter with 20 ml of deionized water, finally were re suspended in 0.4 mL of phosphate buffer 1x a pH 7.4. For the assays with MB-AuNPs@BSA, a ¼ dilution of CL-6B was used for optical microscopy analysis and colloids of 5.2×10^9 NPs/mL, the test with BSA only was carried out with a solution of 0.2 mg/mL of BSA. The samples analyzed by SEM, were prepared with a 1/8 dilution of CL-6B and the same NPs concentration. In the cases of samples of CL-6B mixed with MB-AuNPs, after 5 min of the mix, were washed three times with deionized water. And then, a drop of 20 µL was deposited on an aluminum pin and left to dry. Before the low-vacuum SEM observation, a layer of carbon was deposited on the pins

4.5. Assembly of Results and Discussion

First characterization of the conjugated nanoparticles was the behavior or the localized surface plasmon resonance (LSPR), the absorbance spectra on the Fig. 4.12 show a 7 nm shift of conjugated spectra against the MB-AuNPs spectra. The shift indicates a change in dielectric constant of the nanoparticle surrounding media. In addition, has to be noticed a wider absorption band. Both changes may indicate a possible conjugation of the protein to the nanoparticle surface.
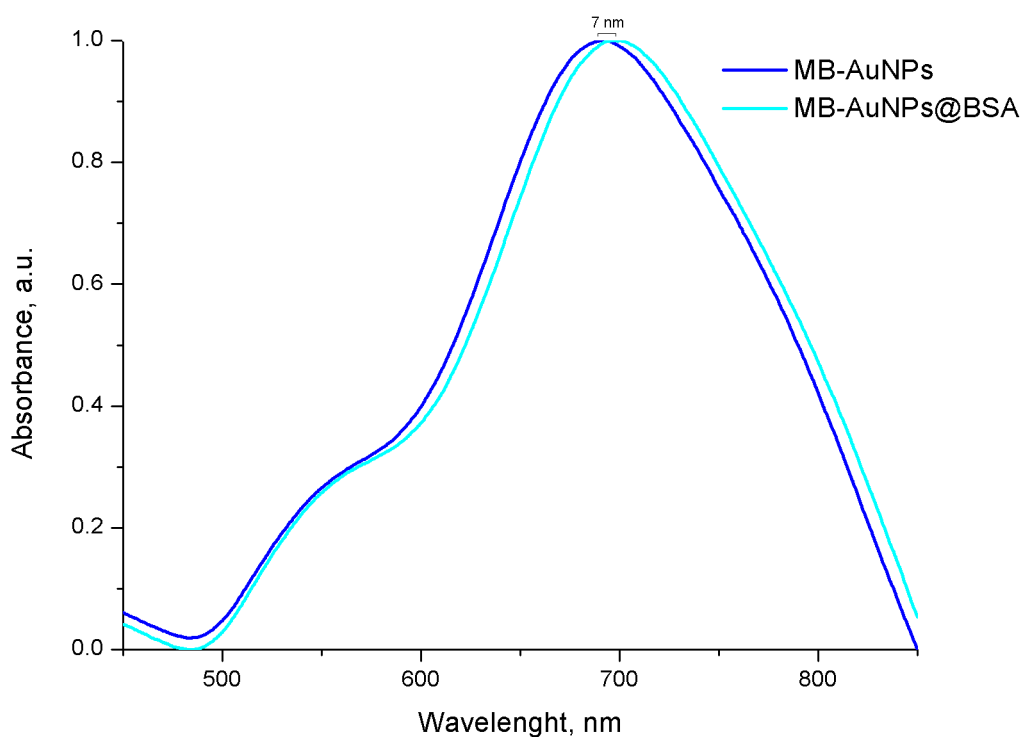
Figure 4.12. UV-Vis spectra of MB-AuNPs and MB-AuNPs@BSA.

For a better analysis of the surrounding area of the MB-AuNPs, samples were analyzed by TEM microscopy before and after the addition of BSA (Fig. 4.13). In the micrographs of albumin samples, a uniform protection of lower contrast is observed (Fig. 4.14); also, at higher magnification a thinner amorphous component was

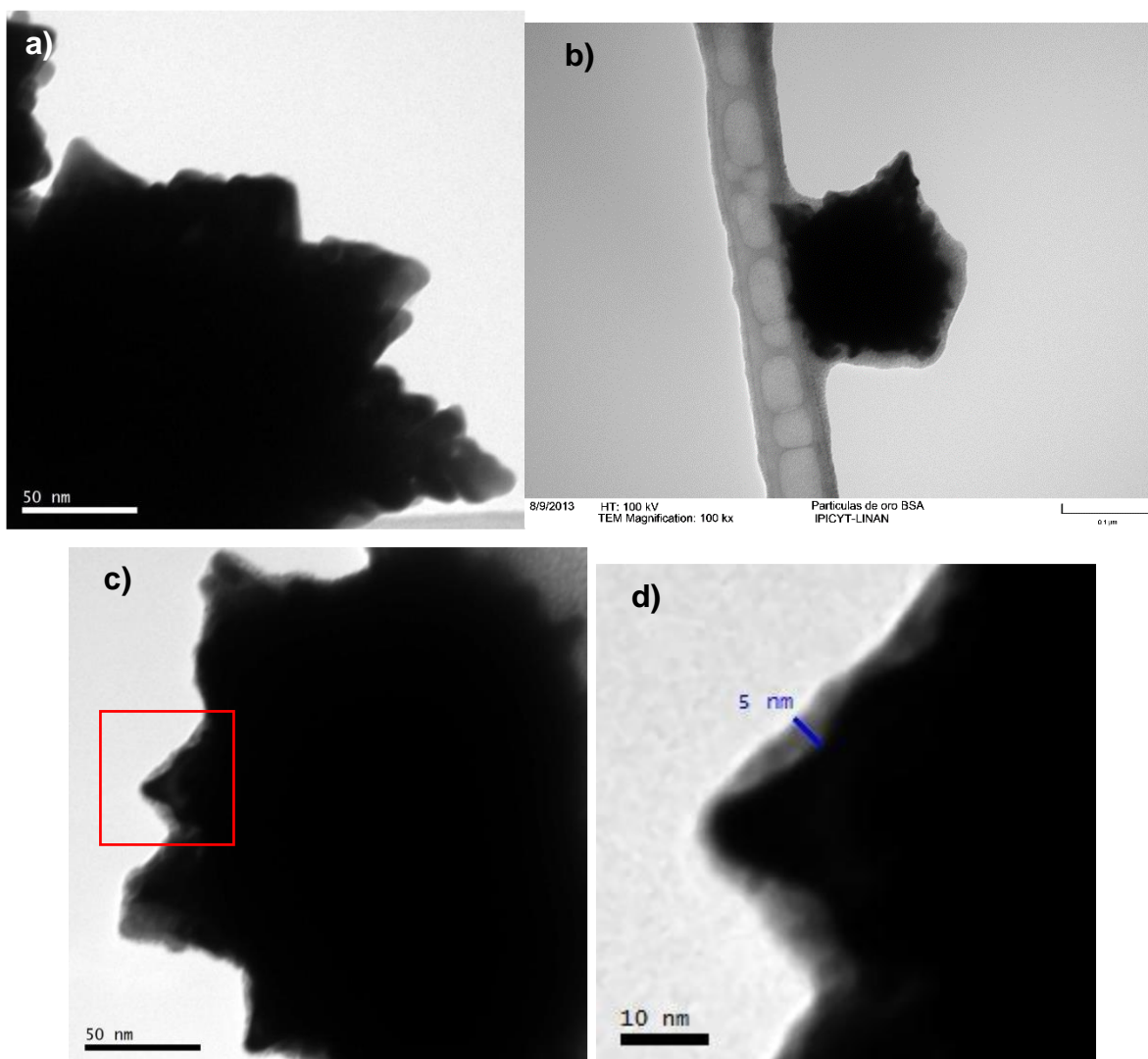observed. There is reported that a layer of HEPES covering a NPs can have a 1.5 nm of thickness.[24]

Figure 4.13. TEM micrographs of MB-AuNPs@BSA **a)** without staining, **b),c)** with positive staining wit uranyl acetate and **d)** the corresponding magnification of red square in **c)**.

Due to the difficulties of preparing this type of samples for TEM analysis, we considered an unreliable technique to ensure de conjugated formation. However, by STEM analysis of no staining samples, an amorphous material surrounding the crystal structure of NPs was observed (Fig. 4.14). Then we have a consistent layer

of amorphous material along the NPs, but at this point we do not know if corresponds to the HEPES layer from the synthesis of NPs or to the protein.
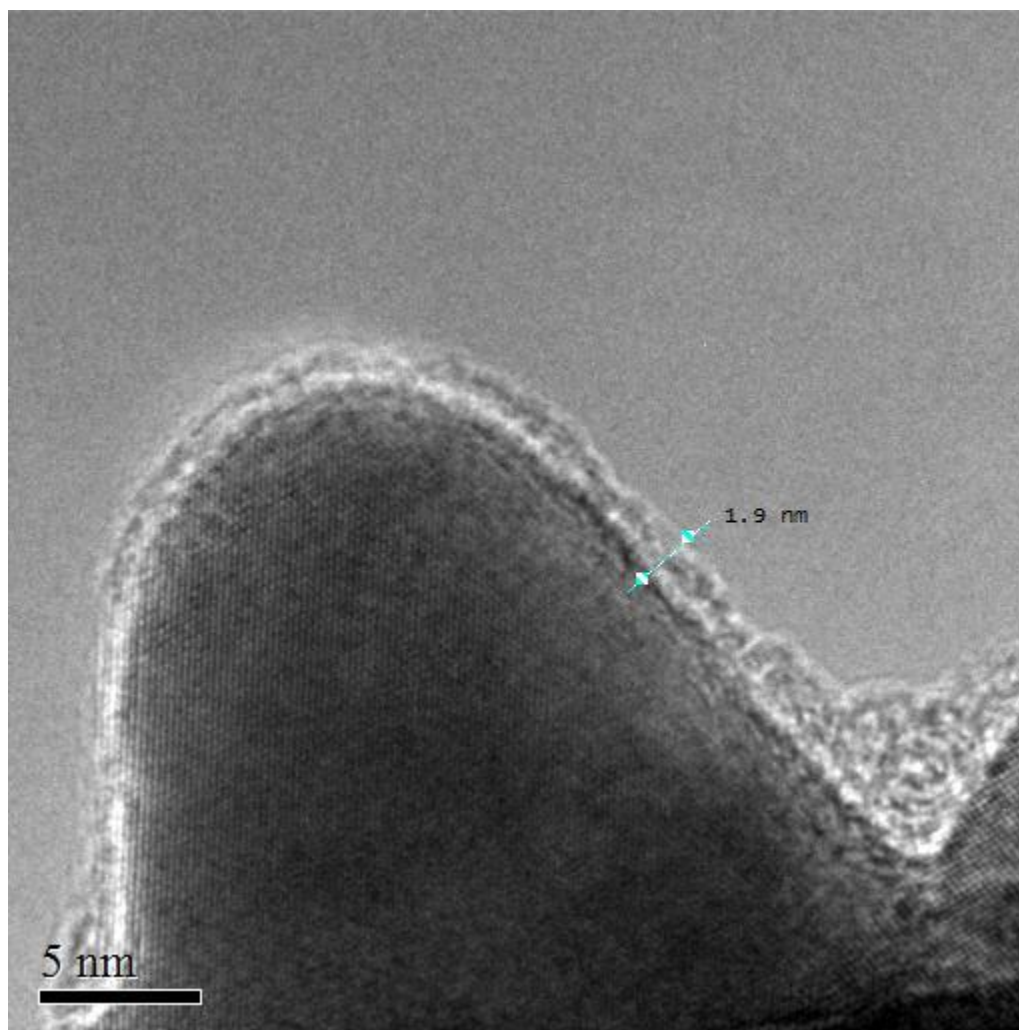

Figure 4.14. STEM micrograph of MB-AuNPs@BSA.

It has been reported and inhibition of fluorescence signal from tryptophan groups from the albumin, due to an interaction of the residues with the NPs surface. Also, a shift in the emission band can be observed if the is a conformational change of the protein structure, with may indicate hydrophobic areas in the residue surroundings due to conjugation.

Then, we carried out fluorescence analysis of conjugated samples, at ambient temperature at different times to detect differences in fluorescence emissions (see Fig. 4.15). Since the beginning of conjugation, an evident attenuation in the intensity band emission was observed, and apparently there is no indication of drastic conformal changes, then que continued with the Raman analysis of the protein structure after interaction with the NPs.
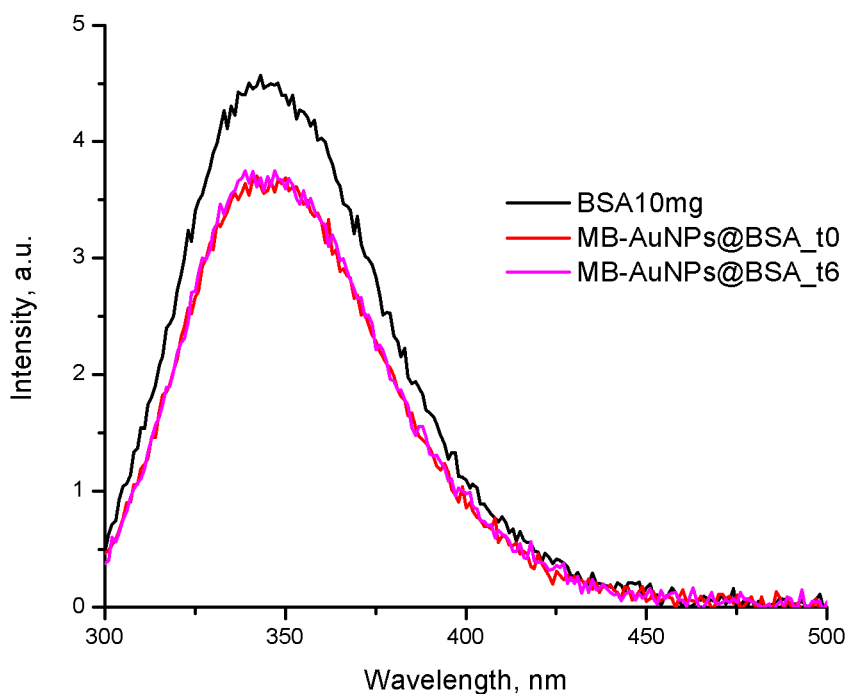

Figure 4.15. Fluorescence spectra of MB-AuNPs@BSA a different times after conjugation begins. The black line spectra correspond to a sample of 10 mg of BSA without NPs, the same concentration of protein was mixed with MB-AuNPs.

The Raman spectra of solid HEPES was acquired for better comparison of the synthesized MB-AuNPs, we may remember that HEPES is the organic molecule that directs the branched formation during synthesis, thus, prior conjugation is the molecule that covers and stabilizes the NPs.

Along the Raman bands of interest in the HEPES spectra (Fig. 4.16), the piperazine ring vibrations appears at 1185, 1120 y 1049 cm^{-1}.[25] It is important to localized these bands because they are in the same region of interest of main protein bands. In the spectra acquired from solid HEPES, we can clearly identify the 1027 cm^{-1} band, and the 1047, 1164, 1206, 1237 cm^{-1} that corresponds to ring vibrations of piperazine ring. The same bands has lower intensity in the spectra from samples prepared with HEPES solution and MB-AuNPs (see Fig. 4.17), in the last the 1044, 1120, 1214, 1238 y 1249 cm^{-1} can be identify, those bands indicates an asymmetric vibration of the SO_3 part.
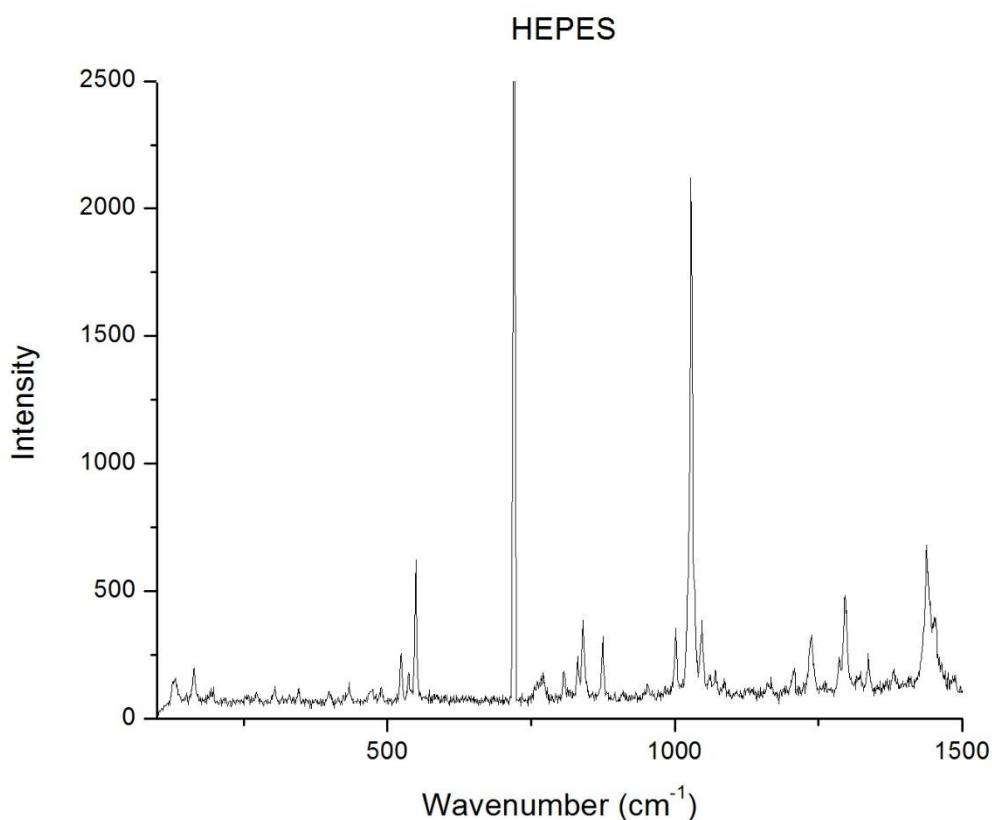

Figure 4.16. Raman spectra of solid HEPES, the laser used was at 633 nm.

In the Raman spectra of crystalized BSA, can be identified the amide I band at 1658 cm⁻¹, the presence of this band indicates an α-helix structure, also the native state of the protein (see Fig. 4.17).
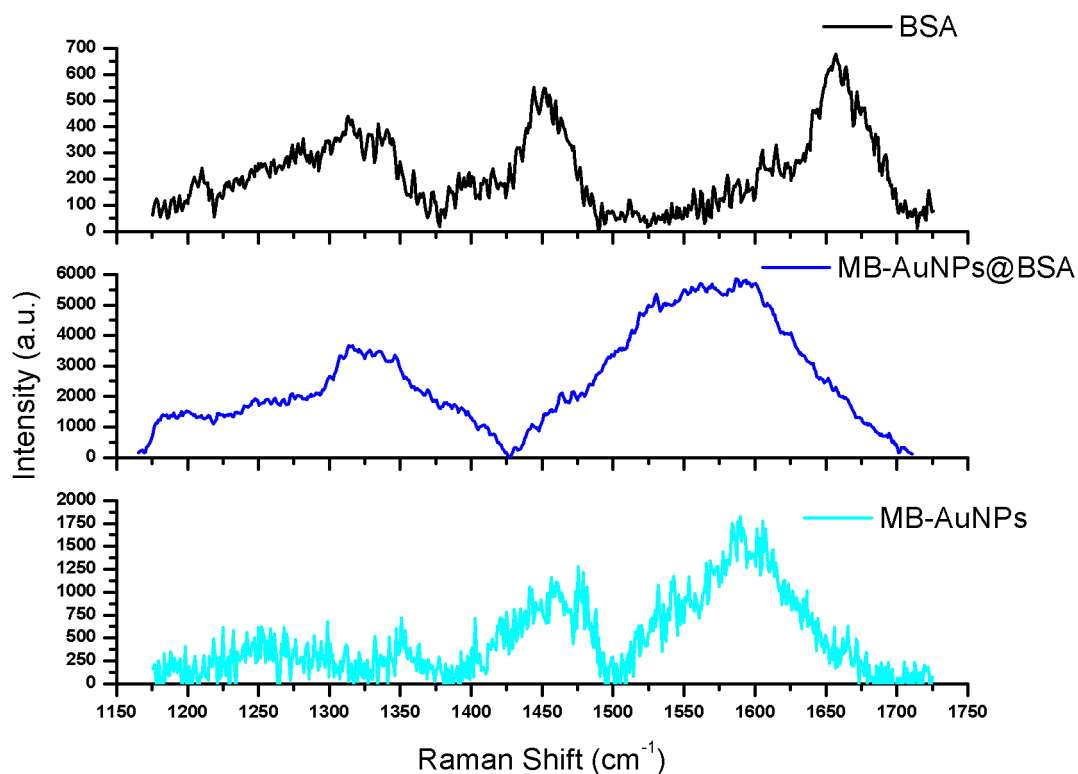

Figure 4.17. Espectros Raman de las nanopartículas multirramificadas, BSA y conjugado.

In the MB-AuNPs@BSA spectra an increase in the band at 1250 cm⁻¹ (amide III band region) and the simultaneous decrease in the 938 cm⁻¹ band, may suggest the possible degradation of protein, as have been seen in studies were protein is exposed to heat.[26]
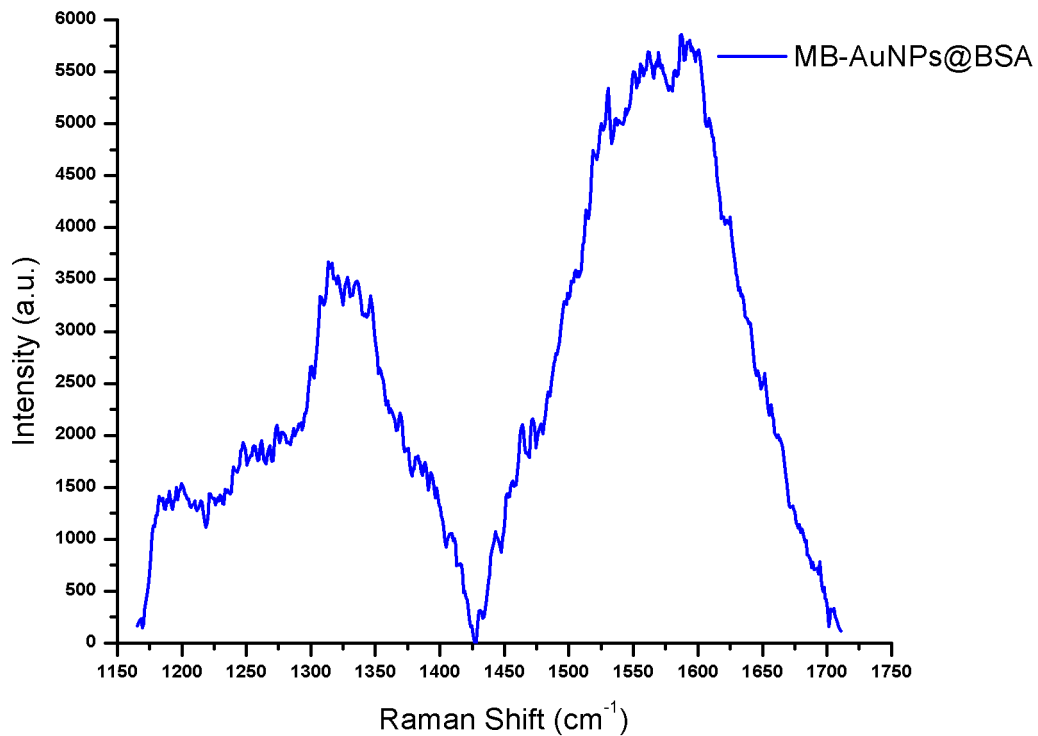
Figure 4.18. Raman spectra of the amide III band, acquired from the MB-AuNPs@BSA simple.

We must considerer that albumin in native state have a 55 % of helix and 45% of random conformation, then, we analyzed the intensities of the amide III band according to Table 4.2, and those corresponds to ratio of native state of protein. Also may be considered that the systems analyzed here has special properties of electromagnetic enhancement fields, then intensity of signals can be affected by the MB-AuNPs properties.[27,28]

191

MB-AuNPs	BSA_solid	BSA_soln	MB-AuNPs@BSA	Vibration mode	Ref.
				Table 4.2. Raman signals presents in the spectra of Fig. 4.17	
138	137		138	C-N Torsional	
488			480	CNC, piperazine ring deformation	25
	511			S-S Strain	
			661	C-S Strain	26
			673	C-S Strain	
	851			Tyrosine	26
	898		900	C-S Strain	29
	947		941		
	1003		988	Bending out of plane, pyrrole	26
1044				C-C o C-N Strain	25
1120		1123	1181		
1214			1197	C-N asymmetric tension	25
1249			1250	Amide III, random conformation	26
1260				C-N asymmetric tension	25
	1266		1279	Amida III, α-helix	26
1296					
	1323	1309	1312	C-H Bending	
	1398		1390	COO Symmetric	26
1465	1451	1454	1461	CH$_3$, CH$_2$ Bending	
			1497		
1532			1524	NH Bending	30
			1558	Amida II, tryptophan N-H Bending out of plane C-N Strain	26
1595			1596		
	1606			C=N Strain of tryptophan pyrrole Pirrol del triptófano	26
	1658	1656		Amida I Hélice-α C=O Strain	26,30
2496				OH Tension	
2863				C-H Strain of aromatic rings	
	2873	2874			
	2930	2929	2902		

Once we have stablished that protein is interacting with the MB-AuNPs and that its structure is preserved, we carried out a quantification of proper amount of BSA needed for full coverage of NPs and the formation of the protein corona. A calibration curve of BSA solutions in HEPES (Fig. 4.19) with increase concentration was acquired to assure proper dilution and constant absorbance value of BSA solutions. As expected, the conjugated albumin tends to increase according to the amount available in the solution, but above the 10mg/mL of BSA available, only the ~3% interacts with the NPs (see Fig. 4.20).
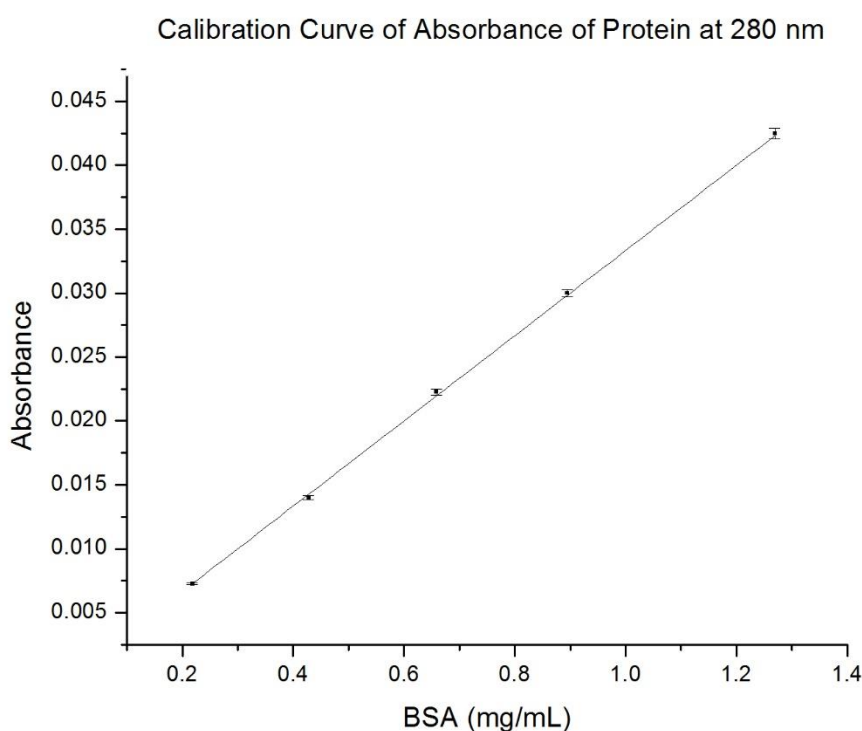

Figure 4.19. Calibration curves of BSA solutions prepared in 25 mM HEPES buffer.

Considering the 3% of BSA conjugated as full coverage of NPs surface, we carried out a Z-potential analysis to detect the changes in surface charge and determine the stability. Results are presented in Table 4.3, the z-potential value corresponds to reported charge for protein corona on NPs.[31]
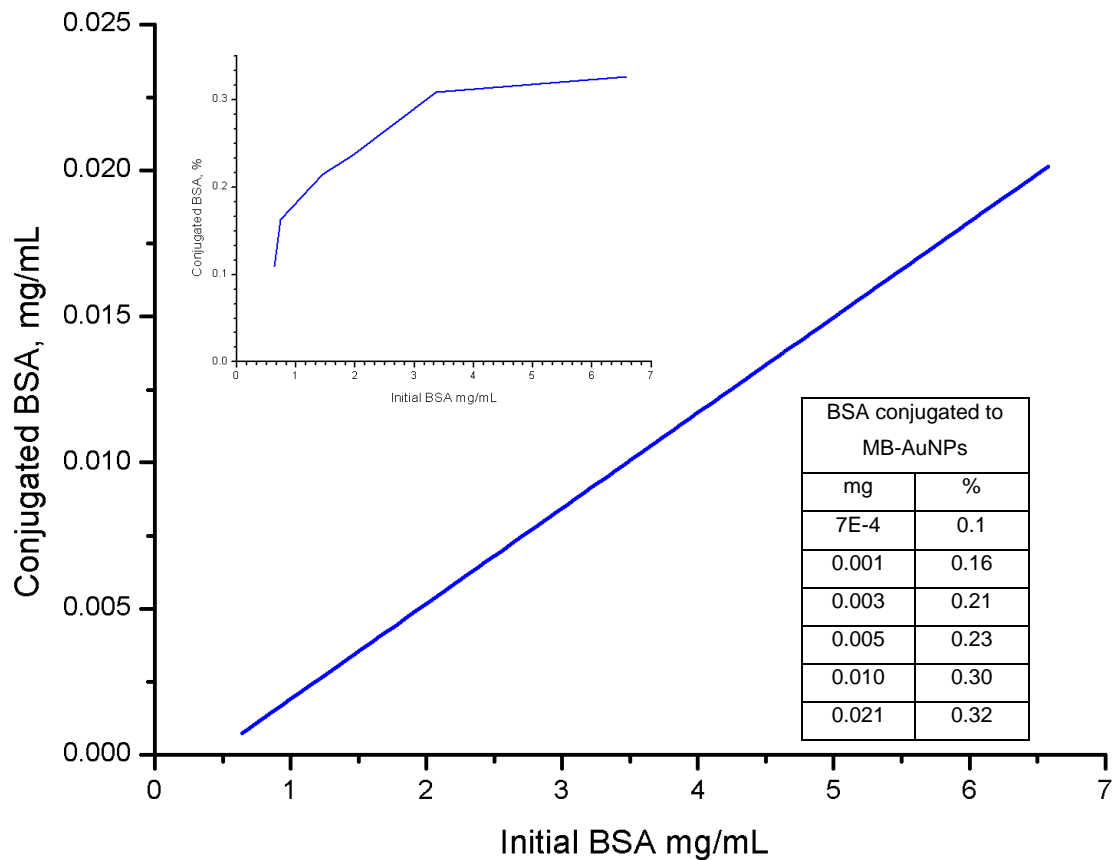
Figure 4.20. Cuantificación de BSA conjugada con MB-AuNPs por espectrofotometría UV-Vis.

		MB-AuNPs	MB-AuNPs@BSA
Table 4.3. DLS results of the readings of MB-AuNPs and MB-AuNPs@BSA.			
Mobilidad	u/s/V/cm	- 2.95	- 2.26
Potencial Z	mV	- 37.72	- 29.66
Carga	fC	- 0.03436	- 0.02279
Conductivity	us/cm	17	71
Size	nm	200	240

Then, at this point we consider we have a conjugated system, MB-AuNPs@BSA where protein BSA preserves its native conformational state and therefore its function. We decide to test the function y determine if the complex will perform as expected when interacts with living cells. For this, agar spheres with cibacron blue (blue sepharose CL-6B) were used as test anchor matrix. Primarily, we mixed the CL-6B with BSA solution to observe the agglutination of spheres and ensure its efficacy (Fig. 4.21), later CL-6B was mixed with MB-AuNPs and MB-AuNPs@BSA. Obvious agglomeration of CL-6B in presence in observed when the agar spheres are mixed with BSA, later, when interact with the NPs, barely difference is perceptible. Samples of CL-6B were exposed to MB-AuNPs and MB-AuNPs@BSA and later observed under scanning electron microscope to better analysis of complex function. In Fig. 4.22 we can observe the bare CL-6B spheres and the EDS analysis, no signals besides de organic material and aluminium pin. The images of Fig. 4.23 corresponds to CL-6B exposed to MB-AuNPs, in the secondary electrons micrographs is observed brighter regions, then in the backscattering electrons can be observed the same regions, then we considered to be because of the presence of heavy material, the EDS analysis performed in this area (inset) shows the Au signal. It is not expected that MB-AuNPs interacts with the cibacron blue, but we must consider that NPs are made from a hard material against the jelly nature of agar. We analyzed the sample of the CL-6B with MB-AuNPs@BSA (Fig. 4.24), in this sample is clearly observed the increased presence of heavy material, once is analyzed with EDS, Au signal is detected again, then the brighter spots corresponds to accumulations of MB-AuNPs@BSA.

When complex MB-AuNPs@BSA is a system that can interact with albumin receptors and improves the stability of the nanoparticles.
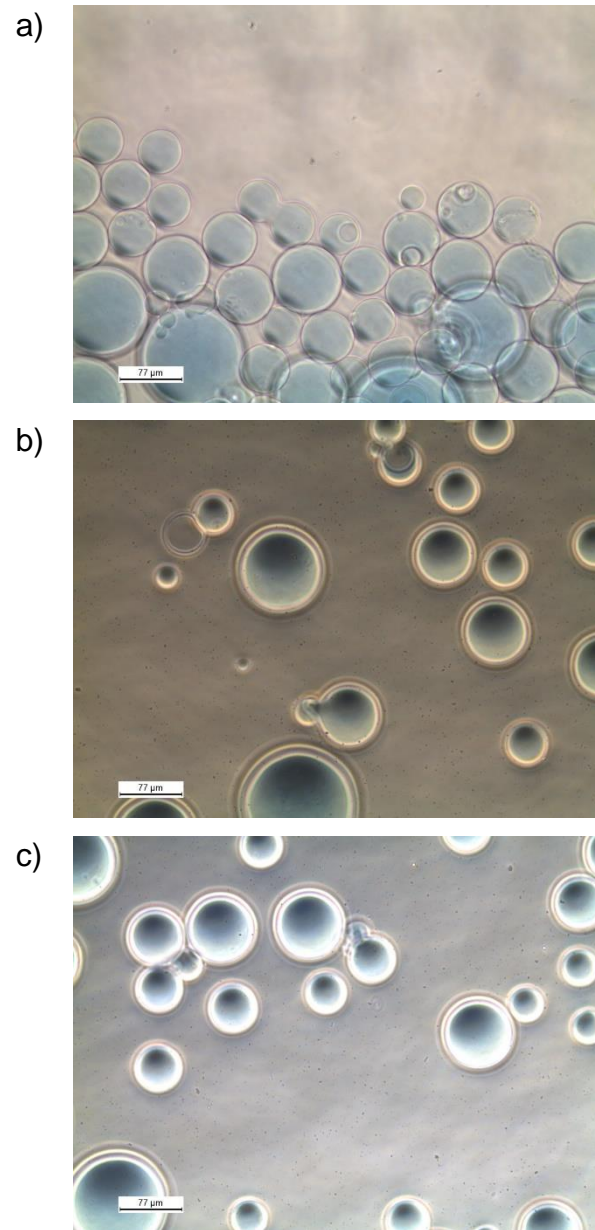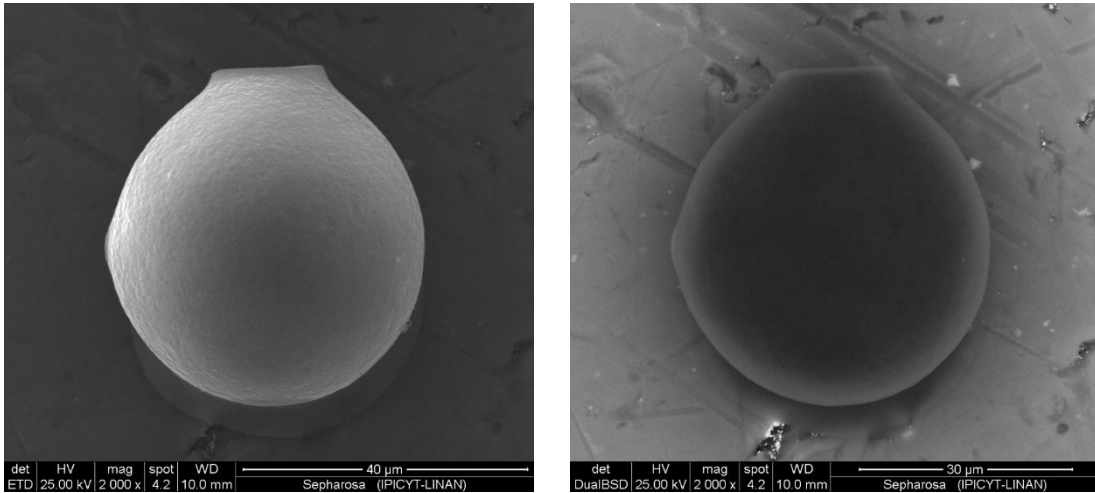
Figure 4.21. Agglutination test of Blue Sepharose CL-6B with **a)** 0.2 mg/mL of BSA, **b)** MB-AuNPs at 5.2×10^9 NPs/mL and **c)** MB-AuNPs@BSA at 5.2 ×10^9 NPs/mL.
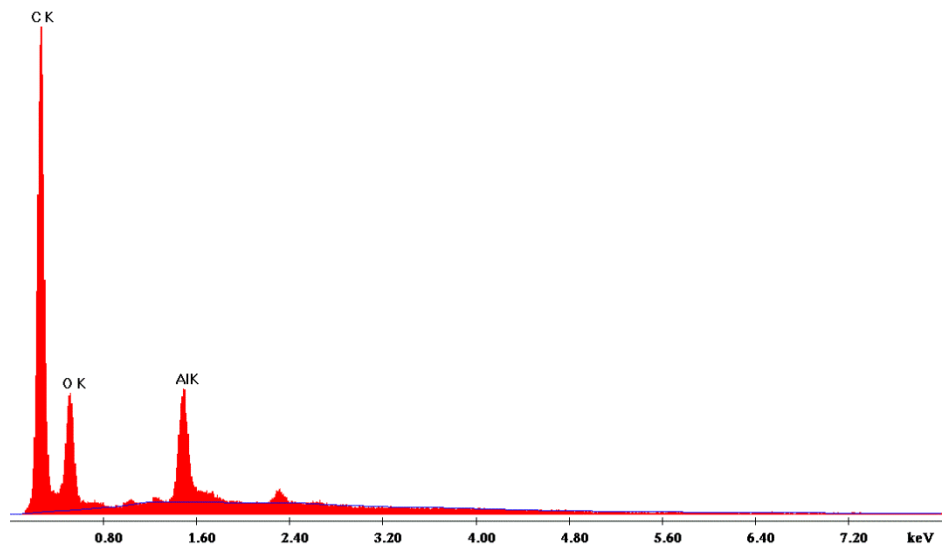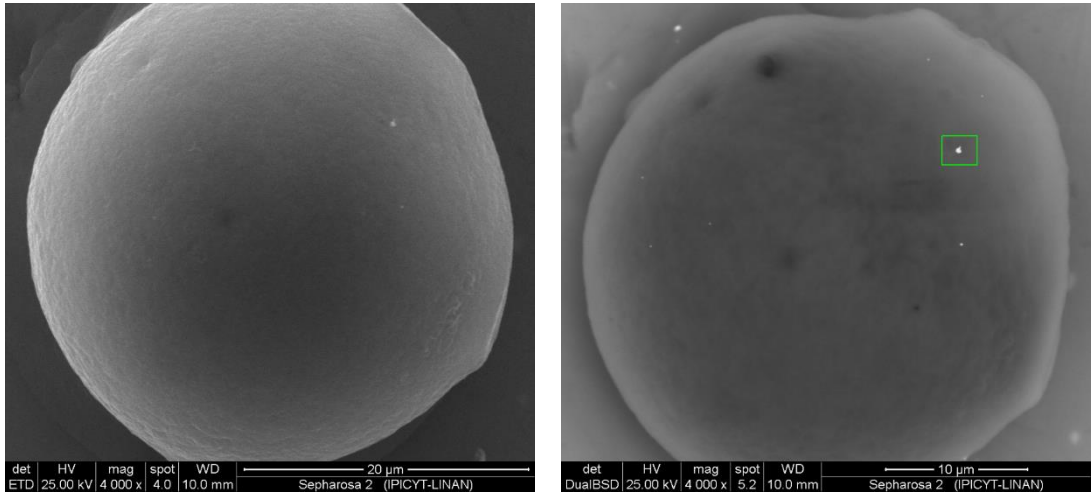
Figure 4.22. Electron micrographs in ETD (up-left) and BSD (up-right) of Blue Sepharose CL-6B. And EDS analysis.
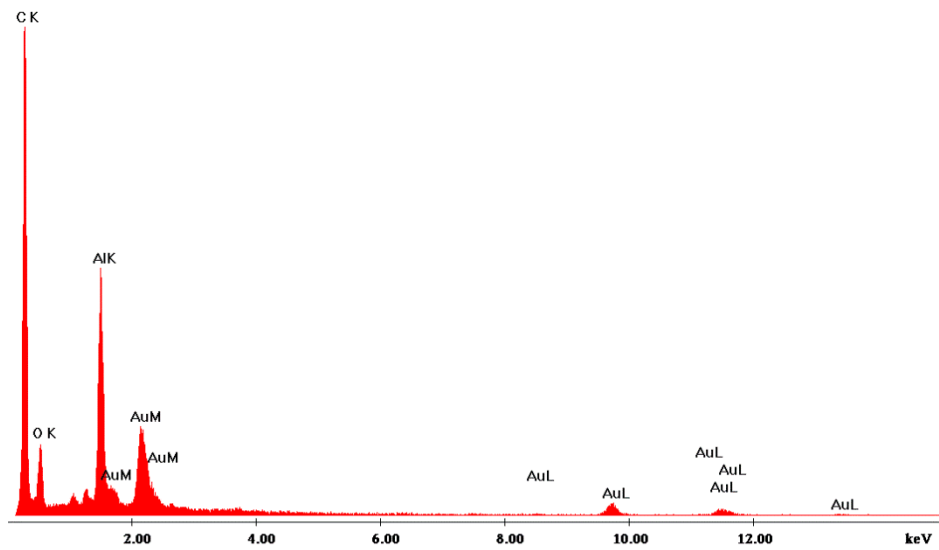
Figure 4.23. Electron micrographs in ETD (up-left) and BSD (up-right) of Blue Sepharose mixed with MB-AuNPs. In BSD the bright spots may due to presence of MB-AuNPs, for correlation an EDS analysis (down) was performed in the area of green inset.
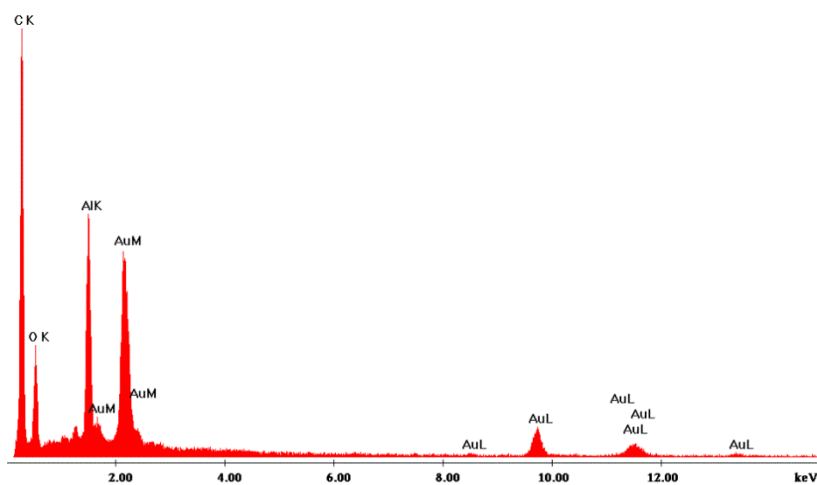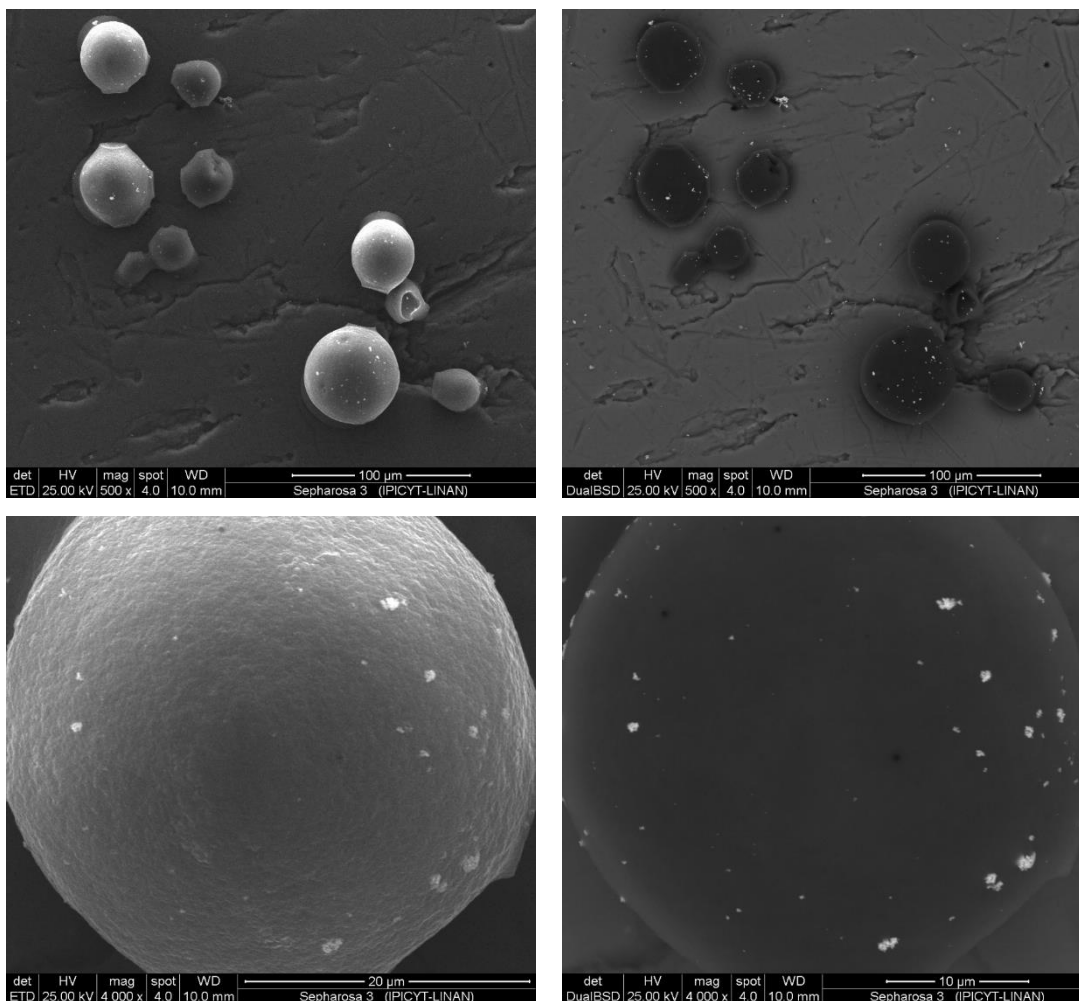
Figure 4.24. Electron micrographs of Sepharose sample prepared with MB-AuNPs@BSA. The BSD micrographs suggest the presence of the NPs, correlation was realized with EDS analysis.

Figures Index

Tables Index

References

(1)   Lista, M.; Liu, D. Z.; Mulvaney, P. Phase Transfer of Noble Metal Nanoparticles to Organic Solvents. *Langmuir* **2014**, *30*, 1932–1938.

(2)   Louis, C.; Pluchery, O. *Gold Nanoparticles for Physics, Chemistry and Biology*; Imperial College Press, 2012.

(3)   Moyano, D. F.; Rotello, V. M. Gold Nanoparticles: Testbeds for Engineered Protein–particle Interactions. *Nanomedicine* **2014**, *9*, 1905–1907.

(4)   Martin, M. N.; Allen, A. J.; MacCuspie, R. I.; Hackley, V. A. Dissolution, Agglomerate Morphology, and Stability Limits of Protein-Coated Silver Nanoparticles. *Langmuir* **2014**, *30*, 11442–11452.

(5)   Wang, X.; Yang, L.; Chen, Z. G.; Shin, D. M. Application of Nanotechnology in Cancer Therapy and Imaging. *CA. Cancer J. Clin.* **2008**, *58*, 97–110.

(6)   Misra, R.; Acharya, S.; Sahoo, S. K. Cancer Nanotechnology: Application of Nanotechnology in Cancer Therapy. *Drug Discov. Today* **2010**, *15*, 842–850.

(7)   Iancu, C.; Mocan, L.; Bele, C.; Orza, A. I.; Tabaran, F. a.; Catoi, C.; Stiufiuc, R.; Stir, A.; Matea, C.; Iancu, D.; *et al.* Enhanced Laser Thermal Ablation for the in Vitro Treatment of Liver Cancer by Specific Delivery of Multiwalled Carbon Nanotubes Functionalized with Human Serum Albumin. *Int. J. Nanomedicine* **2011**, *6*, 129–141.

(8)   G, D. S.; Fiume, L.; Bolondi, L.; Lanza, M.; Pariali, M.; Paquale, C. Enhanced Uptake of Lactosaminated Human Albumin by Rat Hepatocarcinomas : Implications for an Improved Chemotherapy of Primary Liver Tumors. *Liver Int.* **2005**, *25*, 854–860.

(9)   Kratz, F.; Elsadek, B. Clinical Impact of Serum Proteins on Drug Delivery. *J. Control. Release* **2012**, *161*, 429–445.

(10)   Kratz, F. Albumin as a Drug Carrier: Design of Prodrugs, Drug Conjugates and Nanoparticles. *J. Control. Release* **2008**, *132*, 171–183.

(11)   Elsadek, B.; Kratz, F. Impact of Albumin on Drug Delivery--New Applications on the Horizon. *J. Control. Release* **2012**, *157*, 4–28.

(12)   Peng, Q.; Zhang, S.; Yang, Q.; Zhang, T.; Wei, X.-Q.; Jiang, L.; Zhang, C.-L.; Chen, Q.-M.; Zhang, Z.-R.; Lin, Y.-F. Preformed Albumin Corona, a Protective Coating for Nanoparticles Based Drug Delivery System. *Biomaterials* **2013**, *34*, 8521–8530.

(13)   Kennedy, L. C.; Bickford, L. R.; Lewinski, N. a.; Coughlin, A. J.; Hu, Y.; Day, E. S.; West, J. L.; Drezek, R. a. A New Era for Cancer Treatment: Gold-Nanoparticle-Mediated Thermal Therapies. *Small* **2011**, *7*, 169–183.

(14)   Hermanson, G. T. *Bioconjugate Techniques*; Academic Press, 1996.

(15)   Kratz, F. A Clinical Update of Using Albumin as a Drug Vehicle - A Commentary. *J Control. Real* **2014**.

(16)   Prasad, P.; Gordijo, C. R.; Abbasi, A. Z.; Maeda, A.; Ip, A.; Rauth, A. M.; DaCosta, R. S.; Wu, X. Y. Multifunctional Albumin–MnO 2 Nanoparticles Modulate Solid Tumor Microenvironment by Attenuating Hypoxia, Acidosis, Vascular Endothelial Growth Factor and Enhance Radiation Response. *ACS Nano* **2014**, *8*, 3202–3212.

(17)   Gebregeorgis, a; Bhan, C.; Wilson, O.; Raghavan, D. Characterization of Silver/Bovine Serum Albumin (Ag/BSA) Nanoparticles Structure: Morphological, Compositional, and Interaction Studies. *J. Colloid Interface Sci.* **2013**, *389*, 31–41.

(18)   Brewer, S. H.; Glomm, W. R.; Johnson, M. C.; Knag, M. K.; Franzen, S. Probing BSA Binding to Citrate-Coated Gold Nanoparticles and Surfaces. *Langmuir* **2005**, *21*, 9303–9307.

(19)   Shang, L.; Wang, Y.; Jiang, J.; Dong, S. pH-Dependent Protein Conformational

Changes in Albumin:gold Nanoparticle Bioconjugates: A Spectroscopic Study. *Langmuir* **2007**, *23*, 2714–2721.

(20) Nghiem, T. H. L.; La, T. H.; Vu, X. H.; Chu, V. H.; Nguyen, T. H.; Le, Q. H.; Fort, E.; Do, Q. H.; Tran, H. N. Synthesis, Capping and Binding of Colloidal Gold Nanoparticles to Proteins. *Adv. Nat. Sci. Nanosci. Nanotechnol.* **2010**, *1*, 25009.

(21) Walker, J. M. *The Protein Protocols Handbook*; Humana Press: Totowa, New Jersey, 1996.

(22) Lewis, I. R.; Edwards, H. G. M. *Handbook of Raman Spectroscopy*; Marcel Dekker, Inc.: New York, 2001.

(23) Skoog, D. A.; Holler, F. J.; Nieman, T. A. *Principios de Análisis Instrumental*; McGraw Hill: Madrid, España, 2001.

(24) Plascencia-Villa, G.; Bahena, D.; Rodríguez, A. R.; Ponce, A.; José-Yacamán, M. Advanced Microscopy of Star-Shaped Gold Nanoparticles and Their Adsorption-Uptake by Macrophages. *Metallomics* **2013**, *5*, 29–32.

(25) Gunasekaran, S.; Anita, B. Spectral Investigation and Normal Coordinate Analysis of Piperazine. *Indian J. Pure App. Phys.* **2008**, *46*, 833–838.

(26) Lin, V. J.; Koenig, J. L. Raman Studies of Bovine Serum Albumin. *Biopolymers* **1976**, *15*, 203–218.

(27) Zou, X.; Ying, E.; Dong, S. Seed-Mediated Synthesis of Branched Gold Nanoparticles with the Assistance of Citrate and Their Surface-Enhanced Raman Scattering Properties. *Nanotechnology* **2006**, *17*, 4758–4764.

(28) Su, Q.; Ma, X.; Dong, J.; Jiang, C.; Qian, W. A Reproducible SERS Substrate Based on Electrostatically Assisted Aptes-Functionalized Surface-Assembly of Gold Nanostars. *ACS Appl. Mater. Interfaces* **2011**, *3*, 1873–1879.

(29) Nakamura, K.; Era, S.; Ozaki, Y.; Sogami, M.; Hayashi, T.; Murakami, M. Conformational Changes in Seventeen Cystine Disulfide Bridges of Bovine Serum Albumin Proved by Raman Spectroscopy. *FEBS Lett.* **1997**, *417*, 375–378.

(30) Socrates, G. *Infrared and Raman Characteristic Group Frequencies*; Third.; John Wiley & Sons, Ltd., 2001.

(31) Goy-López, S.; Juárez, J.; Alatorre-Meda, M.; Casals, E.; Puntes, V. F.; Taboada, P.; Mosquera, V. Physicochemical Characteristics of Protein–NP Bioconjugates: The Role of Particle Curvature and Solution Conditions on Human Serum Albumin Conformation and Fibrillogenesis Inhibition. *Langmuir* **2012**, *28*, 9113–9126.

5. *In vitro* Evaluation of Gold Nanoparticles Toxicity

Chapter Content

5.1. Introduction

Besides the nanomaterials (NMs) released into the environment due to natural process, the anthropogenic nanomaterials (e.g. flocculation of nanometric metallic oxides into acid mine drainage) has risen the need to define their impact on human health and the environment due to their reactive properties, and the establishing of regulations for their production and subsequent handling according to their material composition and application.[1] Also, the increase interest in the properties of NMs and their many applications, have introduced them into manufacturing chains. Among the fields of applications, the medicine has gain interest in aim to improve the diseases detections methods and treatments.

The present chapter cover the background theory and the experimental work realized for the achievement of the last general objective of the project subject of this thesis: iv) **Evaluation of cytotoxicity of nanoparticles in cultured cells.** The section 5.2 of the present chapter summaries some of the *in vitro* assays available for the evaluation of materials toxicity, we focus on the methods used. Also, is presented a compendium of the published results in toxic evaluation of gold nanoparticles (AuNPs). The methods and experimental work developed for this thesis are presented starting from section 5.3.

5.1.1. The relevance of the toxicity evaluation of nanomaterials on cellular systems

The NMs has been synthesized for several applications in different fields. The field of importance for these thesis is the medicine. The application of nanotechnology to medicine has been called *Nanomedicine,* the research in this area has the goal of improve the medical diagnosis and treatment of diseases.[2] The Nanomedicine is not considered a separate branch of medicine, but the research in this area implies an interdisciplinary interaction between nanoscience, nanoengineering and nanotechnology with life sciences.[2,3] The nanomedicine intends the fabrication of NMs for advanced diagnostics and biosensors, targeted drug delivery and smart drugs.

The nanomedicine, like medicine, can enter the clinics and can be part of conventional clinical practice assuming all aspects of translation are satisfied, including safety, regulatory, and ethical requirements.[3] The success of nanomaterials in medical applications has raised questions about their unintentional effects on the human body. The main concern will be about particles <50 nm, which can enter the cells by endocytic process,[4] and there are still many unanswered questions about their fate in the living body. Because of the diversity of materials used and the wide range in size and shape of nanoparticles, these effects will vary a lot.[2] Then, research the role of nanoparticles in pathogenesis of diseases, and their use in therapy may be the future of medicine.[5] In essence, a fundamental understanding of nanomaterial toxicology (nanotoxicology) is highly desirable.[6] The nanotoxicology,[7,8] can define toxic modes of action that could potentially arise in occupational environmental, or medical applications of NMs.[9,10]

Has been a concern in develop new assays or standardizing the existing ones to evaluate the effects of exposition to NMs,[11] considering routes of exposure as the respiratory system, skin and intestinal tract. Also, to determine if the necessary dose for the chose applications is safe.

With the purpose of provide specific target signals to NPs, they have been conjugated with aptamers and oligonucleotides,[12–14] peptides,[15,16] proteins,[17,18] antibodies,[19,20] and other molecules.[21] With the conjugation, the surface chemical characteristics of NPs may change, therefore, it is important to perform the in-vitro evaluation before and after the conjugation.

5.2. Cytotoxicity of Gold Nanoparticles

The term "cytotoxicity" refers to the toxic effects of a specific material or substance on individual cells. In toxicology studies, identical cell cultures are exposed to different forms and concentrations of the toxin. The toxicological evaluation of a NMs with medical application begins with the *in-vitro* biocompatibility studies with normal and malignant cells, and are followed with studies involving animals, and finally the clinical trials.

5.2.1. Cytotoxicity Assays

Laboratory methods used to identify exposure biomarkers expanded rapidly in the late 1970s and the 1980s, then it became possible to reliably measure potential toxicity from a variety of sources: diet, polluted air, medications, alcoholic beverages, and others. In 1997, International Standard ISO-10993 was formulated in order to provide a comprehensive and general guideline on biocompatibility test for materials intended for medical applications, including *in vitro* genotoxicity, carcinogenicity and reproductive toxicity. Additionally, are described assays to evaluate the interactions of materials with blood, their *in-vitro* cytotoxicity and systemic toxicity, as well as methods for the characterization of physicochemical, morphological and topographical properties of materials.[22]

The Table 5.1 contains the different *in-vitro* assays utilized to evaluate the potential cytotoxicity of several materials.

Table 5.1 Common biological endpoints assessed by *in-vitro* toxicity tests.	
Biological endpoint	**Detection method**
Cell morphology	Cell size and shape Cell-Cell contacts Nuclear number, size, shape and inclusions Nuclear or cytoplasmic vacuolation
Cell viability	Trypan blue dye exclusion Diacetyl fluorescein uptake

	Cell counting
	Replating efficiency
	Cellular proliferation (e.g., IC_{50})
Cell metabolism	Mitochondrial integrity (MTT, MTS and XTT tetrazolium salt assays)
	Lysosome and Golgi body activity (Neutral red uptake)
	Cofactor depletion (e.g., ATP content)
Membrane Leakage	Loss of enzymes (e.g., LDH), ions or cofactors (e.g., Ca^{2+}, K^+, NADPH)
	Leakage of pre-labeled markers (e.g., ^{51}Cr or fluorescein)
Cell proliferation	Cell counting
	Total protein content (e.g., methylene blue,coomassie blue, kenacid blue)
	DNA content (e.g., Hoechst 33342)
	Colony formation
Cell adhesion	Attachment to culture Surface
	Detachment from culture surface
	Cell-Cell adhesion
Radioisotope incorporation	Thymidine incorporation into DNA
	Uridine incorporation into RNA
	Amino acids incorporation into proteins
	Taken from Ref. [23]

The basic evaluation is the visual inspection of cell cultures under bright field microscopy, in order to detect any morphological change, cell adhesion and proliferation. Moreover, the colorimetric assays are a standard evaluation of plasmatic membrane integrity, mitochondrial activity and DNA replication.

The simplest colorimetric assay to evaluate the effect of NPs on viability and membrane integrity is commonly performed through the use of neutral red or trypan blue. The neutral red, or tolylene red, is a weak cationic dye capable of pass through plasmatic membrane by diffusion and accumulate in lysosomes. If the cell membrane is disrupted, the uptake of neutral red decrease or it may leak out, these process allow to differentiate between live and death cells by the spectrophotometric quantification of neutral red uptake. The trypan blue is an azo dye that only permeates in the cells with damage cell membrane; therefore, only the death cells stain blue.

Other viability assays include the use of two different chemicals, Calcein-AM (calcein acetoxymethyl ester) and Ethidium H-1 (ethidium homodimer-1). These assays evaluate the esterase intracellular activity; the calcein-AM (electrically neutral) is internalized into the cell by diffusion, and at the intracellular environment is transformed by the mitochondrial esterase activity in calcein, a green fluorescent molecule that is retained by living cells (exc./em. ~495 nm/~515 nm). On the other hand, the cell membrane integrity is evaluated with ethidium H-1, this molecule does not permeate de plasmatic membrane of living cells, only damage membranes of death cells and increase 40 times its fluorescence to binding nucleic acids, the ethidium H-1 is red fluorescent (exc./em. ~495 nm/~635 nm).[24]

Other cytotoxicity assay involves monitoring the release of lactate dehydrogenase (LDH) due to cellular death. The lactate dehydrogenase (LDH) is an enzyme usually stable present at the cytosol, when the plasmatic membrane is damage the LDH is rapidly released into the cell culture supernatants. In LDH assay, the enzyme released from damaged cells oxidizes lactate to pyruvate, which promotes conversion of tetrazolium salt 2-(4-iodophenyl)-3-(4-nitrophenyl)-5-phenyltetrazolium chloride, (INT) to formazan (see Fig. 5.1), a water-soluble molecule with absorbance at 490 nm. The amount of LDH released is proportional to the number of cells damaged or lysed.[25] Because the practical use and standard assay commercial systems available, this assay has been used for the evaluation of cell death in cultured cells exposed to AuNPs nanoheaters and treated by photothermal therapy (PTT, *PhotoThermal Therapy*).[26]

1st enzymatic reaction

pyruvate

lactate

LDH

2nd enzymatic reaction

Cl⁻

Catalyst

Cl⁻

tetrazolium salt (pale yellow)

formazan salt (red)
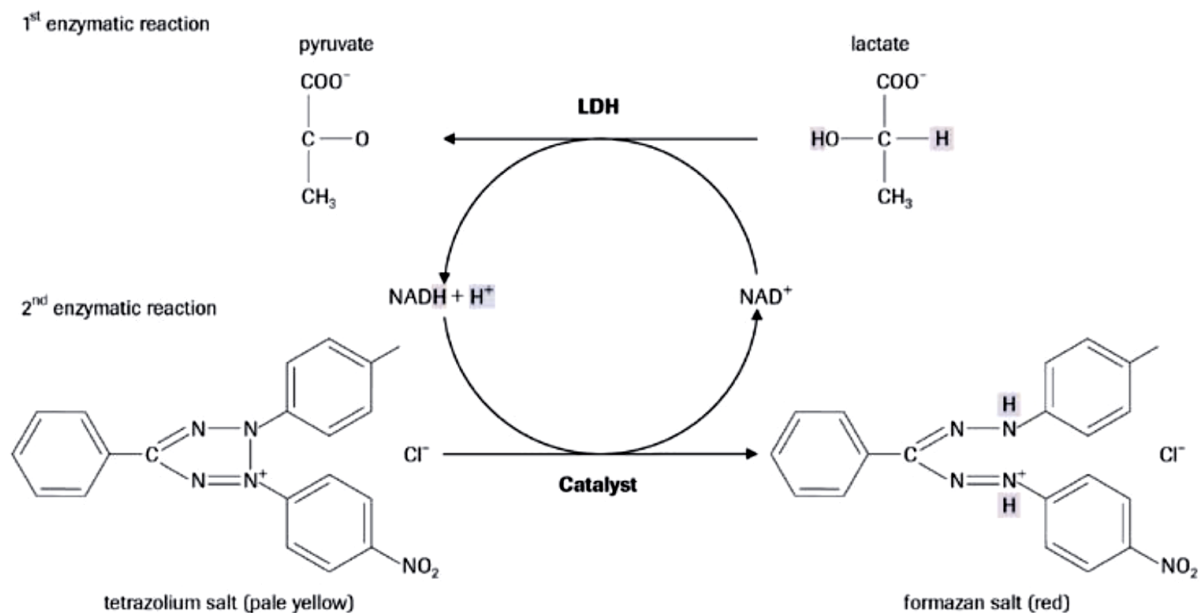
Figure 5.1. Biochemistry of LDH assay. In the first enzymatic reaction, released LDH reduces NAD^+ to $NADH/H^+$ by oxidation of lactate to pyruvate. In the second, the catalyst (diaphorase) transfer H/H+ from NADH/H+ to the tetrazolium salt INT which is reduced to formazan (coupled enzymatic reaction).

The MTS assay is used for the evaluation of mitochondrial activity, it is based on the reduction of yellow tetrazolium salt, to purple formazan crystals by metabolic active cells (Fig. 5.2), then the crystals formed are solubilized and the solution is quantified by UV-VIS spectroscopy.[27] The cellular reduction of tetrazolium salt is believed to occur both in the mitochondria by the enzyme succinate dehydrogenase and also extra-mitochondrial involving the pyridine nucleotide cofactors NADH and NADPH, these cofactors acts as intracellular carries of reducing equivalents (electrons) and they are produced by the dehydrogenation of metabolic active enzymes.

212
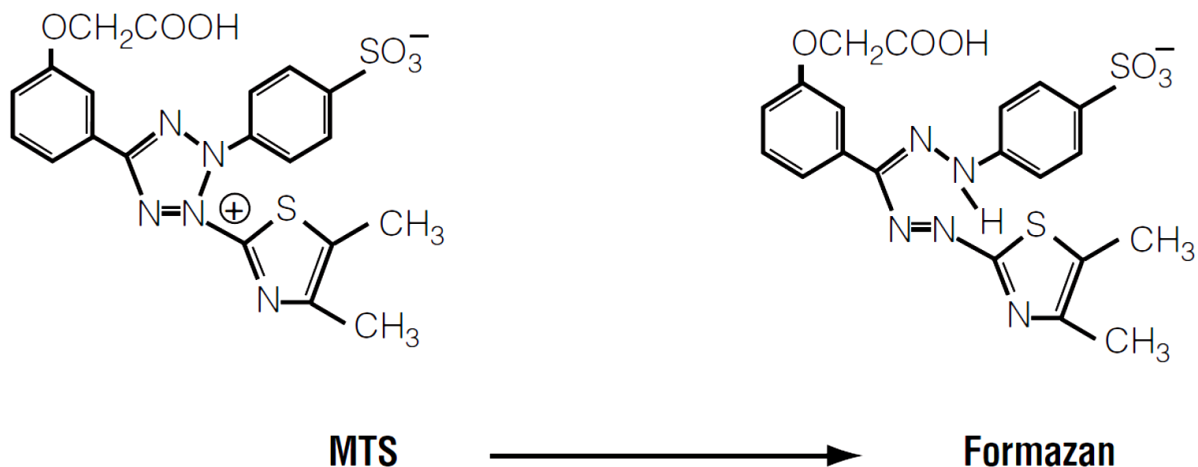
Figure 5.2.   Molecular structures of MTS tetrazolium and its formazan product.

Other evaluation of cytotoxicity based on tetrazolium salts is the WST assay; consist in the quantification at 450 nm of the product yellow-orange formazan.[25] Other, the resazurin or alamar blue is a colorimetric assay where the non-fluorescent dye is reduce by cellular metabolic activity to pink fluorescent dye, since during oxygen consumption is an electron acceptor for NADP and FADH enzymes.

There are cytotoxic assays to evaluate sublethal effects of nanoparticles, since not all effects compromise the cell membrane or affect metabolic functions. The oxidative stress is referred to as an imbalance between the production of reactive oxygen species (ROS) and the cells ability to reduce ROS, which may be as a result an increased ROS production, a decrease in the cells defense mechanisms, or a combination of both. An overproduction of ROS may induce oxidative stress, resulting in cells failing to maintain normal physiological redox-regulated functions further resulting in oxidative modification of proteins to generate protein radicals, initiation of lipid peroxidation, DNA strand breaks and modification of nucleic acids, modulation of gene expression, thereby leading to cell death and genotoxic effects.[28]

Other analysis of viability is the quantification of DNA synthesis at the stages of cell proliferation. The nitrogenous base used is 5-bromo-2'-deoxyuridine (BrdU), and analogue of thymidine, that is incorporated at the DNA synthesis in proliferating cells.

213

Then, a primary antibody anti-BrdU, conjugated with peroxidase (POD), bonds to the BrdU.[24] For label the BrdU incorporated to DNA, the last has to be denaturalized. It is important to mention, that the antibody does not reacts with other cells components as thymidine, uridine or DNA.[29]

The oxidative stress can be detected by glutathione activity assay. The glutathione (GHS) is an antioxidant compound which is oxidized to glutathione disulfide (GSSG) in the presence of reactive oxygen species (ROS). To evaluate glutathione activity as stabilizer of oxidative stress, a high rate of GSH/GSSG have to be maintain by the glutathione reductase enzyme. The assay of the level of GSH is realize with the Ellman reactive 5,5'-dithio-bis-2-nitro-benzoic acid (DTNB), which reacts with the GSH sulfhydryl group and produce a yellow product, 5-thio-2-nitrobenzoic acid (TNB). Glutathione reductase also reutilize GSH of GHS-TNB complex, process that produces more TNB. The rate of production of TNB is directly proportional to GSH concentration in the sample, and can be quantified by absorption at 405 or 412 nm.[25]

The NPs may have the ability to cause damage to the genetic material, since they are capable of crossing the cell membranes and cause chromosomal fragmentation, DNA strand breakages, point mutations, oxidative damage and alterations in gene expression. The DNA is highly susceptible to oxidative damage,[28] and the binding of a carcinogenic molecule to DNA may be the step leading to the damage of DNA. The consequences may range from a simple substitution in one of the DNA base pairs to a large rearrangement of a chromosome.[30]

5.2.2. Interaction of Nanoparticles with Cultured Cells

Besides the indirect exposure to NMs, like gases of combustion engines, sun protection lotions and cleaning products, the intended administration of NMs, points to main systems and cells models to considered for toxic evaluations (see Fig. 5.3).[31] The intravenously administered NPs will travel through the bloodstream to their destiny site, therefore is expected to passed the time of administration, the NPs will

be eliminated by the urine.[32] Then, we consider that immune cells and those lining urinary tract (urothelial cells) are important cells models to primary test of cytotoxicity of NPs. Later, is important to considered cells models of specific organs where NPs can accumulate.
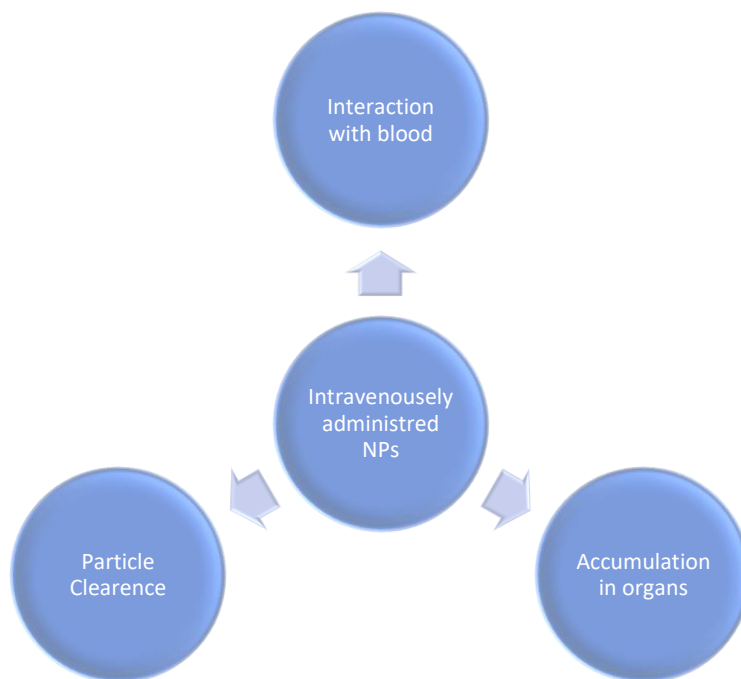
Figure 5.3. For medical applications of NPs, it is important to test the toxicity in the indirect systems of interactions, once the NPs are administered.

5.2.2.1. Urothelial Cells

The wall of the urinary passages, including the surfaces of the renal pelvis, the ureters, the bladder, and proximal parts of the urethra (see Fig. 5.5), is covered by a specialized epithelium, the transitional epithelium or urothelium. The urothelium is stratified and composed of three types of cells: basal precursors cells, intermediate cells and large superficial umbrella cells (see Fig. 5.7).[33]
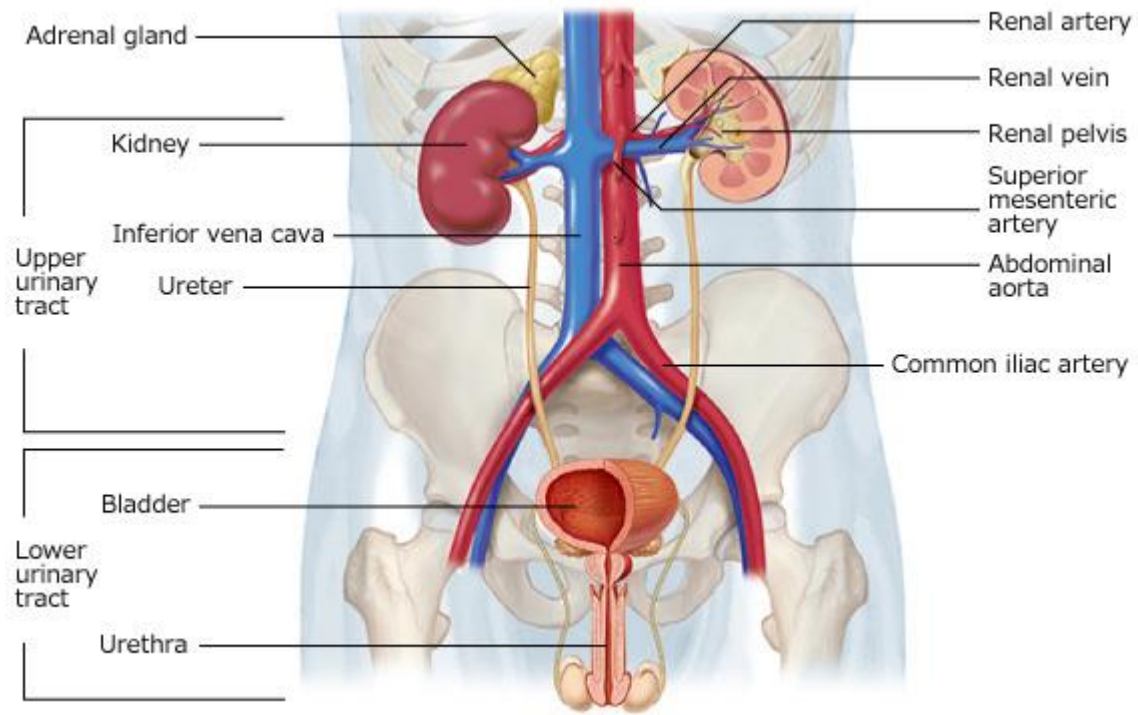
Figure 5.5. Structure of urinary tract. The urinary tract has the function of filters waste products and discharges them to the outside of the body as urine. It consists of the kidney, ureter, bladder and uretra.[34]

Benign nuclei: oval, with nuclear groove, point towards top (normal polarity) and not hyperchromatic

Umbrella cells

Intermediate cells

Basal cells

Urothelium

Lamina propria

A
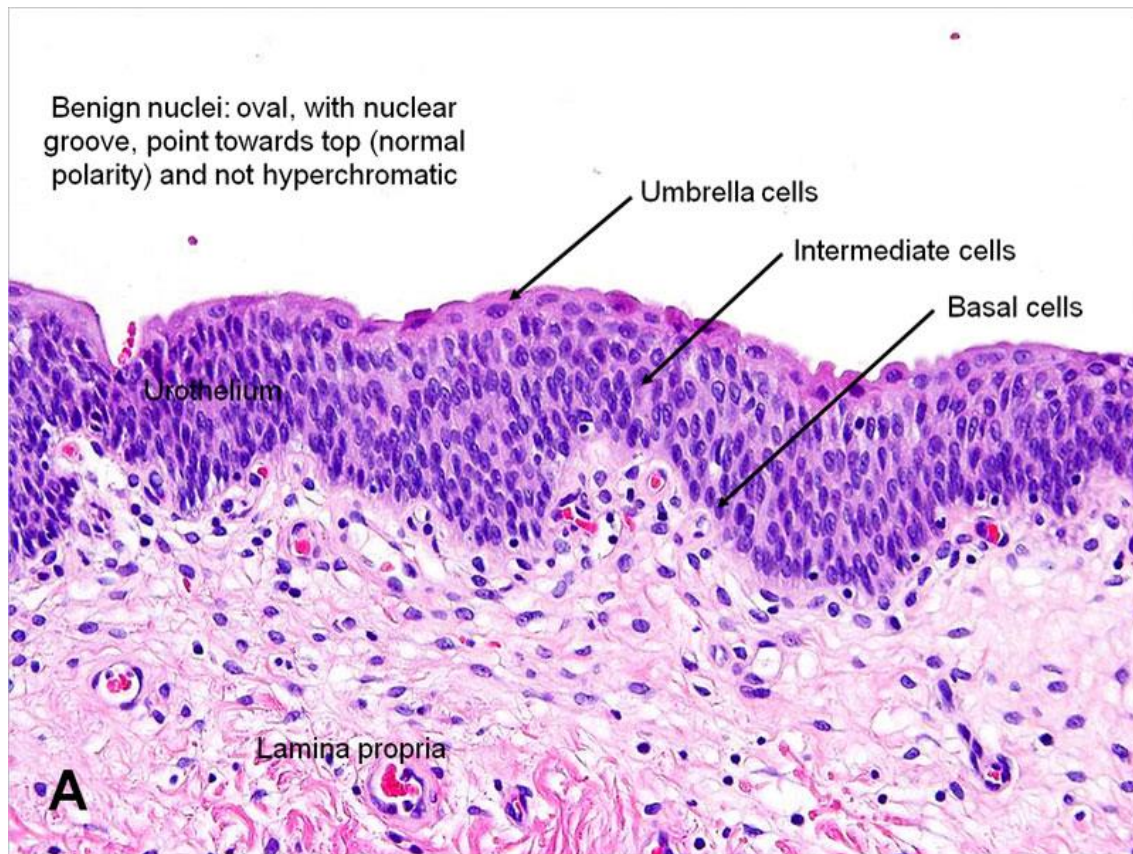
Figure 5.6. The urothelium consists of several layers of transitional cells, divided into (top to base) umbrella, intermediate and basal cells.[35]

5.2.2.2. Adipose Derived Stromal Cells, ADSCs

The adipose tissue is widely distributed all over the body, and exhibits different properties according to their anatomical localization. There are white and brown adipose tissue, both have a highly differing fine structure and location (see Fig. 5.6). White adipose tissue is found in the subcutaneous tissue, where it exists mainly as single adipocytes and in small groups often along capillaries or in the peritoneal cavity where it forms a compact tissue, the visceral fat. The white adipose tissue represents an important source for energy. There are two types of brown adipose tissue, the classical and the beige, that can be found intermingled with white adipocytes, in contrast to white adipocytes, the classical brown adipocytes contain numerous lipid droplets that differ greatly in size. The brown color of the tissue is

due to an abundance of mitochondria. The brown adipose tissue is compact and rich in capillaries and sympathetic nerve fibers. The brown adipose tissue is of vital importance under conditions of need of extra heat.[36]
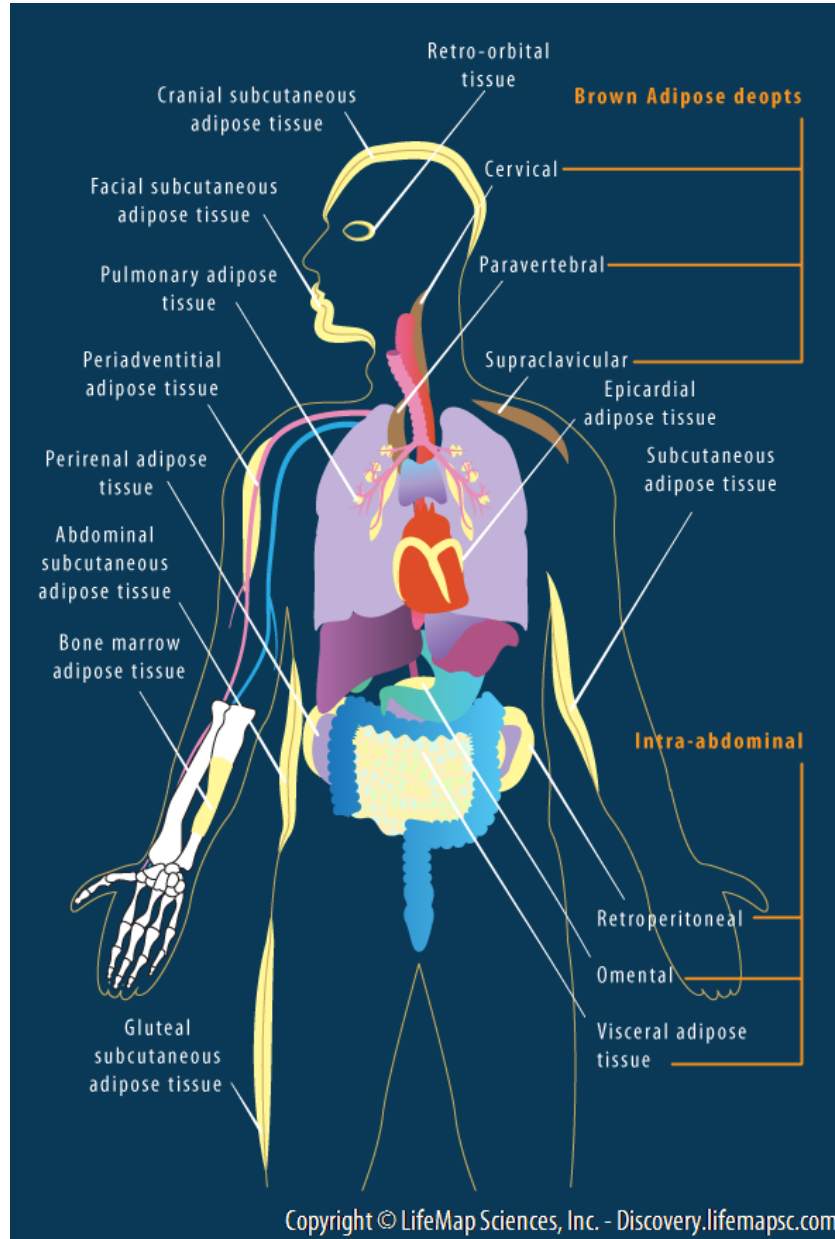
Figure 5.6. Subcutaneous white adipose tissues from different embryonic origins are located in the face and the body regions. Inner white adipose depots are depicted in the intra-abdominal, lung, kidney and heart regions. The brown adipose tissue is mainly distributed in the cervical, paravertebral and sub-clavicle regions.[37]

Adipose tissue, especially white adipose tissue, has been identified as an alternative source of adult stem cells; there is a large reservoir of donor tissue, which is also readily accessible. Since the identification of preadipocytes,[38] a number of investigators have characterized adipose-derived stromal cells (ADSCs) that are easily and relatively painlessly isolated from white adipose tissue. The ADSCs can differentiate into multiple mesenchymal cell types such as osteoblasts, chondrocytes, myocytes, cardiomyocytes, fibroblasts and adipocytes.[39]

Our interest in adipose cells is due to a possible indirect exposure to NMs, after the administration of therapeutic NPs. Studies in male mice, showed that post injection, AuNPs were accumulate predominantly within the periphery of the abdominal fat tissue, few cluster were seen further into the tissue between the adipocytes at 24 h post injection. The SEM micrographs showed that AuNPs were only found in the abdominal fat tissues and the liver. There were no AuNPs present in the other major organs investigated in this study, including brain, kidney and heart.[40]

5.2.3. Reported Cytotoxicity of Gold Nanoparticles

Since de past decade, the AuNPs have gain attention for medical applications, due to their optical properties, relative easy synthesis and surface conjugation. Along with the *in-vitro* test for therapeutic applications, have raised the toxicological assays for evaluate the possible risks at cellular-level (Cell internalization, cytotoxicity, genotoxicity, apoptosis, etc.) and at the whole organism level (organ distribution, accumulation and clearance, degradation and metabolism, immunogenicity, and inflammation).[41]

There are several reports on AuNPs cytotoxicity, even if some of them conclude that AuNPs are not toxic for cells, slight changes in form or surface chemistry may present the opposite results. Studies conducted with AuNPs of less than 2 nm show to be toxic for cells, causing necrosis, mitochondrial damage and oxidative stress. Other groups assaying 2 nm nanoparticles but having different surface charge, negative, demonstrated that AuNPs were not toxic at the same doses compared with the positively charged surface NPs.[8] The Table 5.2 listed some of cytotoxicity assays results performed in different cellular lines using functionalized AuNPs. For interest of comparison with our synthesized MB-AuNPs, we highlight the reports of cytotoxicity of AuNPs prepared with HEPES buffer versus citrate stabilized NPs, show higher *in-vitro* cell viability and lower generation of ROS in L929 mouse fibroblasts. It is important to notice that, at 5 and 10 ppm of HEPES-prepared AuNPs, a higher metabolic activity than control groups was observed, also as AuNPs concentration increased, L929 cell proliferation was inhibited at different degrees. The *in-vivo* test of the HEPES-prepared AuNPs show lower inflammation compared to citrate-NPs exposure.[22]

Table 5.2. Cytotoxicity of gold nanoparticles.

Cell line	Surface conjugation	[Cells]	[NPs]	Assay	Exposure	Toxicity	Year
COS-7	PEI 2	3×10^5/well		MTT	6 h, 42 h	70-80%	2003[42]
HepG2	BSA, peptide	85% confluence	d=20-25 nm	LDH	12h	< 5%	2003[43]
COS-1	NH3, COOH	80% confluence, 96 wells	0.38, 0.75, 1.5 o 3 µm	MTT, trypan blue	1, 2.5, 6, 24 h	LD50	2004[44]
HeLa, 3T3/NIH, HepG2	BSA, peptide	75% confluence	d= 22 nm, 150 pM	LDH	3 h	Reduced viability of 20% in HeLa, and 5% in 3T3	2004[45]
MDA-MB-231	Coumarin-PEG-SH	10^5 /well 96 wells	50-200 µg/mL d=10 nm	Cell Titer 96	24 h	Non toxic	2005[46]
RAW264.7	Lysine, PLL, FITC	10^5/well 96 wells	10-100 µM d=3-8 nm	MTT RNS Pro-inflammatory cytokines Total proteins test	24-72 h	100 µM, 72 h, reduced viability to 85%	2005[47]
CF-31	Citrate	24 wells	0.8 mg/mL, d =13 nm	Proliferation Morphology Protein synthesis	2-6 days	Vacuole present and decrease of cell adhesion and proliferation	2006[48]
L929 HeLa SK-Mel-28 J774A1			0.11 - 6.3 mM d =0.8-15 nm	Morphology MTT IC$_{50}$	0 - 48 h	1.4 nm, necrosis 12 h	2007[49]
J774A1	None	5×10^4/well 24 wells	1-10 ppM d = 2-40 nm	Proliferation Morphology	24-72 h	Short-term inflammatory response	2009[50]
HeLa ATCC 25404	PVP Acrilic resine, AC	2.5×10^4/well	0.831 nM d = 2-25 nm	MTT	24-48 h	25 nm, decrease in activity in 30 %, 2 nm, 90% of activity was maintained	2012[51]

L929	Citrate *HEPES*	96-well plates $1,2\times10^4$ cells/well	5-25 ppm	MTT ROS	24,48 h	Higher activity for 5,10 ppm of Hepes. Inhibition of cell viability for 20 and 25 ppm of citrate	2014[22]
Fibroblast cells RFPECs	Citrate HEPES	5×10^3 cells/well 96-wells plates	$0.2 - 400$ µg/mL	MTS	$1 - 4$ days	Morphology integrity at 24h $IC_{50-citrate-4d} = 27.7$ µg/mL $IC_{50-HEPES-4d} = 13.8$ µg/mL Toxic at 40µg/mL of citrate NPs Reduced viability in 20% for HEPES NPs.	2015[52]
Calu-1	HEPES	4×10^3 cell/well	200 µg/mL	WST-1	72h	Reduced viability in 20%	2016[53]

222

5.3. Experimental Procedure of Cytotoxic Evaluation of Multibranched Gold Nanoparticles in Cultured Cells

The evaluation of naked multibranched gold nanoparticles (MB-AuNPs) that were synthesized according to the methods described in Chapter 3 and MB-AuNPs conjugated with bovine serum albumin (MB-AuNPs@BSA) following protocols of Chapter 4, were performed in cultured human cells.

5.3.1. Cytotoxicity Assays in Cultured Urothelial Cells

The *in-vitro* model used for assays with urotelial cells, was the UROtsa cells. UROtsa cells are derived from normal urothelial cells that were immortalized by transfection with the SV40 virus T-antigen. This antigen inhibits the normal activity of the cell cycle regulatory proteinP53, therefore, cells grow indefinitely without aging.[54]

Although immortalized, UROtsa cells show the normal characteristics of urothelial cells, a normal chromosome number, with no ability of tumor formation in nude mice; cannot grow anchorage independent and they senesce when they reach complete confluence in cell culture. UROtsa cells have been shown to be an excellent model for toxicity studies of different substances targeting the urinary tract.[54,55]

Materials and Methods

UROtsa cells were kindly donated by Dr. Sens from the University of North Dakota. Cells were cultured in 96-well plates (1×10^8 cells/well) in DMEM medium (Dulbecco's Modified Eagle Medium), high-glucose with phenol red and supplemented with 10 % of fetal bovine serum (SFB). 24 h after plating in culture dishes, the medium was replaced by DMEM without phenol red and supplemented with 2% FBS; cells were then treated with MB-AuNPs or MB-AuNPs/BSA at concentrations that ranging from 5.2×10^8 to 10^3 NPs/mL. The different assays were performed at 24 and 48 h after the addition of NPs. For all the assays, the conditions were analyzed by triplicate, with the subtraction of culture medium as background and one-way reverse ANOVA analysis was realized.

The commercial system used for MTS assay was *Cell Titer 96*[56] from Promega, in which 3-(4,5-dimethylthiazol-2-yl)-5-(3-carboxymethoxyphenyl)-2-(4-sulfophenyl)-2H-tetrazolium (MTS) is used. The evaluation of cell proliferation was performed with an ELISA kit of Roche for BrdU quantification in proliferating cells.

Morphological Analysis. The UROtsa cells cultures were observed under bright field microscopy after 24 h exposure at concentration of 5.2×10^5 MB-AuNPs/mL and MB-AuNPs@BSA, with the aim of find visual changes in the cell morphology.

Membrane Integrity Monitoring. The LDH evaluation was carried as follow, 24 and 48 h after UROtsa cells were exposed to different concentrations of MB-AuNPs and MB-AuNPs@BSA, 100 µL of medium of each experimental condition was recovered and transfer to a clean flat-bottom 96 wells-plate. Then 100 µL of 1:45 catalyst (diaphorase/NAD+) and dye (INT) solution was added to each well. The plate was protected from the light and mixed at 60 rpm for 15 min. Absorbance was then measured at 490 nm. The wavelength used as reference was higher than 600 nm. The data cytotoxicity percentage, was evaluated according to the formula:

$$Citotoxicity\ (\%) = \frac{Experimental\ value - Control}{Control^+ - Control} \times 100$$

Positive control corresponds to cells treated with triton X-100, to promotes the total lysis.

Mitochondrial Activity Evaluation. Briefly, after 24 and 48 h of cells exposure to MB-AuNPs and MB-AuNPs@BSA, 20 µL of CellTiter 96 AQ$_{ueous}$ was added to each well, and were left to rest for 2 h in a CO_2 humidified atmosphere at 37 °C. Absorbance was determined at 492 nm.

Evaluation of Cell Proliferation. Briefly, after 24 h of seeded the UROtsa cells in 96 well plate (1×10^4/well), MB-AuNPs and MB-AuNPs@BSA were added at concentrations from 1×10^8 to 10^6 NPs/mL along with 10 µL of BrdU labeling reagent [100 µM], and were reincubated 24 h at humidified atmosphere. After the 24 h, all

medium was removed and was added 200 µL/well of FixDenant solution and left to rest for 30 min at ambient temperature, this solution has the function of fixing cells and denature DNA, to facilitate the access to incorporated BrdU. Then, all liquid was removed and was added 100 µL/well of 1:100 monoclonal antibody conjugated with peroxidase (Anti-BrdU-POD), and was left to rest for 90 min. Later, the liquid was removed and the wells were washed with PBS 1X (Phosphate Buffer Saline), with the end of removing the free antibodies. Finally, to each well was added 100 µL of substrate solution (tetramethyl-benzidine) and was left to rest at ambient temperature for 30 min. Before the UV-Vis analysis, 25 µL of H_2SO_4 [1M] was added per well to stop the reaction. The readings were acquired at 450 nm, using 690 nm as wavelength reference, the one-way reverse ANOVA method was used to analyzed the readings.

5.3.2. Cytotoxicity Assays in Cultured ADSCs

For the evaluation of toxicity due to accumulation of MB-AuNPs in adipose tissue, assays of cell proliferation were carried out in subcutaneous adipose-derived stromal cells (ADSCs).

Materials and methods

The ADSCs were inoculated in 24 well-plate ($1x10^4$ cells/well) in L15 medium supplemented with 10 % of fetal bovine serum (Basal Medium, BM). After 48 h, cells were rinsed with PBS, and new medium with MB-AuNPs@BSA were added, at increasing concentrations of NPs (see Table 5.3). After 24 h of exposure to NPs, the wells were rinsed three times with PBS and re-fed with BM. The cells were maintained at conventional atmosphere, at 37°C in a humidified 5% CO_2 atmosphere with changes of medium every three days. Cell morphology was evaluated with bright field optical microscopy and cell viability was monitored for several days by direct cell counting in a hemacytometer.

Table 5.3. MB-AuNPs concentration		
μgr	Nanoparticles	Au Mol
.35	2.6×10^7	3.6 μM
1.75	1.3×10^8	18 μM
3.5	2.6×10^8	36 μM

5.4. Assembly of Results and Discussion

Cytotoxicity Assays in Cultured Urothelial Cells

The Fig. 5.8 presents the micrographs acquired of UROtsa cells cultures exposed at the concentration of 5.2×10^5 MB-AuNPs/mL and MB-AuNPs@BSA. In the micrographs can be observed that, there is no visual chances in the cells walls neither in the nucleus due to exposure of NPs.

Control
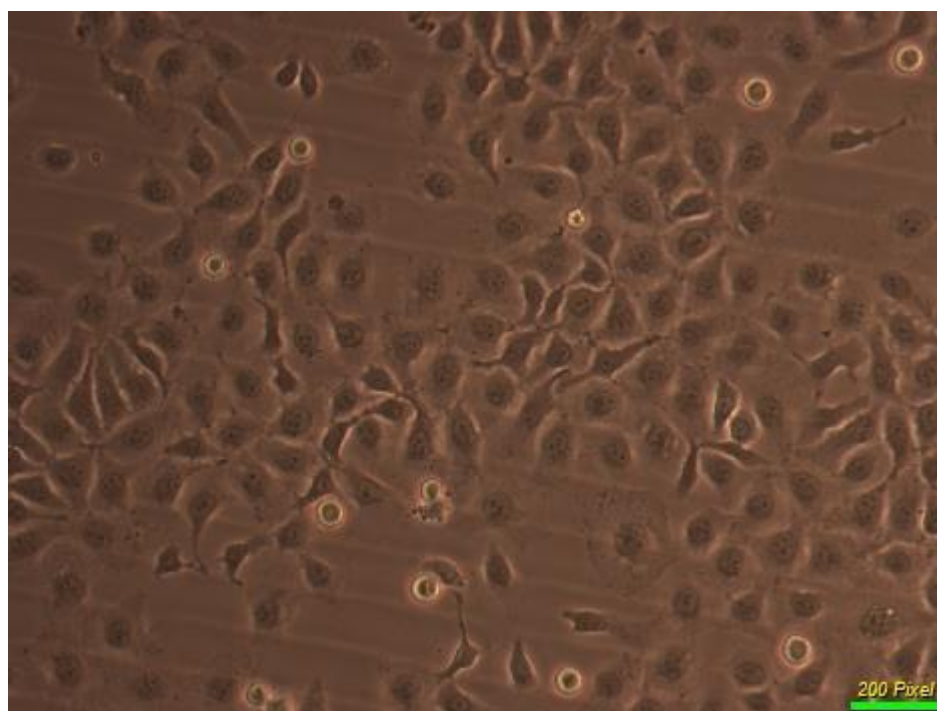
MB-AuNPs
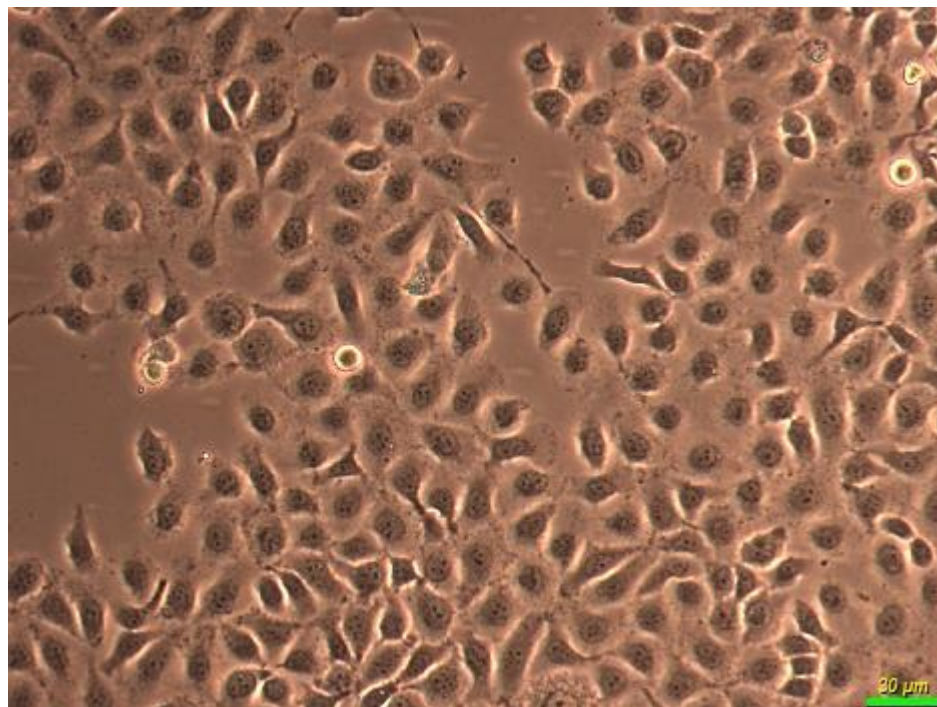
MB-AuNPs/BSA
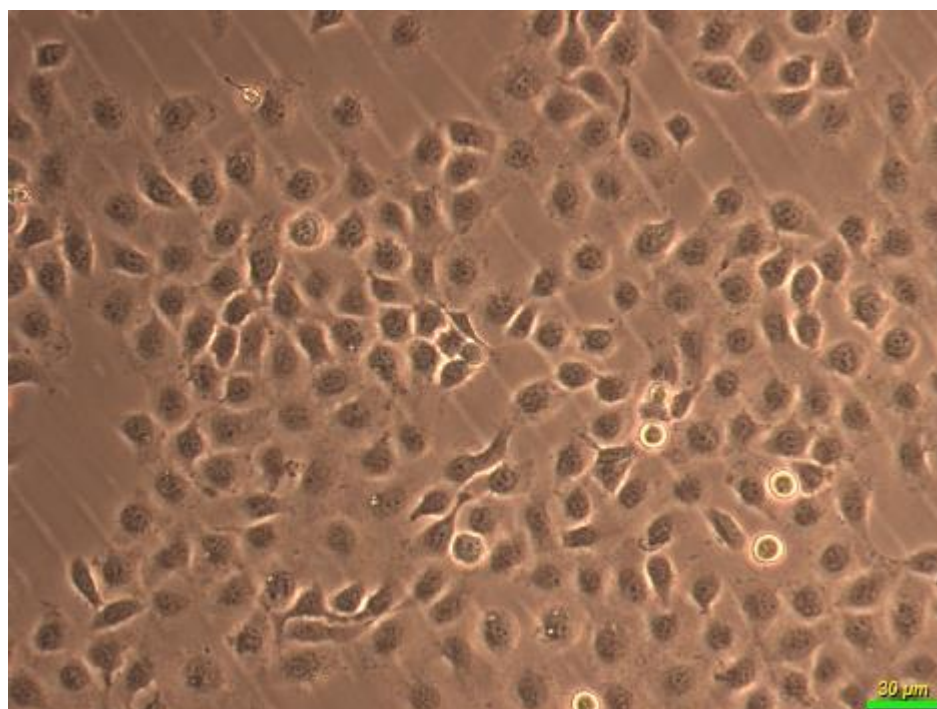
Figure 5.8. Morphological evaluation of UROtsa cell exposed for 24 h to MB-AuNPs.

The results of LDH assay (Fig. 5.9) that evaluate the membrane integrity, showed a bimodal behavior in both types of NPs. A decrease in cytotoxicity is observed as the

concentration of NPs diminish form 10^7 NPs/well, and later is an increase for order of NPs concentration of 10^5-10^4 NPs/well. The increase in LDH release, may due to an internalization of NPs in the cell, because at major NPs dispersitiy in the medium cell, NPs can interact singularly with the cells. In all evaluations, the cytotoxicity in minor for MB-AuNPs@BSA, this may be an indicative of better biocompatibility of NPs, when are conjugated with the protein. From the results can be observed that for 24 and 48 h assays, the concentration of less toxicity was in the order of 10^5 NPs/well for MB-AuNPs@BSA.

Figure 5.9. LDH-bassed cytotoxicity evaluation of UROtsa cells exposed to different concentrations of MB-AuNPs (NPs/mL) naked or conjugated with BSA

The analysis of the mitochondrial activity (MTS assay) is presented in Fig. 5.10. At concentrations of 10^5 NPs/well a decrease in mitochondrial activity is detected for

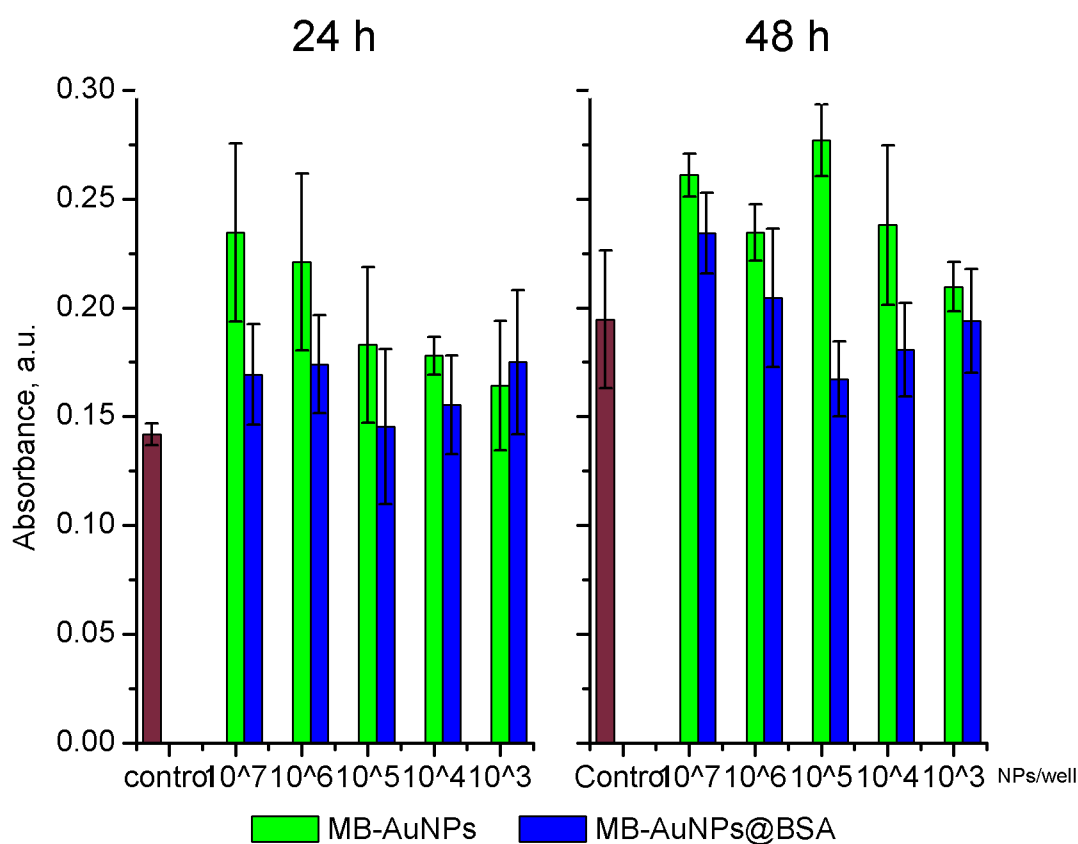24 and 48 h when MB-AuNPs@BSA are used. At 48 for same NPs, higher mitochondrial activity is observed for the lower concentration of NPs.
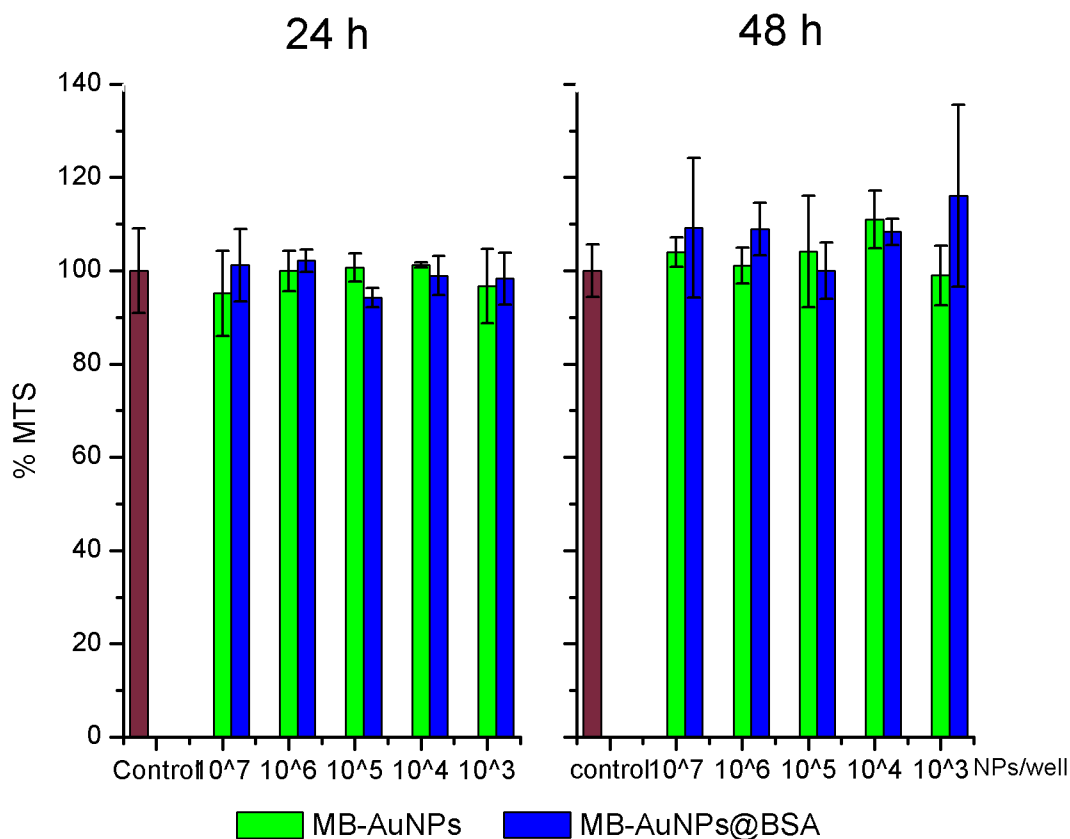
Figure 5.10. MTS quantification of UROtsa cells by absorbance spectroscopy at 490 nm, the measurement was realized after 24 and 48 h of exposure to MB-AuNPs and MB-AuNPs@BSA.

According to LDH assay, it is possible that direct interactions of NPs with cells occurs at concentrations from 10^5 to 10^3 NPs for well. Besides, we have to consider the possible internalization because of BSA conjugation.

The 48 h MTS assays results show an increase in activity of succinate dehydrogenase, this effect can be associated to major mitochondrial activity for the MB-AuNPs interaction, or to a higher proliferation of UROtsa cells, then, for better understanding of NPs effect in cellular activity, we opted for evaluate the cells proliferation throw incorporation of a nitrogenous base analogue to cellular DNA. For

this assay, ELISA kit for quantification of incorporated BrdU in proliferating was used, the analysis of readings are showed in the next figure.
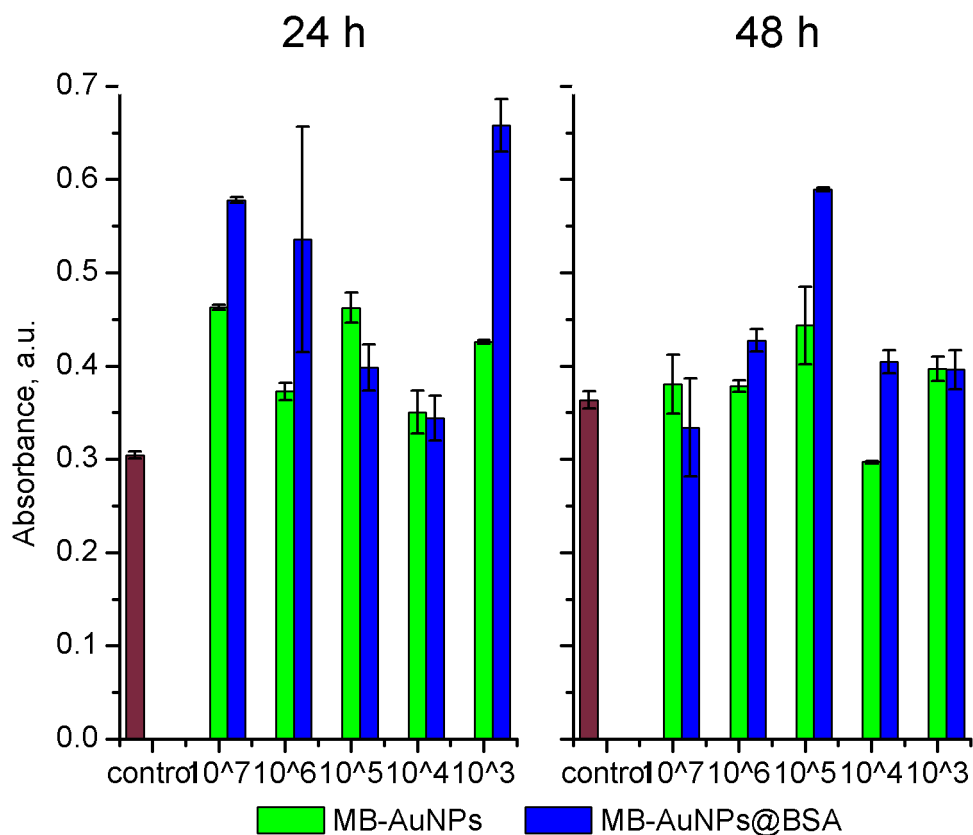
Figure 5.11.   BrdU incorporation assay in UROtsa cells exposed for 24 and 48 h to MB-AuNPs and MB-AuNPs@BSA.

Results from BrdU incorporation, suggest that MB-AuNPs@BSA promotes an increase in UROtsa cells proliferation. The effect is more perceptible when the NPs concentration is decreased, it could be due to less agglomeration of NPs and better interaction of single NPs to cells.

Cytotoxicity Assays in cultured ADSCs

After exposure of ADSCs to MB-AuNPs@BSA, morphological evaluation and cell proliferation was performed by direct observation of the cells by bright field

231

microscopy. At the morphological evaluation (see Fig. 5.12) , no perceptible damage to structure and to cellular proliferation was observed.
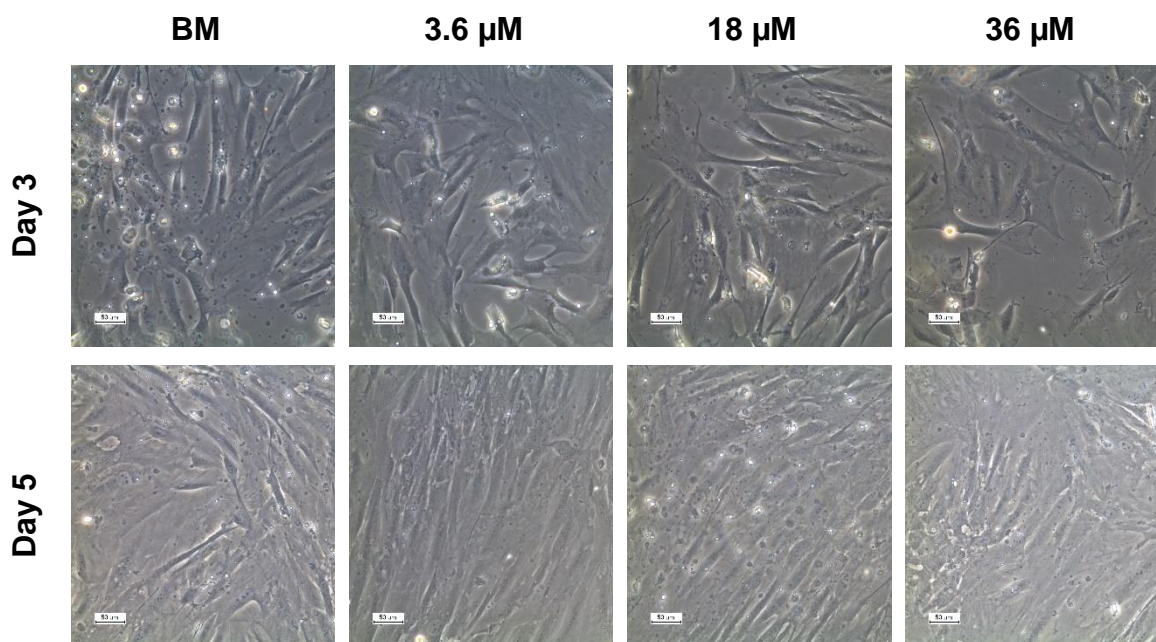
Figure 5.12. Optical micrographs capture of cells wells exposed to MB-AuNPs@BSA, acquired at 20X. A monolayer proliferation and structure integrity is preserved.
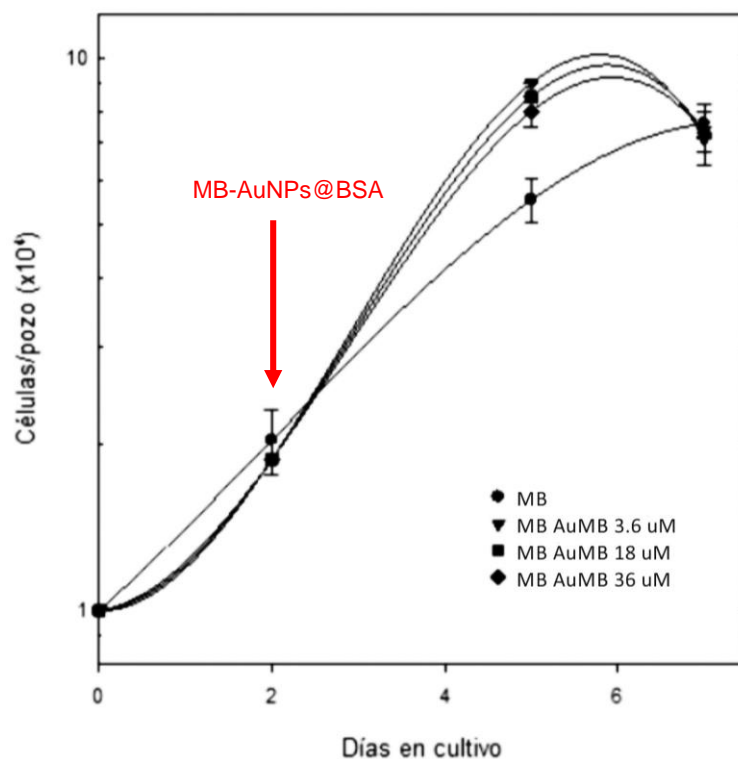
Figure 5.13. Cell proliferation of subcutaneous adipose-derived stromal cells (ADSCs) expose to increase concentration of MB-AuNPs@BSA.

Besides the observation of monolayer proliferation of cells, the wells were monitored for several days by direct cell counting in a hemacytometer, the analysis are presented in the graph of Fig. 5.13. The data corresponds to mean value of two wells. The red arrow indicates the day when the NPs were added to BM. The counting was performed at 48 and 72 h after the BM with NPs was changed.

Figures Index

Tables Index

References

(1)   Safety of Nanomedicine: Neuroendocrine Disrupting Potential of Nanoparticles and Neurodegeneration. In *Frontiers in Nanomedicine*; Rollerova, E.; Mlynarcikova, A.; Tulinska, J.; Kovriznych, J.; Kiss, A.; Scsukova, S., Eds.; BENTHAM SCIENCE PUBLISHERS, 2017; pp. 239–262.

(2)   Jain, K. K. *The Handbook of Nanomedicine*; Humana Press, 2008.

(3)   Pelaz, B.; Alexiou, C.; Alvarez-Puebla, R. A.; Alves, F.; Andrews, A. M.; Ashraf, S.; Balogh, L. P.; Ballerini, L.; Bestetti, A.; Brendel, C.; *et al.* Diverse Applications of Nanomedicine. *ACS Nano* **2017**, acsnano.6b06040.

(4)   Zhang, S.; Gao, H.; Bao, G. Physical Principles of Nanoparticle Cellular Endocytosis. *ACS Nano* **2015**, *9*, 8655–8671.

(5)   Marijnissen, J. C. M.; Gradon, L. *Nanoparticles in Medicine and Environment*; Marijnissen, J. C.; Gradon, L., Eds.; Springer Netherlands: Dordrecht, 2010.

(6)   Suh, W. H.; Suslick, K. S.; Stucky, G. D.; Suh, Y. Nanotechnology, Nanotoxicology, and Neuroscience. *Prog. Neurobiol.* **2009**, *87*, 133–170.

(7)   Zhu, X.; Hondroulis, E.; Liu, W.; Li, C. Z. Biosensing Approaches for Rapid Genotoxicity and Cytotoxicity Assays upon Nanomaterial Exposure. *Small* **2013**, *9*, 1821–1830.

(8)   Alkilany, A. M.; Murphy, C. J. Toxicity and Cellular Uptake of Gold Nanoparticles: What We Have Learned so Far? *J. Nanoparticle Res.* **2010**, *12*, 2313–2333.

(9)   Lowry, G. V; Gregory, K. B.; Apte, S. C.; Lead, J. R. Transformations of Nanomaterials in the Environment. *Environ. Sci. Technol.* **2012**, *46*, 6893–6899.

(10)   Dutta, D.; Sundaram, S. K.; Teeguarden, J. G.; Riley, B. J.; Fifield, L. S.; Jacobs, J. M.; Addleman, S. R.; Kaysen, G. A.; Moudgil, B. M.; Weber, T. J. Adsorbed Proteins Influence the Biological Activity and Molecular Targeting of Nanomaterials. *Toxicol. Sci.* **2007**, *100*, 303–315.

(11)   Dobrovolskaia, M. A.; Germolec, D. R.; Weaver, J. L. Evaluation of Nanoparticle Immunotoxicity. *Nat. Nanotechnol.* **2009**, *4*, 411–414.

(12)   Zhang, C.; Li, X.; Tian, C.; Yu, G.; Li, Y.; Jiang, W.; Mao, C. DNA Nanocages Swallow Gold Nanoparticles (AuNPs) to Form AuNP@DNA Cage Core–Shell Structures. *ACS Nano* **2014**, *8*, 1130–1135.

(13)   Jiang, Q.; Shi, Y.; Zhang, Q.; Li, N.; Zhan, P.; Song, L.; Dai, L.; Tian, J.; Du, Y.; Cheng, Z.; *et al.* A Self-Assembled DNA Origami-Gold Nanorod Complex for Cancer Theranostics. *Small* **2015**, n/a-n/a.

(14)   Dam, D. H. M.; Lee, J. H.; Sisco, P. N.; Co, D. T.; Zhang, M.; Wasielewski, M. R.; Odom, T. W. Direct Observation of Nanoparticle-Cancer Cell Nucleus Interactions. *ACS Nano* **2012**, *6*, 3318–3326.

(15)   Yin, T.; Xie, W.; Sun, J.; Yang, L.; Liu, J. Penetratin Peptide-Functionalized Gold Nanostars: Enhanced BBB Permeability and NIR Photothermal Treatment of Alzheimer's Disease Using Ultralow Irradiance. *ACS Appl. Mater. Interfaces* **2016**, *8*, 19291–19302.

(16)   Aioub, M.; Kang, B.; Mackey, M. A.; El-Sayed, M. A. Biological Targeting of Plasmonic Nanoparticles Improves Cellular Imaging via the Enhanced Scattering in the Aggregates Formed. *J. Phys. Chem. Lett.* **2014**, *5*, 2555–2561.

(17)   Kratz, F. Albumin as a Drug Carrier: Design of Prodrugs, Drug Conjugates and Nanoparticles. *J. Control. Release* **2008**, *132*, 171–183.

(18)   Kratz, F. A Clinical Update of Using Albumin as a Drug Vehicle - A Commentary. *J Control. Real* **2014**.

(19) Yin, L.; Yang, Y.; Wang, S.; Wang, W.; Zhang, S.; Tao, N. Measuring Binding Kinetics of Antibody-Conjugated Gold Nanoparticles with Intact Cells. *Small* **2015**, n/a-n/a.

(20) Qian, X.; Peng, X.-H.; Ansari, D. O.; Yin-Goen, Q.; Chen, G. Z.; Shin, D. M.; Yang, L.; Young, A. N.; Wang, M. D.; Nie, S. In Vivo Tumor Targeting and Spectroscopic Detection with Surface-Enhanced Raman Nanoparticle Tags. *Nat. Biotechnol.* **2008**, *26*, 83–90.

(21) Tsai, S.-W.; Liaw, J.-W.; Hsu, F.-Y.; Chen, Y.-Y.; Lyu, M.-J.; Yeh, M.-H. Surface-Modified Gold Nanoparticles with Folic Acid as Optical Probes for Cellular Imaging. *Sensors* **2008**, *8*, 6660–6673.

(22) Xia, D.-L.; Wang, Y.-F.; Bao, N.; He, H.; Li, X.; Chen, Y.-P.; Gu, H.-Y. Influence of Reducing Agents on Biosafety and Biocompatibility of Gold Nanoparticles. *Appl. Biochem. Biotechnol.* **2014**, *174*, 2458–2470.

(23) Marx, U.; Sadig, V. *Drug Testing In-Vitro*; Wiley-VCH, 2007.

(24) Eynard, A. R.; Valentich, M. A.; Rovasio, R. A. *Histología Y Embriología Del Ser Humano: Bases Celulares Y Moleculares*; Cuarta Edi.; Editorial Médica Panamericana: Buenos Aries, Argentina, 2008.

(25) Lewinski, N.; Colvin, V.; Drezek, R. Cytotoxicity of Nanoparticles. *Small* **2008**, *4*, 26–49.

(26) Raji, V.; Kumar, J.; Rejiya, C. S.; Vibin, M.; Shenoi, V. N.; Abraham, A. Selective Photothermal Efficiency of Citrate Capped Gold Nanoparticles for Destruction of Cancer Cells. *Exp. Cell Res.* **2011**, *317*, 2052–2058.

(27) https://lifescience.roche.com/shop/home https://lifescience.roche.com.

(28) Soloneski, S.; Larramendy, M. L. *Toxicology - New Aspects to This Scientific Conundrum*; Soloneski, S.; Larramendy, M., Eds.; InTech, 2016.

(29) https://lifescience.roche.com.

(30) Saracci, R.; Wild, C. P. *International Agency for Research on Cancer: The First 50 Years, 1965–2015*; International Agency for Research on Cancer: Lyon, France, 2015.

(31) Bertrand, N.; Leroux, J.-C. The Journey of a Drug-Carrier in the Body: An Anatomo-Physiological Perspective. *J. Control. Release* **2012**, *161*, 152–163.

(32) Glazer, E. S.; Zhu, C.; Hamir, A. N.; Borne, A.; Thompson, C. S.; Curley, S. A. Biodistribution and Acute Toxicity of Naked Gold Nanoparticles in a Rabbit Hepatic Tumor Model. *Nanotoxicology* **2011**, *5*, 459–468.

(33) Pavelka, M.; Roth, J. Urothelium. In *Functional Ultrastructure*; Springer Vienna: Vienna, 2015; pp. 290–293.

(34) Structure and functions of the digestive tract and urinary tract | Stoma Life https://www.almediaweb.jp/stomacare/life-e/contents/foundation/003.html (accessed Mar 13, 2018).

(35) American Urological Association - Urinary Bladder: Normal Urothelium http://www.auanet.org/education/auauniversity/education-products-and-resources/pathology-for-urologists/normal-histology-and-important-histo-anatomic-structures/urinary-bladder-normal-urothelium (accessed Mar 13, 2018).

(36) Pavelka, M.; Roth, J. *Functional Ultrastructure*; Springer Vienna: Vienna, 2015.

(37) Human Fat Distribution infographic - LifeMap Discovery https://discovery.lifemapsc.com/library/images/human-fat-distribution (accessed Mar 18, 2018).

(38) Green, H.; Meuth, M. An Established Pre-Adipose Cell Line and It's Differentation in Culture. *Cell* **1974**, *3*, 127–133.

(39) Rajendram, R.; Preedy, V. R.; Patel, V. B. *Stem Cells and Bone Tissue*; CRC Press,

2013.

(40) Chen, H.; Dorrigan, A.; Saad, S.; Hare, D. J.; Cortie, M. B.; Valenzuela, S. M. In Vivo Study of Spherical Gold Nanoparticles: Inflammatory Effects and Distribution in Mice. *PLoS One* **2013**, *8*.

(41) Dykman, L. A.; Khlebtsov, N. G. Multifunctional Gold-Based Nanocomposites for Theranostics. *Biomaterials* **2016**, *108*, 13–34.

(42) Thomas, M.; Klibanov, A. M. Conjugation to Gold Nanoparticles Enhances Polyethylenimine's Transfer of Plasmid DNA into Mammalian Cells. *PNAS* **2003**, *100*, 9138–9143.

(43) Tkachenko, A. G.; Xie, H.; Coleman, D.; Glomm, W.; Ryan, J.; Anderson, M. F.; Franzen, S.; Feldheim, D. L. Multifunctional Gold Nanoparticle-Peptide Complexes for Nuclear Targeting. *J. Am. Chem. Soc.* **2003**, *125*, 4700–4701.

(44) Goodman, C. M.; McCusker, C. D.; Yilmaz, T.; Rotello, V. M. Toxicity of Gold Nanoparticles Functionalized with Cationic and Anionic Side Chains. *Bioconjug. Chem.* **2004**, *15*, 897–900.

(45) Tkachenko, A. G.; Xie, H.; Liu, Y.; Coleman, D.; Ryan, J.; Glomm, W. R.; Shipton, M. K.; Franzen, S.; Feldheim, D. L. Cellular Trajectories of Peptide-Modified Gold Particle Complexes: Comparison of Nuclear Localization Signals and Peptide Transduction Domains. *Bioconjugate Chem.* **2004**, *15*, 482–490.

(46) Shenoy, D.; Fu, W.; Li, J.; Crasto, C.; Jones, G.; DiMarzio, C.; Sridhar, S.; Amiji, M. Surface Functionalization of Gold Nanoparticles Using Hetero-Bifunctional Poly(ethylene Glycol) Spacer for Intracellular Tracking and Delivery. *Int. J. Nanomed.* **2006**, *1*, 51–57.

(47) Shukla, R.; Bansal, V.; Chaudhary, M.; Basu, A.; Bhonde, R. R.; Sastry, M. Biocompatibility of Gold Nanoparticles and Their Endocytotic Fate inside the Cellular Compartment: A Microscopic Overview. *Langmuir* **2005**, *21*, 10644–10654.

(48) Pernodet, N.; Fang, X.; Sun, Y.; Bakhtina, A.; Ramakrishnan, A.; Sokolov, J.; Ulman, A.; Rafailovich, M. Adverse Effects of Citrate/Gold Nanoparticles on Human Dermal Fibroblasts. *Small* **2006**, *2*, 766–773.

(49) Pan, Y.; Neuss, S.; Leifert, A.; Fischler, M.; Wen, F.; Simon, U.; Schmid, G.; Brandau, W.; Jahnen-Dechent, W. Size-Dependent Cytotoxicity of Gold Nanoparticles. *Small* **2007**, *3*, 1941–1949.

(50) Yen, H.-J.; Hsu, S.-H.; Tsai, C.-L. Cytotoxicity and Immunological Response of Gold and Silver Nanoparticles of Different Sizes. *Small* **2009**, *5*, 1553–1561.

(51) Cui, W.; Li, J.; Zhang, Y.; Rong, H.; Lu, W.; Jiang, L. Effects of Aggregation and the Surface Properties of Gold Nanoparticles on Cytotoxicity and Cell Growth. *Nanomedicine* **2012**, *8*, 46–53.

(52) Favi, P. M.; Gao, M.; Johana Sepúlveda Arango, L.; Ospina, S. P.; Morales, M.; Pavon, J. J.; Webster, T. J. Shape and Surface Effects on the Cytotoxicity of Nanoparticles: Gold Nanospheres versus Gold Nanostars. *J. Biomed. Mater. Res. Part A* **2015**, *811170*, n/a-n/a.

(53) Tian, F.; Conde, J.; Bao, C.; Chen, Y.; Curtin, J.; Cui, D. Gold Nanostars for Efficient in Vitro and in Vivo Real-Time SERS Detection and Drug Delivery via Plasmonic-Tunable Raman/FTIR Imaging. *Biomaterials* **2016**, *106*, 87–97.

(54) Rossi, M. R.; Masters, J. R. W.; Park, S.; Todd, J. H.; Garrett, S. H.; Sens, M. A.; Somji, S.; Nath, J.; Sens, D. a. The Immortalized UROtsa Cell Line as a Potential Cell Culture Model of Human Urothelium. *Environ. Health Perspect.* **2001**, *109*, 801–808.

(55) Rossi, M. R.; Masters, J. R.; Park, S.; Todd, J. H.; Garrett, S. H.; Sens, M. a; Somji, S.; Nath, J.; Sens, D. a. The Immortalized UROtsa Cell Line as a Potential Cell Culture

Model of Human Urothelium. *Environ. Health Perspect.* **2001**, *109*, 801–808.

(56)   https:/www.promega.com.

6. General Conclusions

It is presented a seeded-growth synthesis method that uses non-aggressive chemicals for obtaining multi-branched gold nanoparticles and secondary growth branching by tuning the seed size. Analysis of the UV-Vis spectra and SEM micrographs allowed us to understand the role of each reactant in the final shape and optical response of the nanoparticles. The HEPES molecule was used as directing shape agent, it mainly directs the grow of tips from seeds with a random order; and the hydroxylamine was the surface reducing agent that also can act as a directing shape agent, but this role secondary to the reducing role. A faster depletion of the reactants (by higher concentration of hydroxylamine) during the grow reaction promotes the growth of larger tips with second-order branches.

We have determined that the synthesized multi-branched gold nanoparticles increase the temperature in a localized area irradiated with a 785 nm laser. The temperature increment recorded was $\Delta T \sim$ 5 °C, which is good enough for effective and minimally harmful gold nanoparticles based photothermal therapy techniques. Also, the 16MB-AuNPs embedded in the phantom gel is a system that rapidly absorbs the proper incident energy, achieving a plateau of constant temperature within 60 s which is consistent during three different cycles. This evaluation indicates that MB-AuNPs are an interesting system for been tested as nanoantennas in biological models. Furthermore, the evaluation of their photo-thermal behavior in cultured cells is necessary before tests in *in-vivo* models. We also propose to carry on the test with an irradiance lower that the ANSI regulation and because the experimental conditions reached in our phantoms, we expect that the transduction of light into thermal energy will be more effective, due to the limitation of MB-AuNPs reshaping.

The complex designed with the MB-AuNPs conjugated with bovine serum albumin MB-AuNPs@BSA has been proved to be stable as it has a z-potential of -29.66 mV, also the protein preserves the main function after interaction with gold surfaces, the

Raman spectra show the preservation of the α-helix structure, we also observed vibrations of the HEPES molecule, which may indicate that after conjugation the HEPES is partially replaced by the protein. The bonding of the complex to cibacron blue, indicates the signal preservation of protein, which will allow to the protein to perform the function as vehicle until albumin receptors are reached. Finally, is concluded that a full coverage protein corona y generated around the nanoparticles.

If our complex system is suitable as nanoantenna for localized photothermal therapies, we considered important to evaluate the cytotoxic effect of the complex in their passive state, this means when is not acting as heat transducer and interacts with normal cells. The *in-vitro* cytotoxicity assays show no significant toxic response from urothelial and preadipocytes cells when are exposed to MB-AuNPs@BSA. Cell membranes were no affected, neither proliferation and cells continued growing in monolayer; also the mitochondrial activity remain stable. We consider important the further analysis of NPs-cell interaction, by another assays that will provide better idea of the physical mechanism of interaction, and conclude if there is cell internalization of NPs.

Systems as MB-AuNPs@BSA have promising properties, and have given an idea of the path to follow in order to design nanomaterials suited for nanomedicine applications.

Published Research Paper

Research Article

Dynamic Infrared Thermography of Nanoheaters Embedded in Skin-Equivalent Phantoms

K. A. López-Varela [iD],[1] **N. Cayetano-Castro,**[2] **E. S. Kolosovas-Machuca,**[3] **F. J. González** [iD],[3] **F. S. Chiwo,**[3] **and J. L. Rodríguez-López** [iD] [1]

[1]*División de Materiales Avanzados, Instituto Potosino de Investigación Científica y Tecnológica, A.C., Camino Presa San José 2055, Lomas 4ª Secc., 78216 San Luis Potosí, SLP, Mexico*
[2]*Nanoscience, Micro and Nanotechnology Center, National Polytechnic Institute, Av. Luis Enrique Erro s/n, Zacatenco, 07738 Mexico City, Mexico*
[3]*Coordinación para la Innovación y la Aplicación de la Ciencia y la Tecnología, Universidad Autónoma de San Luis Potosí, San Luis Potosí, SLP, Mexico*

Correspondence should be addressed to K. A. López-Varela; karla.lopez@ipicyt.edu.mx
and J. L. Rodríguez-López; jlrdz@ipicyt.edu.mx

Nanoheaters are promising tools for localized photothermal therapy (PTT) of malignant cells. The anisotropic AuNPs present tunable surface plasmon resonances (SPR) with ideal NIR optical response to be applied as theranostic agents. To this purpose, nanoparticles with branches are suitable because of the electromagnetic field concentrated at their vertices. We standardized a protocol to synthesize multibranched gold nanoparticles (MB-AuNPs) by the seed-growth method and found a size-seed dependence tunability on the hierarchy of branching. Once the optical response is evaluated, we tested the temporal stability as nanoheaters of the MB-AuNPs immersed in skin-equivalent phantoms by dynamic infrared thermography (DIRT). The most suited sample presents a concentration of 5.2×10^8 MB-AuNPs/mL showing good thermal stability with $\Delta T = 4.5°C$, during 3 cycles of 10 min at 785 nm laser irradiation with power of 0.15 W. According to these results, the MB-AuNPs are suitable nanoheaters to be tested for PTT in more complex models.

1. Introduction

The last twenty years' research reports on nanostructured materials clearly indicate their potential to develop new technologies for different specialized areas. The extensive investigation work in shape controlled synthesis of metal nanoparticles (NPs) has allowed the achievement of structures with complicated geometric forms and the use of nontoxic chemicals for their synthesis. Gold plays a particular and special role in this area of size and shape controlled synthesis, and because of their properties, those NPs are studied for technological applications in fields such as renewable energies, catalysis, medicine, and photonics. Because of the optical and low-reactive properties of gold nanoparticles (AuNPs), they

have been considered for medical applications as theranostic agents, which means that they can be simultaneously used for drug delivery [1], medical imaging [2–5], localized photothermal therapy (PTT) [6], and biological sensing [7, 8].

Nowadays, for some specific theranostic applications AuNPs are designed with anisotropic shapes, characteristic that tunes their surface plasmon resonance (SPR) from the visible to the near (NIR) and middle infrared (Mid-IR) regions of the spectra, also presenting local concentration of electromagnetic fields on the vertices [9]. The most common anisotropic AuNPs studied and used have been the gold nanorods (AuNRs) and stellated or spiky AuNPs, here termed multibranched gold nanoparticles (MB-AuNPs). The fact that NIR absorbance of MB-AuNPs fits the so-called therapeutic

window present in the human tissue (700–1200 nm) [10], a spectral region where maximum penetration of light occurs due to the minimal absorption of blood components, such as hemoglobin and water [11], is important for these applications.

With the goal to apply these gold nanoheaters on the PTT of cancer (localized heating for killing cancer cells) [12], we have to understand their thermal response under controlled conditions. Thermal response has been evaluated by dynamic thermography technique, as infrared imaging tool for real-time recording of the temperature increases (ΔT). Since the evaluation of nanosystems in real tissue samples presents many out-of-control factors, such as the complexity in the formation of protein corona on the nanoparticles and their interaction with the physiological cellular environment [13, 14], and besides the lack of the reproducibility of results due to the difficulty in finding identical specimens, we decided the use of gel phantoms as skin-equivalent model [12, 15–17] which emulates the dielectric properties of the human body surface. Previous reports had evaluated the thermal response of AuNRs [18] in agar phantoms with intralipid® (fat emulsion) as scattered agent [19] and suggested to be effective for tumor irradiation of 10 mm depth from the illuminated tissue surface. We use for the accurate analysis of MB-AuNPs nanoheaters an optimal agar phantom model, with permittivity close to that of the human skin in the 60 GHz band [20]. The skin-equivalent phantom uses polyethylene powder (PEP) to decrease the real and imaginary parts of the permittivity.

In this report we use the organic molecule HEPES, 2-[4-(2-hydroxyethyl)-1-piperazinyl]ethanesulfonic acid, as shape directing agent. HEPES is one of the good buffers used in cell culture [21] and is also used as reducing and shape directing agent [22, 23] in the synthesis of nanoparticles by wet-chemical [24–26] and hydrothermal methods [27]. The shape promoted by HEPES in nanoparticle formation is mostly multibranched, varying from few to several peaks.

Previously reported seeded-growth synthesis protocol, in which the HEPES act as directing agent and hydroxylamine ($NH_2OH \cdot HCl$) [28–30], is used as reducing agent [31] over the seeds surface; the hydroxylamine has the role of avoiding new nucleation events during the peak growth stage. It has been also reported that hydroxylamine influences or promotes the growth of stellated gold nanoparticles [32]. Thus, we start from this method that involves two molecules, both with capping and direct-shaping properties. The function of the HEPES and hydroxylamine during the growing stage of peaks has been determined by our experimental design on concentrations of the reactants. The seed-growth method allows obtaining good monodispersity in the final product shape and size. We also had found a size-seed dependence tunability on the hierarchy of branching.

In this work, we evaluated the optical response of MB-AuNPs by UV-Vis spectroscopy, and their morphology by electronic microscopy (SEM and HRTEM). Particle density was determined by inducted coupled plasma spectrometry (ICP), and the temporal stability as nanoheaters was tested in skin-equivalent phantoms by dynamic infrared thermography (DIRT).

2. Materials and Methods

Deionized water was used for all experiments. The reagents used for NPs synthesis were obtained from Sigma-Aldrich: $HAuCl_4 \cdot 3H_2O$, HEPES, $NH_2OH \cdot HCl$, and sodium citrate. For the preparation of skin-equivalent-phantom, polyethylene powder (PEP) was obtained from Baker, Agar from Sigma-Aldrich, and TX-151 from Oil Center, and all reagents were used as received without further treatment or purification. All glassware was cleaned with aqua regia ($HCl : HNO_3$, 3 : 1) and rinsed with plenty of deionized water. The samples were characterized with UV-Vis absorption spectroscopy, acquired on a Cary 60 UV-Vis-NIR spectrophotometer at room temperature. ICP elemental quantification was performed on Variant 730-ES spectrometer. The electron micrographs were acquired in a transmission electron microscope JEOL 2100, and scanning electron micrographs in a FEI-Helios Nanolab. The X-ray diffractograms were obtained in a Bruker DX-8 system at CuKα source of wavelength 1.54056 Å. The dynamic thermographs were taken at a distance of 0.3 m from the skin-equivalent phantom [15, 33], using a high-resolution infrared camera with thermal sensitivity better than 40 mK and a 480×360 focal plane array of VOx microbolometers (FLIR T600, FLIR Systems Inc., Wilsonville, OR). The phantoms were evaluated with a 785 nm laser diode with a spot size of 3.5 mm and optical power of 0.15 W. Temperature measurements of the skin-like phantom were taken with and without MB-AuNPs. Data was analyzed with FLIR-IR Research software.

2.1. Synthesis of Multibranched Gold Nanoparticles (MB-AuNPs) Using a Seed-Growth Method. The 16 and 18 gold nanospheres (AuNSs) used as seeds were prepared by a reverse-modified Turkevich method [34] by citrate reduction of gold salt. Shortly, in a three-neck round-bottom flask with a condenser mounted, a citrate solution was brought to boiling by a heating mantle for 5 mins; then a gold solution of initial concentration of 25 mM was added, and after a light red ruby color appeared the system was left to react for half hour. For the synthesis of 16 nm AuNSs, the total concentration of sodium citrate and gold salt was 1.8 mM and 0.16 mM, respectively; and for 18 nm AuNSs were 0.75 mM and 0.25 mM. After the reaction was completed, the seeds solution was left to cool down at ambient temperature and used without modifications.

For the MB-AuNPs synthesis we used three concentrations of HEPES buffer [25, 50, 75 mM] as solution. Briefly, under slowly stirring within an ice bath (~4°C) to 12.5 mL of HEPES 50 μL of AuNSs (16 or 18 nm) was added, as well as 30, 60, or 120 μL of hydroxylamine [0.1 M], and finally the dropwise addition of gold salt solution with rate of 0.375 mL/min to a final concentration of 0.07 or 0.13 mM. For the reaction to be complete it is necessary to leave the sample to rest 8 h in the fridge. The samples were washed three times by centrifugation and a drop of the concentrated colloid was deposited on an aluminum pin for SEM and on a lacey carbon copper grid for HRTEM. For UV-Vis measurements, the samples were analyzed as synthesized. The samples for ICP quantification were centrifuged and the NPs concentrated was dissolved in aqua regia.

2.2. Fabrication of Skin-Equivalent Phantom. For the fabrication of the control phantom a previously reported protocol was used, and the reagents concentration was maintained [20]. The procedure is as follows: a Buchner flask with deionized water and agar was heated until ~80°C under slow magnetic stirring and vacuum. Once the agar was dissolved and the boiling point was reached, the vacuum and heating were turned off, the TX-151 was added and mixed gently with a stirring rod until its complete incorporation, and then the PEP was added to decrease the real and imaginary parts of the permittivity. After complete PEP incorporation the vacuum was turned on for a moment to avoid bubbles in the final phantom. Finally, the mix was placed into a petri box (ø = 55 mm) and left to solidify at ambient temperature. When phantoms with nanoparticles were prepared, a 1x concentrated of prewashed MB-AuNPs colloid was added and completely incorporated before TX-151 addition. For comparison, other phantoms with AuNSs were prepared, at the same NPs concentration of MB-AuNPs.

3. Results

3.1. Multibranched Gold Nanoparticles (MB-AuNPs). In order to prepare monodisperse MB-AuNPs, presynthesized gold single-crystalline and multitwinned nanoparticles are used as seeds for the growth of peaks [28, 29], which grow along preferential crystallographic directions of the metallic core [35]. According to previous reports, the capping agents [36] have preferential adsorption by specific crystalline faces of the metal seeds [37]; and this promotes an accelerated growth rate along specific crystallographic directions [7, 32, 38–40].

The AuNSs, obtained by the reverse Turkevich method, were monodispersed in size (see Figures 1 and SI-1); by ICP spectroscopy was determined the concentration of 2.39×10^{11} and 3.66×10^{11} NPs/mL for 16 and 18 nm AuNSs, respectively. We will see later that the structural characteristics of the AuNSs will influence the growth process of peaks; as can be seen in Figure 1(a), the 16-AuNSs present more symmetrical shape and monocrystalline structure, being different from 18-AuNSs samples (Figure 1(a)) that show multitwinned structure and nonspherical multifaceted shapes. During the stage of peaks formation, the promotion of second-order branching (Figure 3) is up to the seed structure [41] and the stabilizer agent protection [7] at the nanoparticle surface, observed in the MB-AuNPs synthesized from 18 nm nanospheres (18 MB-AuNPs), with 0.13 mM of gold salt. Also, we observed that the growth mechanism of the MB-AuNPs is influenced by the chemical characteristics of the reagents present in the growth solution and by its molar ratio with respect to gold ions.

Therefore, both hydroxylamine and HEPES are dual agents, with reducing and shape capabilities. Manipulation of the role played by each reactive is made through experimental conditions such as temperature (e.g., to slow the HEPES reducing action) and concentration of hydroxylamine (using the necessary to reduce the gold ions). Within the molar rates used in this work, the hydroxylamine governs the reaction kinetics and the final shape of the peaks and the HEPES modulate the peaks growth. A simple way to know if the HEPES has been or not contributing as reducing agent is by

means of UV-Vis spectroscopy (see Figure SI-2), since the nitrogen species from degraded HEPES can be detected by its absorption at ~346 nm [22]. It is important to mention that, in the reaction where no hydroxylamine is used, the color changes of the colloid take place slowly, evidencing that HEPES is a slow reductor. Increasing the concentration of HEPES (from 25 to 50 mM), the growth of narrow peaks is promoted while the cores remain small. Then the addition of hydroxylamine is necessary to modulate the kinetics without excess of HEPES and will help to obtain better definition on the peaks and a monodisperse size and shape sample (see Figure SI-3). From the mechanism reduction of Au^{3+} by hydroxylamine proposed by Minati et al. [42], the molar ratio of $Au^{3+} : NH_2OH$ (1:3) was used to synthesize the sample with 16 nm nanospheres (16 MB-AuNPs), in order to avoid the intervention of HEPES reducing action (see Figure SI-2). We observed that, when hydroxylamine is present and increases its molar rate, the change of colors gets faster indicating the necessary use of a mild reducing agent (hydroxylamine) simultaneously with a directing shape agent (HEPES) for better anisotropic growth. We also have determined that an excess of hydroxylamine promotes the second-order branching in 18 MB-AuNPs, which was synthesized with molar rate of $Au^{3+} : NH_2OH$ of 1:6 (see Figure SI-4).

It had been reported that the size of the NPs used as seeds influences the shape of final products [30, 43]. In our results we observed that from 16-AuNSs, MB-AuNPs of 80 nm of diameter can be obtained, synthesized with 0.07 mM of gold salt (16 MB-AuNPs, see Figure SI-5), and the colloid presents a maximum absorbance at 728 nm (Figure 2). On the other hand, dendritic growth is only perceptible in 18 MB-AuNPs (Figure 3), even if the concentration of gold ions is increased in the samples synthesized from 16-AuNSs (see Figure SI-6). The increase in gold ions leads to bigger cores and smaller length of peaks, due to an addition of gold atoms between peaks for minimization of energy, instead of the growth of longer peaks [44, 45].

At this stage we have shown that both sets of samples (16 and 18 MB-AuNPs) present good optical response for being used as nanoheaters. The next criteria for choosing a sample is the critical size for being used in an in vitro or in vivo environment. Thus, we decided the use of 16 MB-AuNPs for being tested as nanoheaters; however, the optical response of 18 MB-AuNPs in the 830 nm (Figure 3) is suitable for applications in nanostructured system for SERS [46].

3.2. Thermal Response of MB-AuNPs. Infrared (IR) imaging is based on the fact that any object at a temperature above absolute zero (−273°C) will emit IR radiation, even if only weakly. The human body has a low thermal emittance, radiating in a wavelength range that starts at around 3 μm and peaks in the vicinity of 10 μm and trails off from this point into the extreme IR and, negligibly, beyond it. The emissivity of human skin has a constant value between wavelengths of 2 and 14 μm of 0.98 ± 0.01 for black skin and 0.97 ± 0.02 for white skin [47]; thus, human skin has a known and almost invariant emissivity in this wavelength region that makes IR imaging an ideal procedure to evaluate surface temperature of
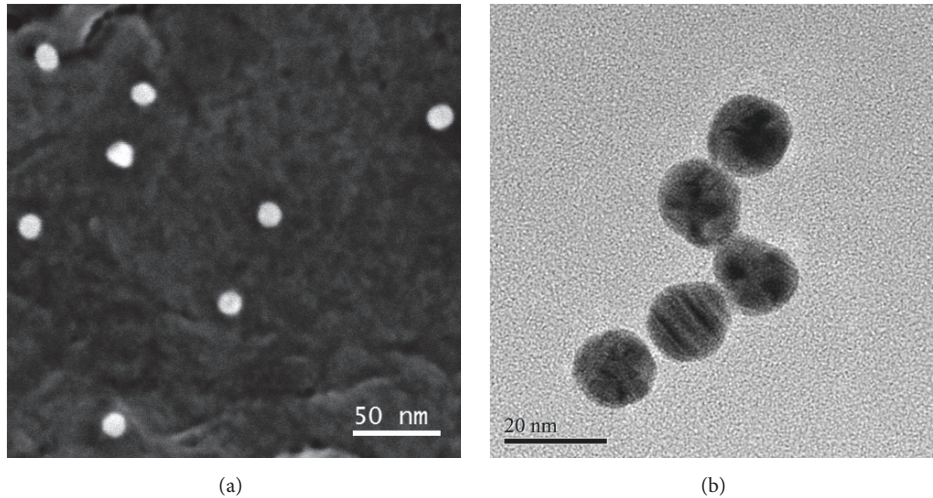
(a)

(b)

FIGURE 1: (a) SEM micrograph of 16 ± 1.69 nm of spheres gold nanoparticles (16-AuNSs). (b) TEM micrograph of 18.18 ± 2.33 nm sphere gold nanoparticles (18-AuNSs) used as seeds.
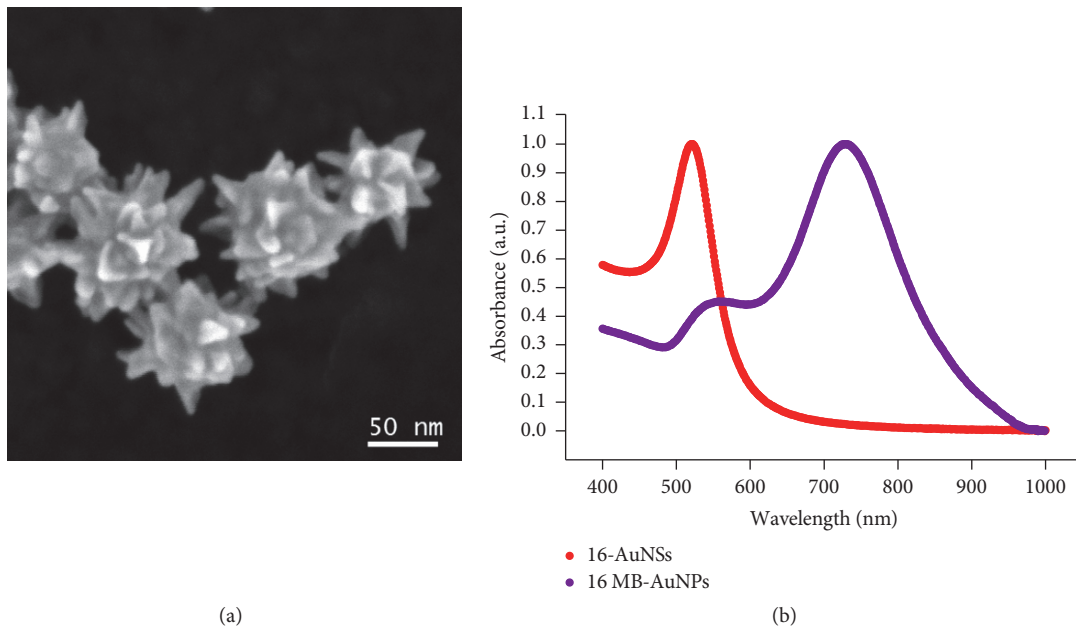

(a)

(b)

FIGURE 2: (a) SEM micrograph of 16 MB-AuNPs synthetized with 16-AuNSs. (b) UV-Vis spectra of 16-AuNSs and 16 MB-AuNPs with a band centered at 520 nm and 729 nm, respectively.

the human body [48, 49]. Because of the above arguments, the skin-equivalent phantoms with 0.62±0.01 reported emittance [17] is a well suited model for IR thermal evaluation.

The thermal response of 16-AuNSs and 16 MB-AuNPs was evaluated inside the skin-equivalent phantoms by dynamic thermography. The samples were irradiated at 0.15 W power laser by 3 cycles of 10 mins and recorded with an IR camera, and the thermographs shown at Figure 4 were extracted at 555 s using the FLIR-RIR software, which allows the analysis of single points, line profiles, and averages of circle/rectangular areas. The plot in Figure 4(a) shows data from a line profile analyzed at different times, and it clearly can be observed that not only the incident laser area has been heated

but also there is a radial propagation by diffusion of the generated heat; thus there is energy transmitted to the adjacent regions due to the immersed NPs. This effect is also observed in the control phantom analysis, but over a smaller area and with more uniform temperature as can be seen in Figure SI-7. Figure 4(b) reports the information on how fast the system absorbs the energy, achieving constant temperature at early irradiation times (60 s). This was also performed for evidence the continuity of the thermal response of immersed 16 MB-AuNPs in the phantom as a function of time.

The plot in Figure 5 corresponds to a dynamic thermal analysis, and from it we can appreciate the difference in the temperature reached by the three phantoms: the largest

(a)

(b)
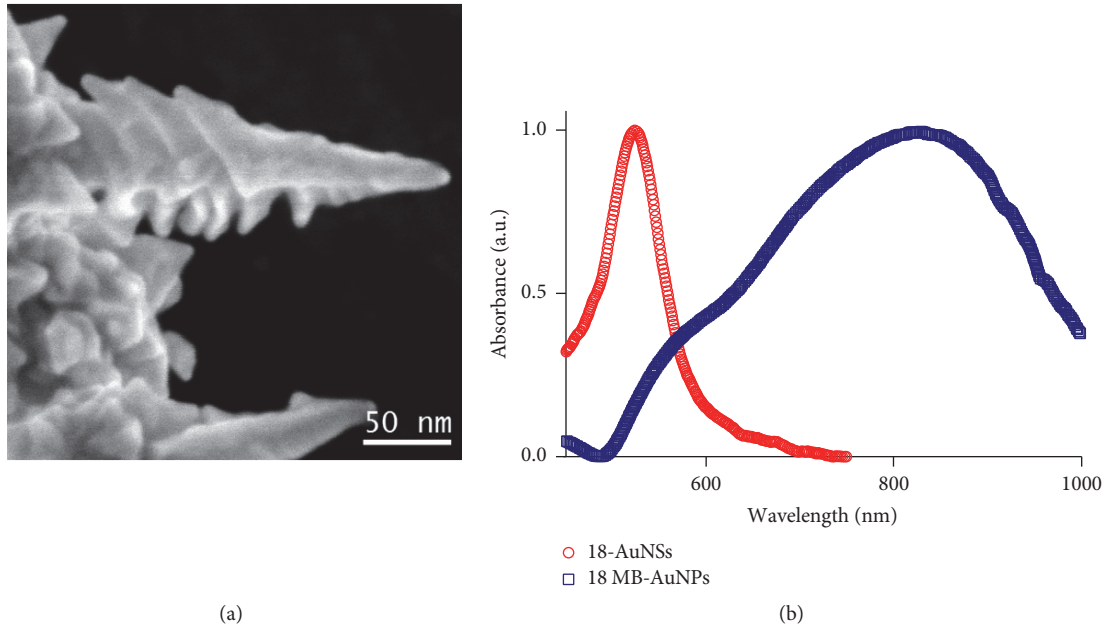
FIGURE 3: SEM micrographs (a) of 18 MB-AuNPs with second order branches and UV-Vis spectra (b) of 18-AuNSs and 18 MB-AuNPs; they have a band centered at 524 nm and 830 nm, respectively.

(a)

(b)
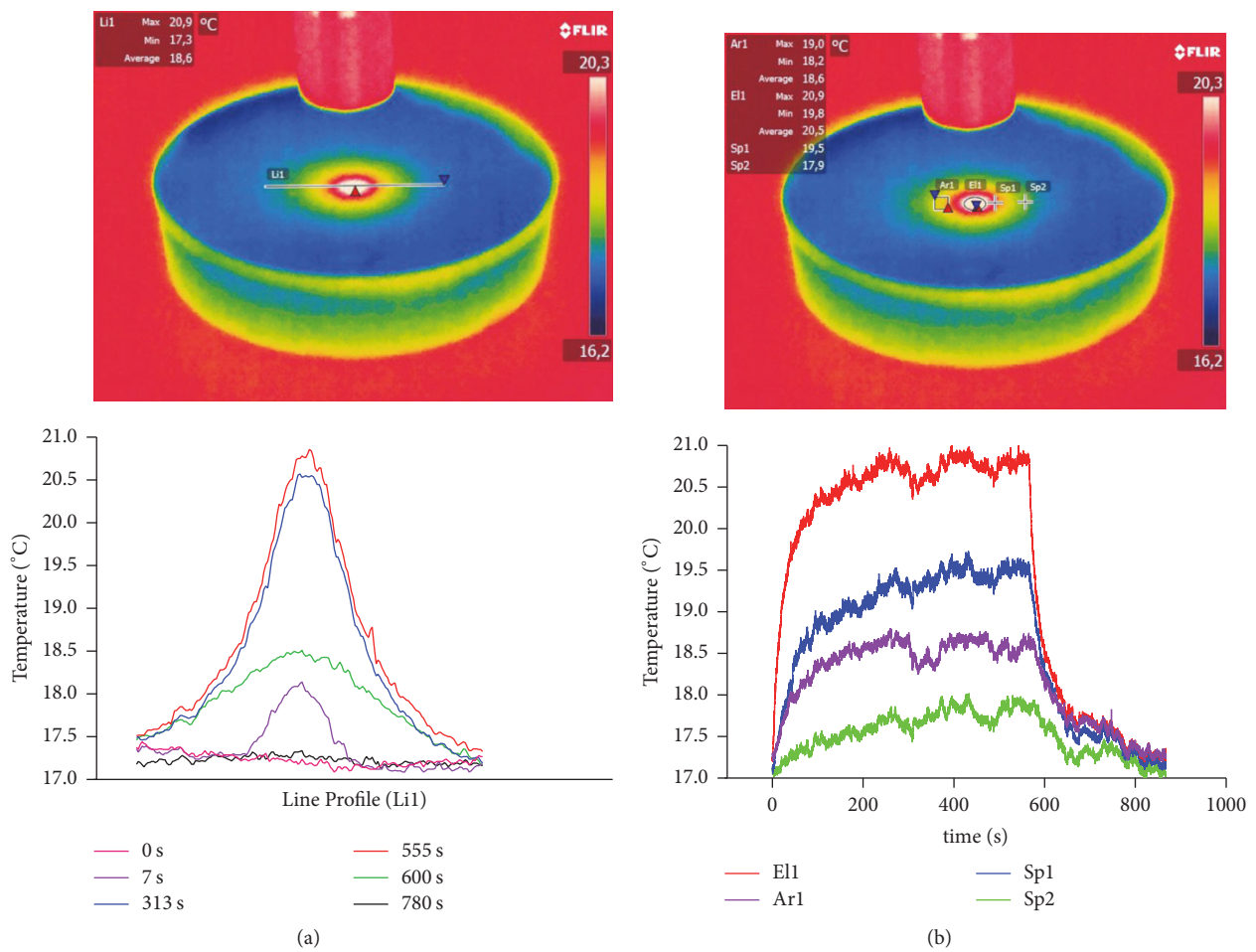
FIGURE 4: The thermography corresponds at the 555 s of laser irradiation. (a) Temperature profiles of the heating area at different times. The profile analyzed is designed as Line 1 (Li1) in the thermography. (b) Temporal analysis of temperature variations of different points and regions marked in the thermography as area (Ar1), elipsoide (El1), and singles points (Sp1, Sp2).

Figure 5: Thermal response of skin-equivalent phantoms with 16-AuNSs, 16 MB-AuNPs, and control.

increase of localized temperature is measured in the sample prepared with 16 MB-AuNPs, compared to the phantom with 16-AuNSs and the one without the addition of NPs, used as a control.

A red-shift of the LSPR is present for anisotropic MB-AuNPs compared with spheres (see Figure 1), and a substantial increase in the heating efficiency with respect the sphere is expected. In our results, th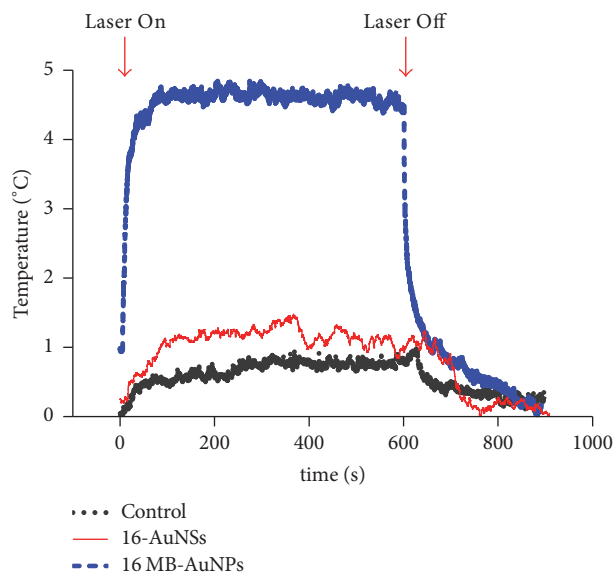e maximum temperature increment in 16 MB-AuNPs phantom was achieved in 60 s and maintained during all the laser irradiation. This temperature increment is $\Delta T = 4.5°C$ and when the light source is turned off, a fast decay is observed. The comparison between the AuNSs and MB-AuNPs at the same concentration shows the evident increase of thermal response due to the anisotropic shape of MB-AuNPs and the localized SPR's synergy, because the MB-AuNPs absorbs closer to the wavelength of laser irradiation. In the case of the phantom with 16-AuNSs, the increment in temperature can be described for the excitation of hot-spots created in the interaction among spherical NPs [50, 51]. The fact that there were not physical changes observed in the phantoms under laser irradiation, as leaking or deformation, even after the three cycles evaluation is important to mention.

4. Discussion

We have shown that the control on the width, the length, the number of peaks, and the degree of dendritic growth gives rise to an easy tuning of the plasmon resonance spectra [6] and their corresponding higher transduction of light into heat, and therefore gold nanoheaters are good candidates for IR absorption for efficient photothermal therapy of malignant cancer cells.

The structural characteristics of the AuNSs influenced the degree of ramification of the nanoparticle tips, resulting in

second-order branches for MB-AuNPs synthesized from 18-AuNSs, which present crystalline defects promoting directed anisotropy. From 16-AuNSs we could obtain monodisperse samples. After analyzing the impact of HEPES and hydroxylamine on the final tips shape, we estimated that the optimal molar ratio of hydroxylamine : Au ions is 3 : 1, where this amount is enough to avoid the intervention of HEPES in the reduction. Even if an excess of hydroxylamine may result in a better definition of tips, it can also cause the agglomeration of MB-AuNPs, due to the resulting high ionic force of the solution, that could not be used for clinical applications, and the same argument is valid for higher concentration of HEPES (75 mM). On the other side, the increase on the molar concentration of Au ions (and necessary hydroxylamine) leads to bigger cores and smaller length of tips; thus it shifts the SPR to lower wavelengths making them not practical for PTT.

Regarding the dynamic thermography results for 16 MB-AuNPs, we found that not only the incident laser area is being heated, but also there is a radial propagation of the released heat, which means there is transmission of energy around the adjacent region of the spot due to the immersed NPs. Therefore, the addition of MB-AuNPs results in the production of more efficient centers for scattering and reemission of energy.

The temperature increment achieved by the nanoheaters in this work ($\Delta T \sim 5°C$) is good enough for effective and minimally harmful gold nanoparticles based photothermal therapy techniques [52]. This temperature increment from multi-branched gold nanoparticles immersed in a phantom gel (as a model approach for the real environment in bioapplications) satisfies biomedical requirement for the treatment of superficial diseases (mycoses, fungal infections, and many different types of skin cancer) [53].

5. Conclusions

A synthesis method that uses nonaggressive chemicals for obtaining multibranched gold nanoparticles and secondary growth branching by tuning the seed size is presented. Analysis of the UV-Vis spectra and SEM micrographs allows us to understand the role of each reactant in the final shape of the nanoparticles. The HEPES molecule mainly grow tips from seeds with a random order; and the hydroxylamine can act as a directing shape agent, but this role only follows after its reduction role has been finished in the reaction. A faster depletion of the reactants (by higher concentration of hydroxylamine) during the grow reaction promotes the growth of larger tips with second-order branches.

We have determined that the synthesized multibranched gold nanoparticles increase the temperature in a localized area irradiated with a 785 nm laser. The temperature increment recorded was $\Delta T = 4.5°C$. The 16 MB-AuNPs embedded in the phantom gel is a system that rapidly absorbs the proper incident energy, achieving a plateau of constant temperature within 60 s which is recovered during at least three different cycles. This evaluation indicates MB-AuNPs as an interesting system for being tested as nanoheater in biological models. Furthermore, the evaluation of their photothermal behavior in cultured cells is necessary for their direct application in

medicine. We also propose to carry on the test with an irradiance lower than the ANSI regulation. Due to the experimental conditions reached in our phantoms, we expect that the transduction of light into thermal energy will be more effective, due to the limitation of MB-AuNPs reshaping.

Conflicts of Interest

The authors declare that they have no conflicts of interest.
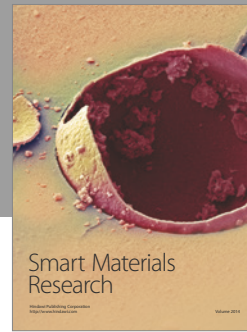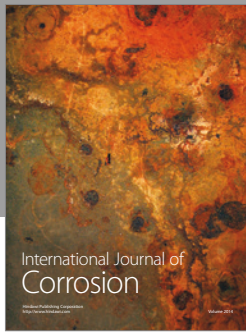
Acknowledgments

Supplementary Materials

Figure SI-1. Histograms of diameters and frequency distribution data of populations of (a) 200 AuNSs for 16-AuNSs and (b) 100 for 18-AuNSs. Figure SI-2. The increase of the molar concentration of HEPES promotes strong anisotropic formation of the MB-AuNPs. Figure SI-3. Scanning electron microscopy micrograph of 16 MB-AuNPs; the monodispersity and nonagglomeration of the NPs can be observed. Figure SI-4. Diagram of the concentrations of reactants used for the samples analyzed. Figure SI-5. Histograms of diameters and frequency distribution data of populations of 50 16 MB-AuNPs. Figure SI-6. SEM micrographs of MB-AuNPs synthesized in a medium of HEPES [50 mM], with a molar ratio Au3+/NH2OH of 1 : 3, with (a) 16-AuNSs and (b)-(c) 18-AuNSs. Figure SI-7. Thermography of skin-equivalent phantom used as control. *(Supplementary Materials)*

References

[1] T. Lajunen, L. Viitala, L.-S. Kontturi et al., "Light induced cytosolic drug delivery from liposomes with gold nanoparticles," *Journal of Controlled Release*, vol. 203, pp. 85–98, 2015.

[2] A. Guerrero-Martínez, S. Barbosa, I. Pastoriza-Santos, and L. M. Liz-Marzán, "Nanostars shine bright for you: colloidal synthesis, properties and applications of branched metallic nanoparticles," *Current Opinion in Colloid & Interface Science*, vol. 16, no. 2, pp. 118–127, 2011.

[3] Z. Fan and H. Zhang, "Template synthesis of noble metal nanocrystals with unusual crystal structures and their catalytic applications," *Accounts of Chemical Research*, vol. 49, no. 12, pp. 2841–2850, 2016.

[4] W. Park, S. Cho, X. Huang, A. C. Larson, and D. Kim, "Branched Gold Nanoparticle Coating of Clostridium novyi-NT Spores for CT-Guided Intratumoral Injection," *Small*, vol. 13, no. 5, Article ID 1602722, 2017.

[5] Y. Ponce De León, J. L. Pichardo-Molina, N. Alcalá Ochoa, and D. Luna-Moreno, "Contrast enhancement of optical coherence tomography images using branched gold nanoparticles," *Journal of Nanomaterials*, vol. 2012, Article ID 571015, 9 pages, 2012.

[6] A. Espinosa, A. K. A. Silva, A. Sánchez-Iglesias et al., "Cancer cell internalization of gold nanostars impacts their photothermal efficiency in vitro and in vivo: toward a plasmonic thermal fingerprint in tumoral environment," *Advanced Healthcare Materials*, vol. 5, no. 9, pp. 1040–1048, 2016.

[7] J. P. Xie, Q. B. Zhang, J. Y. Lee, and D. I. C. Wang, "The synthesis of SERS-active gold nanoflower tags for in vivo applications," *ACS Nano*, vol. 2, no. 12, pp. 2473–2480, 2008.

[8] M. Aioub and M. A. El-Sayed, "A Real-time surface enhanced raman spectroscopy study of plasmonic photothermal cell death using targeted gold nanoparticles," *Journal of the American Chemical Society*, vol. 138, no. 4, pp. 1258–1264, 2016.

[9] X.-L. Liu, J.-H. Wang, S. Liang et al., "Tuning plasmon resonance of gold nanostars for enhancements of nonlinear optical response and raman scattering," *The Journal of Physical Chemistry C*, vol. 118, no. 18, pp. 9659–9664, 2014.

[10] F. J. González, "Noninvasive detection of filaggrin molecules by raman spectroscopy," in *Filaggrin*, pp. 93–101, Springer Berlin Heidelberg, Berlin, Germany, 2014.

[11] H. Berlien and G. J. Müller, *Applied Laser Medicine*, Springer, Berlin, Heidelberg, Germany, 2003.

[12] R. Ahmad, J. Fu, N. He, and S. Li, "Advanced Gold Nanomaterials for Photothermal Therapy of Cancer," *Journal of Nanoscience and Nanotechnology*, vol. 16, no. 1, pp. 67–80, 2016.

[13] P. Foroozandeh and A. A. Aziz, "Merging worlds of nanomaterials and biological environment: factors governing protein corona formation on nanoparticles and its biological consequences," *Nanoscale Research Letters*, vol. 10, no. 1, p. 221, 2015.

[14] D. Walczyk, F. B. Bombelli, M. P. Monopoli, I. Lynch, and K. A. Dawson, "What the cell "sees" in bionanoscience," *Journal of the American Chemical Society*, vol. 132, no. 16, pp. 5761–5768, 2010.

[15] G. P. Mazzara, R. W. Briggs, Z. Wu, and B. G. Steinbach, "Use of a modified polysaccharide gel in developing a realistic breast phantom for MRI," *Magnetic Resonance Imaging*, vol. 14, no. 6, pp. 639–648, 1996.

[16] M. N. Iizuka, M. D. Sherar, and I. A. Vitkin, "Optical phantom materials for near infrared laser photocoagulation studies," *Lasers in Surgery and Medicine*, vol. 25, no. 2, pp. 159–169, 1999, http://www.ncbi.nlm.nih.gov/pubmed/10455223.

[17] Y. Okano, K. Ito, I. Ida, and M. Takahashi, "The SAR evaluation method by a combination of thermographic experiments and biological," *IEEE Trans. Microw. Theory Tech*, vol. 48, pp. 2094–2103, 2000.

[18] N. R. Jana, L. Gearheart, and C. J. Murphy, "Wet chemical synthesis of high aspect ratio cylindrical gold nanorods," *The Journal of Physical Chemistry B*, vol. 105, no. 19, pp. 4065–4067, 2001.

[19] C. L. Didychuk, P. Ephrat, A. Chamson-Reig, S. L. Jacques, and J. J. L. Carson, "Depth of photothermal conversion of gold nanorods embedded in a tissue-like phantom," *Nanotechnology*, vol. 20, no. 19, Article ID 195102, 2009.

[20] N. Chahat, M. Zhadobov, S. Alekseev, and R. Sauleau, "Human skin-equivalent phantom for on-body antenna measurements in 60GHz band," *IEEE Electronics Letters*, vol. 48, no. 2, pp. 67-68, 2012.

[21] N. E. Good and S. Izawa, "Hydrogen Ion Buffers," *Methods in Enzymology*, vol. 24, no. C, pp. 53–68, 1972.

[22] A. Habib, M. Tabata, and Y. G. Wu, "Formation of Gold Nanoparticles by Good's Buffers," *Bulletin of the Chemical Society of Japan*, vol. 78, no. 2, pp. 262–269, 2005.

[23] J. Xie, J. Y. Lee, and D. I. C. Wang, "Seedless, surfactantless, high-yield synthesis of branched gold nanocrystals in HEPES buffer solution," *Chemistry of Materials*, vol. 19, no. 11, pp. 2823–2830, 2007.

[24] R. Chen, J. Wu, H. Li, G. Cheng, Z. Lu, and C.-M. Che, "Fabrication of gold nanoparticles with different morphologies in HEPES buffer," *Rare Metals*, vol. 29, no. 2, pp. 180–186, 2010.

[25] Y. Bao, H.-C. Yeh, C. Zhong et al., "Formation and stabilization of fluorescent gold nanoclusters using small molecules," *The Journal of Physical Chemistry C*, vol. 114, no. 38, pp. 15879–15882, 2010.

[26] S. Chen, Q. Lei, W.-X. Qiu et al., "Mitochondria-targeting "Nanoheater" for enhanced photothermal/chemo-therapy," *Biomaterials*, vol. 117, pp. 92–104, 2017.

[27] H. Li, Z. Lu, J. Wu, H. Yu, X. Yu, and R. Chen, "Hydrothermal synthesis of transition metal oxide nanomaterials in HEPES buffer solution," *Materials Letters*, vol. 64, no. 18, pp. 1939–1942, 2010.

[28] G. Maiorano, L. Rizzello, M. A. Malvindi et al., "Monodispersed and size-controlled multibranched gold nanoparticles with nanoscale tuning of surface morphology," *Nanoscale*, vol. 3, no. 5, pp. 2227–2232, 2011.

[29] G. Plascencia-Villa, D. Bahena, A. R. Rodríguez, A. Ponce, and M. José-Yacamán, "Advanced microscopy of star-shaped gold nanoparticles and their adsorption-uptake by macrophages," *Metallomics*, vol. 5, no. 3, pp. 29–32, 2013.

[30] F. Tian, J. Conde, C. Bao, Y. Chen, J. Curtin, and D. Cui, "Gold nanostars for efficient in vitro and in vivo real-time SERS detection and drug delivery via plasmonic-tunable Raman/FTIR imaging," *Biomaterials*, vol. 106, pp. 87–97, 2016.

[31] K. R. Brown and M. J. Natan, "Hydroxylamine seeding of colloidal Au nanoparticles in solution and on surfaces," *Langmuir*, vol. 14, no. 4, pp. 726–728, 1998.

[32] L. Jiang, Y. Tang, C. Liow et al., "Synthesis of fivefold stellate polyhedral gold nanoparticles with 110-facets via a seed-mediated growth method," *Small*, vol. 9, no. 5, pp. 705–710, 2013.

[33] K. Ito, K. Furuya, Y. Okano, and L. Hamada, "Development and Characteristics of a Biological Tissue-Equivalent Phantom for Microwaves," *Electron. Commun. Japan Part I Commun*, vol. 84, pp. 67–77, 2001.

[34] S. K. Sivaraman, S. Kumar, and V. Santhanam, "Monodisperse sub-10nm gold nanoparticles by reversing the order of addition in Turkevich method - The role of chloroauric acid," *Journal of Colloid and Interface Science*, vol. 361, no. 2, pp. 543–547, 2011.

[35] M. Zhu, B. Lei, F. Ren et al., "Branched Au Nanostructures enriched with a uniform facet: facile synthesis and catalytic performances," *Scientific Reports*, vol. 4, no. 1, article 05259, 2015.

[36] W. Ahmed, E. Stefan Kooij, A. Van Silfhout, and B. Poelsema, "Controlling the morphology of multi-branched gold nanoparticles," *Nanotechnology*, vol. 21, no. 12, Article ID 125605, 2010.

[37] P. Senthil Kumar, I. Pastoriza-Santos, B. Rodríguez-González, F. Javier García De Abajo, and L. M. Liz-Marzán, "High-yield synthesis and optical response of gold nanostars," *Nanotechnology*, vol. 19, no. 1, Article ID 015606, 2008.

[38] L. Zhao, X. Ji, X. Sun, J. Li, W. Yang, and X. Peng, "Formation and stability of gold nanoflowers by the seeding approach: the effect of intraparticle ripening," *The Journal of Physical Chemistry C*, vol. 113, no. 38, pp. 16645–16651, 2009.

[39] D. H. M. Dam, J. H. Lee, P. N. Sisco et al., "Direct observation of nanoparticle-cancer cell nucleus interactions," *ACS Nano*, vol. 6, no. 4, pp. 3318–3326, 2012.

[40] H. Yuan, M. Wanhong, C. Chen et al., "Shape and SPR evolution of thorny gold nanoparticles promoted by silver ions," *Chemistry of Materials*, vol. 19, no. 7, pp. 1592–1600, 2007.

[41] O. Bibikova, A. Popov, A. Bykov et al., "Plasmon-resonant gold nanostars with variable size as contrast agents for imaging applications," *IEEE Journal of Selected Topics in Quantum Electronics*, vol. 22, no. 3, Article ID 2526602, pp. 13–20, 2016.

[42] L. Minati, F. Benetti, A. Chiappini, and G. Speranza, "One-step synthesis of star-shaped gold nanoparticles," *Colloids and Surfaces A: Physicochemical and Engineering Aspects*, vol. 441, pp. 623–628, 2014.

[43] A. Gole and C. J. Murphy, "Seed-mediated synthesis of gold nanorods: role of the size and nature of the seed," *Chemistry of Materials*, vol. 16, no. 19, pp. 3633–3640, 2004.

[44] R. G. Weiner and S. E. Skrabalak, "Metal dendrimers: Synthesis of hierarchically stellated nanocrystals by sequential seed-Directed overgrowth," *Angewandte Chemie International Edition*, vol. 54, no. 4, pp. 1181–1184, 2015.

[45] M. S. Bakshi, "How surfactants control crystal growth of nanomaterials," *Crystal Growth and Design*, vol. 16, no. 2, pp. 1104–1133, 2016.

[46] A. Zoppi, S. Trigari, G. Margheri, M. Muniz-Miranda, and E. Giorgetti, "Gold nanostars as SERS-active substrates for FT-Raman spectroscopy," *RSC Advances*, vol. 5, no. 11, pp. 8523–8532, 2015.

[47] B. F. Jones, "A reappraisal of the use of infrared thermal image analysis in medicine," *IEEE Transactions on Medical Imaging*, vol. 17, no. 6, pp. 1019–1027, 1998.

[48] J. Teich, "Digital infrared imaging for medicine. Recent advances in I.R. focal plane array imaging technology," in *Proceedings of the 18th Annual International Conference of the IEEE Engineering in Medicine and Biology Society*, pp. 2079-2080, Amsterdam, Netherlands.

[49] J. P. Gore and L. X. Xu, "Thermal imaging for biomedical and medical diagnostics," in *Biomedical Photonics Handbook*, T. Vo-Dinh, Ed., CRC Press, Boca Raton, FL, USA, 2003.

[50] C. Farcau and S. Astilean, "Mapping the SERS efficiency and hot-spots localization on gold film over nanospheres substrates," *The Journal of Physical Chemistry C*, vol. 114, no. 27, pp. 11717–11722, 2010.

[51] A. J. Pasquale, B. M. Reinhard, and L. Dal Negro, "Engineering photonic-plasmonic coupling in metal nanoparticle necklaces," *ACS Nano*, vol. 5, no. 8, pp. 6578–6585, 2011.

[52] X. Zhu, W. Feng, J. Chang et al., "Temperature-feedback upconversion nanocomposite for accurate photothermal therapy at facile temperature," *Nature Communications*, vol. 7, Article ID 10437, 2016.

[53] G. Chirico, P. Pallavicini, and M. Collini, "Gold nanostars for superficial diseases: A promising tool for localized hyperthermia?" *Nanomedicine*, vol. 9, no. 1, pp. 1–3, 2014.

Journal of
Nanotechnology

International Journal of
Corrosion

International Journal of
Polymer Science

Smart Materials
Research

Journal of
Composites

BioMed
Research International

Journal of
Metallurgy

Journal of
Materials

Hindawi

Submit your manuscripts at
https://www.hindawi.com

Journal of
Nanoparticles

Advances in
Materials Science and Engineering

Scientifica

Journal of
Nanomaterials

The Scientific
World Journal

International Journal of
Biomaterials

Journal of
Nanoscience

Journal of
Coatings

Journal of
Crystallography

Journal of
Ceramics

Journal of
Textiles